

Evaluating MRI biomarkers of tumour hypoxia

Elise Yuri Lopicard

A thesis submitted for the degree of
Doctor of Philosophy
of the
University of London



August 2020

Division of Radiotherapy & Imaging
Institute of Cancer Research
University of London

Declaration

I hereby declare that this thesis reports on my own original work. Any contribution made to this research by others whom I have worked with is explicitly acknowledged in the thesis.

Elise Yuri Lopicard

Table of contents

Declaration	2
Table of contents	3
List of equations	12
Abstract	13
Acknowledgements	15
Conference proceedings and papers	16
List of abbreviations	18
Chapter 1 Introduction	21
<i>1.1 Hypoxia in head and neck cancer</i>	<i>21</i>
1.1.1 Head and neck cancer	21
1.1.2 Definition of hypoxia	22
1.1.3 Causes of hypoxia	23
1.1.3.1 Hypoxia and tumour vasculature.....	23
1.1.3.2 Classification of hypoxia	24
1.1.4 Effects of hypoxia on cancer cells.....	27
1.1.4.1 Malignant progression.....	28
1.1.4.2 Radioresistance.....	29
1.1.4.3 Chemoresistance	30
1.1.4.4 Resistance to immunotherapy.....	31
1.1.4.5 Hypoxia, a hallmark of cancer?.....	31
1.1.5 Hypoxia targeting therapies	32
1.1.5.1 Improving tumour oxygenation	32
1.1.5.2 Drugs targeting hypoxia.....	33

1.1.5.3 Adapting radiation	36
1.1.6 Assessment of hypoxia	36
1.2 Imaging hypoxia	41
1.2.1 Requirements of a good imaging biomarker of hypoxia	41
1.2.2 Introduction to the imaging modalities available for assessing hypoxia.....	42
1.2.2.1 Positron Emission Tomography	42
1.2.2.2 Electron Paramagnetic Resonance	43
1.2.2.3 ¹⁹ F MRS of fluorinated 2-nitroimidazoles.....	43
1.2.2.4 ¹⁹ F MR oximetry of perfluorocarbons	44
1.2.2.5 Magnetic resonance spectroscopy	44
1.2.2.6 Optical spectroscopy	45
1.2.2.7 Photoacoustic tomography	45
1.2.3 Imaging hypoxia with ¹ H MRI	48
1.2.3.1 ¹ H-MRI principles	48
1.2.3.2 Dynamic contrast enhanced MRI.....	56
1.2.3.3 Susceptibility MRI	57
1.1.1.1 Oxygen- enhanced MRI.....	61
1.2.3.4 Mapping oxygen by lipid enhancement MRI	67
1.3 Thesis aims and structure.....	68
Chapter 2 Experimental material and methods	69
2.1 Cell lines and culture	69
2.2 Animal experiments.....	71
2.2.1 Tumour propagation	72
2.2.2 Atovaquone treatment.....	74
2.2.3 Magnetic resonance imaging	74
2.2.3.1 Administration of pimonidazole and Hoechst 33342	74
2.2.3.2 MR image acquisition	75

2.3 Evaluation of the stability of R_1 measurements	78
2.4 MRI image analysis	78
2.4.1 Tumour delineation	78
2.4.2 MRI parametric maps	79
2.5 Histopathology	80
2.5.1 Tissue preparation	80
2.5.1.1 Frozen tumour tissue	80
2.5.1.2 Formalin-fixed paraffin-embedded tumour tissue	81
2.5.2 Pimonidazole adducts and Hoechst 33342 imaging	81
2.5.2.1 Fluorescence imaging	81
2.5.2.2 Pimonidazole chromogenic imaging	82
2.5.3 Haematoxylin and eosin staining	82
2.5.3.1 Frozen tissue	82
2.5.3.2 Formalin-fixed paraffin-embedded tissue	82
2.5.4 Microscopy imaging analysis	83
2.6 Overview of the MRI experiment	83
2.7 In vitro radiotherapy preliminary study	85
2.7.1 Spheroid formation	85
2.7.2 Radiation treatment and response monitoring	85
2.7.3 CellTiter-Glo® assay	87
2.8 Statistical analysis	88

Chapter 3 Optimisation of an OE-MRI protocol incorporating susceptibility MRI for imaging tumour hypoxia **89**

3.1 Introduction	89
3.2 Results & Discussion	91
3.2.1 Stability and repeatability of the R_1 measurement	91

3.2.1.1 Repeatability of R_1 measurements using the IR-True FISP sequence on the new 7T MRI system	91
3.2.1.2 Repeatability of R_1 measurements using the refined IR-True FISP sequence.....	94
3.2.2 Optimisation of the perfusion threshold.....	96
3.2.2.1 Repeatability of R_2^* measurements using the MGE sequence.....	96
3.2.2.2 Evaluation and validation of SC-MRI-derived enhancing fraction as a perfusion mask for the OE-MRI protocol.....	96
3.3 Conclusion	99

Chapter 4 Evaluation of susceptibility MRI for imaging hypoxia in HNSCC

xenografts	100
4.1 Introduction.....	100
4.2 Results.....	101
4.2.1 Characterisation of HNSCC tumour engraftment and growth	101
4.2.2 Histological characterisation of hypoxia and perfusion in HNSCC xenograft models	103
4.2.3 Assessment of hypoxia using intrinsic susceptibility MRI.....	105
4.2.3.1 Assessment of baseline R_2^* as a biomarker of hypoxia.....	105
4.2.3.2 Assessment of $\Delta R_2^*_{O_2-air}$ as a biomarker of hypoxia	107
4.2.3.3 Assessing combined baseline R_2^* and $\Delta R_2^*_{O_2-air}$ as a biomarker of hypoxia.....	109
4.2.4 Assessment of tumour perfusion using susceptibility MRI	111
4.2.5 Relationship between tumour perfusion and hypoxia using susceptibility MRI	113
4.3 Discussion.....	115
4.3.1 Histological assessment of tumour hypoxia	115
4.3.2 Baseline R_2^* as a biomarker of tumour hypoxia.....	115
4.3.3 $\Delta R_2^*_{O_2-air}$ as a biomarker of tumour hypoxia	117
4.3.4 Combined baseline R_2^* and $\Delta R_2^*_{O_2-air}$ as a biomarker for hypoxia	119
4.3.5 Susceptibility MRI for perfusion imaging.....	120

4.3.6 Combined IS and SC-MRI derived R_2^* biomarkers for imaging tumour hypoxia.....	121
4.4 Conclusion	122
Chapter 5 Evaluation of OE-MRI for imaging hypoxia in HNSCC xenografts	123
5.1 Introduction.....	123
5.2 Results.....	124
5.2.1 Characterisation of HNSCC tumour engraftment and growth	124
5.2.2 Histological characterisation of hypoxia and perfusion in HNSCC xenograft models	126
5.2.3 Assessment of OE-MRI for hypoxia imaging in HNSCC models	129
5.2.3.1 Assessment of baseline R_1 as a biomarker of hypoxia.....	131
5.2.3.2 Assessment of $\Delta R_{1\text{O}_2\text{-air}}$ as a biomarker of hypoxia.....	131
5.2.3.3 Assessment of OxyR as a biomarker of hypoxia	132
5.2.3.4 Assessment of tumour perfusion using susceptibility MRI.....	136
5.2.3.5 Assessing pOxyR as a biomarker of hypoxia	136
5.2.3.6 Comparison between OE-MRI and susceptibility MRI derived biomarkers.....	140
5.3 Discussion.....	143
5.3.1 Histological characterisation of hypoxia in HNSCC xenografts.....	143
5.3.2 Evaluation of OE-MRI for imaging hypoxia.....	144
5.3.2.1 Assessment of R_1 biomarkers for imaging hypoxia.....	144
5.3.2.2 Assessment of OE-MRI-derived biomarkers of hypoxia	147
5.3.3 Comparison of OE-MRI with IS-MRI	148
5.4 Conclusion	153
Chapter 6 Assessment of HNSCC response to atovaquone using OE-MRI.....	154
6.1 Results.....	155
6.1.1 Tumour growth characteristics	155
6.1.2 Histopathological assessment of atovaquone-induced changes in hypoxia	157

6.1.3 Assessment of atovaquone-induced changes in tumour hypoxia using OE-MRI	159
6.2 Discussion	162
6.2.1 Atovaquone did not inhibit LICR-LON-HN5 tumour growth	162
6.2.2 LICR-LON-HN5 HNSCC xenografts did not respond to atovaquone.....	162
6.2.3 OE-MRI did not detect any atovaquone-induced change in hypoxia in LICR-LON-HN5 xenografts.....	164
6.3 Conclusion	165
Chapter 7 General discussion	166
7.1 Summary of main findings	166
7.2 OE-MRI for detecting and imaging hypoxia	167
7.2.1 Novelty of the OE-MRI protocol	167
7.2.2 Advantages and limitations of OE-MRI.....	168
7.2.2.1 R ₁ measurements	168
7.2.2.2 SC-MRI using USPIO particles	169
7.2.3 Histological validation of MRI biomarkers.....	172
7.2.4 Clinical translation of OE-MRI.....	174
7.3 OE-MRI applications for therapy.....	176
7.3.1 OE-MRI as a predictive imaging tool for tumour response to therapy	176
7.3.2 OE-MRI for monitoring tumour response to pharmacological modification of hypoxia	179
7.4 Future work	180
7.4.1 Validation of OE-MRI biomarkers for hypoxia.....	180
7.4.2 OE-MRI biomarkers for prediction and monitoring of tumour response.....	181
7.4.2.1 Radiotherapy	181
7.4.2.2 Pharmacological modification of hypoxia.....	182
7.5 Conclusion	183

Bibliography..... 188

List of figures

FIGURE 1.1 CHRONIC AND ACUTE HYPOXIA.	25
FIGURE 1.2 TUMOUR CELL HIF MEDIATED RESPONSE TO HYPOXIA.	28
FIGURE 1.3 2-NITROIMIDAZOLES.	34
FIGURE 1.4 THE ELECTRON TRANSPORT CHAIN.	36
FIGURE 1.5 SPIN PRECESSION.	49
FIGURE 1.6 MR SIGNAL.	50
FIGURE 1.7 GRADIENT -ECHO SEQUENCE.	51
FIGURE 1.8 SPIN ECHO SEQUENCE.	52
FIGURE 1.9 MAGNETIC TRANSVERSE AND LONGITUDINAL RELAXATIONS.	54
FIGURE 1.10 T_1 AND T_2 RELAXATION.	55
FIGURE 1.11 OXYGEN SATURATION CURVE.	58
FIGURE 1.12 PRINCIPLES OF OE-MRI AND IS-MRI. OE-MRI.	63
FIGURE 1.13 CHARACTERISATION OF HYPOXIA USING OE-MRI.	65
FIGURE 2.1 CUSTOM-BUILT PERSPEX TUMOUR PLATFORM.	76
FIGURE 2.2 WORKFLOW OF THE OE-MRI IMAGING EXPERIMENT.	84
FIGURE 2.3 WORKFLOW OF THE SPHEROID RADIATION TREATMENT.	86
FIGURE 2.4 SCHEMATIC DIAGRAM OF THE SAMPLE HOLDER USED TO TREAT SPHEROIDS REPRODUCIBLY IN PCR TUBES USING THE SARRP.	87
FIGURE 3.1 INITIAL CHALLENGES WITH THE REPEATABILITY OF R_1 MEASUREMENTS USING THE IR-TRUE FISP SEQUENCE ON THE NEW BRUKER 7T SYSTEM.	93
FIGURE 3.2 STABILITY OF R_1 ASSESSED USING A TEST OBJECT CONTAINING GELATINE PHANTOMS.	95
FIGURE 3.3 STABILITY OF R_1 MEASUREMENTS ASSESSED IN VIVO.	95
FIGURE 3.4 EVALUATION OF TUMOUR PERFUSION USING SC-MRI.	98
FIGURE 4.1 CHARACTERISATION OF TUMOUR GROWTH.	102
FIGURE 4.2 HISTOLOGICAL CHARACTERISATION OF TUMOUR HYPOXIA AND PERFUSION.	104
FIGURE 4.3 CHARACTERISATION OF TUMOUR BASELINE R_2^*	106

FIGURE 4.4 CHARACTERISATION OF TUMOUR $\Delta R_2^*_{O_2-AIR}$	108
FIGURE 4.5 RELATIONSHIP BETWEEN TUMOUR BASELINE R_2^* AND $\Delta R_2^*_{O_2-AIR}$	110
FIGURE 4.6 CHARACTERISATION OF TUMOUR PERFUSION.....	112
FIGURE 4.7 RELATIONSHIP BETWEEN TUMOUR PERFUSION AND HYPOXIA.....	114
FIGURE 5.1 CHARACTERISATION OF TUMOUR GROWTH.	125
FIGURE 5.2 HISTOLOGICAL CHARACTERISATION OF TUMOUR HYPOXIA AND PERFUSION.	127
FIGURE 5.3: MORPHOLOGY OF HYPOXIC REGIONS OF HNSCC TUMOURS.....	128
FIGURE 5.4 ANATOMICAL AND FUNCTIONAL IMAGING DATA OBTAINED USING OE-MRI.	130
FIGURE 5.5 ASSESSMENT OF TUMOUR BASELINE R_1 FOR THE CHARACTERISATION OF HYPOXIA.....	133
FIGURE 5.6 CHARACTERISATION OF HYPOXIA USING TUMOUR $\Delta R_1_{O_2-AIR}$	134
FIGURE 5.7 CHARACTERISATION OF HYPOXIA USING TUMOUR OXYR	135
FIGURE 5.8 CHARACTERISATION OF TUMOUR PERFUSION.....	138
FIGURE 5.9 CHARACTERISATION OF HYPOXIA USING TUMOUR pOXYR.	139
FIGURE 5.10 RELATIONSHIP BETWEEN R_1 AND R_2^*	141
FIGURE 5.11 CHARACTERISATION OF TUMOUR HYPOXIA USING COMBINED R_1 AND R_2^* -DERIVED BIOMARKERS. .	142
FIGURE 5.12 SCHEMATIC REPRESENTATION OF THE THEORETICAL RELATIONSHIPS BETWEEN HYPEROXIA-INDUCED $\Delta R_1_{O_2-AIR}$ AND $\Delta R_2^*_{O_2-AIR}$	152
FIGURE 6.1 CHARACTERISATION OF LICR-LON-HN5 XENOGRAFT GROWTH WITH ATOVAQUONE TREATMENT. ..	156
FIGURE 6.2. HISTOLOGICAL CHARACTERISATION OF TUMOUR HYPOXIA AND PERFUSION.	158
FIGURE 6.3 ANATOMICAL IMAGES AND CORRESPONDING FUNCTIONAL MRI MAPS OF HNSCC XENOGRAFT RESPONSE TO ATOVAQUONE.	160
FIGURE 6.4 QUANTITATIVE ANALYSIS OF LICR-LON-HN5 XENOGRAFT RESPONSE TO ATOVAQUONE.....	161
FIGURE 7.1 SC-MRI STUDY USING FERUMOXYTOL OF A MOUSE BEARING A SUBCUTANEOUS SW1222 COLORECTAL XENOGRAFT USING FERUMOXYTOL.	172
FIGURE 7.2 MRI PARAMETRIC MAPS OF A REPRESENTATIVE ADVANCED HNC PATIENT.	175
FIGURE 7.3 LICR-LON-HN5 AND LICR-LON-HN6 SPHEROID RESPONSE TO RADIOTHERAPY.....	178
FIGURE 7.4 OE-MRI INVESTIGATION OF AN RH41 RHABDOMYOSARCOMA XENOGRAFT.....	181

FIGURE B-1 COMPARISON OF TUMOUR VOLUME ASSESSMENT METHODS.....	185
FIGURE B-2 EXAMPLE OF TUMOUR DELINEATION ON HISTOLOGICAL SECTIONS.....	186
FIGURE C-1 EXAMPLES OF ANATOMICAL AND FUNCTIONAL IMAGING DATA OBTAINED USING OE-MRI.	187

List of tables

TABLE 1.1 SUBTYPES OF ACUTE AND CHRONIC HYPOXIA AND THEIR PATHOPHYSIOLOGICAL CONSEQUENCES.....	26
TABLE 1.2 SUMMARY OF pO_2 HISTOGRAPHY METHODS.	39
TABLE 1.3 SUMMARY OF MAIN HISTOLOGICAL MARKERS USED TO STUDY HYPOXIA EX VIVO AND VALIDATE IMAGING BIOMARKERS OF HYPOXIA IN HNSCC ^{26,145}	40
TABLE 1.4 SUMMARY OF PRECLINICAL AND CLINICAL IMAGING MODALITIES USED TO DETECT HYPOXIA.	47
TABLE 2.1 DESCRIPTION OF CELL LINES USED IN THIS THESIS.....	71
TABLE 2.2 CELL LINES AND MICE USED TO ESTABLISH TUMOUR MODELS.	73
TABLE 2.3 MRI SEQUENCE PARAMETERS USED IN THE IMAGING PROTOCOL.	77
TABLE A-1 STR PROFILE OF THE DIFFERENT CELL LINES STUDIED IN THIS THESIS.....	184

List of equations

EQUATION 1.1 LARMOR FREQUENCY EQUATION.	48
EQUATION 2.1 TUMOUR ELLIPSOIDAL VOLUME CALCULATION.....	72
EQUATION 2.2 OxyR THRESHOLD.	79
EQUATION 2.3 PERFUSION THRESHOLD.....	80
EQUATION 2.4 FRACTIONAL BLOOD VOLUME (FBV) FORMULA.....	80
EQUATION 2.5 SPHEROID VOLUME FORMULA.....	87

Abstract

Tumour hypoxia is associated with resistance to radiotherapy and chemotherapy, and represents a major challenge in the treatment of head and neck squamous cell carcinoma (HNSCC).

Non-invasive imaging methods to repeatedly and rapidly quantify the degree and spatial distribution of hypoxia would offer clinical benefit.

This thesis focusses on the evaluation of oxygen-enhanced magnetic resonance imaging (OE-MRI) for mapping and quantifying hypoxia in HNSCC xenografts *in vivo*. OE-MRI relies on the quantification of changes in the longitudinal MRI relaxation rate R_1 , induced by excess paramagnetic oxygen molecules dissolved in blood plasma and interstitial fluid with inhalation of oxygen.

A refined OE-MRI protocol was first developed, designed to incorporate susceptibility MRI in the same imaging session, thereby providing measurements of tumour R_1 and R_2^* during air and 100% O_2 breathing, and fractional blood volume (fBV) using ultrasmall superparamagnetic iron oxide particles. MRI biomarkers were validated through comparison with image-aligned tissue sections stained for the hypoxia marker pimonidazole, and the perfusion marker Hoechst 33342.

Susceptibility MRI revealed that hyperoxia-induced $\Delta R_2^*_{O_2-air}$ inversely correlated with pimonidazole-derived hypoxic fraction, and fBV positively correlated with Hoechst 33342 uptake. Parcellation of the voxelwise $\Delta R_2^*_{O_2-air}$ identified voxels non-responsive to hyperoxia that may inform on cycling hypoxia.

OE-MRI showed that both tumour sub-volumes refractory to hyperoxia-induced changes in R_1 (OxyR), and perfused OxyR (pOxyR) were associated with an extensive and heterogeneous distribution of hypoxia across the HNSCC xenografts. Both OxyR and pOxyR positively correlated with pimonidazole-derived hypoxic fraction, suggesting that binarisation of hyperoxia-induced ΔR_1 data with a perfusion mask may not be necessary in strongly hypoxic tumours such as HNSCC.

Finally, the potential utility of OE-MRI for monitoring tumour response to the hypoxia-alleviating drug atovaquone was investigated.

OE-MRI can identify and quantify hypoxia in HNSCC and could provide an easily translatable imaging tool for patient stratification and treatment management.

Acknowledgements

First and foremost, I would like to thank my supervisor, Dr Simon Robinson, without whose guidance I wouldn't have gone so far on this extraordinary journey. Many thanks are owed to my supervisory team, Jess, Yann, Carol and Rafal, who guided me throughout this adventure. Thank you for your help, patience and support. This thesis couldn't exist without you.

I would like to thank the Oracle Cancer Trust and their generous donors for their financial support and encouragement for this project. Their resilience and dedication has been a great source of motivation.

I would also like to thank the SPR group members, past and present, for making this experience enjoyable, especially Jin, Mariama, Konstantinos and Emma. Appreciation goes to the temporary members of the SPR team, Tom and my summer student Tim. A special thank goes to my yoga students. Sharing my little experience with them, and witnessing the small but consistent changes from a committed practice was inspirational for my own exploration during my PhD.

I would like to thank my friends all around the world including Kingswood Drive, for travelling along the bumpy road I've taken.

I am eternally grateful for the unconditional love of my parents and my sister Céline. Finally, thanks to my soon-to-be husband Valéry, who made the path that lied ahead look less scary throughout the PhD.

Conference proceedings and papers

Papers

Baker LCJ, Sikka A, Price JM, Boulton JKR, Lepicard EY, Box G, Jamin Y, Spinks TJ, Kramer-Marek G, Leach MO, Eccles SA, Box C and Robinson SP (2018) Evaluating Imaging Biomarkers of Acquired Resistance to Targeted EGFR Therapy in Xenograft Models of Human Head and Neck Squamous Cell Carcinoma. *Frontiers in Oncology* 8:271.

Bernauer C, Man YK, Chisholm J, Lepicard EY, Robinson SP and Shipley JM (Accepted July 2020) Hypoxia and its therapeutic possibilities in paediatric cancers. *British Journal of Cancer*.

Poster presentations

Exploiting combined oxygen enhanced and intrinsic susceptibility MRI for the spatial characterisation of hypoxia in head and neck cancer. 25th British Chapter of the International Society for Magnetic Resonance in Medicine (BC-ISMRM) postgraduate symposium (March 2017).

Oxygen enhanced MRI for imaging hypoxia in head and neck cancer xenografts. 26th BC-ISMRM postgraduate symposium (May 2018).

Oxygen enhanced MRI for imaging hypoxia in head and neck cancer xenografts. ICR annual conference (June 2018).

Oral presentations

Lepicard EY, Boulton JKR, Jamin Y, Zormpas-Petridis K, Featherstone A, Box C, Panek R, O'Connor JPB and Robinson SP. Imaging hypoxia in head and neck cancer xenografts with oxygen-enhanced MRI. ISMRM virtual conference (August 2020).

Public outreach

From 2016 to 2019: Poster presentation at the Oracle cancer trust annual research reception.

June 2019: Oral presentation for Oracle cancer trust donor visit.

September 2019: Oral presentation for Oracle cancer trust donor visit.

Awards

- BC-ISMRM 2nd prize for Best poster presentation (2017)
- BC-ISMRM 3rd prize for Best abstract submitted (2017)
- University of London scholarship fund for the attendance of the 26th ISMRM annual conference (2018)
- ISMRM new entrant stipend (2018)
- ISMRM educational stipend (2020)
- ISMRM Magna cum laude Merit Award (2020)

List of abbreviations

5-FU. : *5-fluorouracil*
ADC. : *apparent diffusion coefficient*
ANOVA. : *analysis of variance*
ARCON. : *accelerated radiotherapy with carbogen and nicotinamide*
ARRIVE. : *animals in research: reporting in vivo experiments*
ASCC. : *anal squamous cell carcinoma*
ATP. : *adenosine triphosphate*
BOLD-MRI. : *blood oxygen level dependent MRI*
CAIX. : *carbonic anhydrase IX*
CoV. : *coefficient of variation*
CTG®. : *CellTiterGlo®*
DCE-MRI. : *Dynamic-contrast enhanced MRI*
dHb. : *deoxyhaemoglobin*
DMEM. : *Dulbecco's modified Eagle's medium*
DNA. : *deoxyribonucleic acid*
dOE-MRI. : *Dynamic OE-MRI*
DSC-MRI. : *dynamic susceptibility contrast MRI*
DSMZ. : *Leibniz-Institut- Deutsche Sammlung von Mikroorganismen und Zellkulturen*
DW-MRI. : *diffusion-weighted MRI*
EF5. : *2-(2-nitro-1[H]-imidazol-1-yl)-N-(2,2,3,3,3-pentafluoropropyl)-acetamide*
EGFR. : *epidermal growth factor receptor*
EPI. : *echo planar imaging*
EPO. : *erythropoietin*
EPR. : *Electron paramagnetic resonance*
FA. : *flip angle*
FAZA. : *fluoroazomycin-arabioside*
FBS. : *foetal bovine serum*
fBV. : *fractional blood volume*
FDA. : *food and drug administration*
FFPE. : *formalin-fixed paraffin-embedded*
FID. : *free induction decay*
FITC. : *fluorescein isothiocyanate*
FOV. : *field of view*
Gd. : *gadolinium*
Gd-DTPA. : *gadolinium-diethylenetriamine penta-acetic acid*
GLUT-1. : *glucose transporter 1*

H&E. : *haematoxylin and eosin*
HAPs. : *hypoxia-activated prodrugs*
Hb. : *oxyhaemoglobin*
HBSS. : *Hank's balanced salt solution*
HIF. : *hypoxia-inducible factor*
HNC. : *head and neck cancer*
HNSCC. : *head and neck squamous cell carcinoma*
HPV. : *human papillomavirus*
IAUGC₆₀. : *initial area under the gadolinium curve at 60 seconds*
ICA. : *independent component analysis*
IHC. : *immunohistochemistry*
IMRT. : *intensity-modulated radiotherapy*
IR-TrueFISP. : *inversion recovery fast imaging with steady-state precession*
IS-MRI. : *intrinsic susceptibility-weighted MRI*
ITPP. : *myo-inositol trispyrophosphate*
K^{trans}. : *volume transfer constant*
MGE. : *multi-gradient echo*
MISO. : *misonidazole*
MOBILE-MRI. : *mapping oxygen by lipid enhancement MRI*
MRI. : *Magnetic resonance imaging*
MR-LINAC. : *magnetic resonance guided- linear accelerator*
MRS. : *magnetic resonance spectroscopy*
NMR. : *nuclear magnetic resonance*
NP. : *non perfused*
NSCLC. : *non-small cell lung cancer*
O₂. : *oxygen*
OCR. : *oxygen consumption rate*
OE-MRI. : *Oxygen-enhanced MRI*
OXPHOS. : *oxidative phosphorylation*
PAT. : *Photoacoustic tomography*
PBS. : *phosphate-buffered saline*
PCR. : *polymerase chain reaction*
PDX. : *patient-derived xenograft*
PET. : *Positron emission tomography*
PFC. : *perfluorocarbon*
pO₂. : *partial pressure of oxygen or oxygen tension*
pOxyE. : *perfused oxygen enhanced*
pOxyR. : *perfused oxygen refractory*
R₁. : *spin-lattice or longitudinal relaxation rate*
R₂^{*}. : *effective spin-spin or transverse relaxation rate*

RCA. : *renal adenocarcinoma*
RF. : *radiofrequency*
RMH. : *Royal Marsden Hospital*
RMS. : *rhabdomyosarcoma*
ROI. : *region of interest*
s.e.m.. : *standard error of the mean*
SARRP. : *small animal radiation research platform*
SC-MRI. : *susceptibility-contrast MRI*
SGRE. : *spoiled gradient echo*
SI. : *signal intensity*
SNR. : *signal to noise ratio*
STR. : *short tandem repeat*
 T_1 . : *spin-lattice or longitudinal relaxation time*
 T_2 . : *spin-spin or transverse relaxation time*
TE. : *echo time*
TI. : *inversion time*
TKI. : *tyrosine kinase inhibitor*
TR. : *repetition time*
TurboRARE. : *Turbo rapid acquisition with refocused echoes*
ULA. : *ultra-low attachment*
USPIO. : *ultra small paramagnetic iron oxide*
 v_e . : *extravascular extracellular volume fraction*
VEGF. : *vascular endothelial growth factor*
VEGFR. : *vascular endothelial growth factor receptor*
VFA. : *variable flip angle*
 v_p . : *blood plasma volume fraction*

Chapter 1 Introduction

1.1 Hypoxia in head and neck cancer

1.1.1 Head and neck cancer

Head and neck cancer (HNC) is the 7th most common cancer and cause of cancer-related deaths in the world, accounting for 2% of new cases and 1.9% of cancer-related deaths worldwide in 2018¹. In the UK, HNC is the 8th most common cancer, accounting for 3% of new cases, but the 15th most common cause of cancer-related deaths (2%, 2017)^{2,3}. Head and neck squamous cell carcinoma (HNSCC), arising from epithelial cells lining the mucosa of the oral cavity, oropharynx, hypopharynx and larynx, represents over 90% of HNC. The most prominent risk factors are tobacco consumption, alcohol abuse and chronic human papillomavirus (HPV) infection⁴⁻⁷. Smokers have a ten-fold higher chance of developing HNC than non-smokers. Overall prognosis is better and tumour radiosensitivity is higher in HPV-positive patients⁸⁻¹⁰. Epidermal growth factor receptor (EGFR) is a tyrosine kinase overexpressed in more than 80% of HNSCC and is a negative factor in poor prognosis and treatment resistance¹¹⁻¹³. Standard of care treatment of HNC typically involves surgical resection, radiotherapy and chemotherapy, or a combination of these approaches, depending on the primary location^{14,15}.

One of the major factors associated with adverse clinical response to therapy and poor prognosis in HNSCC is hypoxia^{16–19}. Hypoxia, defined as a deficiency in the amount of oxygen reaching tissues, is prevalent in most solid malignancies, including HNSCC, as well as other carcinomas, such as that of the uterine cervix²⁰, and sarcomas²¹.

1.1.2 Definition of hypoxia

Physiological hypoxia occurs due to an imbalance between a lack of sufficient oxygen supply, resulting from anarchic and inefficient tumour vasculature, and metabolic reprogramming of tumour cells. Whilst normal tissues typically have oxygen tensions of ~40 mmHg^{22,23}, tumours typically exhibit partial pressure of oxygen (pO_2) lower than 10 mmHg^{24,25}, with localised tissue regions lower than 2.5 mmHg, often referred to as being radiobiologically hypoxic^{26,27}.

In a series of studies in human HNSCC, pO_2 was measured using Eppendorf electrodes. Overall median pO_2 values of approximately 10 mmHg have been consistently reported, with an overall fraction of pO_2 values lower than 2.5mmHg of around 25%^{28–30}.

1.1.3 Causes of hypoxia

1.1.3.1 Hypoxia and tumour vasculature

Hypoxia is closely linked to the aberrant pathophysiology of tumour vasculature, which can be characterised by³¹:

- i. A lack of sufficient arteriolar supply. The scarcity of arterioles and their distance to the main arterial vessel affect oxygen delivery.
- ii. A low vascular density. Oxygen can typically diffuse a distance of 180-200 μm , therefore a greater distance between vessels in tumours can lead to hypoxia³².
- iii. A chaotic organisation of vessels, leading to poor oxygen delivery and regional variations in pO_2 .
- iv. Fluctuations in erythrocyte flux. Variations in erythrocyte concentration in blood, or the absence thereof due to leaking microvessels, can impede oxygen delivery to the tumour.
- v. Inefficient oxygen transportation by erythrocytes. Erythrocytes can shrink, fold or stiffen, thus modifying blood viscosity and erythrocyte distribution, especially at bifurcations.
- vi. Dynamic remodelling of vasculature, causing shunts that drive blood away from the tumour tissue.
- vii. Increased oxygen demand and poorer oxygen delivery compared to normoxic tissue.

1.1.3.2 Classification of hypoxia

Historically, hypoxia has been divided into two types (Figure 1.1):

- i. Chronic or diffusion-limited hypoxia, resulting from an increase in the oxygen diffusion distance between tumour vessels with tumour expansion^{32–34}. Thomlinson and Gray first identified chronic hypoxia in regions of lung squamous carcinoma located far from the main blood vessel, beyond the diffusion distance of oxygen³².
- ii. Acute or perfusion-limited hypoxia, also described as cycling, transient or intermittent hypoxia, arises from spatial and temporal modifications of red cell flux^{35,36}. Cycles of variations in pO₂ can range from minutes to several hours^{36–41} (see 1.1.4). Acute hypoxia was first described in murine SCVII squamous cell carcinoma, using a double perfusion marker strategy, in which tumour cells close to blood vessels were found to be hypoxic at a given time due to transient perfusion⁴². In patients with HNC, acute hypoxia has recently been shown to be a stronger determinant of poor prognosis after chemoradiotherapy than chronic hypoxia⁴³.

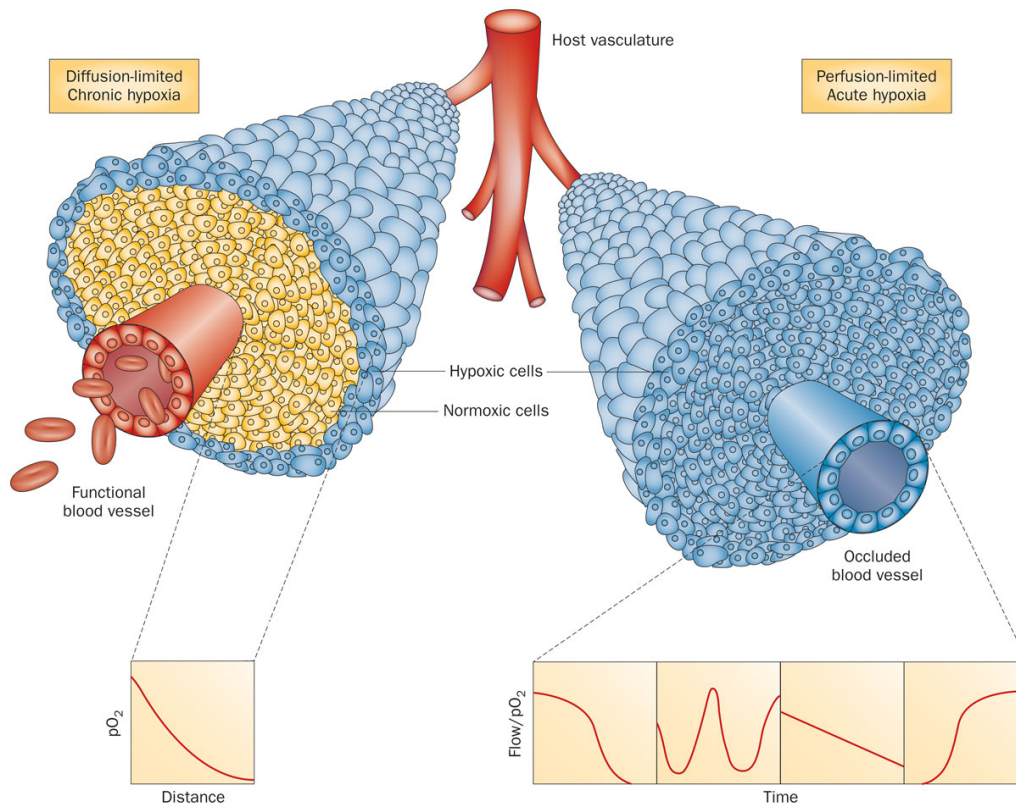


Figure 1.1 Chronic and acute hypoxia.

Chronic or diffusion-limited hypoxia results from the diffusion of oxygen from the blood vessel (around 180-200 μ m) thus the formation of a gradient of pO_2 . Acute or perfusion-limited hypoxia is the consequence of an impaired blood perfusion, leading to transient variations in blood flow and pO_2 . Dysfunctional perfusion can be caused by structural flaws, including chaotic architecture, and/or functional impairments due to a dynamic remodelling of vasculature or changes of erythrocyte characteristics. Taken from Horsman et al⁴⁴.

However, it is now recognised that this classical view of tumour hypoxia is an over-simplification: the distinction between the two types of hypoxia is often unclear, and both can be observed in heterogeneous patterns in the same tumour. A revised classification that includes sub-types of acute and chronic hypoxia has been proposed³⁴ and is summarised in Table 1.1.

Type hypoxia of	Subtype of hypoxia	Causative mechanism	Perfusion	Oxygen supply	Drug delivery
Acute hypoxia	Ischaemic hypoxia due to transient flow stop	Temporary shut-down of flow due to physical obstructions	Flow stop	Abolished	Abolished
	Hypoxaemic hypoxia	Severe reduction of O ₂ in tumour microvessels	Maintained but may be abnormal, plasma only or reversed flow	Strongly reduced	Maintained
Chronic hypoxia	Diffusion-limited hypoxia	Surpassing the maximum O ₂ diffusion distance in the perivascular space; Adverse diffusion due to vascular geometry	Maintained	Reduced/abolished (distance dependent)	Reduced/abolished (distance dependent)
	Hypoxaemic hypoxia	Long-lasting reduced O ₂ content in blood, extreme longitudinal intravascular O ₂ gradients	Maintained	Reduced	Maintained
	Hypoxia due to interstitial hypertension in the tumour centre	Abolished perfusion pressure differences between up- and downstream microvessels	Reduced (compromised perfusion of leaky vessels)	Reduced	Reduced
Macroscopic regional hypoxia		Longitudinal arteriole gradients in larger tumours	Maintained	Reduced	

Table 1.1 Subtypes of acute and chronic hypoxia and their pathophysiological consequences.
Adapted from Bayer et al., 2011³⁴.

1.1.4 Effects of hypoxia on cancer cells

Hypoxia influences two key aspects of cancer:

- i. Tumour pathophysiology. Hypoxia-induced genomic and proteomic instabilities promote tumour cell survival, proliferation and metastasis in tumours²⁴.
- ii. Treatment response and resistance. Most treatment strategies, especially radiotherapy, rely on the presence of oxygen to mediate deoxyribonucleic acid (DNA) damage through the formation of free radicals. But other mechanisms, linked to the effects of hypoxia on tumour pathophysiology, may also negatively influence tumour response to therapy.

In HNC, hypoxia is associated with a poor prognosis, tumour aggressiveness, metastasis and treatment resistance^{16,17,20}. A number of hypoxia-targeting strategies, described in 1.1.5, have been shown to improve locoregional control, disease-specific survival, and overall survival in HNSCC patients^{45(p201)}.

In recent years, recognition of the role of hypoxia in cancer progression and treatment resistance has been dramatically enhanced through increased understanding of the molecular mechanisms regulating hypoxia and discovery of the hypoxia-inducible factor (HIF) signalling pathway, for which William G. Kaelin Jr., Sir Peter J. Ratcliffe, and Gregg L. Semenza were awarded the 2019 Nobel Prize in Physiology or Medicine⁴⁶.

1.1.4.1 Malignant progression

Hypoxia is a powerful trigger for changes in tumour cell gene expression, and tumour cells adapt to hypoxic stress through activation of the HIF pathway. Under hypoxic conditions, HIF is stabilised, translocates to the nucleus and initiates transcription of numerous genes which regulate many biological activities that contribute to tumour growth and invasion, including angiogenesis, metabolic reprogramming, DNA repair, modulation of apoptosis, immortalisation and pH regulation (Figure 1.2)^{20,47}. The ensuing genetic instability associated with these processes drives the tumour towards a more malignant phenotype, resulting in more hypoxia. The balance between opposite pathways mediated by HIF, such as apoptosis vs cell survival⁴⁸, is yet to be fully understood, and represents the “Janus face” of hypoxia.

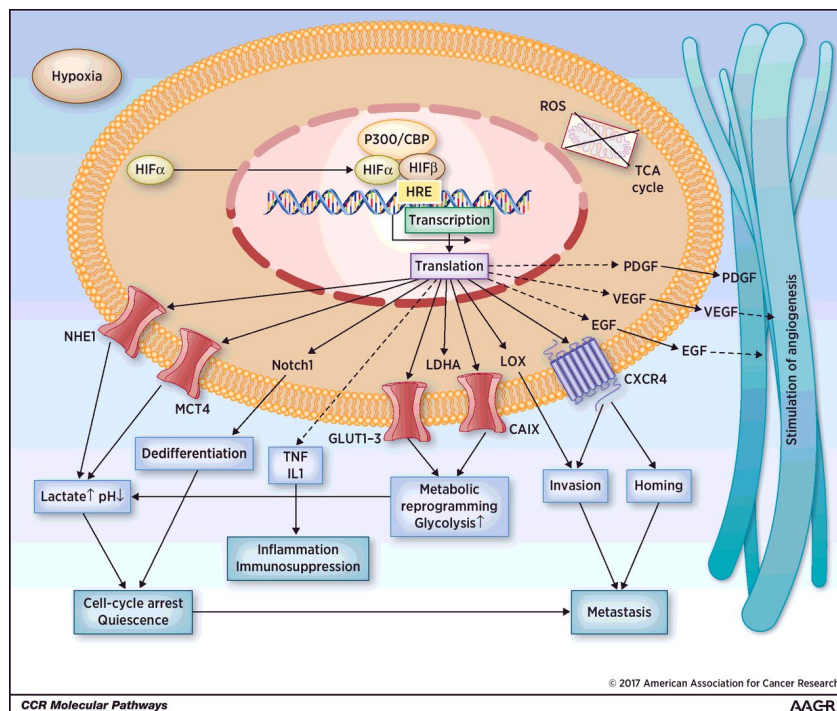


Figure 1.2 Tumour cell HIF mediated response to hypoxia.

Under hypoxia, HIF1 α is stabilised and undergoes heterodimerization with the HIF- β subunit. The heterodimer is then translocated to the nucleus, and activates hypoxia-dependent gene transcription for survival reprogramming. Taken from Baran and Konopleva⁴⁹.

1.1.4.2 Radioresistance

Radiotherapy is one of the main treatment approaches for HNSCC, administered either alone, in combination with chemotherapy, or as an adjuvant following surgical resection. Ionizing radiation causes DNA damage and subsequent cell death by a direct photon interaction, or indirectly through the production of radiation-induced free radicals. In the presence of oxygen, free radical oxidation induces DNA damage, also called the oxygen enhancing effect^{50,51}. The impact of oxygen on radioresistance depends on the local tumour pO₂, histological type, the radiation dose and linear energy transfer of the radiation⁵².

Hypoxia is a well-known cause of radioresistance, with three times more radiation required to kill hypoxic than normally oxygenated cells⁵³. Hypoxia-mediated proteomic, genomic and metabolic changes increase the number of tumour cells with impaired apoptosis, increased DNA repair, proliferative and metastatic potential⁵⁴. Radiotherapy-induced modification of hypoxia has resulted in improved locoregional control and survival^{17,45}. The emergence of advanced radiotherapy delivery such as intensity-modulated radiotherapy (IMRT) with dose-painting may allow the targeting of hypoxic subregions and adaptation of radiation doses, whilst sparing adjacent normal tissue.

1.1.4.3 Chemoresistance

In HNSCC, chemotherapy is typically administered as an adjuvant treatment preceding or following surgery and/or radiotherapy, or concurrent with radiotherapy. Conventional chemotherapy for HNSCC includes platinum-based drugs such as cisplatin or carboplatin, often concurrent to radiotherapy^{55,56}. Cisplatin has been combined with 5-fluorouracil (5-FU), with limited success⁵⁷. Expression of the epidermal growth factor receptor (EGFR) is associated with a poor outcome^{58,59}. Cetuximab, an EGFR inhibitor, is cytotoxic and has been found to enhance the cytotoxic activity of cisplatin in HNSCC^{60,61}. A combination of platinum, 5-FU and cetuximab is a first-line treatment in the clinic^{62,63}. Combining cisplatin, 5-FU and taxanes, such as paclitaxel, has also been successfully used^{64,65}.

Hypoxia can have a negative impact on the efficacy of chemotherapy. This influence can be direct, as some drugs need oxygen to reach their optimal cytotoxicity. Hypoxia can also indirectly affect the efficacy of anticancer drugs due to their limited diffusion to hypoxic cells distal from the main blood supply. Furthermore, hypoxia may also limit chemotherapy efficacy, which is higher in rapidly proliferating cells, by inducing cell cycle arrest or slower growth, or through hypoxia-induced genetic and proteomic instabilities, and clonal selection, leading to improved survival^{54,66}. Hypoxia-induced intracellular acidosis may also inhibit the activity of cytotoxic drugs that are weak bases⁵⁴.

1.1.4.4 Resistance to immunotherapy

Recently, immunotherapy has emerged as an effective treatment for some cancers. This approach harnesses the host's immune system to target tumours during the immune surveillance⁶⁷. For example, pembrolizumab has recently been approved in Europe and the United States as first-line treatment for patients with advanced stages of HNC⁶⁸. Hypoxia also influences the efficacy of immunotherapy by regulating the activity and infiltration of the immune cells such as T-cells and natural killer cells, thus inducing immune suppression and immune tolerance^{69–71}.

1.1.4.5 Hypoxia, a hallmark of cancer?

Hanahan and Weinberg identified a number of biologically acquired capabilities of cancer and described them as hallmarks^{72,73}. As detailed above, hypoxia, mainly through the HIF-1 α pathway, is both a cause and a consequence of many of these hallmarks. Moreover, hypoxia has a strong prevalence in many tumour types, and a negative impact on prognosis, survival and response to therapy. The evidence shows that hypoxia should be considered as a hallmark of cancer, and, like the other hallmarks, used to guide therapy development.

1.1.5 Hypoxia targeting therapies

Four hypoxia-targeting strategies have been pursued to circumvent the negative effects of hypoxia, often in combination with standard radio- or chemotherapy:

- i. Improving tumour oxygenation and tumour blood flow.
- ii. Targeting hypoxic cells with radiosensitisers, hypoxia-activated prodrugs (HAPs) or drugs that decrease oxygen consumption.
- iii. Modulating radiotherapy according to the spatial heterogeneity of tumour hypoxia.
- iv. Targeting the adaptive mechanisms of hypoxic cells.

1.1.5.1 Improving tumour oxygenation

Historically, hyperbaric oxygen chambers, and the combination of carbogen gas (95%O₂, 5%CO₂) and nicotinamide (Accelerated Radiotherapy with Carbogen and Nicotinamide or ARCON trials) have been used to increase oxygen concentration in tumours^{19,74–77}. However, although hyperbaric oxygen could improve tumour oxygenation, the effect was transient and decreased within minutes, and patients experienced discomfort that affected compliance^{74,78}. ARCON improved tumour control and survival in HNC patients, especially anaemic patients with laryngeal cancer, but the efficacy was comparable to that of a chemoradiotherapy approach which is clinically used in these tumour sites^{77,79}.

Improving oxygen delivery may also be achieved by improving tumour perfusion. Numerous pharmacological vasomodulators have been identified

for improving tumour pO_2 ⁸⁰. Nicotinamide, used in the ARCON trials, alleviates acute hypoxia⁸¹. High levels of vascular endothelial growth factor (VEGF), the most potent angiogenic growth factor, are associated with poor prognosis and overall survival in HNSCC patients^{82–84}. VEGF inhibitors, such as bevacizumab, transiently normalise tumour vascular architecture and reduce hypoxia, thereby providing a window of opportunity for radiosensitisation^{85–89}. Phase I and II clinical trials of bevacizumab combined with chemoradiotherapy in HNC patients reported encouraging results, but were associated with significant side effects, such as thrombosis, or haemorrhages^{90–92}.

In HNC, anaemia is associated with a poor outcome following radiotherapy and/or surgery^{93–95}, and is correlated with increased levels of hypoxia⁹⁶. Blood transfusion preceding therapy is routinely used, but this procedure did not improve tumour oxygenation in HNSCC patients during radical chemo-radiotherapy⁹⁷. An alternative is the use of erythropoietin (EPO) to increase haemoglobin levels. EPO effectively improved haematocrit in HNC patients but did not improve cancer outcome^{98–100}.

1.1.5.2 Drugs targeting hypoxia

1.1.5.2.1 Hypoxia-activated prodrugs

HAPs exploit the difference in pO_2 between hypoxic and normoxic cells: the conversion of HAPs into cytotoxic products by reductases only under hypoxic conditions allow the specific targeting of hypoxic cells. HAPs encompass five chemical classes: nitroimidazoles, nitrobenzenes, quinones, N-oxides and metal complexes.

HAPs can act as radiosensitisers to improve tumour response to radiation. Hypoxic cell radiosensitisers mimic the oxygen enhancement effect on radiotherapy through their high affinity for electrons. Nitroimidazoles such as misonidazole, nimoradazole and etanidazole have been investigated as hypoxia radiosensitisers in HNC. *In vivo*, nitroimidazoles remain oxygenated under normoxia. Under hypoxic conditions, they are reduced by nitroreductases associated with the cytoplasm, mitochondria and microsomes, into highly reactive species that bind to cellular nucleophiles, such as proteins or DNA, thus retain in cells^{101–103} (Figure 1.3). Strong adduct formation occurs when the pO₂ falls below 10 mmHg, and this property makes nitroimidazoles, such as pimonidazole, good immunohistochemical (IHC) markers of hypoxia at the cellular level¹⁰⁴.

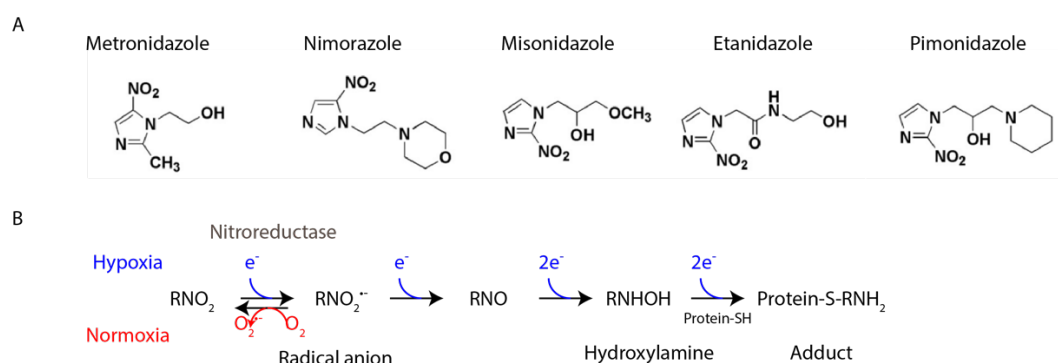


Figure 1.3 2-Nitroimidazoles.

A) Chemical formulae of 5 commonly used 2-nitroimidazoles. B) *In-vivo* reductive activation of 2-nitroimidazoles under normoxic and hypoxic conditions. Adapted from Kizaka-Kondoh and Konse-Kanagawa, 2009¹⁰⁴.

The early nitroimidazoles, such as misonidazole, showed side effects and were soon replaced by nimorazole with similar radiosensitising properties¹⁰⁵. Nimorazole has been demonstrated to significantly improve overall survival of HNSCC patients when given concomitantly with radiotherapy¹⁰⁵. The use of

nimorazole with IMRT is being tested in a phase III clinical trial with HNSCC patients¹⁰⁶. The nitroimidazole evofosfamide showed efficacy in HNSCC patient-derived xenograft (PDX) models as a single agent and in combination with radiotherapy, but its antitumour activity only weakly correlated with hypoxia assessed using pimonidazole^{107,108}. HNSCC patients treated with evofosfamide exhibited a partial response¹⁰⁷. The N-oxide tirapazamine combined with radiotherapy and cisplatin did not show any added benefit to the response of cervical carcinoma and HNSCC patients in phase III and phase II clinical trials, respectively^{109,110}. More recently, the N-oxide banoxantrone was found to enhance the efficacy of radiation in a fibrosarcoma model overexpressing inducible nitric oxide synthase¹¹¹, and selectively targeted hypoxic regions in a Phase I clinical trial¹¹².

1.1.5.2.2 Decreasing the oxygen consumption rate

Improving oxygen availability by decreasing the oxygen consumption rate (OCR) has also been explored with the repurposing of drugs such as the anti-malarial atovaquone, which inhibits complex 3 of the electron transport chain^{113,114}, or metformin, primarily used to treat type 2 diabetes, that inhibits complex 1^{113,115,116} (Figure 1.4). Other compounds have also recently been shown to decrease OCR *in vivo*, including myo-inositol trispyrophosphate (ITPP), an allosteric effector of haemoglobin¹¹⁷, vandetanib, an inhibitor of vascular endothelial growth factor receptor (VEGFR)-dependent angiogenesis¹¹⁸, and NS-398, a non-steroidal anti-inflammatory drug¹¹⁹. Clinical trials to assess the efficacy of metformin in cervical squamous cell carcinoma patients¹²⁰, and atovaquone in lung cancer patients in the UK (ATOM trial)¹²¹ are ongoing.

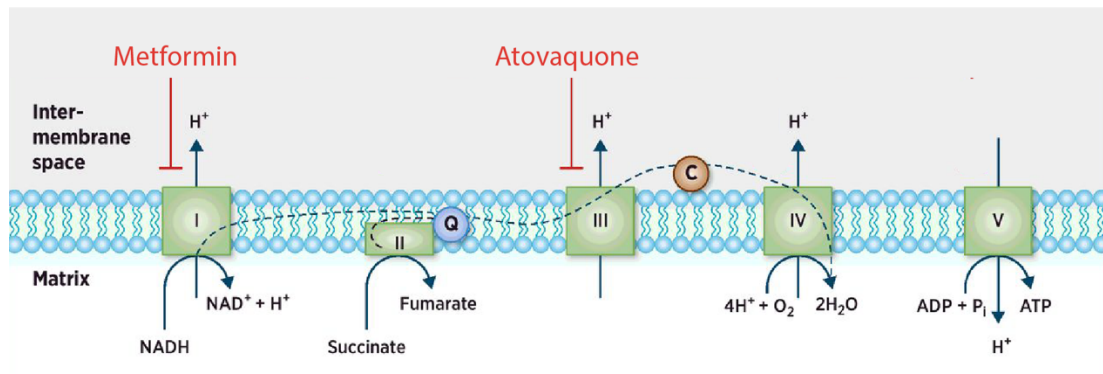


Figure 1.4 The electron transport chain.

Mitochondrial oxidative phosphorylation (OXPHOS) metabolism occurs via the electron transport chain, and is composed of 5 complexes that eventually produce adenosine triphosphate (ATP), the main source of cellular energy. Metformin inhibits complex I and atovaquone inhibits complex III. Adapted from Ashton et al, 2018¹²².

1.1.5.3 Adapting radiation

Radiation treatment aims to adequately target malignant tumours while minimising toxicity in surrounding normal tissues such as salivary glands. This can be achieved by IMRT, which targets and delivers non-uniform doses of radiation to hypoxic tumour subvolumes. IMRT planning requires a reliable imaging technique that provides sufficiently high spatial resolution to accurately identify and map hypoxic subvolumes, as well as organs at risk¹²³.

1.1.6 Assessment of hypoxia

Whilst clinical trials of hypoxia-modifying therapies have shown encouraging results, none have been adopted for routine clinical use. A major limitation of these trials has been the absence of screening for hypoxia prior to patient enrolment. Retrospective analyses have shown that HNSCC tumours identified as hypoxic prior to treatment responded better to hypoxia radiosensitisers^{77,124,125}. Moreover, evaluating hypoxia as a prognostic marker and a tool for IMRT management could help clinicians identify patients who

could benefit, and facilitate treatment stratification^{126,127}. The absence of patient selection is due to the lack of clinically available biomarkers and methods with which to assess hypoxia and monitor tumour response to hypoxia-alleviating treatments¹²⁸.

Three distinct approaches have been developed to detect and measure hypoxia:

- i. Physical measurements of tumour pO₂ *in vivo*: polarographic sensors such as the Eppendorf electrode (preclinical and clinical) and the OxyLite sensor (preclinical)¹²⁹
- ii. Identification and quantification of exogenously administered hypoxia markers by IHC: 2-nitroimidazoles such as pimonidazole, EF5¹³⁰.
- iii. Identification by IHC of endogenous markers upregulated by hypoxia, such as HIF, and downstream markers such as carbonic anhydrase IX (CAIX) and glucose transporter 1 (GLUT-1)¹³⁰.

Modalities to directly measure tumour oxygenation are presented in Table 1.2. However, these techniques are invasive, provide a limited subsampling of the whole tumour and lack information about heterogeneity of hypoxia within the tumour or patient. Moreover, repeat measurements are impractical¹³¹.

The main approaches used for histological detection of hypoxia are summarised in Table 1.3. However, biopsies may be challenging or impossible to obtain from some tumour types/sites, and single biopsies may not be representative of a whole tumour. Despite the excellent spatial resolution, histology provides static information on hypoxia, which may be difficult to interpret when investigating dynamic processes such as cycling hypoxia. Moreover, although these markers have been associated with poor prognosis,

loco-regional control and survival¹³², staining patterns and co-localization are not perfectly identical between the endogenous markers hypoxia-inducible factor 1 α (HIF-1 α), carbonic anhydrase IX (CAIX) and glucose transporter 1 (GLUT-1), reflecting the complexity of the metabolic response to hypoxia^{130,133,134}. Other hypoxia-independent mechanisms may regulate HIF-1 α ¹³⁵⁻¹³⁸, CAIX¹³⁹ and GLUT-1¹⁴⁰. For example, HIF stabilisation can occur under normoxic conditions¹⁴¹. Even though differentiation-associated binding may occur, pimonidazole remains the main hypoxia biomarker used for histopathology¹⁴².

Imaging methods can bypass these obstacles by providing spatial and temporal information on hypoxia in both whole tumour volumes and subregions thereof.

	pO₂ histography	
	Eppendorf¹⁴³	OxyLite¹⁴⁴
Basis of O₂ measurement	Current generated from O ₂ ionization	Lifetime decay of fluorescent dye
Quantitative biomarker	pO ₂ (mmHg)	
pO₂ compartment	Both vascular and tissue compartments	
Range	Sensitive at low pO ₂ (pO ₂ <2.5mmHg)	Highest signal at low pO ₂ (pO ₂ <2.5mmHg)
Sensitivity	<1 mmHg	
Temporal resolution	Seconds	
Spatial resolution	Sub mm	
Preclinical/ clinical	Preclinical and clinical	Preclinical
Direct/ indirect	Direct	
Invasive	Yes	
Availability	Poor (No longer commercially supported)	Good
Costs	Inexpensive	

Table 1.2 Summary of pO₂ histography methods.
Adapted from Rickard et al., 2019³¹.

Marker	Exogenous or endogenous	Biological role	Ease and robustness of use	Measurement	Validated in animals	Validated in radiotherapy	Approved for clinical use	Availability
HIF-1α	Endogenous	Transcription factor overexpressed in cancer cells, under hypoxic (but also normoxic) conditions	Good	Biological hypoxia	?	Yes	No	Good
GLUT-1	Endogenous	Glucose transporter upregulated in hypoxic conditions (HIF-1 α downstream target).	Good	HIF trans-activation	Yes	Yes	Yes	Good
CA-IX	Endogenous	Regulates pH under hypoxia-induced acidosis (HIF-1 α downstream target).	Good	HIF trans-activation	?	Yes	Yes	Good
Nitroimidazoles (e.g. pimonidazole, EF5)	Exogenous	Nitroimidazole reduced in hypoxic conditions in presence of nitroreductases, in viable cells.	Good	Acute/chronic hypoxia	Yes	Yes	Yes	Average

Table 1.3 Summary of main histological markers used to study hypoxia ex vivo and validate imaging biomarkers of hypoxia in HNSCC^{26,145}.

HIF: Hypoxia-Inducible Factor; GLUT: Glucose Transporter; CA: Carbonic Anhydrase. Adapted from Swartz et al, 2015¹³² and Tatum et al., 2006¹⁴⁶.

1.2 Imaging hypoxia

An imaging modality for hypoxia must meet several requirements¹⁴⁷:

- i. Accurate distinction between hypoxia, normoxia and necrosis. Necrotic areas are hypoxic or anoxic, but are medically irrelevant.
- ii. Sensitivity to hypoxic pO₂ (equal or lower than 10 mmHg).
- iii. High spatial resolution to assess the diffusion distance of oxygen (180-200 μm).
- iv. High temporal resolution to image cycling hypoxia.
- v. Broad access to any depth of solid tumour location.
- vi. Non-invasive.
- vii. Repeatable.
- viii. Translatable to the clinic for routine use, including costs and patient compliance.

1.2.1 Requirements of a good imaging biomarker of hypoxia

A biomarker is defined as “a characteristic that is measured as an indicator of normal biological processes, pathogenic processes or responses to an exposure or intervention, including therapeutic interventions”¹⁴⁸. Imaging biomarkers of hypoxia must be:

- i. Technically achievable.
- ii. Validated biologically and clinically.
- iii. Sensitive to pO₂ changes and related to clinical outcome.

To date, no standardised hypoxia imaging biomarkers are used routinely in the clinic because they have failed to meet all these criteria¹⁴⁹.

1.2.2 Introduction to the imaging modalities available for assessing hypoxia

The development and application of non-invasive methods to rapidly determine the distribution and extent of hypoxia in an individual tumour would clearly enhance cancer treatment strategies and be of considerable clinical use. Here the underlying principles of some imaging approaches being exploited to investigate tumour hypoxia are briefly introduced (Table 1.4).

1.2.2.1 Positron Emission Tomography

Positron emission tomography (PET) is the most commonly used imaging modality in the clinic and in clinical trials for imaging tumour hypoxia. PET involves the injection of a radiolabelled biological molecule. Imaging of the radiotracer uptake and distribution in a tumour can identify and quantify specific pathophysiological processes such as hypoxia. Common PET tracers for hypoxia are nitroimidazole derivatives linked to short-lived radionuclides, such as fluorine-18 (¹⁸F)- misonidazole (MISO)^{123,150}, [¹⁸F]-fluoroazomycin-araboside ([¹⁸F]-FAZA)¹⁵¹, and [¹⁸F]-2-(2-nitro-1[H]-imidazol-1-yl)-N-(2,2,3,3,3-pentafluoropropyl)-acetamide ([¹⁸F]-EF5)^{152,153(p5)}, which are similarly reduced under oxygenation conditions of less than 10 mmHg (cf. Section 1.1.5.2.1). However, PET is an indirect method that cannot provide absolute values of pO₂. Moreover, PET imaging involves exposure to ionizing radiation and its accessibility in terms of availability and costs remains limited.

1.2.2.2 Electron Paramagnetic Resonance

Electron paramagnetic resonance (EPR) oximetry is based on the effects of oxygen on the EPR spectra of implanted particulate paramagnetic materials, which occur due to the presence of two unpaired electrons in molecular oxygen. These electrons generate a strong fluctuating magnetic field that modifies the EPR spectra in proportion to the local pO_2 ^{80,154}. The paramagnetic spin probe, such as trityl radicals¹⁵⁵, must be implanted in the tumour tissue, but once in place can remain indefinitely because of their extreme inertness, facilitating longitudinal imaging studies. The spatial and temporal resolution of EPR thus allows a direct measurement of pO_2 and can be used to track progression and treatment-induced changes in hypoxia, as well as cycling hypoxia^{156,157}. However, EPR spatial resolution is relatively low, and the probe implantation is minimally invasive¹⁵⁸.

1.2.2.3 ¹⁹F MRS of fluorinated 2-nitroimidazoles

2-nitroimidazoles undergo a hypoxia-dependent bioreductive metabolism via a number of highly reactive and unstable intermediates, which can undergo binding to cellular macromolecules. Fluorinated 2-nitroimidazoles enable the detection of these reduced adducts non-invasively using ¹⁹F magnetic resonance spectroscopy (MRS). Tumour hypoxia is assessed by comparing the ¹⁹F MR spectrum of the retained, reduced adducts acquired at a late time point after administration of a 2-nitroimidazole to the ¹⁹F MR spectrum acquired at an early time point, when the parent 2-nitroimidazole predominates. The degree of tumour hypoxia is then described by a retention index i.e. how

much of the fluorinated 2-nitroimidazole is retained within the tumour^{159,160}. Nevertheless, the accumulation remains difficult to quantify due to the T₂ broadening effects of the bound adducts¹⁶¹.

1.2.2.4 ¹⁹F MR oximetry of perfluorocarbons

¹⁹F MR oximetry relies on the linear increase of the MRI spin-lattice relaxation rate R₁ of perfluorocarbon (PFC) emulsions, hydrocarbons in which the protons are replaced with fluorine nuclei, with increasing oxygen tension. Molecular oxygen has a very high solubility in PFC emulsions, permitting oxygen tension measurements in tumour locations where the PFC is sequestered^{162–165}. The measurement of PFC spin-lattice relaxation rates *in vivo* is currently the only nuclear magnetic resonance (NMR) methodology that can yield absolute tumour pO₂ measurements. However, methods of PFC probe administration are minimally invasive and affect the sensitivity of the method. If directly injected into the tissue, the signal, and hence pO₂, is restricted to the site in which the probe resides. If administered intravenously, the low signal-to-noise ratio (SNR) in poorly vascularised areas makes pO₂ measurements challenging^{166,167}. Moreover, intravenous injection of PFCs have also been reported to cause pulmonary embolisms in mice¹⁶².

1.2.2.5 Magnetic resonance spectroscopy

Magnetic resonance spectroscopy (MRS) offers a non-invasive, non-destructive method of studying tissue biochemistry *in situ*. ¹H-MRS assessment of tumour lactate, the end product of glycolysis, has been shown to be associated with tumour pO₂ measured by Eppendorf histography in

HNSCC patients¹⁶⁸. Hyperpolarized ¹³C-MRS detects and quantifies real time conversion of [¹³C]-labelled pyruvate to [¹³C]-labelled lactate, which has been shown to reflect tumour oxygenation status measured by EPR^{169,170}. ³¹P MRS monitors endogenous phosphorus-containing tumour metabolites such as phosphocreatine, nucleoside triphosphates and phospholipids, used to inform on tumour energetics, pH and proliferation. These high-energy metabolites may reflect tumour oxygenation^{171,172}. However, this technique relies on surrogate markers of hypoxia. Metabolic reprogramming from oxidative phosphorylation (OXPHOS) towards glycolysis is a hallmark of cancer, but can vary amongst tumour types⁷³. Although mediated by HIF-1 α , glycolysis may occur in aerobic conditions (Warburg effect), reducing the sensitivity of MRS-derived readouts^{173,174}.

1.2.2.6 Optical spectroscopy

Optical spectroscopy relies on the absorption of near-infrared (800 nm) light by oxyhaemoglobin and deoxyhaemoglobin. Total haemoglobin concentration can be used to determine the oxygen saturation sO₂, providing indirect but reliable measurements of tumour hypoxia¹⁷⁵. The main drawback lies in the limited penetration depth due to high tissue absorption and scattering. Moreover, information on tumour hypoxia is limited to the vascular compartment.

1.2.2.7 Photoacoustic tomography

Photoacoustic tomography (PAT) combines the sensitivity of optical imaging with the resolution of ultrasound. The absorption of light in the visible and near-

infrared spectrum (from 700 to 900 nm) by haemoglobin leads to a localised heating and a thermoelastic expansion, which generates pressure waves (ultrasound). Calculation of the oxygen saturation from the PAT signal provides an assessment of tumour perfusion, closely linked to hypoxia¹⁷⁶.

The challenges of this technique reside in the tissue composition, which may lead to the loss and distortion of optic and acoustic waves, complicating the image reconstruction process¹⁷⁷.

	PET	MRI				EPR	MRS		Optical spectroscopy	PAT
		DCE-MRI	IS-MRI	OE-MRI	MOBILE-MRI		Metabolites	Chemicals		
Basis of O₂ measurement	Accumulated signal of positron emitting labelled isotope	Tissue water containing accumulated paramagnetic gadolinium-based contrast agent	Magnetic state of dHb erythrocytes	[O ₂] in vascular and interstitial tissue	[O ₂] dissolved in lipids	Change in line width of paramagnetic probe upon interaction with O ₂	Concentration of metabolites such as lactate, with ¹ H-MRS, high-energy phosphates with ³¹ P-MRS	Concentration of reduced [¹⁹ F]-labelled 2-nitroimidazoles with ¹⁹ F-MRS and [¹⁹ F]-perfluorocarbons (O ₂ sensors)	Optical absorbance of Hb	Optical absorbance of Hb
Quantitative biomarker	SUV	K ^{trans} , V _e , V _p	ΔR ₁ and ΔR ₂ * (s ⁻¹)			pO ₂ (mmHg)	Ratio of metabolite concentrations		HbT(μM), sO ₂ (%)	
pO₂ compartment	Tissue	Both	Vascular	Both	Tissue	Tissue	Tissue	Vascular	Vascular	
Range	Marker dependent. [¹⁸ F]-nitroimidazoles (¹⁸ F-EF5, ¹⁸ F-MISO, ¹⁸ F-FAZA): 0-10 mmHg	DCE-derived biomarkers based on pharmacodynamic modelling	ΔR ₂ * from air to hyperoxic gas proportional to starting [dHb]/[Hb]	ΔR ₁ from air to hyperoxic gas	ΔR ₁ from air to hyperoxic gas	0-100 mmHg	Marker dependent	0-100% Hb saturation	0-100% Hb saturation	
Sensitivity	Dependent on voxel spatial distribution of hypoxia	Not applicable	Not applicable	>1 mmHg	>1 mmHg	<1mmHg	>1mmHg	Hb saturation	Hb saturation	
Temporal resolution	Minutes to hours	Minutes	Seconds	Minutes	Minutes	Minutes-hours (real time)	Minutes	Seconds	Seconds	
Spatial resolution	Few mm	Sub mm	Machine dependent; sub mm-cm	Sub mm	Sub mm	Mm	Mm	Mm-cm	Mm	
Preclinical/clinical	Both	Both	Both	Preclinical (+early clinical studies)	Preclinical (+early clinical studies)	Preclinical (+clinical trials)	Both	Both	Preclinical	
Direct/ indirect	Indirect	Indirect	Indirect	Indirect	Indirect	Direct	Indirect	Indirect	Indirect	
Invasive	Minimally	Minimally	No	No	No	Minimally	No	No	No	
Availability	Moderate	Wide	Poor	Poor	Poor	Poor	Poor	Poor	Poor	
Costs	Costly	Costly	Costly	Costly	Costly	Average	Costly	Inexpensive	Inexpensive	

Table 1.4 Summary of preclinical and clinical imaging modalities used to detect hypoxia.

PET: Positron-Emission Tomography; DCE: Dynamic Contrast Enhanced; IS: Intrinsic Susceptibility; OE: Oxygen-Enhanced; MOBILE: Mapping Oxygen By Imaging Lipids Enhancement; EPR: Electron Paramagnetic Resonance; MRS: Magnetic Resonance Spectroscopy; PAT: PhotoAcoustic Tomography; Hb: haemoglobin; dHb: deoxyhaemoglobin; HbT: total haemoglobin concentration, sO₂: oxygen saturation. Adapted from Rickards et al., 2019³¹.

1.2.3 Imaging hypoxia with ^1H MRI

1.2.3.1 ^1H -MRI principles

1.2.3.1.1 Magnetic moment of protons

Magnetic resonance imaging (MRI) is based on the magnetic resonance signal of hydrogen nuclei in water molecules, composed of a single proton. Protons possess an intrinsic half-integer spin, a form of angular momentum. Placed in a strong external static magnetic field B_0 , these spins align with the direction of B_0 and rotate or precess at an angle around their axes at a specific frequency known as the Larmor frequency (ω_0). Doing so, they generate their own microscopic magnetic field and magnetic moment μ (Figure 1.5A). Spins are oriented in either of two directions or states, parallel or anti-parallel to B_0 , which depends on their energy: the parallel state requires less energy than the anti-parallel state (Figure 1.5B). The sum of all the spins, called the net magnetization M_0 , is aligned with B_0 and is conventionally represented as the z direction (Figure 1.5C). ω_0 is proportional to B_0 as stated by the Larmor equation:

$$\omega_0 = \gamma B_0$$

Equation 1.1 Larmor frequency equation.

ω_0 : Larmor frequency, γ : gyromagnetic ratio a constant for a particular species e.g. $\gamma(^1\text{H})=2.67519 \times 10^8 \text{ rad}\cdot\text{s}^{-1}\cdot\text{T}^{-1}$, B_0 : magnetic field strength.

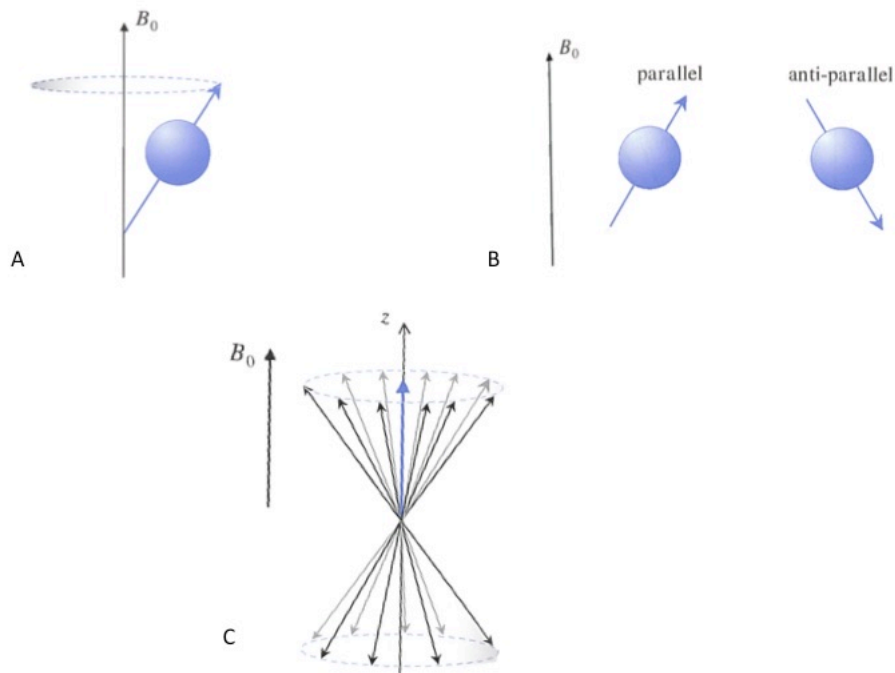


Figure 1.5 Spin precession.

A) Precession of the magnetic moment μ . B) Two possible orientations for the spin in an external magnetic field B_0 . C) Net magnetization M_0 (in blue) or average of many magnetic moments. Taken from McRobbie et al¹⁷⁸.

When a radiofrequency (RF) pulse is applied at the Larmor frequency, a magnetic field B_1 , perpendicular to B_0 , is created, aligned along the x' axis, which is the x direction in the rotating frame (Figure 1.6A). M_0 spirals away from the z axis and down towards the transverse xy plane (Figure 1.6B). The strength of the pulse, proportional to B_1 , RF duration and γ , defines the flip angle (FA). For a 90° RF pulse, M_0 tends towards the transverse plane, whereas for a RF pulse greater than 90° , the spins are oriented towards the $-z$ axis (Figure 1.6C), and eventually inverted (FA= 180°). When the RF pulse is stopped, the amplitude of the signal induced in the receiver coil by M_0 voltage precessing in the transversal plane (laboratory frame) decays as the

protons dephase thus cancelling each other out, as shown in the free induction decay (FID) chart (Figure 1.6D).

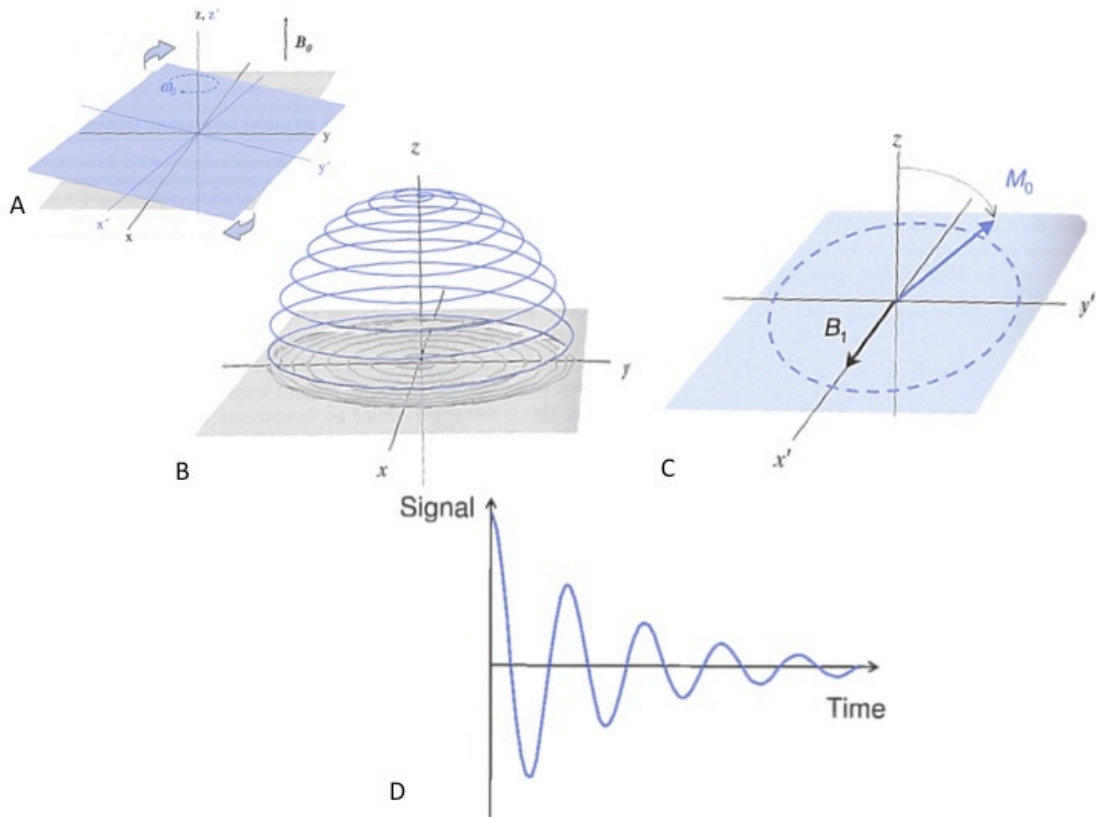


Figure 1.6 MR signal.

A) The rotating frame of reference. The coordinate system x', y' and z' is considered to be rotating at the Larmor frequency at the same direction as the spins, which thus appear stationary. B) During the RF pulse, M_0 spirals away from the z axis and down towards the transverse plane xy . C) M_0 precesses around B_1 until the RF is switched off. D) Free Induction Decay (FID), signal induced in the receiver coil. Adapted from McRobbie et al.¹⁷⁸

In MRI, it is not the direct FID but sets of echoes that are detected and used to generate images. This requires combinations of RF pulses and spatially varying magnetic field gradients.

In the gradient echo sequence (Figure 1.7A), a negative magnetic field gradient is applied immediately after the excitation pulse, affecting the spins in phase (Figure 1.7B). This causes spin dephasing (Figure 1.7C), and a subsequent fading of the signal. A positive gradient is then applied (Figure

1.7D), causing the spins to rephase and form an echo (Figure 1.7E). Flip angles smaller than 90° are used in gradient echo sequences.

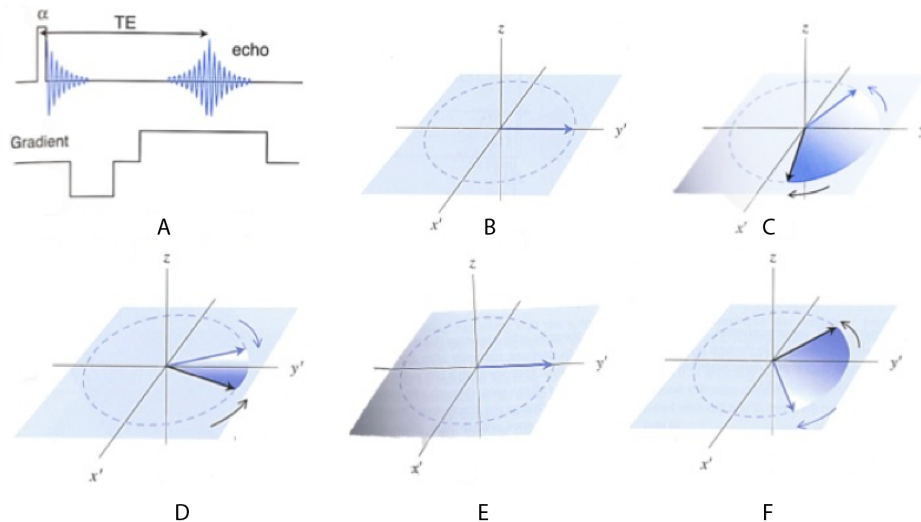


Figure 1.7 Gradient-echo sequence.

A). Simple gradient-echo sequence. B) Spins are initially along the y' axis. C) The spins are rapidly dephased by the negative gradient lobe. D) When the gradient is switched to positive, the spins begin to rephase. E) The spins form an echo. F) If the gradient is left on, dephasing will occur again. From McRobbie et al.¹⁷⁸.

In the spin echo sequence (Figure 1.8A), after the initial period of dephasing caused by transverse relaxation, a second RF pulse is applied (Figure 1.8B). This RF pulse has a flip angle of 180° , which inverts the spins along the y' axis, reversing their phase (Figure 1.8D). The spins will continue to evolve with their characteristic phases, causing rephasing (Figure 1.8E). After a time equal to the delay between the 90° and 180° pulses, all the spins are in phase again (Figure 1.8F), forming the spin echo.

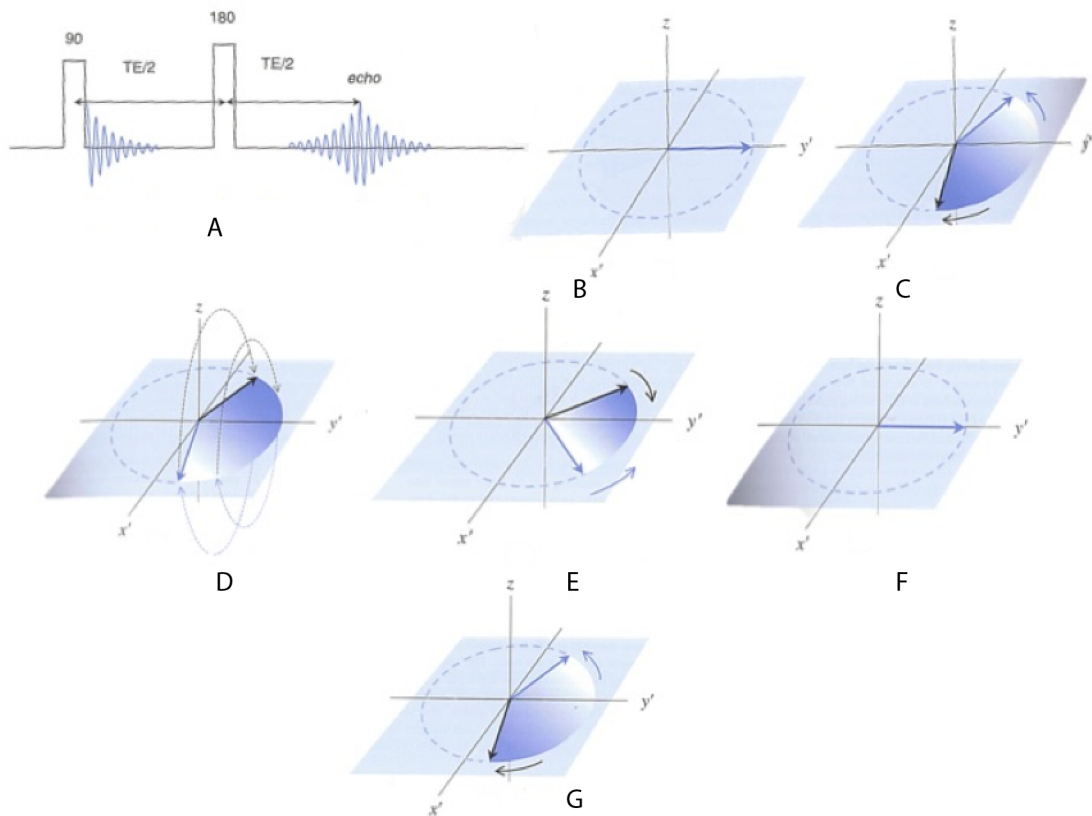


Figure 1.8 Spin echo sequence.

A) Simple spin echo pulse sequence. B) Spins are initially in phase. C) Spins dephase naturally after the 90° excitation pulse. D) The 180° pulse reverses spin phases E) But spins continue to evolve according to their characteristic phases, causing rephasing. F) Spins form an echo. G) and then dephase again. Adapted from McRobbie et al.¹⁷⁸

The sequences of RF pulses and gradients are repeated in order to acquire sets of echoes required to generate MR images. The time between initial sequence excitations (e.g. consecutive 90° RF pulses in spin echo sequence) is the repetition time (TR), and the delay between the RF pulse and the centre of the generated echo is called the echo time (TE).

1.2.3.1.2 Relaxation times

There are two different spin relaxation processes happening at the same time: spin-spin or transverse relaxation and spin-lattice or longitudinal

relaxation. The net magnetization is only equal to the equilibrium magnetization immediately after the initial 90° pulse and after full relaxation (Figure 1.9E).

The transverse relaxation is the dephasing of the spins on the transverse plane and loss of coherence and signal due to the random interactions between spins (Figure 1.9A and B). The transverse relaxation time is described as T_2 and is the time taken for the transverse magnetization to drop to 37% of its initial size (Figure 1.10C).

The longitudinal relaxation is the realignment of the spins along the z axis or recovery of magnetization (Figure 1.9C and D), and is due to the random interaction of the spins with their environment or lattice (cell membranes, etc.) which can absorb energy. The longitudinal relaxation time is known as T_1 and is the time taken for the magnetization to recover to 63% of its equilibrium value (Figure 1.10B). T_2 is always shorter than T_1 for a given tissue (Figure 1.10A).

As a consequence of the main magnetic field inhomogeneity, the apparent transverse relaxation time becomes shorter but the longitudinal relaxation time remains unchanged. This is due to accelerated dephasing caused by local differences in the magnetic field. The combined T_2 and magnetic field inhomogeneity is called T_2^* . T_2^* relaxation is one of the main determinants of image contrast in gradient echo sequences.

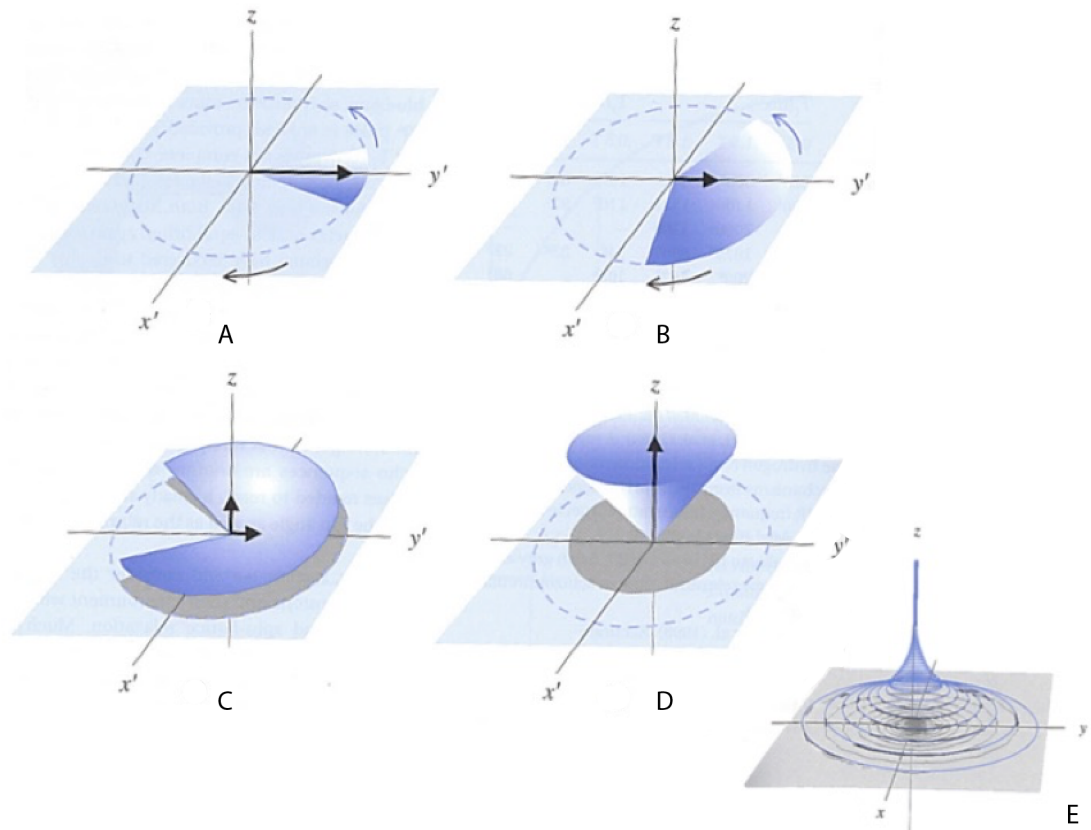


Figure 1.9 Magnetic transverse and longitudinal relaxations.

A) and B) T_2 relaxation causes rapid fanning out of the protons in the transverse plane. C) and D) T_1 relaxation, causing a fanning out in the longitudinal plane, is much slower and can be thought of as an umbrella closing up. E) Relaxation as viewed from the laboratory frame of reference. Adapted from McRobbie et al¹⁷⁸.

Fluids (e.g. cerebrospinal fluid, blood) have long relaxation times; tissues with a high water content (e.g. brain) exhibit mid-range relaxation times whereas dense tissues (e.g. bones) have short relaxation times. Due to the different signal loss behaviour, fluids appear dark on T_1 -weighted images and bright on T_2 - weighted images. The signal can be modulated using exogenously administered contrast agents, such as paramagnetic gadolinium-based agents (see 1.2.3.2), or small paramagnetic iron oxide particles (SPIO) (see 1.2.3.3).

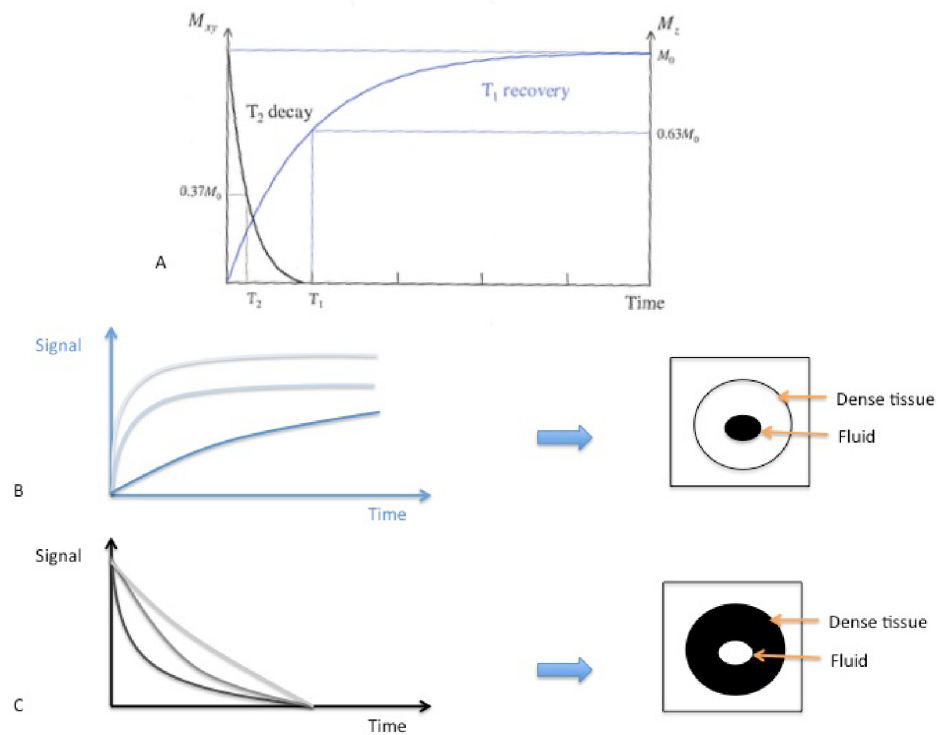


Figure 1.10 T_1 and T_2 relaxation.

T_1 and T_2 relaxations occur simultaneously but T_2 is quicker than T_1 . B. T_1 is the time taken for the magnetization to recover to 63% of its equilibrium value and the process is random thus exponential. The darker the signal line, the longer the T_1 . In the T_1 -weighted images, fluids appear dark and dense, tissues appear bright. C. T_2 is the time taken for the transverse magnetization to drop to 37% of its initial size. The darker the signal line, the shorter the T_2 . In the T_2 -weighted images, fluids appear bright and dense, tissues appear dark. Adapted from McRobbie et al¹⁷⁸.

In addition to high resolution images with exquisite soft tissue contrast, MR image acquisition can also be sensitised to numerous independent contrast mechanisms, from which parametric maps can be calculated and used to provide additional information on tumour structure and function.

1.2.3.2 Dynamic contrast enhanced MRI

1.2.3.2.1 Principle

Dynamic-contrast enhanced MRI (DCE-MRI) is the most common functional application of MRI in clinical oncology, informing on patent tumour vasculature. This technique relies on the intravenous injection of a low molecular weight paramagnetic gadolinium (Gd)-chelated contrast agent which shortens the tissue T_1 relaxation time, with malignant tumours demonstrating faster and higher signal enhancement in T_1 -weighted images compared to normal tissues, a consequence of their hyperpermeable vasculature. Rapidly acquired serial (“dynamic”) T_1 measurements are related to contrast agent extravasation from the blood plasma compartment to the extravascular extracellular compartment. Pharmacokinetic modelling of the data enables the volume transfer constant K^{trans} , the extravascular extracellular volume fraction v_e , and the blood plasma volume fraction v_p to be estimated¹⁷⁹. It is important to note that when using a low molecular weight gadolinium chelate, increasing contrast agent concentration into the extracellular leakage space is related to both tumour perfusion and permeability.

1.2.3.2.2 Hypoxia measurement

Poor perfusion, typically observed in malignancies, is often linked to a poor oxygenation^{180,181}. Moreover, VEGF is a target gene of HIF signalling and VEGF-dependent neovasculature¹⁸². Therefore DCE-MRI was suggested as an indirect imaging method to assess neovasculature permeability associated with hypoxia. However, unclear results have been observed in preclinical and clinical studies. For example, K^{trans} was shown to inversely correlate with

hypoxic fraction, measured by Eppendorf histography, in cervical squamous cell carcinoma patient-derived xenografts and head and neck patients^{180,183,184}. However, K^{trans} did not correlate with hypoxic fraction as measured by pimonidazole in both preclinical models of glioma and glioblastoma patients¹⁸⁵. Nevertheless, DCE- MRI is a valuable tool for the assessment of functional tumour vasculature, and can be particularly used for delineating non-perfused, often necrotic tumour sub-regions¹⁸⁶.

1.2.3.3 Susceptibility MRI

1.2.3.3.1 Principle

Two complementary magnetic susceptibility-based MRI approaches are being actively exploited to assess tumour hypoxia. The first approach, intrinsic susceptibility-weighted MRI (IS-MRI), (also known as blood oxygen level dependent MRI or BOLD-MRI), depends on the ratio between paramagnetic deoxyhaemoglobin (dHb) and diamagnetic oxyhaemoglobin (Hb) in erythrocytes (Figure 1.12). In deoxyhaemoglobin, iron (Fe^{2+}) is in a paramagnetic state with 4 unpaired electrons. The high $[\text{dHb}]/[\text{Hb}]$ ratio creates magnetic susceptibility perturbations, causing an increase in the effective transverse relaxation rate R_2^* ($=1/T_2^*$) of water in blood. Therefore, deoxyhaemoglobin can serve as an intrinsic contrast agent. The relationship between blood R_2^* and pO_2 can be modelled by a quadratic function, which suggests that IS-MRI is more sensitive in low oxygenation tissues such as tumours¹⁸⁷.

Vascular factors affecting R_2^* include blood oxygen saturation, haematocrit and blood volume¹⁸⁸. Moreover, R_2^* can be affected by static tissue

components such as paramagnetic species associated with necrotic debris and/or arising from the degradation of haemoglobin¹⁸⁹. Cysts, often observed in HNC patients with metastatic lymph nodes, can also contribute to R_2^* contrast⁴¹. Vasoactivity can also influence tumour blood flow and blood volume¹⁹⁰, the magnitude of its effect on R_2^* being dependent on its balance with the $[dHb]/[Hb]$ ratio¹⁸⁸. Therefore R_2^* may also inform on tumour architecture and dynamic function^{191,192}. Moreover, changes in tumour pathophysiology can introduce confounding factors in R_2^* measurements. A decrease in blood pH can cause a rightward shift of the oxygen dissociation curve, thus a decrease in oxygen saturation due to the Bohr effect, resulting in an increase in dHb detected by an increase in R_2^* (Figure 1.11)^{193,194}. Shift from oxidative phosphorylation to glycolysis (Warburg effect) can occur, causing a transient reduction in OCR and a potential increase in R_2^* ¹⁹⁵.

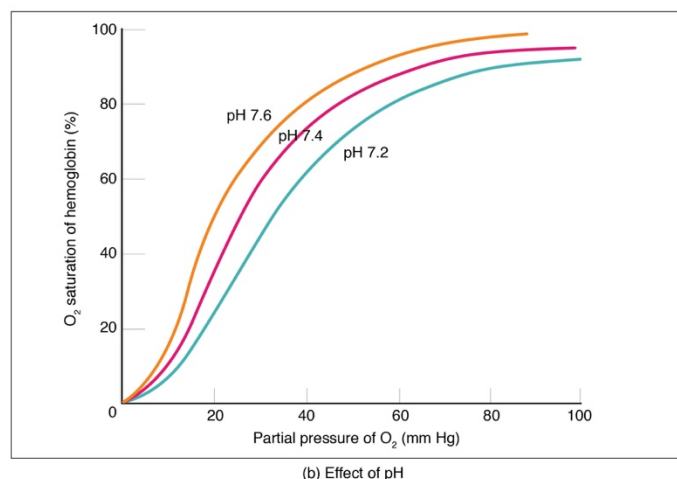


Figure 1.11 Oxygen saturation curve.

Effects of pH on haemoglobin saturation in O_2 ¹⁹³. Taken from Betts et al., 2013¹⁹⁶.

The low specificity of baseline R_2^* on tumour oxygenation led investigators to study the changes in R_2^* following hyperoxic challenge with carbogen (95% O_2 ; 5% CO_2) or 100% oxygen gas. Carbogen was being used to improve

oxygen availability in order to enhance tumour response to accelerated radiotherapy (ARCON trials), and the early IS-MRI studies aimed to measure the carbogen-induced positive effect on tumour oxygenation¹⁹⁷. Carbogen was then used to characterise tumour oxygenation in many preclinical tumour models^{191,198–202}, and cancer patients^{197,203,204}. However, breathing of carbogen gas can be difficult to tolerate in clinical setup. As a result, 100% oxygen became the preferred hyperoxic gas for IS-MRI studies.

The second approach, susceptibility-contrast (SC)-MRI, relies on the intravenous injection of superparamagnetic iron oxide (SPIO) particles to provide information on tumour perfusion, closely linked to hypoxia²⁰⁰. Contrary to the gadolinium-based contrast agents used for DCE-MRI, iron oxide based agents do not readily permeate vessel walls, allowing steady state acquisition of higher resolution images, as well as the calculation of voxel-wise fractional blood volume. Ultrasmall superparamagnetic iron oxide (USPIO) particles have been successfully used to study the patent vasculature in preclinical models of brain tumours^{205,206}, pancreatic ductal adenocarcinoma²⁰⁷, and prostate tumours^{200,208}. Encouraging results in HNC patients were mitigated by the technical issues caused by susceptibility artefacts such as air-tissue interfaces present in the oral cavity, throat and ears^{209,210}. Ferumoxytol, an FDA-approved drug for anaemia treatment²¹¹, has been emerging as a safe off-label USPIO particle MRI contrast agent^{212,213} for use in patients^{214,215}.

1.2.3.3.2 Hypoxia measurement

Since the oxygenation saturation of haemoglobin is proportional to the arterial blood p_aO_2 , and therefore in equilibrium with tissue pO_2 , measurements of R_2^* should provide a sensitive index related to tissue oxygenation. However, there

is no direct relationship between baseline R_2^* and tumour pO_2 , because the longitudinal O_2 gradient from the vessel to the tumour prevents adequate oxygen delivery to the tumour¹⁹⁰. In normoxic tissues, the redundancy of arterioles compensates for the loss of oxygen, whilst the inefficient and poor tumour vasculature in tumours fails to deliver sufficient oxygen.

Several studies have linked hypoxic subregions to faster baseline tumour R_2^* , including in HNSCC and prostate cancer patients^{216,217}. In prostate cancer patients, a significant positive correlation between R_2^* and the fraction of tumour exhibiting a $pO_2 < 5\text{mmHg}$, and a negative trend between R_2^* and pO_2 , were observed²¹⁸. A weak correlation between baseline R_2^* and pO_2 , using the OxyLite probe, was reported in fibrosarcoma xenografts¹⁸⁷. In preclinical models of prostate cancer, a positive correlation between baseline R_2^* and pimonidazole adduct formation was observed²¹⁹. Conversely, baseline R_2^* was negatively correlated with pimonidazole adduct formation in chemically-induced rat mammary carcinomas²²⁰. Collectively, these studies suggest that the complex relationship between baseline R_2^* and hypoxia is dependent on the underlying tumour physiology and needs further investigation in various tumour types.

Hypoxic areas, rich in deoxyhaemoglobin, have been associated with a greater hyperoxia-induced reduction in R_2^* . Improved tumour oxygenation measured using pO_2 histography was associated with a hyperoxia-induced reduction in R_2^* in rat mammary carcinoma and intracranial gliomas^{221,222}. Several preclinical studies have shown strong spatial and quantitative positive relationships of ΔR_2^* with pimonidazole adduct formation^{202,220,223,224}. However, in a preclinical study of fibrosarcoma, no direct relationship between baseline

R_2^* or ΔR_2^* values and pO_2 values, obtained using OxyLite, was observed¹⁸⁷. In the clinic, IS-MRI has successfully been implemented²²⁵ and used to assess hypoxia in prostate cancer and HNC patients^{197,204,216,218}.

R_2^* signal can fluctuate in the absence of hyperoxic challenge, reflecting cycling hypoxia, with cycles ranging from 15 min to an hour. Serial IS-MRI has been used to image cycling hypoxia preclinically in fibrosarcoma, colorectal carcinoma and HNC xenografts, and also in HNC patients³⁹⁻⁴¹. As cycling hypoxia has been associated with a poor outcome in HNC patients, baseline R_2^* without gas challenge may provide a prognostic imaging biomarker⁴³.

1.1.1.1 Oxygen- enhanced MRI

1.2.3.3.3 Principle

Oxygen-enhanced MRI (OE-MRI) relies on the paramagnetic properties of dissolved molecular oxygen. When a hyperoxic gas is inhaled, excess oxygen is carried in the blood plasma or interstitial fluid in tissues with adequate perfusion. Since well-oxygenated tissues have near complete saturation of haemoglobin molecules, the excess delivered oxygen remains dissolved in blood plasma and interstitial tissue fluid, increasing the MRI longitudinal relaxation time R_1 ($R_1=1/T_1$)²²⁶ (Figure 1.12). In hypoxic tissues, haemoglobin is mainly in its deoxygenated form, inhalation of hyperoxic gas increases the oxygen saturation of haemoglobin, resulting in a lower concentration of dissolved oxygen, and thus an absence of change in R_1 . Due to the influence of iron on the relaxivity of deoxyhaemoglobin, R_1 may even decrease^{227,228}.

The relaxivity of O_2 molecules decreases with the magnetic field strength^{186,201}, but this drawback is offset by the high signal to noise ratio (SNR) at high

magnetic field strengths^{201,229,230}. Furthermore, other factors, such as blood inflow²³¹, size of the interstitial compartment²³², necrosis^{233,234}, tissue water content²³³, haematocrit in the blood compartment^{227,235,236}, a high concentration of deoxyhaemoglobin^{227,237} and temperature^{231,238} may have an impact on R_1 , limiting its specificity and preventing a direct quantitative comparison with tumour pO_2 .

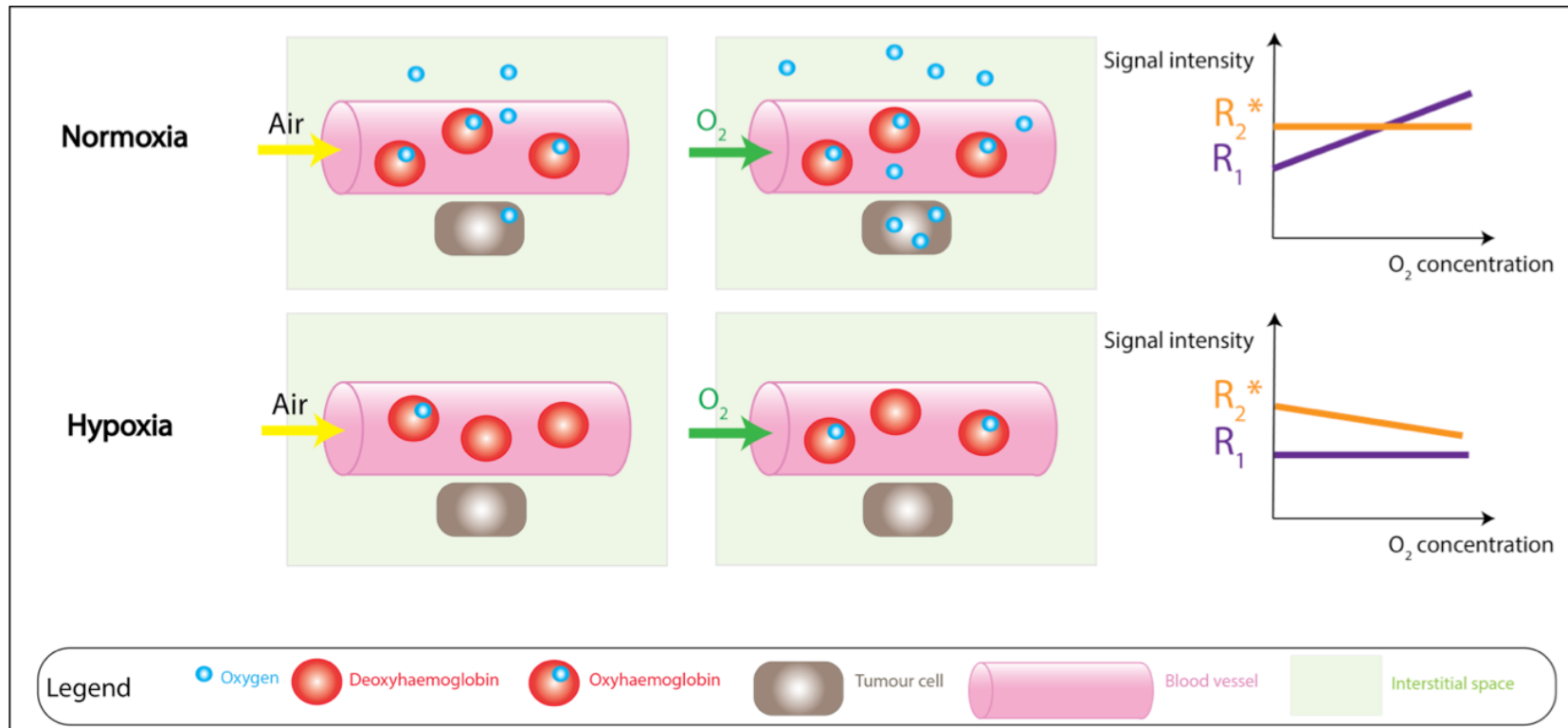


Figure 1.12 Principles of OE-MRI and IS-MRI. OE-MRI.

Under normoxia, haemoglobin is under its oxygenated form. Hyperoxic gas challenge induces the accumulation of paramagnetic oxygen dissolved in the vascular and extracellular compartments, leading to an increase in R_1 . In hypoxic tissue, such as that in tumours, the proportion of deoxyhaemoglobin is far higher. Therefore, with hyperoxia challenge, oxygen molecules bind to haemoglobin, and R_1 thus remains stable. Note that a decrease in R_1 may occur due to the influence of paramagnetic iron bound to the deoxyhaemoglobin. IS-MRI: Under normoxia, the proportion of paramagnetic deoxyhaemoglobin compared to diamagnetic oxyhaemoglobin is low. After hyperoxic gas inhalation, this proportion does not significantly change, therefore R_2^* remains stable. Under hypoxia, haemoglobin is mainly deoxygenated. With hyperoxic challenge, and haemoglobin saturation, the $[dHb]/[Hb]$ ratio decreases, thereby decreasing in R_2^* . Adapted from O'Connor et al., 2016¹⁸⁶.

1.2.3.3.4 Hypoxia measurement

Since R_1 variations are directly sensitive to changes in tissue pO_2 ⁷⁶, OE-MRI can identify poorly oxygenated tumour subregions using a hyperoxia challenge^{223,238,239}. Positive ΔR_1 identifies, maps and quantifies tissue with fully saturated haemoglobin but does not directly measure tissue hypoxia. Tumour subregions exhibiting low haemoglobin oxygen saturation are refractory to hyperoxic gas challenge^{185,221}. O'Connor *et al* demonstrated that spatial assessment of perfused tumour subregions that were refractory to the oxygen challenge (referred to as the pOxyR fraction) enabled the identification, quantification and mapping of tumour hypoxia better than whole tumour median ΔR_1 (Figure 1.13)¹⁸⁶. DCE-MRI was performed in the same imaging session to assess perfusion and to correct for necrosis, whereby non-perfused areas defined by lack of contrast agent enhancement were excluded from the analysis volume. Moreover, pOxyR fraction also correctly informed on dynamic changes in hypoxia induced by the vasomodulator agent hydralazine¹⁸⁶.

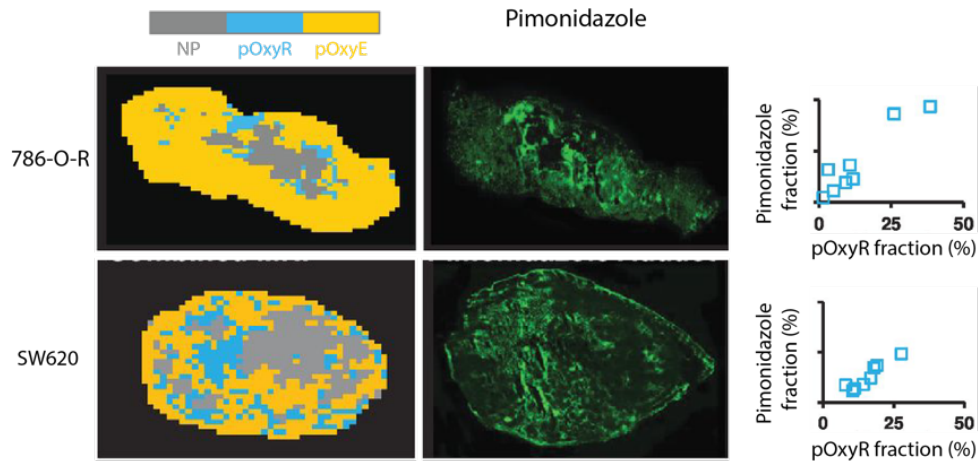


Figure 1.13 Characterisation of hypoxia using OE-MRI.

Parametric maps of perfused oxygen refractory voxels (pOxyR, cyan), perfused oxygen enhanced voxels (pOxyE, yellow) and non-perfused voxels (NP, grey) (left panel), and fluorescence images of pimonidazole adducts (green, hypoxia) from representative 786-O-R renal adenocarcinoma and SW620 colorectal carcinoma. Adapted from O'Connor et al., 2016¹⁸⁶.

Perfused OxyR fraction positively correlated with pimonidazole adduct fraction in 786-O-R renal cell adenocarcinoma (RCA), Calu6 non small cell lung cancer (NSCLC) and U87 glioma xenografts^{224,240}. Moreover, pOxyR subregions exhibited a fast baseline R_2^* and a greater $\Delta R_2^*_{O_2-air}$, cross-validating OE-MRI measurements of hypoxia using IS-MRI in the well-perfused but hypoxic 786-O-R RCA model²²⁴. OE-MRI detected chemoradiotherapy-induced changes in tumour hypoxia in Calu6 NSCLC and U87 glioma xenograft models, in which pOxyR volume decreased following one single 10 Gy radiation fraction or fractionated radiotherapy combined with cisplatin²⁴⁰. OE-MRI has shown promise as a prognostic tool of response to radiation in RMS, 9L glioma and Dunning R3327-AT1 rat prostate tumour models^{241–243}.

OE-MRI has successfully been implemented in the clinic in patients with HNC lymph node metastases, RCA, NSCLC and anal squamous cell carcinoma (ASCC)^{224,240,244,245}. Moreover, OE-MRI could monitor response to chemoradiotherapy. pOxyR volume decreased after radiotherapy in NSCLC patients, and a significant decrease in T_1 following chemoradiotherapy was detected in ASCC patients^{240,245}.

OE-MRI allows for repeated measurements, which enables assessment of cycling hypoxia during the same imaging session and response to hypoxia-modifying treatments over several separate imaging sessions. Moreover, since ΔR_1 does not directly depend on haemoglobin saturation¹⁴⁷, OE-MRI is complementary to IS-MRI, which informs on the tumour vasculature. Other R_1 -weighted OE-MRI approaches have recently emerged, with the aim of improving the sensitivity of OE-MRI. Dynamic OE-MRI (dOE-MRI) acquisition using cycling gas challenge, paired with independent component analysis (ICA), was shown to increase OE-MRI sensitivity and decreased the acquisition time in several preclinical cancer models²⁴⁶. Hypoxic gas challenge (16% O_2) has been used in preclinical models of breast cancer, in order to mask the reduction of R_1 induced by paramagnetic deoxyhaemoglobin, which may offset R_1 response to a hyperoxic gas challenge²⁴⁷. An increase in R_2^* but either an increase or decrease in R_1 , was observed, indicating a dominant effect of increased paramagnetic deoxyhaemoglobin, outweighing the decreased tumour oxygenation induced by the hypoxic gas.

1.2.3.4 Mapping oxygen by lipid enhancement MRI

1.2.3.4.1 Principle

Similar to OE-MRI, mapping oxygen by lipid enhancement MRI (MOBILE-MRI) detects hyperoxia-induced changes in R_1 of lipids in tumours. Instead of focussing on oxygen dissolved in fluids, MOBILE-MRI measures oxygen dissolved in lipids²⁴⁸. The higher solubility of oxygen in lipids increases the sensitivity of R_1 signal²⁴⁹. MOBILE-MRI has been successfully performed on normal and tumour tissues, as well as in healthy volunteers and neuroepithelial tumour patients^{248,250}.

1.2.3.4.2 Hypoxia assessment

The higher solubility of oxygen in lipids compared to water was able to monitor R_1 changes after gas or pharmacological modification of oxygenation, in preclinical mammary tumour models and in patients^{242,243,248,250}.

However, this technique is only efficient for tissues with a high lipid content, and requires an efficient water signal suppression.

1.3 Thesis aims and structure

The overall aim of this thesis is to evaluate OE-MRI for the assessment of hypoxia in HNSCC cancer xenograft models, and assess this method for the prediction and assessment of tumour response to hypoxia-modifying therapy.

The hypotheses of this thesis are OE-MRI derived biomarkers can (i) accurately detect, map and quantify hypoxia in HNSCC xenografts, and (ii) detect changes in tumour oxygenation induced by hypoxia-modifying drug.

To address this, the thesis focusses on the following objectives:

- i. Optimisation of the MRI protocols and investigation of SC-MRI for perfusion imaging.
- ii. Evaluation of susceptibility MRI for imaging hypoxia.
- iii. Assessment of OE-MRI and combined OE-susceptibility MRI for imaging hypoxia.
- iv. Application of the technique to assess response to a hypoxia-alleviating drug intervention.

Chapter 2 Experimental material and methods

2.1 Cell lines and culture

During the course of this PhD, six human cancer derived cell lines were used: Cal^S, Cal^R, LICR-LON-HN5 and LICR-LON-HN6 HNSCC, 786-O-R RCA (RCA) and RH41 alveolar rhabdomyosarcoma (RMS). These HNSCC xenograft models were chosen based on the established clinical impact of hypoxia on tumour progression, metastasis, poor prognosis and response to therapy in patients with HNSCC-. The 786-O-R cell line was used to compare the new OE-MRI protocol described in this thesis against previously published OE-MRI data¹⁸⁶. Rhabdomyosarcoma also present a poor oxygenation and a dysfunctional vasculature²⁵². Details about each cell line are shown in Table 2.1.

Cells were maintained at 37°C in a humidified incubator with an atmosphere of 95% air, 5% CO₂. Cells were passaged when reaching 80-90% confluence, using a trypsin-like enzyme, TrypLE™(Gibco Life Technologies, UK), for gentle detachment of the cells, after a gentle wash with Dulbecco's phosphate-buffered saline (PBS) (Sigma-Aldrich, UK). For experiments, cells were used in the exponential growth phase and at the lowest number of passages from thawing as possible. Cells were routinely screened for mycoplasma by

polymerase chain reaction (PCR) using an external service (Surrey Diagnostics, UK), and short tandem repeat (STR) profiling was performed using a GenePrint® 10 kit (Promega, UK) and a 3730xl DNA analyser (Applied Biosystems, UK) (Table 1-1).

Cell line	Cell origin	Characteristic	Source	Culture medium	Ref
Cal ^S	HNSCC – tongue	EGFR-TKI-sensitive Cal27	Dr C. Box, from Cal27	DMEM, 10% FBS	
Cal ^R	HNSCC – tongue	EGFR-TKI-resistant Cal27	Dr C. Box, from Cal27	DMEM, 10% FBS	253,254
LICR-LON-HN5	HNSCC – tongue		Dr M. O'Hare	DMEM, 10% FBS	255
LICR-LON-HN6	HNSCC – tongue		Dr M. O'Hare	DMEM, 10% FBS	255
786-O-R	RCA	Sunitinib resistant 786-O	Dr A. Reynolds	RPMI 1640, 10% FBS	
RH41	Alveolar RMS		DSMZ	RPMI 1640, 10% FBS	258

Table 2.1 Description of cell lines used in this thesis.

DMEM (Dulbecco's modified Eagle's medium) and RPMI 1640 media (both from Gibco Life Technologies, UK) were supplemented with 10% (v/v) foetal bovine serum (FBS) (Pan Biotech, UK). Cal27 (CRL-2095) and 786-O (CRL-1932) cell lines were originally obtained from ATCC. EGFR: epidermal growth factor receptor; TKI: tyrosine kinase inhibitor; DSMZ: Leibniz-Institut- Deutsche Sammlung von Mikroorganismen und Zellkulturen, GmbH.

2.2 Animal experiments

All experiments were performed in accordance with the local ethical review panel, the UK Home Office Animals (Scientific Procedures) Act 1986, the United Kingdom National Cancer Research Institute guidelines for the welfare

of animals in cancer research²⁵⁹ and with the Animals in Research: Reporting In Vivo Experiments (ARRIVE) guidelines²⁶⁰.

2.2.1 Tumour propagation

Tumour cells in 100 μL of sterile Hank's balanced salt solution (HBSS) (Gibco Life Technologies, UK) were injected subcutaneously into the right flank of female mice under isoflurane anaesthesia. Details of the different tumour models are shown in Table 2.2. Tumour size was monitored using callipers to measure the three orthogonal dimensions and volume was calculated using an ellipsoid volume formula (Equation 2.1).

$$\text{Tumour volume} = \frac{\pi}{6} \times \text{length} \times \text{width} \times \text{depth}$$

Equation 2.1 Tumour ellipsoidal volume calculation

Growth curves were plotted for each individual tumour and doubling times were calculated using an exponential interpolation based on the volume measurements as a function of time²⁶¹. Mice were typically imaged when tumours approached a volume of approximately 400 mm^3 .

Cell line	Number of cells	Mice	Notes
Cal ^S	5 x 10 ⁶	6-week-old female NCr-Foxn1 ^{nu}	
Cal ^R	5 x 10 ⁵	6-week-old female NCr-Foxn1 ^{nu}	Lower number of cells to compensate for rapid growth <i>in vivo</i> ²⁵³
LICR-LON-HN5	5 x 10 ⁶	6-week-old female NCr-Foxn1 ^{nu}	
LICR-LON-HN6	5 x 10 ⁶	6-week-old female NCr-Foxn1 ^{nu}	
786-O-R	3 x 10 ⁶	8-week-old female C.B17-scid	Depilation (Veet depilatory cream) 24 h prior to cell injection
RH41	2.5 x 10 ⁶	6-week-old female NCr-Foxn1 ^{nu}	

Table 2.2 Cell lines and mice used to establish tumour models.

NCr-Foxn1^{nu} female athymic nude mice were bred in-house. C.B17-scid were purchased from Charles River (UK).

2.2.2 Atovaquone treatment

A stock solution of atovaquone (5 mg/mL in water for injection) was prepared every other day from a clinical suspension (Wellvone, GlaxoSmithKline, UK), and was administered every 24 hours. Mice bearing LICR-LON-HN5 tumours of approximately 150 mm³ were stratified to be treated with either 50 mg/kg/day p.o. of atovaquone or sterile water (control) for either 3 or 7 days. The study was not randomised in order to ensure even tumour volumes in each group at enrolment. MR imaging was performed at the end of treatment.

2.2.3 Magnetic resonance imaging

2.2.3.1 Administration of pimonidazole and Hoechst 33342

Intraperitoneal administration of the hypoxia marker pimonidazole (60 mg/kg, Hydroxyprobe Inc., USA), dissolved in PBS to a concentration of 20 mg/mL and stored at 4°C, was performed at least 45 min prior to MRI to allow maximal bioreduction of pimonidazole in hypoxic tumour regions prior to oxygen challenge. Following MRI, the perfusion marker Hoechst 33342 (15mg/kg, Sigma-Aldrich, UK), dissolved in sterile water to a concentration of 6 mg/mL and stored at -20°C protected from light, was administered intravenously and allowed to circulate for one minute prior to sacrifice by cervical dislocation. Tumours were then rapidly excised and carefully bisected as close as possible to the MR imaging plane. One half was snap frozen over liquid nitrogen for subsequent fluorescence imaging, and the other half was fixed in 10% neutral

buffered formalin solution (Sigma Aldrich, UK) for 24 h then transferred into PBS prior to dehydration in graded alcohols and embedding in paraffin.

2.2.3.2 MR image acquisition

Mice were anaesthetised with a 10 mL/kg intraperitoneal injection of fentanyl citrate (0.315 mg/mL) and fluanisone (10 mg/mL; Hypnorm; Janssen Pharmaceutical Ltd., UK), midazolam (5 mg/mL; Hypnovel; Roche), and sterile water at 1:1:2 ratio. A lateral tail vein was cannulated with a heparinized 27G butterfly catheter (Terumo, Japan and Vyrgon, France) to facilitate the remote intravenous injection of P904 (Guerbet, France) during the MRI protocol. P904 is an ultrasmall superparamagnetic iron oxide (USPIO) particle preparation consisting of a maghemite core coated with a biocompatible low molecular weight amino-alcohol derivative of glucose²⁶², with an overall particle size of ~25-30nm, used in this work to provide an MRI perfusion readout. In order to reduce motion/respiratory imaging artefacts, mice were positioned and secured on a custom-built platform through which the tumour hung through uncompressed (Figure 2.1). To minimise susceptibility artefacts caused by a differential in proton density between air and tissue, dental paste (Xantalgin, Kulzer, Germany) was poured and left to set around the tumour²⁰⁰. Core body temperature was maintained in the magnet bore using a thermo-regulated water-heated blanket (Bruker, Germany). Medical air or 100% oxygen were delivered continuously through a nosepiece (0.7L/min) and respiration was monitored using an ERT monitoring and gating system (Small Animal Instruments, Inc, USA).

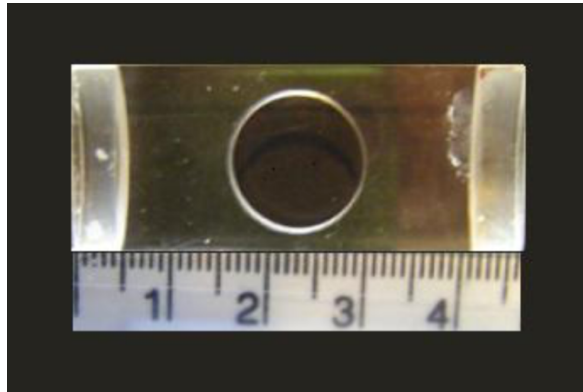


Figure 2.1 Custom-built perspex tumour platform.

Each tumour was positioned so that it hung through the hole but was not compressed and dental paste subsequently poured and left to set around the tumour. Scale shown in cm. Platform measurements: approximately 4.5cm x 2cm x 0.7cm. Photo taken from Lauren Baker's thesis.

^1H -MRI was performed on a 7T Biospec 70/20 USR horizontal MRI system controlled by Paravision 6 (Bruker, Germany) using a 40 mm volume coil. 1 mm-thick images were acquired in the transaxial plane, over a 30 x 30 mm field of view (FOV) (128 x 128 matrix), with an in-plane resolution of 0.234 mm. Whilst the animal breathed air, a Turbo Rapid Acquisition with Refocused Echoes (TurboRARE) T_2 -weighted sequence was first acquired for tumour localisation and subsequent tumour volume measurement. After B_0 mapping, field homogeneity was then optimised by iterative shimming over an ellipsoidal volume encompassing the whole tumour. Two consecutive baseline R_1 and R_2^* measurements were then acquired from a single central slice using an inversion recovery fast imaging with steady-state precession (IR-TrueFISP) and multi-gradient echo (MGE) sequences, respectively²⁶³. Four minutes after switching the gas supply to 100% oxygen, a second set of identical IR-TrueFISP and MGE images were acquired. USPIO particles were then administered intravenously (150 μM Fe/kg P904) and allowed to circulate for

2 min in order to equilibrate before a final set of MGE images were acquired.

The parameters used for each MRI sequence are summarised in Table 2.3.

Sequence	Parameters				
	TE (ms)	TR (ms)	Averages	Acquisition time	Additional information
Turbo-RARE	36	4500	1	1 min 12 s	30 slices
IR-TrueFISP	1.7	3.4 (total scan TR 10 s)	4	5 min 20 s	50 TI (72.1 ms- 2738 ms spaced 54 ms apart); $\alpha=60^\circ$
MGE	3-24 (8 TE spaced 3 ms apart)	200	8	3 min 25 s	

Table 2.3 MRI sequence parameters used in the imaging protocol.

TE: echo time; TR: repetition time; TI: inversion time.

2.3 Evaluation of the stability of R_1 measurements

The stability of R_1 measurements using the IR-TrueFISP sequence was assessed using a test object containing 5 small cylindrical phantoms containing a range of gelatine concentrations replicating R_1 values typically determined in soft tissue^{264–267}. Gelatine powder (Sigma-Aldrich, UK) was dissolved in distilled water at 5 different concentrations (3%, 5%, 7%, 9%, 12% (w/v)). The solutions were heated to 50°C, degassed and left to set for at least 12 hours in 2 mL cryovials (ThermoFisher, UK) prior to imaging.

Four sequential IR-TrueFISP acquisitions were performed at room temperature, using the same gelatine phantom, stored at 4°C and allowed to reach room temperature for approximately one hour, and repeated over four consecutive days.

2.4 MRI image analysis

2.4.1 Tumour delineation

Regions of interest (ROIs) encompassing the whole tumour but excluding the surrounding tissues were drawn based on T_2 -weighted images, using software developed in-house (ImageView, developed in IDL, ITT Visual Information Systems, USA), and subsequently applied to all data. Non-solid tumour components such as cysts were excluded from the ROI for quantitative MRI measurements.

T₂-weighted images were used to quantify tumour volumes by drawing a ROI around the whole tumour using the DICOM reader software OsiriX (USA). The results were compared with the calliper measurements (Figure 2-2).

2.4.2 MRI parametric maps

Data were fitted voxel-wise in ImageView using a Bayesian maximum *a posteriori* approach, which took into account the Rician noise distribution, and provided voxel-wise estimates of R₁ and R₂* values. Voxel-wise R₁ and R₂* values were exported from ImageView and parametric R₁ and R₂* maps were generated using an in-house Matlab script (MathWorks, USA), developed in collaboration with Dr Adam Featherstone (University of Manchester) and Konstantinos Zormpas-Petridis (ICR). For the IR-TrueFISP data, tumour voxels for which the calculated T₁ value was smaller than 200 ms or greater than 3000 ms were excluded from the analysis to ensure signal recovery and avoid noise. Oxygen-enhanced (OxyE) and oxygen-refractory (OxyR) voxels were mapped using a threshold derived from the repeatability of the R₁ measurement (Equation 2.2).

$$\text{OxyR threshold} = 2 \times \text{tumour baseline } R_1 \times \text{cohort } R_1 \text{ coefficient of variation}$$

Equation 2.2 OxyR threshold.

Similarly, perfused voxels were defined as voxels with a $\Delta R_2^*_{\text{USPIO}}$ greater than the threshold defined in Equation 2.3:

Perfusion threshold = $2 \times$ tumour baseline R_2
 \times cohort R_2^* coefficient of variation

Equation 2.3 Perfusion threshold.

Tumour fractional blood volume (fBV) maps were derived from perfused voxels (Equation 2.4):²⁶⁸

$$\text{fBV} = \frac{3}{4 \times \pi} \times \frac{\Delta R_2^* \text{USPIO}}{\gamma \times \Delta \chi \times B_0}$$

Equation 2.4 Fractional blood volume (fBV) formula.

γ : gyromagnetic ratio; $\Delta \chi$: change in susceptibility; B_0 : magnetic field strength.

OxyR and fBV maps were subsequently combined to identify non-perfused (NP) voxels, perfused OxyE (pOxyE) voxels and perfused OxyR (pOxyR) voxels.

2.5 Histopathology

2.5.1 Tissue preparation

2.5.1.1 Frozen tumour tissue

Frozen tumour tissue was embedded in Cryo-M-Bed freezing medium (Bright Instruments, UK), and 10 μm sections aligned to the MR imaged slice were cut using a Clinicut 60 cryotome (Bright Instruments, UK) and mounted on glass Superfrost® slides (VWR, UK). The sections were air dried and then stored at -20°C . For fluorescence microscopy, frozen sections were fixed for 5 min in ice-cold acetone, and then re-hydrated in PBS prior to assessment of Hoechst 33342 uptake.

2.5.1.2 Formalin-fixed paraffin-embedded tumour tissue

5 µm-thick formalin-fixed paraffin-embedded (FFPE) sections closely matched to the MR imaged slice were cut from the formalin-fixed tumour tissue using a microtome and processed by the ICR Breast Cancer Now histopathology service (Dr Naomi Guppy).

2.5.2 Pimonidazole adducts and Hoechst 33342 imaging

2.5.2.1 Fluorescence imaging

Hoechst 33342 fluorescence signals from whole frozen tumour sections were recorded at 365 nm and acquired using a x40 objective and a motorised scanning stage (Prior Scientific Instruments, UK) attached to a BX51 microscope with a DP74 camera driven by cellSense 1.18 software (all Olympus, UK), and the stage co-ordinates saved. The sections were then incubated with a blocking solution of 2% (w/v) bovine serum albumin (Sigma-Aldrich, UK) and 5% (v/v) goat serum (Sigma-Aldrich, UK) in PBS for 60 min, followed by an incubation with fluorescein isothiocyanate (FITC)-conjugated mouse anti-pimonidazole antibodies (Hydroxyprobe, USA) 1:200 in blocking solution overnight, at 4°C, in the dark. The slides were then washed three times with 0.1% Tween®-20 (Sigma-Aldrich, UK) in PBS. Pimonidazole adduct formation was then detected at 450–490 nm using the same fluorescence microscope system and stage co-ordinates as used for Hoechst 33342 imaging.

2.5.2.2 Pimonidazole chromogenic imaging

FFPE sections were immunohistochemically processed for pimonidazole adduct formation according to the protocol recommended by Hydroxyprobe²⁶⁹. The sections were imaged using a Nano Zoomer XR digital slide scanner using a x20 lens driven by NDP scan software (both from Hamamatsu, Japan) and acquired at a x40 mode.

2.5.3 Haematoxylin and eosin staining

2.5.3.1 Frozen tissue

Following fluorescence microscopy, haematoxylin and eosin (H&E) staining was performed to characterise tumour morphology and guide ROI drawing. The sections were dipped in Gill's haematoxylin for 1 min, then washed under running tap water for 4 min before differentiation with 1% acid alcohol (1% hydrochloric acid in 70% ethanol in distilled water) for 2 seconds. Following further washing under running tap water for 4 min, the sections were counter-stained with aqueous eosin solution for 30 s, followed by dehydration in 2 changes of 100% ethanol and 2 changes of xylene. The sections were then mounted with DPX mountant (Sigma-Aldrich, UK) and a coverslip for brightfield imaging, using the same stage coordinates defined for fluorescence microscopy.

2.5.3.2 Formalin-fixed paraffin-embedded tissue

FFPE sections were counter-stained for H&E by the ICR Breast Cancer Now histopathology department (Dr Naomi Guppy), and were imaged using the same digital slide scanner and magnification.

2.5.4 Microscopy imaging analysis

Microscopy image analysis was performed using cellSens 1.18 (Olympus, UK). For both Hoechst 33342 and pimonidazole adduct imaging, an ROI was delineated over the H&E image, excluding any overlying skin which was kept attached to the tumour to facilitate slide orientation (Figure 2-2). Fluorescence quantification was based on an intensity threshold defined on individual tumours to account for any variation in staining, and quantified as the mean percentage over the whole tumour section.

2.6 Overview of the MRI experiment

A workflow of the whole OE-MRI experiment is shown in Figure 2.2.

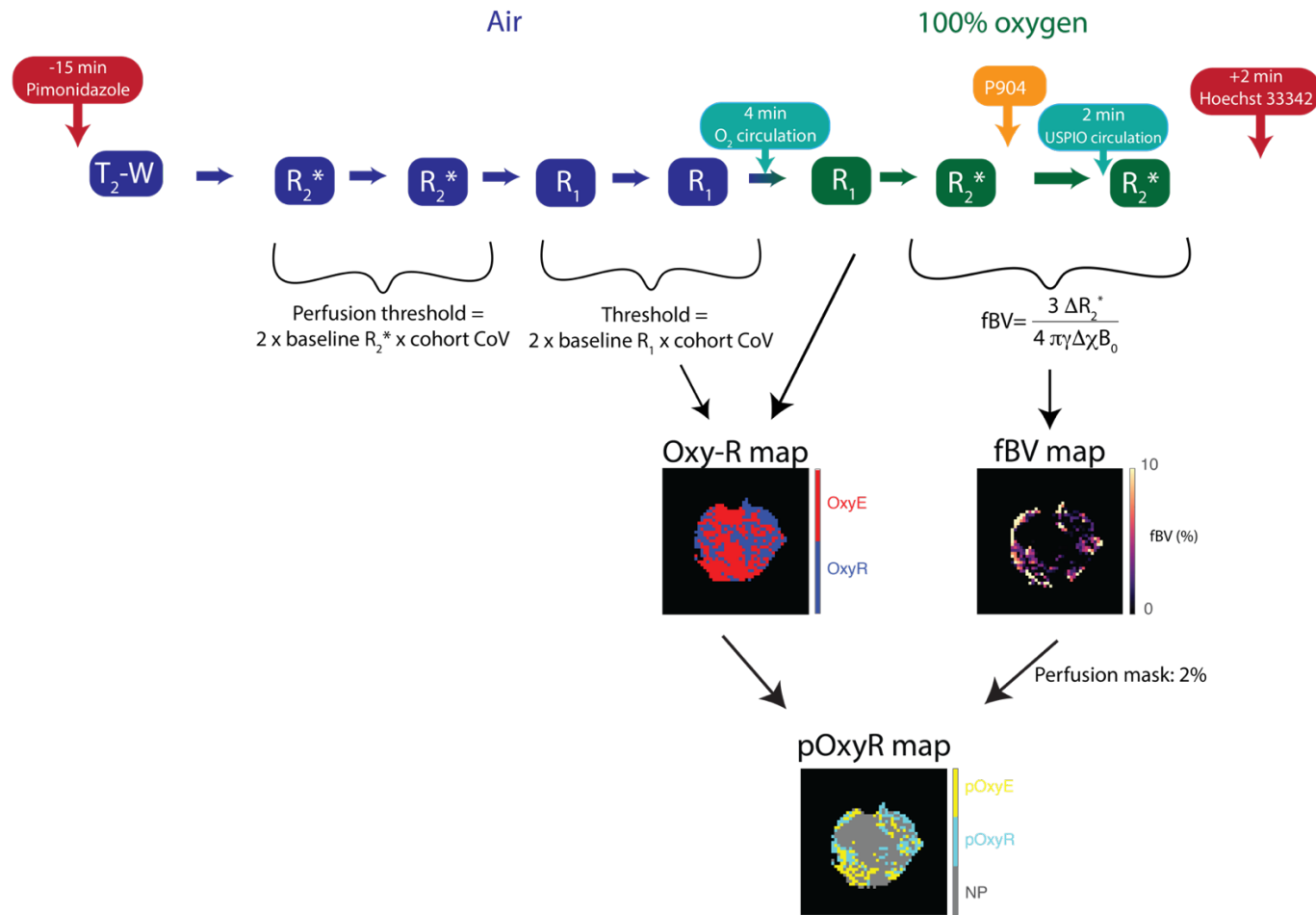


Figure 2.2 Workflow of the OE-MRI imaging experiment.

Pimonidazole was injected 15 min prior to imaging. After a multi-slice T₂-weighted anatomical scan, R₂^{*} and R₁ measurements were performed under air and subsequently 100% oxygen-breathing, from a central 1 mm transverse tumour slice. USPIO particles were then injected and a final set of MGE images acquired for determination of fBV maps to provide a perfusion mask. $\Delta R_{1 \text{ O}_2\text{-air}}$ maps were binarised to identify voxels that enhanced (OxyE) with or were refractory (OxyR) to hyperoxia. These maps were combined with fBV to identify perfused voxels refractory to hyperoxia (pOxyR). Following MRI, the perfusion marker Hoechst 33342 was administered and tumours rapidly excised and processed for histology.

2.7 *In vitro* radiotherapy preliminary study

2.7.1 Spheroid formation

Subconfluent LICR-LON-HN5 and LICR-LON-HN6 cell monolayers were detached from flasks and seeded into round bottomed, ultra-low attachment (ULA) 96-well plates (ULA plates # 7007, Corning B.V. Life Sciences, NL) at a density of 2000 and 4000 cells in 200 μ L of medium per well, respectively. The seeding density was optimised to obtain dense spheroids of approximately 300 μ m diameter on the treatment day 4 days after seeding, allowing for cell aggregation and establishment of nutrient and oxygen gradients²⁷⁰.

2.7.2 Radiation treatment and response monitoring

The workflow for spheroid irradiation is shown in Figure 2.3. Four days after seeding, spheroids in 100 μ L of medium were transferred into sterile 200 μ L PCR tubes using wide-bore pipette tips (Alpha Labs, UK) to reduce the risk of spheroid dissociation/damage. The sealed tubes were placed in blocks of solid water²⁷¹ in a water bath at room temperature (Figure 2.4). The sample holder was aligned with the isocentre of a small animal radiation research platform (SARRP, Xstrahl, UK) using the positioning lasers of the device, allowing reproducible localisation of the tubes. After warm-up, the SARRP was operated at 220 kVp, 13 mA, and a 0.15 mm copper filter used to harden the beam. Using a fixed sized 1 x 1 cm² collimator, the dose rate applied was 63.5 mGy/s (less than 5% uncertainty) at the PCR tube locations. The spheroid-containing PCR tubes were irradiated with a single fraction of 0, 3, 6, 9, 12, 15, 18, 21, 24 or 27 Gy. This range of radiation doses was guided by radiation

response data of Cal^R and LICR-LON-HN5 xenografts acquired *in vivo* from Dr Márcia Costa and Dr Sarah Brueningk (ICR)^{272,273}. Each radiation dose was performed in at least 3 independent repeat experiments, including 3 to 6 spheroids in each. Appropriate temperature and chamber calibration corrections were performed.

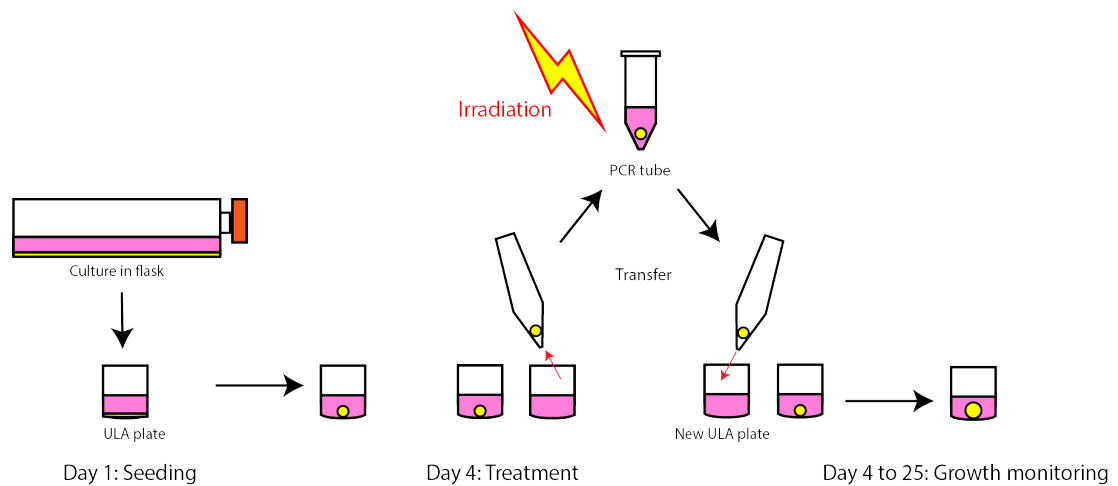


Figure 2.3 Workflow of the spheroid radiation treatment.

Cells were cultured in flasks before being transferred to a 96-well ULA plate for spheroid formation (yellow). After 4 days of incubation, spheroids were transferred into PCR tubes for irradiation. Following treatment, they were transferred into fresh ULA plates and imaged every other day to monitor spheroid growth.

Treated spheroids were transferred back into a fresh ULA plate and medium was renewed every other day by removing 100 μ L medium, and adding back 100 μ L fresh complete growth medium, supplemented with 1% penicillin and streptomycin solution (Sigma-Aldrich, UK) to prevent any bacterial contamination, until 21 days after irradiation. Spheroid growth was monitored every other day by acquiring a single plane bright field image of each spheroid using a CeligoTM imaging cytometer (Nexcelom Biosciences, USA). Due to post-treatment shedding and spheroid deformation, the segmentation was performed manually using ImagePro Analyzer 7.0 (Media Cybernetics, USA) by an experienced operator, Dr Carol Box (ICR), and spheroid volume was

calculated using the measured diameter and assuming a spherical volume (Equation 2.5).

$$\text{Spheroid volume} = \frac{4}{3} \times \pi \times \left(\frac{\text{diameter}}{2}\right)^3$$

Equation 2.5 Spheroid volume formula.
Based on the formula of a sphere volume.

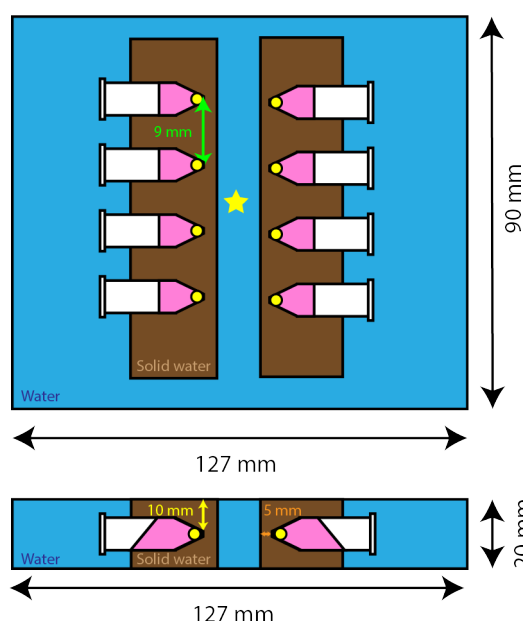


Figure 2.4 Schematic diagram of the sample holder used to treat spheroids reproducibly in PCR tubes using the SARRP.

Top: top view, beam direction perpendicular to the plane shown. Bottom: side view, beam direction from top. Spheroids (yellow) were allowed to sediment to the bottom of the tube before being positioned in a solid water holder (brown) within a small water bath (blue). The isocentre is indicated by a yellow star.

2.7.3 CellTiter-Glo® assay

In addition to spheroid growth, tumour cell viability was assessed using the CellTiterGlo® (CTG®) 3D reagent kit (Promega, UK). The assay is dependent upon cell lysis therefore was performed only at the end of the experiment (21 days post irradiation). It relies on a proprietary thermostable luciferase, which

generates a quantifiable bioluminescent signal in the presence of adenosine triphosphate (ATP), an indicator of metabolically active cells.

100 µl of culture medium was replaced with an equal volume of CTG® reagent. The well contents were incubated with gentle agitation on a plate-shaker, in the dark for 30 min, which allowed cell lysis and release of intracellular ATP. The contents of each well were then transferred to a white, flat bottom 96-well plate and the luminescent signal measured using a spectrophotometer multi-plate reader (FLUOstar Optima, BMG Labtech, UK).

2.8 Statistical analysis

Statistical analysis was performed using Prism 8.4.1 (GraphPad, USA). Unless otherwise stated, all data are presented as mean \pm 1 standard error of the mean (s.e.m.). Statistical significance was tested using Student's two-tailed t-test assuming groups have equal variance, with a p value smaller than 0.05 denoting significance. When comparing several groups, a one-way ANOVA test was performed, after testing for normality and assuming that groups have equal variance.

Chapter 3 Optimisation of an OE-MRI protocol incorporating susceptibility MRI for imaging tumour hypoxia

3.1 Introduction

OE-MRI studies to date have evaluated pOxyR voxels following binarization of hyperoxia-induced ΔR_1 maps with a perfusion mask typically generated from DCE-MRI data using an exogenously administered low molecular weight gadolinium contrast agent^{186,240,274}. Such paramagnetic contrast agents readily extravasate through the typically hyperpermeable tumour vasculature into the extracellular-extravascular space²⁷⁵. The resulting observed signal enhancement thus reflects a compound measurement of both vascular perfusion and permeability that can be difficult to interpret.

Both IS- and SC- MRI are alternative imaging approaches being exploited for the evaluation of tumour perfusion^{191,192,200,276,277}. SC-MRI relies on the intravenous administration of USPIO particles. The uptake and distribution of USPIO particles within tumours causes regional increases in tumour R_2^* ($\Delta R_2^*_{USPIO}$), from which tumour fBV can be derived²⁷⁸. The long intravascular half-life of USPIO particles enables steady state acquisition and high-

resolution mapping of regional variations in perfused tumour vasculature. Fractional blood volume maps have been used to visualise tumour perfusion in preclinical models of brain^{205,206,215}, colorectal²⁰⁰, prostate¹⁹² and renal cancer²⁷⁹, and neuroblastoma²⁷⁷, with reported fBV's ranging from ~3 to 21%.

One aim of this thesis is to exploit the greater specificity of fBV to patent tumour vasculature to provide a perfusion mask for the evaluation of pOxyR as an imaging biomarker of hypoxia. The acquisition of MGE data under air, 100% O₂ and following administration of USPIO particles would also enable an appraisal of baseline R₂^{*}, hyperoxia-induced ΔR_2^* and fBV as putative biomarkers of tumour hypoxia, all acquired in the same imaging session.

Figure 2.2 shows the OE-MRI workflow, as well as the incorporation of susceptibility MRI within the protocol. The original preclinical OE-MRI investigations for mapping tumour hypoxia were performed on an ageing Bruker 7T horizontal bore microimaging system running Paravision version 4^{186,274}. The installation of a new state-of-the-art Bruker 7T Biospec 70/20 USR horizontal MRI system running Paravision version 6 in the ICR Centre for Cancer Imaging demanded the careful migration and validation of the requisite MR pulse sequences that underpin the OE-MRI methodology within the latest software and programming environment.

This chapter describes the optimisation and implementation of an OE-MRI protocol which incorporates susceptibility MRI for imaging hypoxia in tumour xenografts on the new 7T scanner.

3.2 Results & Discussion

3.2.1 Stability and repeatability of the R_1 measurement

3.2.1.1 Repeatability of R_1 measurements using the IR-True FISP sequence on the new 7T MRI system

In order to observe and quantify a change in tumour R_1 associated with hyperoxia, the OE-MRI approach relies on the stability of the R_1 measurements being made. Inversion-recovery based spin echo sequences have been the preferred method to quantify R_1 ^{280,281}. The IR-TrueFISP sequence, which uses a magnetisation preparation to rapidly reach a steady state for imaging^{282,283}, has been shown to provide excellent accuracy and signal-to-noise in both phantoms and humans^{263,284}. The coefficient of variation (CoV) between two consecutive R_1 measurements, acquired using this method on our previous 7T system, was $\sim 1\%$ ¹⁸⁶.

Initial evaluation of the IR-TrueFISP sequence migrated onto the new 7T system on a phantom suggested quantitation of precise and reproducible R_1 values over a few days. However, *in vivo* measurements revealed marked signal instability, and, as a result, a high variability in R_1 values calculated from consecutive scans. Consequently, under hyperoxia, changes in R_1 could not be solely attributed to the gas challenge. Acquisition of four consecutive baseline scans in six tumour-bearing mice (Figure 3.1A and B) further confirmed the instability of the baseline R_1 measurements. The individual

CoVs ranged from 1 to 7% (data not shown). Such poor repeatability would mask the effects of a hyperoxic gas challenge on R_1 , which are typically less than 5%¹⁸⁶. Imaging of a 10% gelatine phantom further revealed the oscillating variations in R_1 , leading to a progressive 30% increase over a period of 3 hours (Figure 3.1C).

The possibility of this R_1 instability resulting from magnetic field inhomogeneities caused by a fault in the volume coil, or via temperature fluctuations arising from the system shim-heater, were first investigated with the help of a Bruker engineer and eliminated. Subsequent interrogation of the IR-TrueFISP sequence in Paravision 6 established that, unlike the IR-TrueFISP sequence in Paravision 4, there was no automatic adjustment for off-resonance frequencies, which are known to greatly affect the accuracy of R_1 measurements with this sequence²⁶³. The oscillations in R_1 values observed *in vivo* and in the gelatine phantom were therefore due to an uncorrected frequency drift. Incorporating a frequency adjustment before each of six consecutive R_1 measurements on a 10% gelatine phantom at three different occasions resulted in stable R_1 measurements (Figure 3.1D), with a CoV of 0.5%.

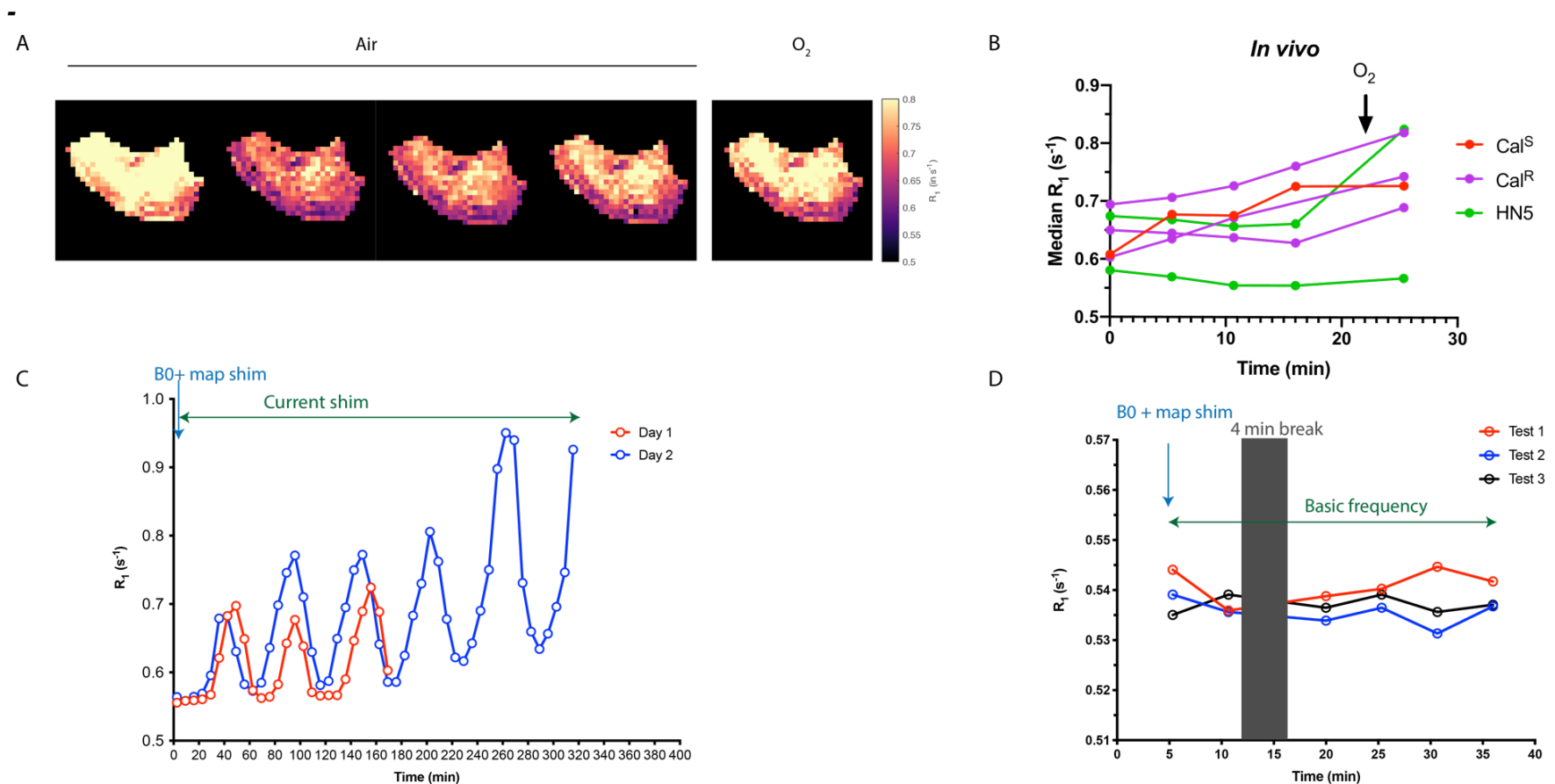


Figure 3.1 Initial challenges with the repeatability of R_1 measurements using the IR-True FISP sequence on the new Bruker 7T system.

A) Representative parametric R_1 maps of 5 consecutive measurements under air and oxygen breathing acquired from a Cal^R xenograft. Note the change in R_1 values across the tumour under air breathing. B) Summary of the median R_1 determined from 5 consecutive measurements under air and oxygen breathing acquired from Cal^S ($n=1$), Cal^R ($n=3$) and LICR-LON-HN5 ($n=2$) xenografts. C) Instability of R_1 measurements acquired consecutively using a 10% gelatine phantom, after an initial B0 measurement and map shim. The measurements were acquired based on the initial shim. D) R_1 measurements of a 10% gelatine phantom after introducing a basic frequency adjustment before each scan.

3.2.1.2 Repeatability of R_1 measurements using the refined IR-True FISP sequence

To subsequently assess the improvement in the frequency stability for R_1 acquisition, a test object was constructed containing 5 small cylindrical gelatine phantoms, with a range of gelatine concentrations replicating the R_1 values typically measured in tumours *in vivo*. Median voxel-wise R_1 measurements incorporating the frequency adjustment were found to be consistent over a time course of 20 minutes (Figure 3.2A and B). The mean relaxation rates and associated CoVs were stable for each gelatine concentration (Figure 3.2C).

Subsequent *in vivo* experiments performed in one scanning session demonstrated a stable R_1 signal (Figure 3.3), and an associated CoV in baseline voxel-wise R_1 of 0.1%. This level of repeatability was considered adequate for OE-MRI experiments, the low variation between the baseline R_1 measurements indicating higher measurement precision than that previously reported¹⁸⁶.

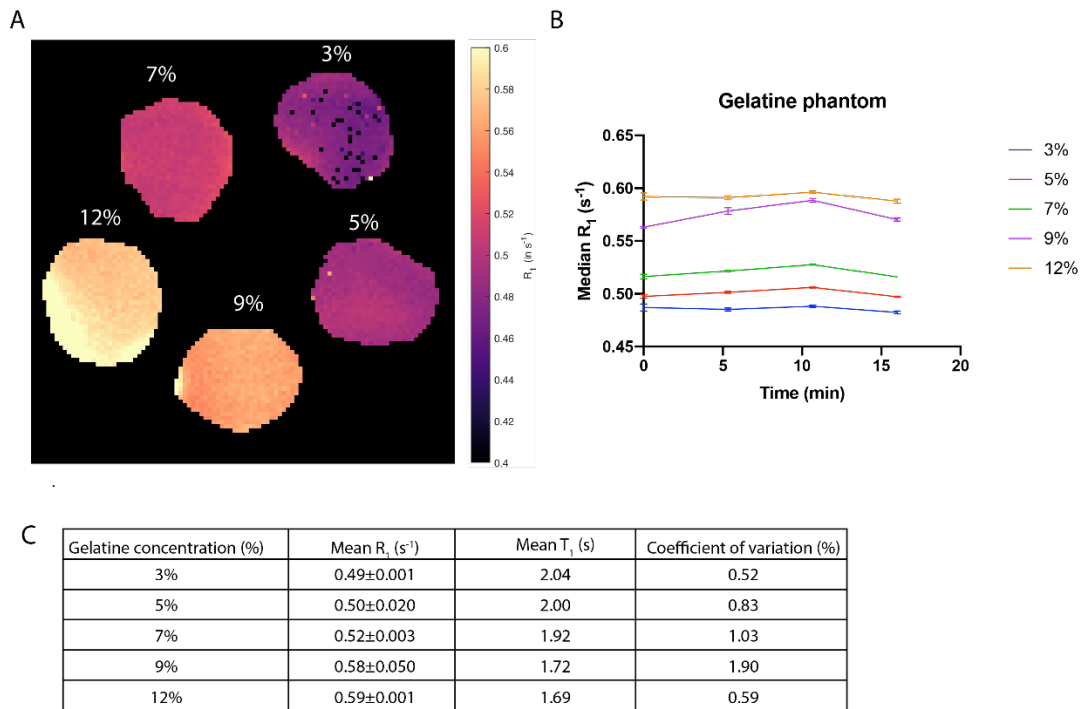


Figure 3.2 Stability of R_1 assessed using a test object containing gelatine phantoms.

A) Parametric R_1 maps acquired from 3%, 5%, 7%, 9% and 12% gelatine phantoms as indicated. B) Summary of the median R_1 values obtained from the gelatine phantoms from 4 sequential measurements acquired on 4 separate occasions. Error bars are 1 s.e.m. C) Summary of R_1 mean values (± 1 s.e.m.), corresponding longitudinal relaxation times T_1 , and the CoV measured for each gelatine phantom.

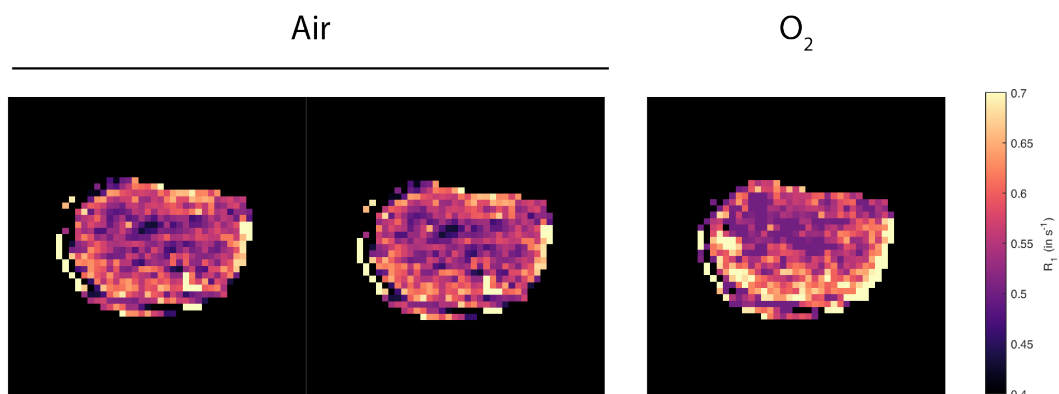


Figure 3.3 Stability of R_1 measurements assessed in vivo.

Example parametric R_1 maps acquired consecutively under air breathing and subsequently under 100% oxygen breathing in a representative LICR-LON-HN5 HNSCC xenograft.

3.2.2 Optimisation of the perfusion threshold

3.2.2.1 Repeatability of R_2^* measurements using the MGE sequence

The MGE sequence, which is sensitive to local susceptibility variations around blood vessels due to the presence of paramagnetic deoxyhaemoglobin, is a well-established and accurate sequence with which to quantify R_2^{*285} . Sampling the MGE MRI signal intensity (SI) at several echo times (TE) allows the slope of $\ln(\text{SI})$ versus TE to be calculated, which determines R_2^* (1.2.3.1.2). This sequence was used to quantify tumour R_2^* , hyperoxia-induced $\Delta R_2^{*192,200,202,205,223,239}$, and fBV following intravenous administration of USPIO particles^{200,205,277}. The *in vivo* experiments performed herein in a single imaging session revealed a CoV in baseline voxel-wise R_2^* of 1.6%. This level of repeatability was considered adequate to measure changes in R_2^* upon oxygen challenge and USPIO delivery to the tumour.

3.2.2.2 Evaluation and validation of SC-MRI-derived enhancing fraction as a perfusion mask for the OE-MRI protocol

Initially, a perfusion threshold calculated individually from the CoV of baseline R_2^* was applied to $\Delta R_2^*_{\text{USPIO}}$ to calculate fBV on a voxel basis. However, preliminary visual inspection of Hoechst 33342 uptake in tumour sections aligned with the MRI slices revealed that the extent of perfused regions was smaller than that of the perfused voxels identified on the fBV maps (Figure 3.4A), although the median value of tumour fBV correlated with the Hoechst

33342-derived perfused fraction (data not shown). Using these four examples as an investigation set, perfusion masks were generated using increasing empirical fBV thresholds (1%, 2% and 3%). These range of thresholds were chosen to reflect the expected relatively poorly perfused phenotype of the HNSCC xenografts. The perfusion mask generated using a threshold of fBV= 2% was found to best match the perfused areas defined by Hoechst 33342 uptake (Figure 3.4A and B). Application of the 2% threshold revealed that the resulting MRI enhancing fraction was significantly correlated to the histological perfused fraction as determined by Hoechst 33342 uptake ($r^2=0.59$, $p<0.001$, Figure 3.4C). The 2% threshold was then applied and incorporated in the calculation of pOxyR for all OE-MRI data presented in Chapter 5 and 6.

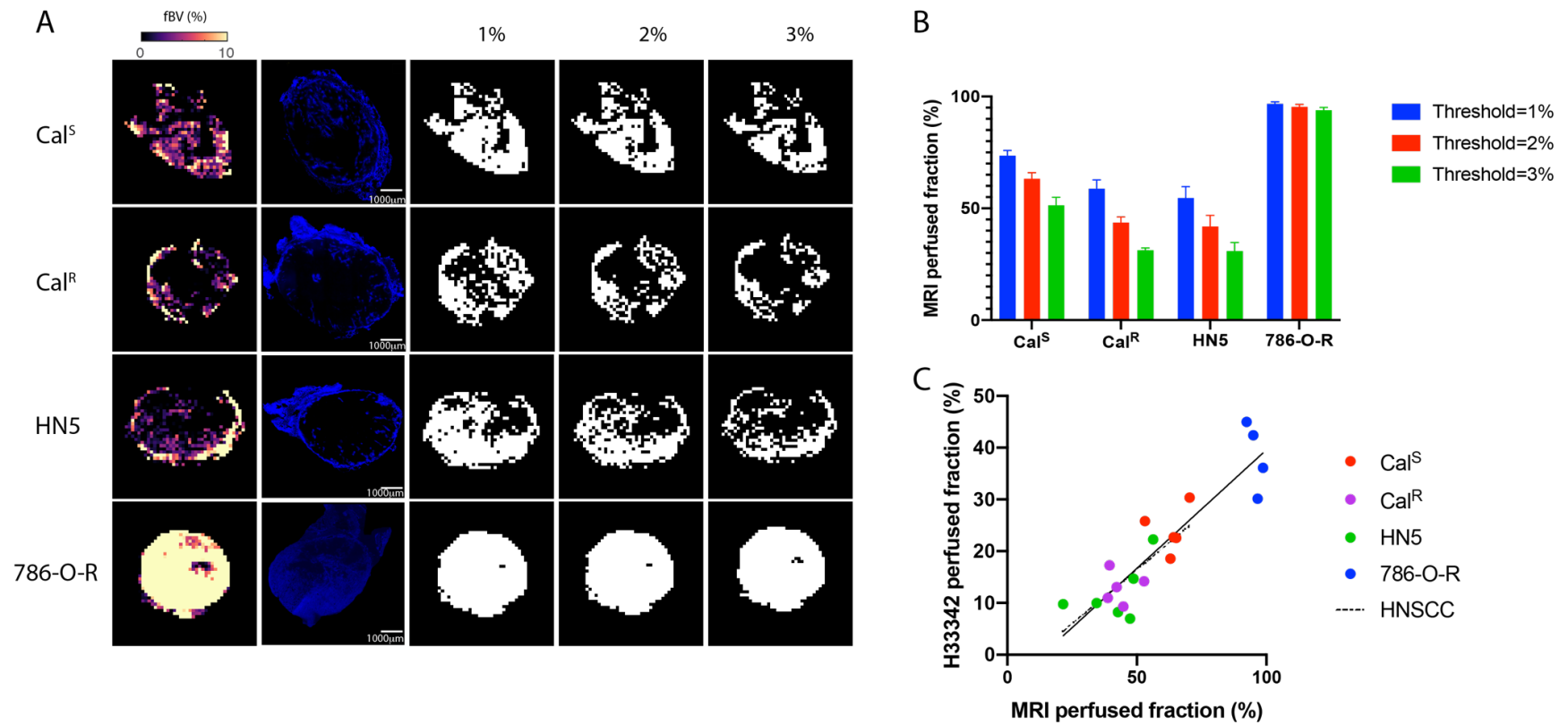


Figure 3.4 Evaluation of tumour perfusion using SC-MRI

A) Parametric maps of fBV (%), fluorescence images of Hoechst 33342 uptake (blue, scale bar =1mm), and perfusion maps with an empirical threshold applied of 1%, 2% or 3%, in representative Cal^S, Cal^R, LICR-LON-HN5 (HNSCC) and 786-O-R (RCA) xenografts. Note that for orientation purposes, skin was left on the histological tumour sections. B) Summary of the tumour perfused fraction values determined for each fBV threshold. Values are mean \pm 1 s.e.m. C) Relationship between tumour MRI perfused fraction determined using a fBV threshold of 2%, and Hoechst 33342 uptake fraction (solid line: all tumours, $r^2=0.80$, $p<0.0001$; dashed line: HNSCC only, $r^2=0.59$, $p<0.001$).

3.3 Conclusion

In summary, a refined OE-MRI protocol incorporating SC-MRI was successfully established to allow rapid, accurate and stable measurements of tumour R_1 and R_2^* under air and 100% oxygen breathing, and following administration of USPIO particles, in the same imaging session. The following two chapters describe the application of these SC-MRI and OE-MRI protocols, and the evaluation of their associated parameters, as imaging biomarkers of hypoxia in HNSCC xenografts.

Chapter 4 Evaluation of susceptibility MRI for imaging hypoxia in HNSCC xenografts

4.1 Introduction

The presence of paramagnetic deoxyhaemoglobin creates magnetic susceptibility perturbations in the proximity of blood vessels, increasing the transverse MRI relaxation rate R_2^* of the surrounding tissue in proportion to the tissue deoxyhaemoglobin concentration (see 1.2.3.3). As the oxygenation of haemoglobin is proportional to the arterial blood oxygen saturation, and therefore in equilibrium with tissue oxygen tension (pO_2), intrinsic susceptibility (IS)-MRI measurements of baseline R_2^* and hyperoxia-induced ΔR_2^* are being actively investigated as sensitive indices of tumour hypoxia^{165,187,190,201,204,286–289}. Susceptibility contrast (SC)-MRI using a paramagnetic iron oxide based contrast agent provides additional insight on tumour vasculature which, given the relationship of hypoxia to vascular development, may also inform on tumour oxygenation²⁰⁰.

This chapter describes the evaluation of baseline R_2^* , hyperoxia-induced ΔR_2^* and fractional blood volume (fBV) as putative imaging biomarkers of hypoxia in HNSCC xenografts.

4.2 Results

4.2.1 Characterisation of HNSCC tumour engraftment and growth

The growth characteristics of Cal^S, Cal^R, LICR-LON-HN5 and LICR-LON-HN6 HNSCC xenografts, and 786-O-R RCA tumours, are shown in Figure 4.1. Tumours were palpable at similar times after cell injection but progressed at different rates. Cal^S tumours were scanned around 32 days post-injection (Figure 4.1A). Cal^R (Figure 4.1B) and LICR-LON-HN5 (Figure 4.1C) tumours grew more rapidly and were imaged around 21 days after engraftment, at a volume ~200 to 500 mm³. The apparent decrease in tumour volume observed in some Cal^S and Cal^R tumours was a consequence of calliper measurements being influenced by cystic pockets arising in these models. LICR-LON-HN6 tumours, for which no previous *in vivo* growth data was available, showed a very heterogeneous growth pattern (Figure 4.1D). Tumours were palpable after 45 days, and subsequently grew rapidly. 786-O-R xenografts developed at the same time but exhibited a plateau in growth before progressing exponentially from day 22 after engraftment (Figure 4.1E).

Tumour doubling times, calculated from the exponential regression analysis of individual growth curves from the day they are palpable until imaging, were not significantly different between the models (one-way ANOVA, $p=0.14$, Figure 4.1F).

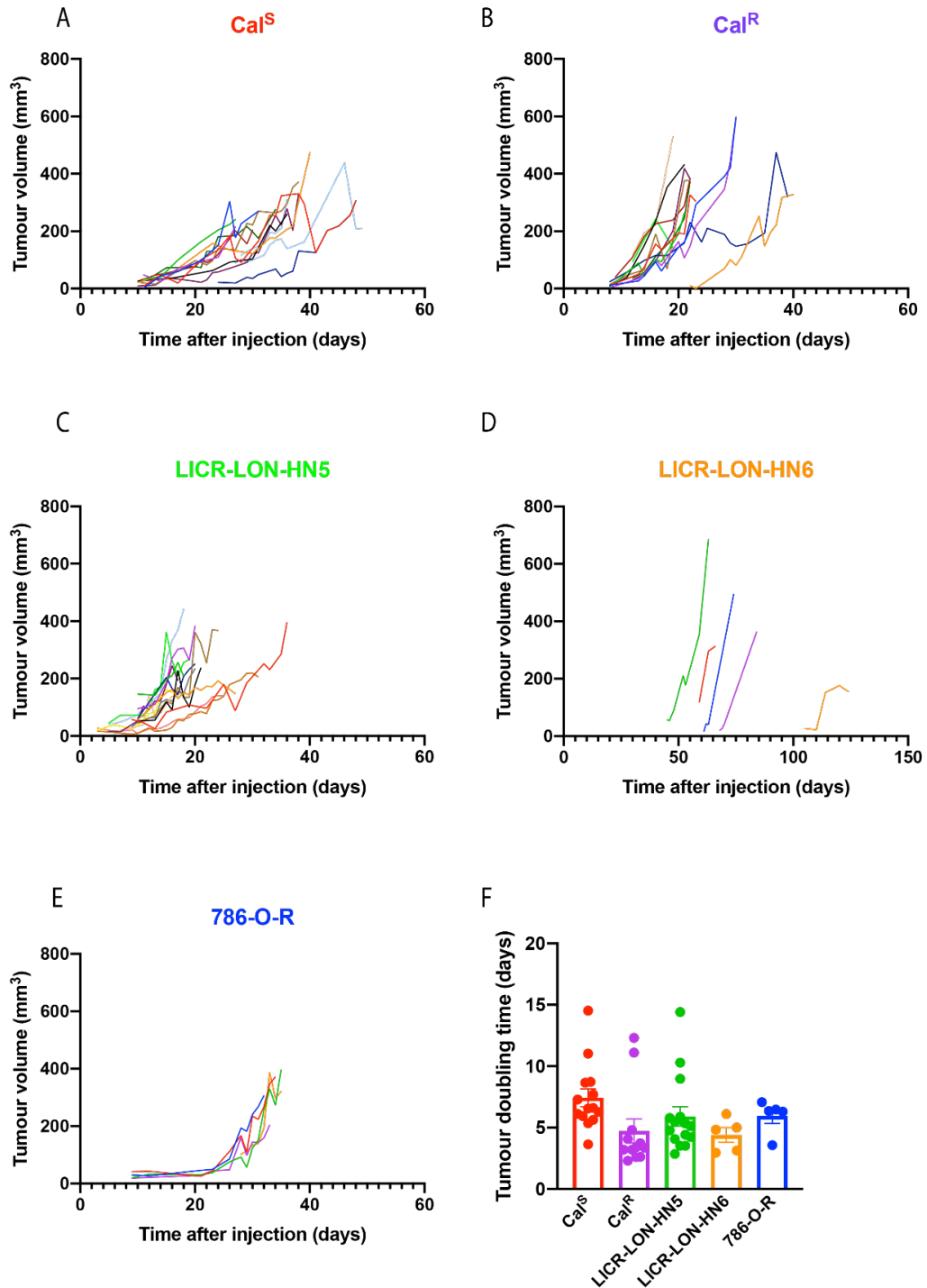


Figure 4.1 Characterisation of tumour growth.

Growth curves measured from A) Cal^S ($n=14$), B) Cal^R ($n=13$), C) LICR-LON-HN5 ($n=16$) D) LICR-LON-HN6 ($n=5$) (note extended x-axis scale) and E) 786-O-R (RCA, $n=5$) xenografts. Measurements were performed every other day using callipers. Each solid line represents an individual tumour. F) Tumour doubling times calculated from Cal^S, Cal^R, LICR-LON-HN5, LICR-LON-HN6 and 786-O-R xenografts. Bars are mean ± 1 s.e.m.

4.2.2 Histological characterisation of hypoxia and perfusion in HNSCC xenograft models

Tumour tissue sections aligned with the MRI plane were processed for fluorescence detection of pimonidazole adducts (hypoxia) and Hoechst 33342 (functional vasculature or perfusion), shown in Figure 4.2.

Extensive pimonidazole adduct formation was typically observed towards the centre of the HNSCC xenografts, whereas it was very limited in 786-O-R tumours (Figure 4.2A). There was a significant difference in pimonidazole-derived hypoxic fraction between the HNSCC and the RCA models (respectively $23 \pm 2\%$ and $4 \pm 1\%$) (Figure 4.2B). There was no significant difference in hypoxic fraction between the LICR-LON-HN6 and 786-O-R tumours.

Hoechst 33342 uptake was typically restricted towards the periphery of the HNSCC xenografts, whereas uptake was markedly higher and more homogeneous in the 786-O-R tumours (respectively $19 \pm 1\%$ and $38 \pm 3\%$) (Figure 4.2C).

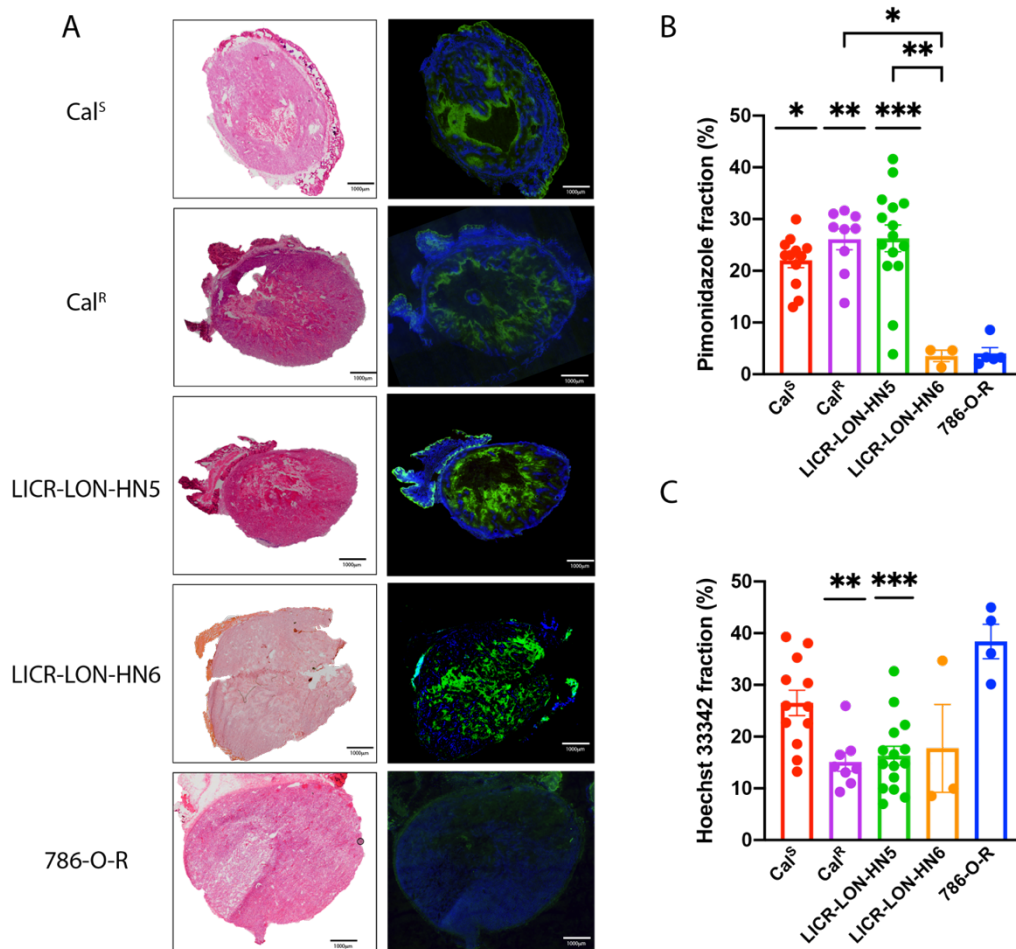


Figure 4.2 Histological characterisation of tumour hypoxia and perfusion.

A) Bright field images of haematoxylin & eosin staining (left panel), and composite fluorescence images of pimonidazole adducts (green, hypoxia) and Hoechst 33342 uptake (blue, perfusion), from representative Cal^S, Cal^R, LICR-LON-HN5, LICR-LON-HN6 and 786-O-R tumours. Summary of (B) tumour pimonidazole-derived hypoxic fraction and (C) Hoechst 33342-derived perfused fraction. Values are mean \pm 1 s.e.m. Significance lines are relative to 786-O-R. * $p < 0.05$; ** $p < 0.01$; *** $p < 0.001$.

4.2.3 Assessment of hypoxia using intrinsic susceptibility MRI

4.2.3.1 Assessment of baseline R_2^* as a biomarker of hypoxia

Parametric baseline R_2^* maps of representative Cal^S, Cal^R, LICR-LON-HN5, LICR-LON-HN6 HNSCC xenografts and 786-O-R RCA tumours, and composite fluorescence images of pimonidazole adduct formation and Hoechst 33342 uptake from sections aligned with the MR imaging plane, are shown in Figure 4.3. In HNSCC tumours, regions of relatively fast R_2^* were located towards the periphery. In RCA tumours, a similar pattern was apparent, albeit over a smaller dynamic range. These regions were spatially associated with areas of Hoechst 33342 uptake. Pimonidazole adducts were apparent towards the tumour core. Median baseline R_2^* values were similar for all HNSCC and RCA models (respectively $55 \pm 2\%$ and $49 \pm 5 \text{ s}^{-1}$) (Figure 4.3B), whilst the hypoxic fraction determined from pimonidazole staining was significantly higher in the HNSCC xenografts compared to the 786-O-R tumours (Figure 4.3C). No significant relationship was found between median baseline R_2^* and hypoxic fraction (Figure 4.3D).

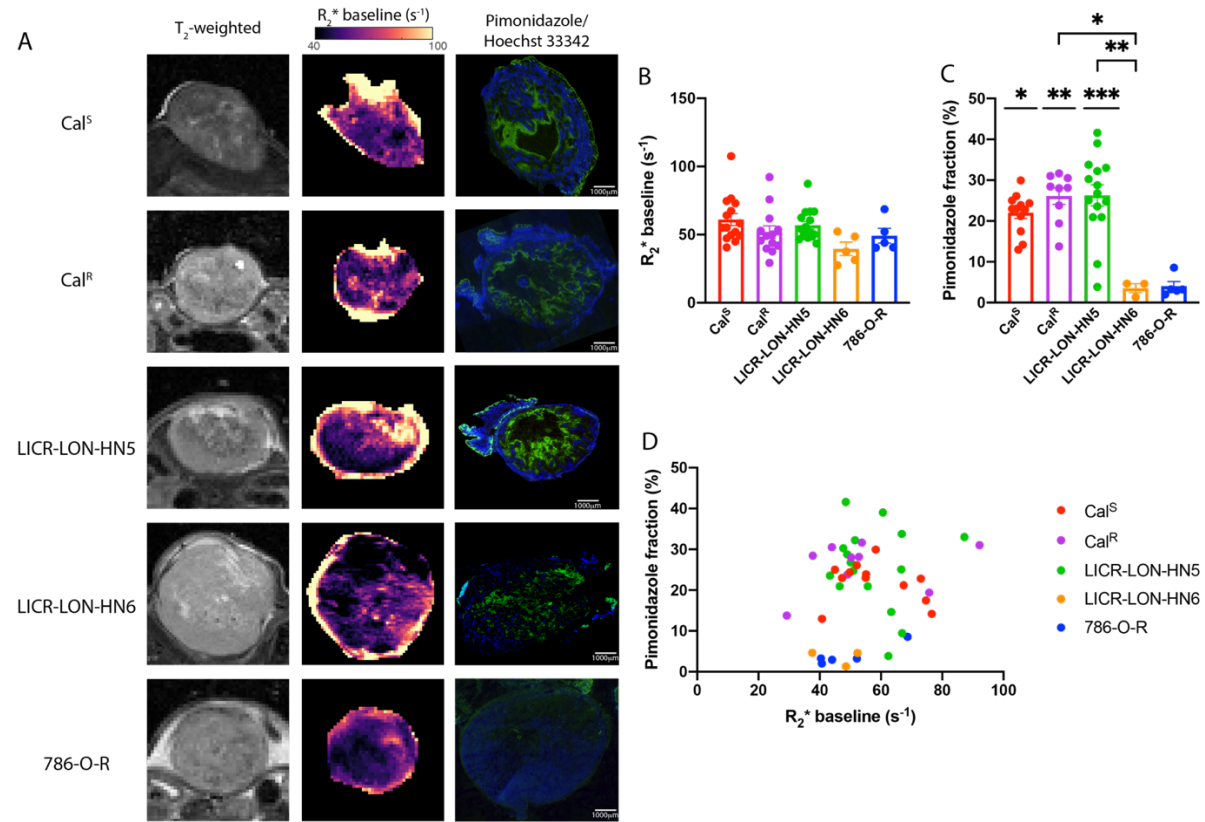


Figure 4.3 Characterisation of tumour baseline R_2^* .

A) From left to right: T_2 -weighted anatomical image, parametric R_2^* maps, and composite fluorescence images of pimonidazole adducts (green, hypoxia) and Hoechst 33342 uptake (blue, perfusion), from representative Cal^S, Cal^R, LICR-LON-HN5, LICR-LON-HN6 and 786-O-R tumours. B) Summary of median baseline R_2^* values for each model. Bars are mean \pm 1 s.e.m. C) Summary of pimonidazole adduct fraction. Values are mean \pm 1 s.e.m. Significance lines are relative to 786-O-R. * p <0.05; ** p <0.01; *** p <0.001. D) Relationship between median tumour baseline R_2^* and pimonidazole-derived hypoxic fraction.

4.2.3.2 Assessment of $\Delta R_{2^*O_2-air}$ as a biomarker of hypoxia

Parametric maps of hyperoxia-induced changes in R_{2^*} obtained from representative HNSCC and RCA tumours are shown in Figure 4.4. The HNSCC xenografts typically exhibited a spatially heterogeneous and quantitatively wide distribution of $\Delta R_{2^*O_2-air}$ voxels, whereas RCA tumours displayed a more limited response to hyperoxia (Figure 4.4A). Positive $\Delta R_{2^*O_2-air}$ subregions were more apparent in LICR-LON-HN5 and Cal^R xenografts, and were located at the rim of the tumours. The Cal^S, LICR-LON-HN6 and 786-O-R tumours exhibited more abundant negative $\Delta R_{2^*O_2-air}$ voxels. These negative $\Delta R_{2^*O_2-air}$ areas were observed towards the periphery of the tumours. Less responsive voxels were typically associated with the tumour core. The HNSCC and RCA median $\Delta R_{2^*O_2-air}$ values (respectively $-5 \pm 1 \text{ s}^{-1}$ and $-8 \pm 6 \text{ s}^{-1}$) were not significantly different (Figure 4.4B). Voxels exhibiting a smaller $\Delta R_{2^*O_2-air}$ were spatially associated with pimonidazole adduct positive regions in the HNSCC models, whereas subregions exhibiting a smaller $\Delta R_{2^*O_2-air}$ did not present any pimonidazole adducts in the RCA tumours (Figure 4.4A). A weak yet statistically significant positive correlation was identified between hyperoxia-induced $\Delta R_{2^*O_2-air}$ and pimonidazole-derived hypoxic fraction across the HNSCC models (Figure 4.4D). The proportion of voxels refractory to hyperoxia, defined as having a $\Delta R_{2^*O_2-air}$ greater than -0.5 s^{-1} , were found to not relate to hypoxic fraction (Figure 4.4E). The empirical threshold of -0.5 s^{-1} was thus chosen to reflect the absence of change in R_{2^*} after hyperoxia.

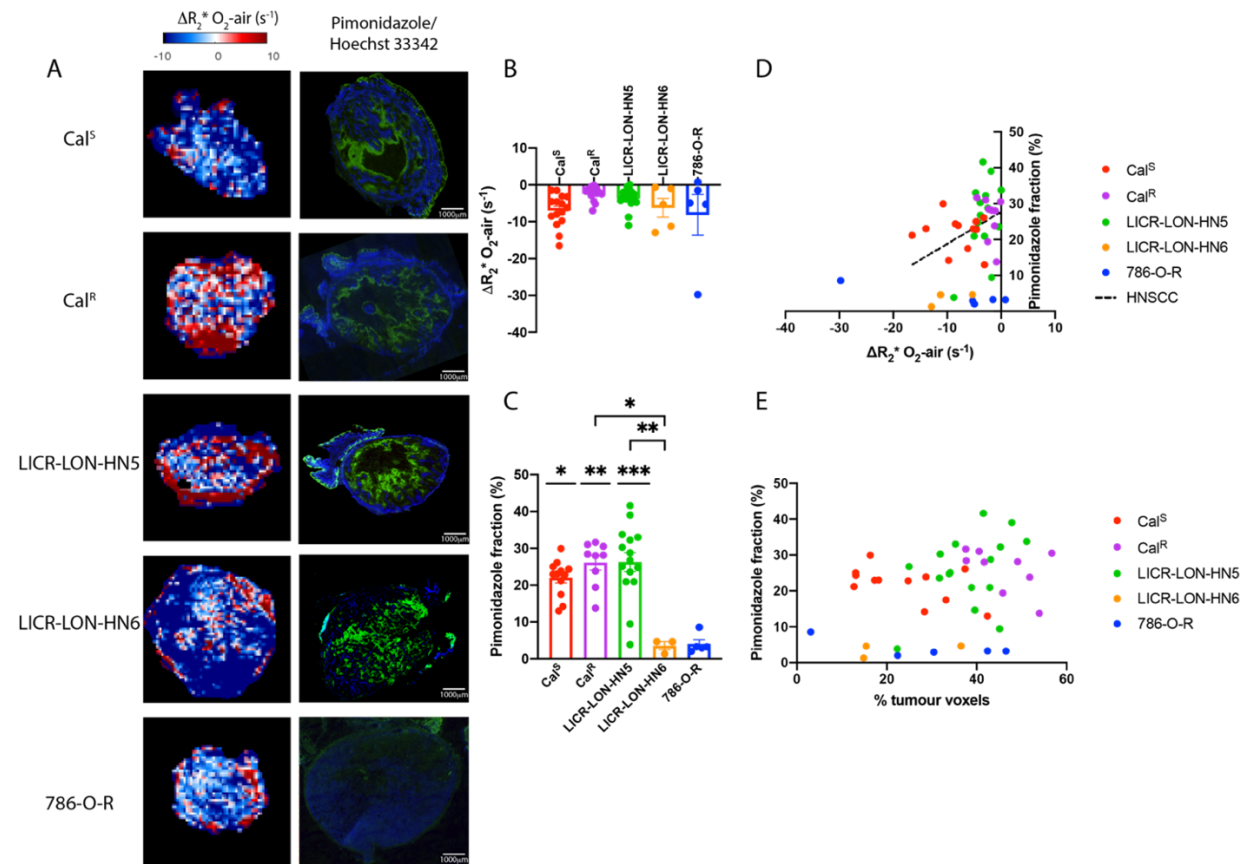


Figure 4.4 Characterisation of tumour $\Delta R_2^*O_{2-air}$.

A) Parametric maps of hyperoxia-induced $\Delta R_2^*O_{2-air}$ (left panel), and composite fluorescence images of pimonidazole adducts (green, hypoxia) and Hoechst 33342 uptake (blue, perfusion), from representative Cal^S , Cal^R , LICR-LON-HN5, LICR-LON-HN6 and 786-O-R tumours. B) Summary of median $\Delta R_2^*O_{2-air}$ values for each model. Bars are mean \pm 1 s.e.m. C) Summary of pimonidazole adduct fraction. Values are mean \pm 1 s.e.m. Significance lines are relative to 786-O-R. * $p < 0.05$; ** $p < 0.01$; *** $p < 0.001$. Relationship between pimonidazole-derived hypoxic fraction and D) median tumour hyperoxia-induced $\Delta R_2^*O_{2-air}$ and pimonidazole-derived hypoxic fraction (dashed line: HNSCC xenografts only, $r^2 = 0.15$, $p = 0.01$), E) voxels exhibiting a $\Delta R_2^*O_{2-air}$ greater than $-0.5 s^{-1}$.

4.2.3.3 Assessing combined baseline R_2^* and $\Delta R_2^*_{O_2\text{-air}}$ as a biomarker of hypoxia

The relationship between tumour baseline R_2^* and $\Delta R_2^*_{O_2\text{-air}}$ during hyperoxia is shown in Figure 4.5. In the HNSCC xenografts, relatively slow baseline R_2^* subregions typically exhibited a smaller negative change under hyperoxia at the core, whereas relatively faster baseline R_2^* were associated with greater negative $\Delta R_2^*_{O_2\text{-air}}$ at the tumour periphery (Figure 4.5A). Both spatially corresponded to pimonidazole positive regions. Rim areas presenting faster baseline R_2^* were spatially associated with positive $\Delta R_2^*_{O_2\text{-air}}$ and with Hoechst 33342 uptake. Weak but statistically significant negative correlations were found between median baseline R_2^* and $\Delta R_2^*_{O_2\text{-air}}$ across all the tumours, and for the HNSCC xenografts only (Figure 4.5B).

A voxel-wise analysis was performed in which baseline R_2^* voxels were classified as fast or slow using a cut-off value of 60s^{-1} (based on the median baseline R_2^* for the HNSCC xenografts), and null or positive $\Delta R_2^*_{O_2\text{-air}}$ (oxygen-refractory) voxels as greater than -0.5 s^{-1} . There was no significant correlation between pimonidazole-derived hypoxic fraction and voxels refractory to hyperoxia and presenting a slow (Figure 4.5C) or fast (Figure 4.5D) baseline R_2^* .

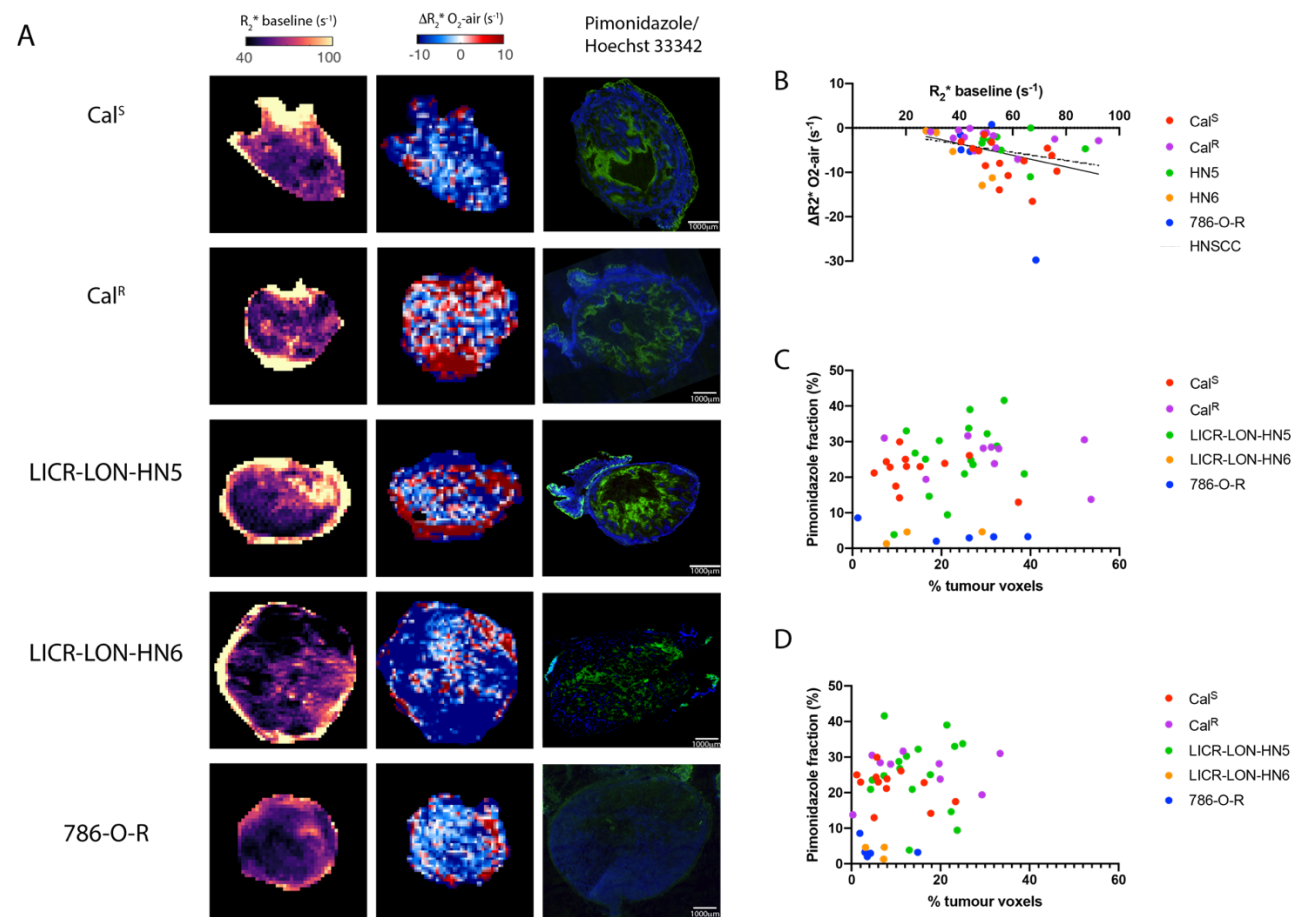


Figure 4.5 Relationship between tumour baseline R_2^* and $\Delta R_2^*_{O_2-air}$.

A) Parametric maps of (from left to right) baseline R_2^* , $\Delta R_2^*_{O_2-air}$ and composite fluorescent images of pimonidazole adduct formation and Hoechst 33342 uptake (scale bar: 1mm) from representative Cal^S, Cal^R, LICR-LON-HN5, LICR-LON-HN6 and 786-O-R tumours. B) Relationship between tumour median baseline R_2^* and $\Delta R_2^*_{O_2-air}$ (solid line: all tumours, $r^2=0.11$, $p=0.01$; dashed line: HNSCC xenografts only, $r^2=0.10$, $p=0.03$). Relationship between pimonidazole-derived hypoxic fraction and voxels exhibiting a $\Delta R_2^*_{O_2-air}$ greater than -0.5 s^{-1} and a baseline R_2^* C) smaller than 60 s^{-1} , D) greater than 60 s^{-1} .

4.2.4 Assessment of tumour perfusion using susceptibility MRI

The relationship between baseline R_2^* , $\Delta R_2^*_{O_2-air}$, $\Delta R_2^*_{USPIO}$, fBV, MRI perfusion determined using an empirical fBV threshold, and perfusion assessed by Hoechst 33342 uptake, is shown in Figure 4.6. Tumour fBV was calculated from the change in R_2^* following intravenous injection of USPIO particles, using equation Equation 2.4 described in 2.4.2. MRI perfusion was determined using an empirical fBV threshold of 2%, as described in 3.2.2.2. The HNSCC xenografts generally presented a low and heterogeneously distributed fBV typically located at the tumour periphery, whereas the 786-O-R tumours exhibited a markedly higher and more homogeneously distributed fBV (respectively $2 \pm 1 \%$ and $22 \pm 2 \%$) (Figure 4.6A). Tumour fBV and Hoechst 33342 uptake were spatially related (Figure 4.6A), and tumour median fBV significantly correlated with median Hoechst 33342-derived perfused fraction (Figure 4.6B). MRI perfused regions were spatially associated with Hoechst 33342 positive areas, except from LICR-LON-HN6 tumours which displayed an extended perfused area compared to Hoechst 33342 uptake (Figure 4.6A). Tumour median MRI perfused fractions correlated with Hoechst 33342-derived perfused fractions (Figure 4.6C). Hoechst 33342-derived perfused fraction did not relate to median baseline R_2^* (Figure 4.6D), but significantly correlated with tumour median $\Delta R_2^*_{O_2-air}$ (Figure 4.6E).

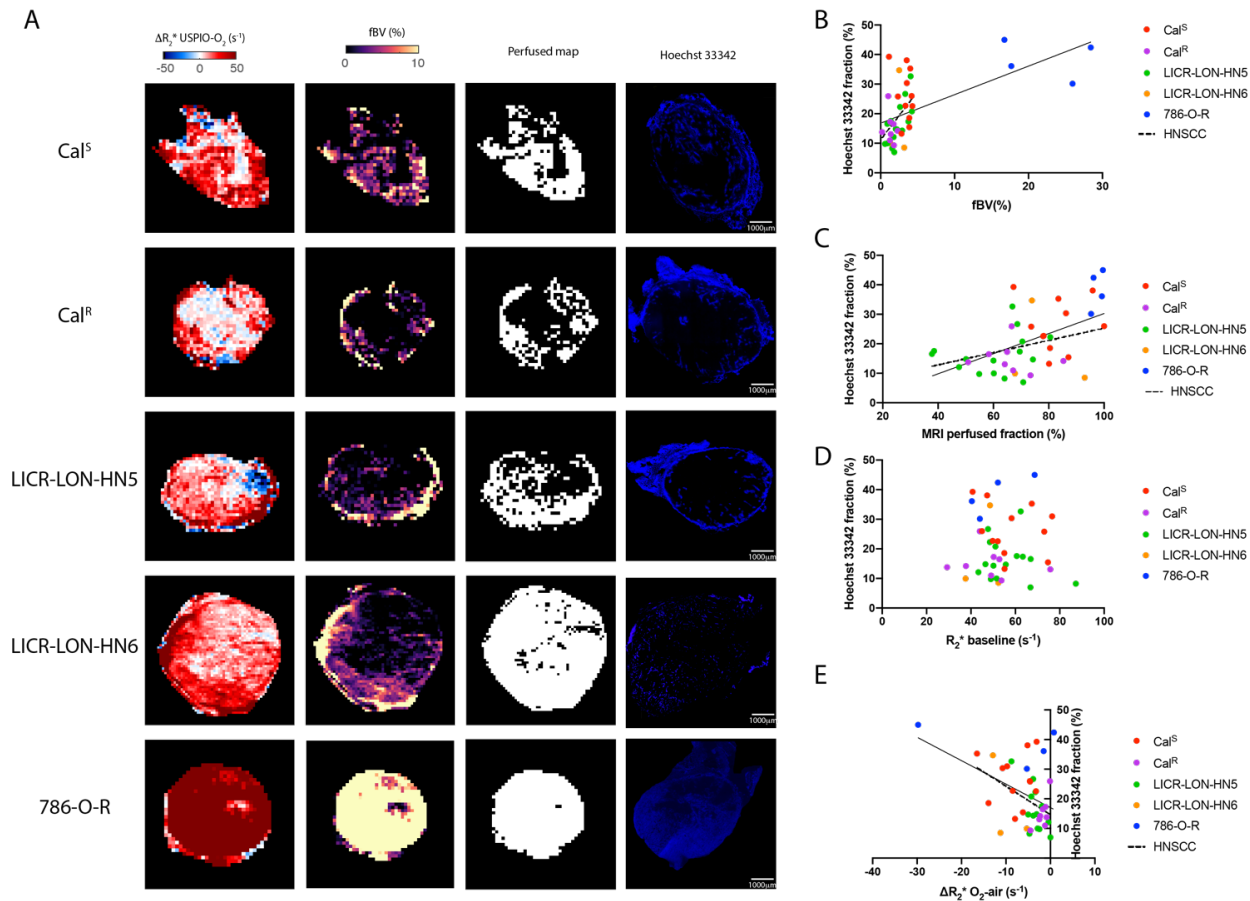


Figure 4.6 Characterisation of tumour perfusion

A) Parametric maps of (from left to right): $\Delta R_2^*_{USPIO-O_2}$, fBV, MRI perfusion as defined using an empirical fBV threshold of 2%, and fluorescence images of Hoechst 33342 uptake (scale bar=1mm), from representative Cal^S, Cal^R, LICR-LON-HN5, LICR-LON-HN6 and 786-O-R tumours. Relationships between Hoechst 33342-derived perfused fraction and B) tumour median fBV (solid line: all tumours, $r^2=0.34$, $p<0.0001$; dashed line: HNSCC xenografts only, $r^2=0.19$, $p<0.01$), C) MRI perfused fraction (solid line: all tumours, $r^2=0.28$, $p<0.001$; dashed line: HNSCC xenografts only, $r^2=0.11$, $p=0.04$), D) tumour baseline R_2^* and E) $\Delta R_2^*_{O_2-air}$ (solid line: all tumours, $r^2=0.18$, $p<0.01$; dashed line: HNSCC xenografts only, $r^2=0.18$, $p<0.01$).

4.2.5 Relationship between tumour perfusion and hypoxia using susceptibility MRI

Whilst voxels identified as perfused ($fBV > 2\%$) and refractory to hyperoxia ($\Delta R_{2^*O_2-air} > -0.5 \text{ s}^{-1}$) were spatially associated with pimonidazole adducts, their extent appeared to underestimate hypoxia (Figure 4.7A). A weak yet significant negative correlation was found between pimonidazole adduct formation and Hoechst 33342 uptake (Figure 4.7B). Tumour fBV (Figure 4.7C) and MRI perfused ($fBV > 2\%$) fraction (Figure 4.7D) inversely correlated with pimonidazole-derived hypoxic fraction across all the HNSCC and RCA xenografts, but not for the HNSCC alone.

MRI perfused voxels exhibiting a $\Delta R_{2^*O_2-air} > -0.5 \text{ s}^{-1}$ were significantly correlated with pimonidazole-derived hypoxic fraction in HNSCC tumours only ($r^2=0.23$, $p < 0.01$) (Figure 4.7E).

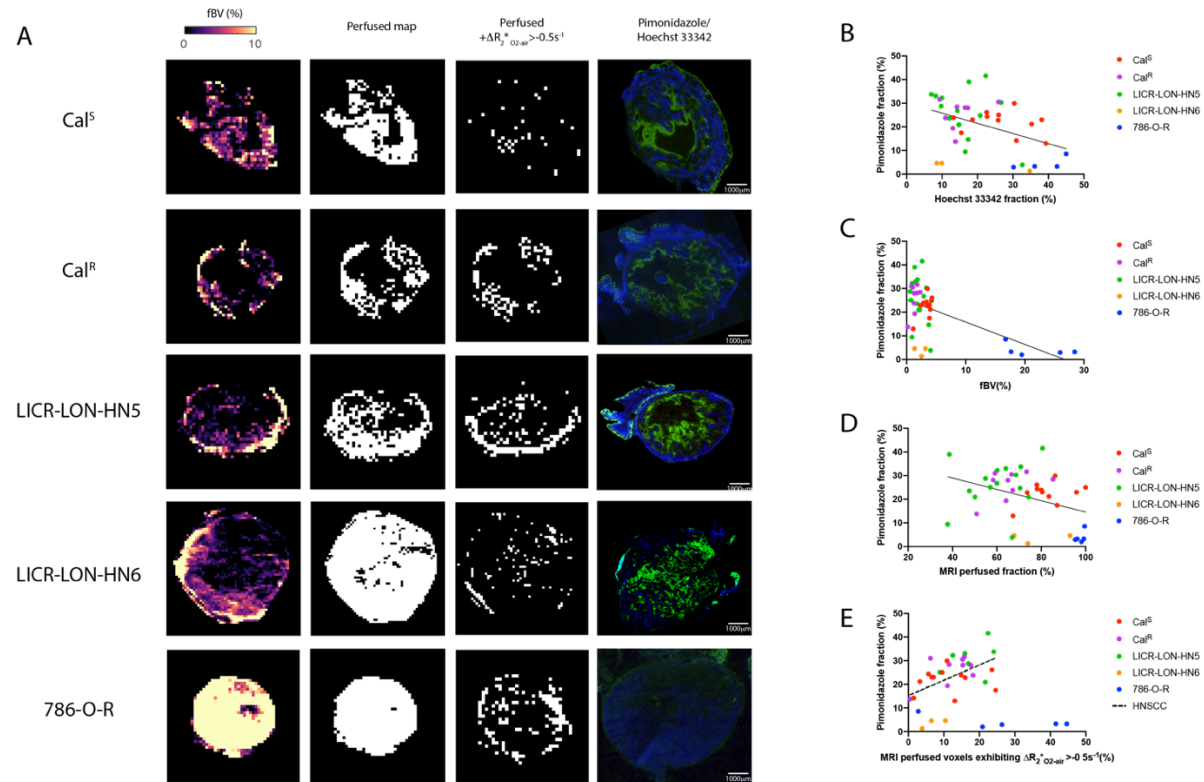


Figure 4.7 Relationship between tumour perfusion and hypoxia

A) Parametric maps of (from left to right): fBV, MRI perfusion as defined using an empirical fBV threshold of 2%, voxels exhibiting a positive fBV and a $\Delta R_2^*_{O_2-air}$ greater than -0.5 s^{-1} , composite fluorescence images of pimonidazole adducts (green, hypoxia) and Hoechst 33342 uptake (blue, perfusion) (scale bar=1mm), from representative Cal^S, Cal^R, LICR-LON-HN5, LICR-LON-HN6 and 786-O-R tumours. Relationships between pimonidazole-derived hypoxic fraction and B) Hoechst 33342 uptake fraction (solid line: all tumours, $r^2=0.18$, $p<0.01$), C) tumour median fBV (solid line: all tumours, $r^2=0.32$, $p<0.0001$), D) MRI perfused fraction (solid line: all tumours, $r^2=0.13$, $p=0.02$), E) MRI perfused voxels exhibiting a $\Delta R_2^*_{O_2-air}$ greater than -0.5 s^{-1} (dashed line: HNSCC xenografts only, $r^2=0.23$, $p<0.01$).

4.3 Discussion

Both IS- and SC-MRI have and continue to be exploited for imaging tumour oxygenation. This chapter describes the evaluation of both susceptibility MRI approaches to map and quantify hypoxia in preclinical models of HNSCC, predicted to exhibit a strong hypoxic phenotype. Collectively, hyperoxia and USPIO particle-induced changes in R_2^* provided spatial and quantitative information on tumour hypoxia, vascular architecture and function.

4.3.1 Histological assessment of tumour hypoxia

Immunohistochemical detection of pimonidazole adducts in MRI-aligned histological sections showed that Cal^S, Cal^R and LICR-LON-HN5 HNSCC xenografts hypoxic and poorly perfused, whereas 786-O-R RCA tumours were well vascularised and more oxic. In these HNSCC tumours, hypoxia was heterogeneously distributed. Interestingly, these studies showed, for the first time, that LICR-LON-HN6 HNSCC xenografts exhibited an unexpectedly relatively oxic phenotype. The LICR-LON-HN6 model may thus provide a useful comparator for future hypoxia and radiation response studies, and for the evaluation of novel strategies designed to alleviate hypoxia for therapeutic gain.

4.3.2 Baseline R_2^* as a biomarker of tumour hypoxia

The transverse MRI relaxation rate R_2^* is sensitive to paramagnetic deoxyhaemoglobin and hence to the arterial blood pO_2 , which is in equilibrium

with tumour tissue pO_2 (see 1.2.3.3), and may thus provide a sensitive imaging biomarker of hypoxia. The median baseline R_2^* values in the Cal^S and Cal^R HNSCC xenografts were in good agreement with those previously reported²²³, and with those quantified from other preclinical tumour models at 7T^{239,289}.

In this study, there was no relationship between tumour baseline R_2^* and hypoxia, as identified by pimonidazole adduct formation. A recent study in patients with HNSCC showed that mean baseline R_2^* was faster in hypoxic subvolumes, identified by ¹⁸F-MISO PET, compared to non-hypoxic regions²¹⁷. Positive correlations of tumour R_2^* with pimonidazole adduct formation were found in PC3 and DU145 prostate cancer xenografts²¹⁹. A clinical study on hypoxia in prostate cancer showed that fast R_2^* correlated with pimonidazole adduct formation and found to have a high sensitivity in depicting tumour hypoxia²¹⁶. In investigating the relationship between IS-MRI and oxygen electrode measurements in human prostate cancer, a significant positive correlation was found between tumour R_2^* and the fraction of tumour exhibiting pO_2 values $<5\text{mmHg}$, and a negative trend between R_2^* and pO_2 ²¹⁸. However, opposite observations of R_2^* values in relation to hypoxia have been observed in other tumour types. For example, baseline R_2^* was negatively correlated with pimonidazole staining in chemically-induced rat mammary carcinomas²²⁰. The relationship of native R_2^* to tissue hypoxia appears to vary according to the underlying histology, and this relationship needs to be defined across a range of different tumour types²⁹⁰.

Collectively these data highlight the complex relationship between R_2^* and tumour oxygenation^{1,2}. Indeed, R_2^* informs on vascular pO_2 and the surrounding tumour tissue but not directly on tumour tissue pO_2 . R_2^* is

sensitive to haematocrit, blood volume, pH, flow, vessel density, temperature^{188,286}. Moreover, R_2^* can be affected by static tissue components such as paramagnetic species associated with necrotic debris and/or arising from the degradation of haemoglobin (e.g. hemichromes)¹⁸⁹. Although they were excluded from the analysis in this study, areas of necrosis or cysts, often observed in clinical MRI examinations of patients with metastatic head and neck lymph nodes, display a hypointense R_2^* signal.

Furthermore, R_2^* is susceptible to magnetic field inhomogeneities arising from variations due to air-tissue interface or haemorrhage, especially at higher field strengths. This is particularly relevant to human head and neck cancer due to the air-tissue interfaces present in the oral cavity, throat and ears, as well as swallowing-induced motion artefacts. Such artefacts can be compensated to an extent by localised shimming²⁸⁶.

4.3.3 $\Delta R_2^*_{O_2\text{-air}}$ as a biomarker of tumour hypoxia

In the HNSCC xenografts, hyperoxia-induced changes in R_2^* were found to inversely correlate with hypoxia. Hypoxic areas, rich in deoxyhaemoglobin, have been associated with a greater reduction in R_2^* with hyperoxia^{224,239,289,291}. Theoretically, normoxic, well-perfused tumours with a high concentration of oxyhaemoglobin should show little to no change in R_2^* under hyperoxia. The positive correlation between $\Delta R_2^*_{O_2\text{-air}}$ and Hoechst 33342 suggests that the lack of response to oxygen challenge is due to impaired perfusion, leading to a deficient oxygen delivery.

The ranges of hyperoxia-induced $\Delta R_2^*_{O_2\text{-air}}$ and pimonidazole adduct-derived hypoxic fraction observed here were similar to previous studies in the same

HNSCC models²²³. The relatively smaller R_2^* response to hyperoxia, and higher level of hypoxia, determined in the Cal^R HNSCC model were consistent with its more aggressive phenotype (note that tumours were propagated using 10-fold fewer cells than Cal^S), and has previously been associated with a switch to a more glycolytic metabolism²²³.

In accordance with previous studies²²⁴, an association between $\Delta R_{2^*O_2-air}$ and pimonidazole adduct formation was not evident in the well-perfused 786-O-RCA tumours, implying that in more perfused tumour types, such as renal and prostate cancer, a greater blood volume could mask R_2^* changes in hypoxic regions^{216,219}.

The main limitation of susceptibility MRI is that the tumour pathophysiology is assumed to remain unchanged during the hyperoxia challenge. For example, haematocrit has been found to decrease and plasma flow increase under hyperoxia²⁹². Hypoxia can induce acidosis, which consequently shifts the oxygen saturation curve to the right, thus decreasing haemoglobin saturation (Bohr effect) and resulting in a smaller negative $\Delta R_{2^*O_2-ai}$. Moreover, tumour cell metabolism can reprogram between oxidative phosphorylation²⁹³ and glycolysis^{195,294}. Haemoglobin saturation may not change if the tumour cells use anaerobic respiration to survive, resulting in a lack of change in R_2^* . Furthermore, the putative vasoconstrictive property of oxygen gas on tumour and/or systemic vasculature may also influence blood flow and volume¹⁹⁰. Hyperoxia-induced changes in R_2^* can monitor variations of tumour oxygenation in HNSCC xenografts.

4.3.4 Combined baseline R_2^* and $\Delta R_2^*_{O_2-air}$ as a biomarker for hypoxia

A spatial and quantitative association was found between baseline R_2^* and $\Delta R_2^*_{O_2-air}$ across all the tumours, and the HNSCC xenografts alone. Similar relationships have been reported in chemically-induced rat mammary carcinomas²²⁰, subcutaneous PC3 prostate and HCT116 colon carcinoma xenografts²³⁹, and in syngeneic rhabdomyosarcoma and 9-L glioma subcutaneous tumours²⁴³. However, classification of voxels according to their median baseline R_2^* coupled with their response to hyperoxia did not correlate with pimonidazole-derived hypoxic fraction. Together, these data underline the multi-factorial, non-linear relationship between baseline R_2^* , $\Delta R_2^*_{O_2-air}$ and tumour pO_2 , most likely related to the tumour vascular architecture and pathophysiology.

This study describes the first IS-MRI investigation performed in the LICR-LON-HN6 HNSCC model *in vivo*, which exhibited a slow baseline R_2^* and a small, negative $\Delta R_2^*_{O_2-air}$, consistent with a more oxidic MRI phenotype and similar to that of the 786-O-R tumours. Whilst only a small number of tumour-bearing mice were investigated, the data suggest that the LICR-LON-HN6 model may also provide a useful model for future comparative studies focussed on identifying MRI-derived predictive biomarkers of response to radiotherapy.

4.3.5 Susceptibility MRI for perfusion imaging

No relationship between baseline R_2^* and perfusion, as measured by Hoechst 33342 uptake, was identified across the models investigated. Several studies have investigated the use of IS-MRI to inform on incipient tumour angiogenesis and showed that enhanced vascular development was associated with a faster baseline R_2^* , independent of oxygenation status^{191,295}. In the HNSCC xenografts, tumour median $\Delta R_2^*_{O_2-air}$ was spatially and quantitatively associated with Hoechst 33342-derived perfused fraction. SC-MRI derived tumour fBV strongly correlated with Hoechst 33342 uptake, a relationship seen across a number of preclinical investigations^{200,296}, reinforcing the utility of fBV as a sensitive imaging biomarker of patent tumour vasculature. Application of an MRI perfusion mask described in 3.2.2.2 revealed intratumoural variations in the perfusion of the HNSCC and RCA xenografts, with the exception of the LICR-LON-HN6 tumours, for which the MRI perfusion map did not visually agree with Hoechst 33342 uptake. Although LICR-LON-HN6 has the similar tissue origin as the other HNSCC cell lines studied here (human tongue carcinoma)²⁵⁵, its unknown pathophysiology could explain the difference in perfusion, and needs further investigation. These results suggest that whilst IS- and SC-MRI can provide imaging biomarkers that inform on haemodynamic and patent tumour vasculature respectively, their individual lack of specificity towards tumour oxygenation makes their association with hypoxia difficult to interpret¹⁹¹.

4.3.6 Combined IS and SC-MRI derived R_2^* biomarkers for imaging tumour hypoxia

The inverse correlation between Hoechst 33342 uptake, tumour median fBV, MRI perfused fraction and pimonidazole-derived hypoxic fraction underlines the close relationship between perfusion and hypoxia.

In the HNSCC xenografts, perfused (fBV>2%) voxels exhibiting a lack of or positive response to hyperoxia were associated with hypoxia. These tumour subregions likely exhibit tortuous, constricted capillaries that are not haemodynamically active (lack of erythrocytes, leading to a lack of hyperoxia-induced change in R_2^*) due to their small calibre²⁹⁷, and/or functional vascular shunts (leading to an accumulation of erythrocytes, therefore a positive $\Delta R_2^*_{O_2-air}$). Consequently, the altered red blood cell rheology and flow lead to intermittent perfusion and cycling hypoxia⁴¹. The experimental protocol, initially designed for the acquisition of both R_2^* and R_1 in one imaging session, resulted in a delay of approximately 15 min between R_2^* measurements pre- and post- hyperoxia, a length of time similar to the reported periodicity of oxygenation fluctuations, between 15 min to an hour³⁹⁻⁴¹.

The IS and SC-MRI derived R_2^* biomarkers could thus be useful for imaging intermittent perfusion linked to cycling hypoxia, and for monitoring hypoxia-modifying treatment outcome, in HNSCC¹⁹⁷.

4.4 Conclusion

In conclusion, susceptibility MRI-derived R_2^* biomarkers have the potential to monitor temporal changes in tumour oxygenation, and can provide additional information on tumour vasculature. However, combining susceptibility MRI with other techniques, such as R_1 mapping and quantification, may help bypass some of the challenges of the technique for more direct imaging of tumour hypoxia^{223,238,239,298}.

In the next chapter, the combined use of both R_1 and R_2^* biomarkers is assessed to image hypoxia in the same HNSCC models, using the OE-MRI protocol described in 2.2.3.

Chapter 5 Evaluation of OE-MRI for imaging hypoxia in HNSCC xenografts

5.1 Introduction

Oxygen-enhanced MRI exploits the paramagnetic properties of oxygen molecules. In normoxic tissues, where haemoglobin is mostly present in its oxygenated form, hyperoxia challenge induces an accumulation of excess oxygen molecules in the interstitial and vascular compartments, inducing an increase in the MRI longitudinal relaxation rate R_1 . Conversely, in hypoxic regions, where deoxyhaemoglobin predominates, hyperoxia results in preferential binding of oxygen to haems, with R_1 remaining essentially static. OE-MRI is being actively investigated for imaging hypoxia in tumours^{186,224,240}. In this chapter, OE-MRI was evaluated for imaging hypoxia in HNSCC xenografts. Additionally, OE-MRI was compared with susceptibility MRI data for the assessment of tumour hypoxia. For comparison, a model of renal cell adenocarcinoma (RCA), previously well characterised in our laboratory, was investigated using the same protocol.

5.2 Results

5.2.1 Characterisation of HNSCC tumour engraftment and growth

The tumour growth characteristics of Cal^S, Cal^R, LICR-LON-HN5 (HNSCC models) and 786-O-R (RCA model) xenografts are shown in Figure 5.1.

Tumours became palpable at similar times after cell injection, except for the LICR-LON-HN5 xenografts, which were quicker to establish. Cal^R tumours were initiated with 10-fold fewer cells to compensate for its previously described aggressiveness²⁵³ (cf Chap.2). Tumours progressed at different rates: Cal^S tumours grew slowly (Figure 5.1A), whilst Cal^R (Figure 5.1B) and LICR-LON-HN5 (Figure 5.1C) tumour growth was relatively fast. The 786-O-R (Figure 5.1D) tumours grew exponentially from 22 days post-engraftment. Variations in some of the HNSCC tumour growth curves arose from calliper measurements being influenced by cystic pockets, as alluded to in Chap.4. Mean tumour doubling times (Figure 5.1E), calculated from the exponential regression analysis of the individual growth curves from the day the tumours become palpable, were not significantly different between the models (one-way ANOVA).

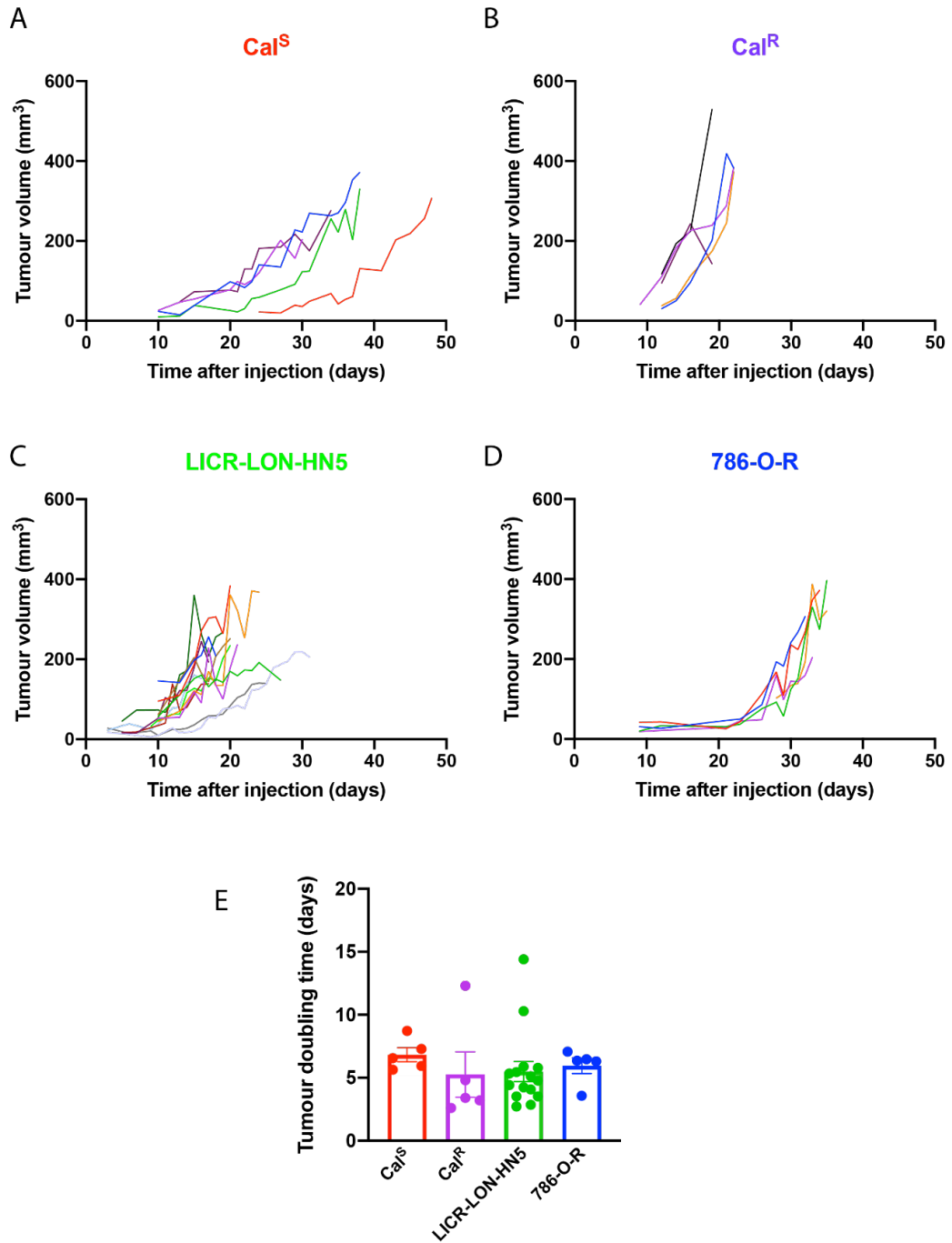


Figure 5.1 Characterisation of tumour growth.

Growth curves of A) Cal^S (n=5), B) Cal^R (n=5), C) LICR-LON-HN5 (n=15) HNSCC tumours and D) 786-O-R (n=5) RCA xenografts. Measurements were performed every other day using callipers. Each line represents an individual tumour. E) Tumour doubling times calculated from Cal^S, Cal^R, LICR-LON-HN5 and 786-O-R xenografts. Bars are mean \pm 1 s.e.m.

5.2.2 Histological characterisation of hypoxia and perfusion in HNSCC xenograft models

Immunofluorescence staining was performed on frozen sections aligned with the MR imaging plane, using a FITC-conjugated antibody to detect pimonidazole adducts, a marker of hypoxia (green), and Hoechst 33342 as a fluorescent marker of perfusion (blue) (Figure 5.2).

Abundant pimonidazole adducts formed towards the core of the HNSCC tumours, whereas pimonidazole adduct formation was less evident in the RCA model (Figure 5.2A). Pimonidazole adduct fraction (Figure 5.2B) was significantly higher in the HNSCC models than in the RCA model ($26 \pm 2\%$ and $4 \pm 1\%$, respectively).

Hoechst 33342 uptake was typically located towards the rim of the HNSCC tumours, whereas RCA tumours showed a more extensive and homogeneous distribution (Figure 5.2A). With the exception of the Cal^S model, Hoechst 33342 uptake fraction was significantly lower in the Cal^R and LICR-LON-HN5 tumours than in RCA tumours ($17 \pm 1\%$ and $38 \pm 3\%$, respectively) (Figure 5.2C).

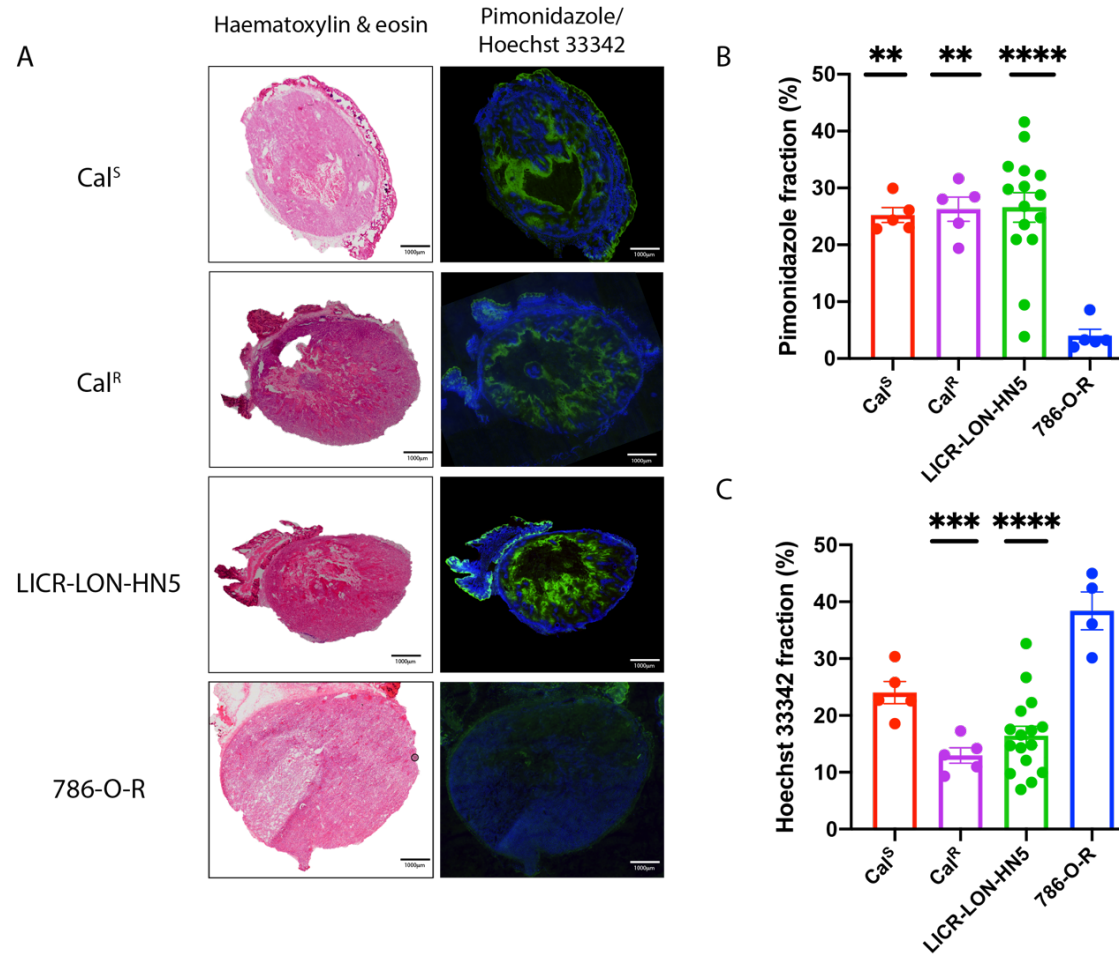


Figure 5.2 Histological characterisation of tumour hypoxia and perfusion.

A) Bright field images of haematoxylin & eosin staining (left panel), and composite fluorescence images of pimonidazole adducts (green, hypoxia) and Hoechst 33342 uptake (blue, perfusion), from representative Cal^S, Cal^R, LICR-LON-HN5 (HNSCC models) and 786-O-R (RCA model) tumours. Summary of B) tumour pimonidazole adduct fraction and C) Hoechst 33342 uptake fraction. Bars are mean \pm 1 s.e.m. Significance lines are relative to 786-O-R. ** $p < 0.01$; *** $p < 0.001$, **** $p < 0.0001$.

High magnification (x200) images of representative adjacent formalin-fixed paraffin-embedded HNSCC tumour sections stained either with H&E or chromagens to detect pimonidazole adducts are shown in Figure 5.3. Intense pink areas surrounded by tumour cells forming a 'swirl', independently identified as keratin pearls by an independent pathologist (Dr Ionnis Roxanis, personal communication), were observed on the H&E stained sections, and were negative to pimonidazole. Outer concentric flattened tumour cells surrounding the keratin pearl-like pink regions stained positive for pimonidazole adducts and exhibited an eosinophilic cytoplasm.

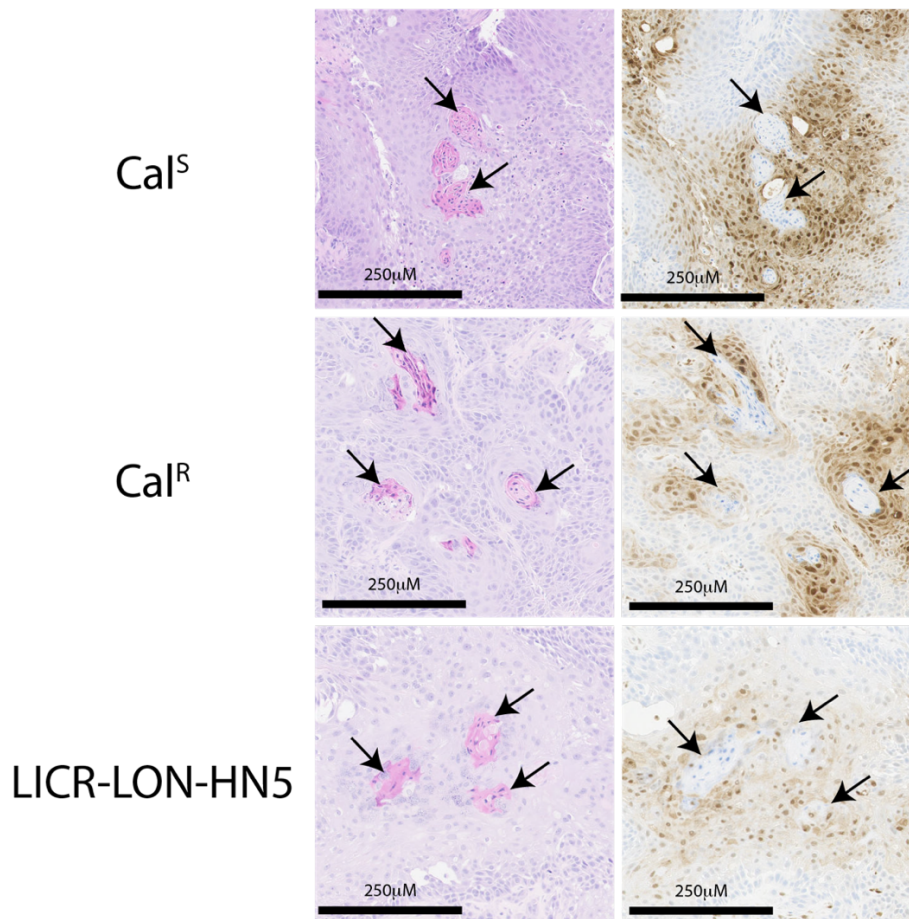


Figure 5.3: Morphology of hypoxic regions of HNSCC tumours.

High magnification (x200) brightfield images from haematoxylin & eosin stained sections (left panel) and chromogenically-detected pimonidazole adducts (right panel) from adjacent sections of Cal^S, Cal^R and LICR-LON-HN5 HNSCC tumours. Arrows indicate keratin pearls.

5.2.3 Assessment of OE-MRI for hypoxia imaging in HNSCC models

T₂-weighted anatomical images and corresponding OE-MRI-derived parametric maps acquired from representative Cal^S, Cal^R, LICR-LON-HN5 and 786-O-R xenografts are shown in Figure 5.4. Cystic areas and susceptibility artefacts, arising from either air-tissue interfaces or mouse movement, were excluded from the analysis. Overall, HNSCC models presented a wider dynamic range and a more heterogeneous distribution of the different MRI parameters than the RCA model.

In the HNSCC xenografts, baseline R₁ and R₂^{*} were generally faster, with faster subregions present at the periphery of the tumours. $\Delta R_{1\ O_2\text{-air}}$ and $\Delta R_{2\text{ }^*O_2\text{-air}}$ were heterogeneously distributed, with no pattern or spatial association, and presented a wider range of voxel-wise values, positive or negative. Fractional blood volumes presented a rim/core pattern. The OxyR and pOxyR extent were greater than the RCA tumours. Cal^R and LICR-LON-HN5 phenotypes appeared very similar with regard to spatial distribution and dynamic range.

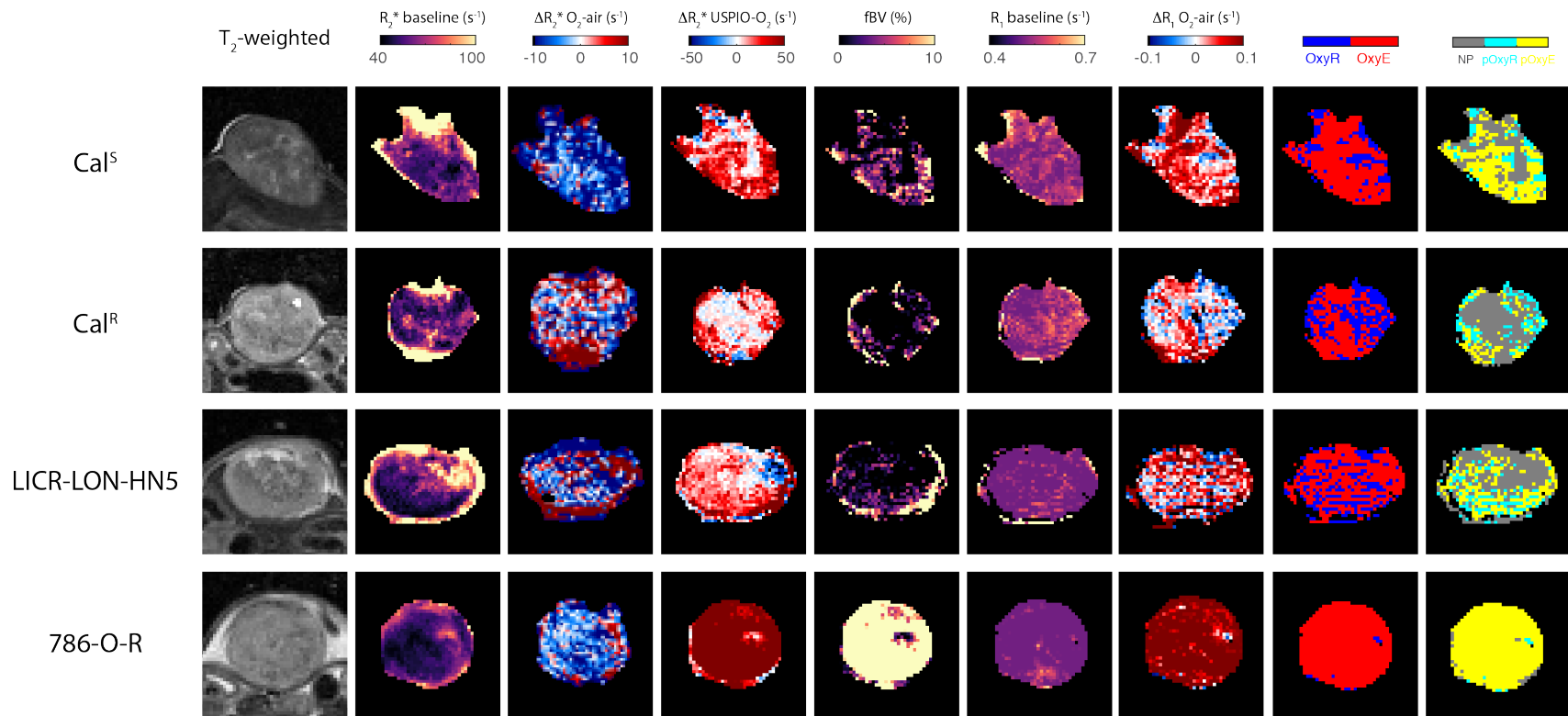


Figure 5.4 Anatomical and functional imaging data obtained using OE-MRI.

*T*₂-weighted images of Cal^S, Cal^R, LICR-LON-HN5 (HNSCC) and 786-O-R (RCA) xenografts, and the associated parametric maps of baseline R_2^* , hyperoxia-induced $\Delta R_2^*_{O_2-air}$, USPIO-induced $\Delta R_2^*_{USPIO-O_2}$, fractional blood volume (fBV), baseline R_1 , hyperoxia-induced $\Delta R_1_{O_2-air}$, oxygen-refractory (OxyR, blue) and oxygen-enhanced (OxyE, red) voxels, perfused oxygen-refractory (pOxyR, cyan), oxygen-enhanced (pOxyE, yellow) voxels and non-perfused (NP, grey) voxels.

5.2.3.1 Assessment of baseline R_1 as a biomarker of hypoxia

Since R_1 is sensitive to paramagnetic dissolved oxygen, baseline R_1 was investigated as a potential biomarker of hypoxia. Parametric baseline R_1 maps of representative tumours, and composite immunohistochemistry microscope images of pimonidazole adduct formation and Hoechst 33342 uptake from tumour sections aligned with the MR imaging plane are shown in Figure 5.5. Overall, there was no spatial association between R_1 and pimonidazole adduct formation (Figure 5.5A). All HNSCC xenografts presented similar tumour baseline R_1 values, whilst RCA tumours exhibited a slower R_1 (Figure 5.5B). Quantitatively, there was no relationship between R_1 and pimonidazole adduct formation (Figure 5.5D).

5.2.3.2 Assessment of $\Delta R_{1\ O_2\text{-air}}$ as a biomarker of hypoxia

Hyperoxia-induced $\Delta R_{1\ O_2\text{-air}}$ maps calculated from representative HNSCC and RCA tumours, and their corresponding histology, are shown in Figure 5.6. Overall, HNSCC tumours exhibited a heterogeneous R_1 response to hyperoxia, whilst R_1 greatly increased in a more homogeneous fashion in the RCA xenografts (Figure 5.6A). Compared to the RCA model, $\Delta R_{1\ O_2\text{-air}}$ was significantly smaller in each of the HNSCC models (Figure 5.6B).

Typically, voxels exhibiting a lack of change in R_1 after oxygen challenge (white voxels) were heterogeneously distributed but were not completely aligned with pimonidazole positive subregions (Figure 5.6A). A significant

negative correlation was found between tumour median $\Delta R_{1 \text{ O}_2\text{-air}}$ and pimonidazole adduct fraction ($r^2=0.55$, $p<0.0001$) (Figure 5.6D).

5.2.3.3 Assessment of OxyR as a biomarker of hypoxia

$\Delta R_{1 \text{ O}_2\text{-air}}$ voxels were thresholded into voxels refractory to oxygen challenge (OxyR) or enhanced by oxygen (OxyE), using a threshold described in Chap.3. Representative maps of the spatial distribution of OxyR voxels, as well as the associated immunofluorescence images, are shown in Figure 5.7. Except for the Cal^S model, OxyR voxels spatially co-localised with pimonidazole adduct rich areas (Figure 5.7A), and OxyR fraction was significantly higher in every HNSCC model compared to the RCA model (Figure 5.7B). Median OxyR fraction significantly correlated with hypoxic fraction across all models ($r^2=0.50$, $p<0.0001$). A weaker positive correlation was also observed for the HNSCC xenografts only ($r^2=0.20$, $p=0.03$) (Figure 5.7D).

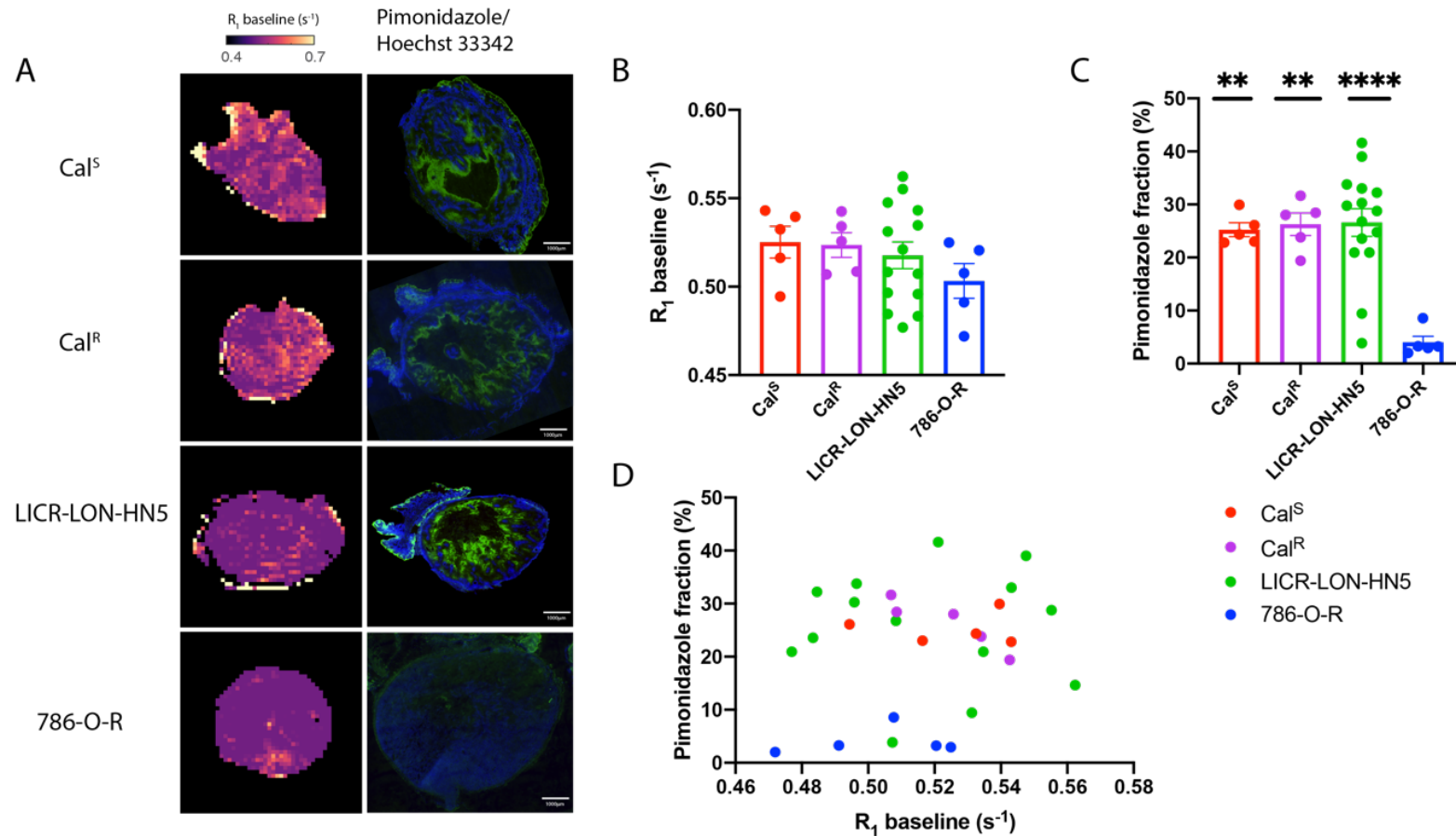


Figure 5.5 Assessment of tumour baseline R_1 for the characterisation of hypoxia.

A) From left to right: parametric baseline R_1 maps and composite fluorescence images of pimonidazole adducts (green, hypoxia) and Hoechst 33342 uptake (blue, perfusion), from representative Cal^S, Cal^R, LICR-LON-HN5 and 786-O-R tumours. Summary of B) tumour median baseline R_1 values and C) pimonidazole adduct fraction. Bars are mean \pm 1 s.e.m. Significance lines are relative to 786-O-R. ** $p < 0.01$; **** $p < 0.0001$. D) Relationship between tumour median baseline R_1 and pimonidazole adduct fraction.

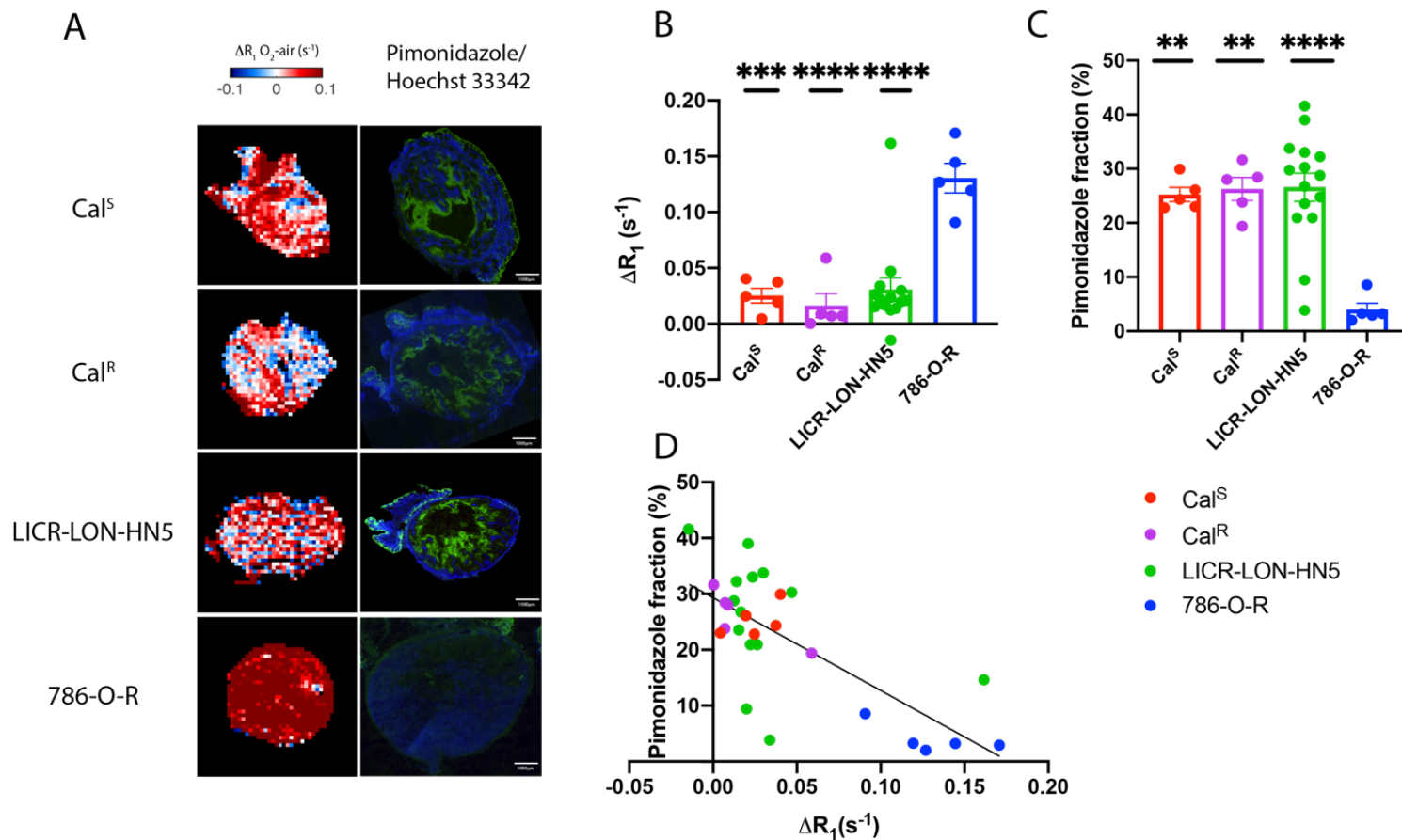


Figure 5.6 Characterisation of hypoxia using tumour $\Delta R_1 \text{ O}_2\text{-air}$.

A) Parametric maps of hyperoxia-induced $\Delta R_1 \text{ O}_2\text{-air}$ (left panel), and composite fluorescence images of pimonidazole adducts (green, hypoxia) and Hoechst 33342 uptake (blue, perfusion), from representative Cal^S, Cal^R, LICR-LON-HN5 and 786-O-R tumours. Summary of B) tumour median $\Delta R_1 \text{ O}_2\text{-air}$ and C) pimonidazole adduct fraction values. Bars are mean \pm 1 s.e.m. Significance lines are relative to 786-O-R. ** $p < 0.01$; *** $p < 0.001$; **** $p < 0.0001$. D) Relationship between median tumour hyperoxia-induced $\Delta R_1 \text{ O}_2\text{-air}$ and pimonidazole adduct fraction (solid line: all tumours, $r^2 = 0.55$, $p < 0.0001$).

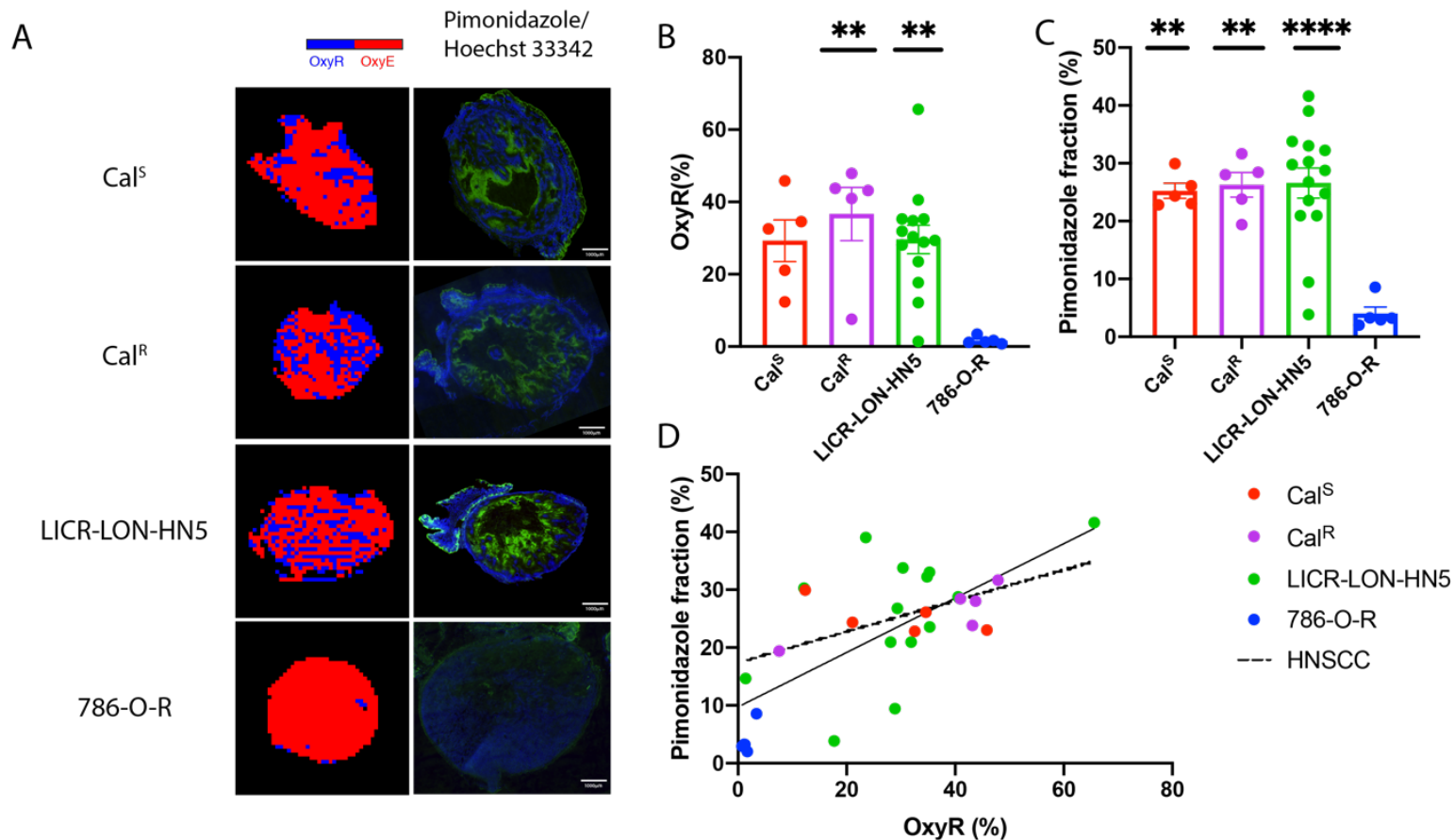


Figure 5.7 Characterisation of hypoxia using tumour OxyR.

A) Parametric maps of OxyR voxels (blue), OxyE voxels (red) (left panel), and composite fluorescence images of pimonidazole adducts (green, hypoxia) and Hoechst 33342 uptake (blue, perfusion), from representative Cal^S, Cal^R, LICR-LON-HN5 and 786-O-R tumours. Summary of B) tumour median OxyR fractions and C) pimonidazole adduct fraction values for each model. Bars are mean \pm 1 s.e.m. Significance lines are relative to 786-O-R. ** $p < 0.01$; **** $p < 0.0001$. D) Relationship between tumour OxyR fraction and pimonidazole adduct fraction (solid line: all tumours, $r^2 = 0.50$, $p < 0.0001$; dashed line: HNSCC only, $r^2 = 0.20$, $p = 0.03$).

5.2.3.4 Assessment of tumour perfusion using susceptibility MRI

Fractional blood volume (fBV) was determined from the change in tumour R_2^* following intravenous injection of USPIO particles. Figure 5.8 shows fBV, thresholded MRI perfusion and $\Delta R_{2^*O_2-air}$ maps and corresponding immunofluorescence images obtained from representative HNSCC and RCA tumours. A spatial association was apparent between fBV voxels and Hoechst 33342 uptake in the RCA xenografts which was generally homogeneous (Figure 5.8A). Greater fBV areas and Hoechst 33342 uptake regions were typically located at the periphery of the HNSCC tumours. A strong positive correlation was observed between fBV and Hoechst 33342 across all tumours ($r^2=0.66$, $p<0.0001$) and for the HNSCC xenografts only ($r^2=0.48$, $p=0.0001$) (Figure 5.8B). MRI perfused voxels (voxels exhibiting a fBV greater than 2%, as defined in 3.) were spatially co-localised with Hoechst 33342 uptake (Figure 5.8A); MRI perfused fraction was correlated with Hoechst 33342-derived perfused fraction for all models ($r^2=0.73$, $p<0.0001$) and for HNSCC models only ($r^2=0.50$, $p<0.0001$) (Figure 5.8C). Negative $\Delta R_{2^*O_2-air}$ voxels and Hoechst 33342 subregions were colocalised (Figure 5.8A), and $\Delta R_{2^*O_2-air}$ fraction was significantly correlated for all tumours ($r^2=0.18$, $p=0.02$) and for HNSCC only ($r^2=0.30$, $p<0.01$) (Figure 5.8D).

5.2.3.5 Assessing pOxyR as a biomarker of hypoxia

fBV maps were thresholded to determine perfused and non-perfused areas, as discussed in Chapter 3, and combined with OxyR maps to identify pOxyR voxels, previously shown to indicate tumour hypoxia^{186,224} (Figure 5.9). MRI

non-perfused tumour sub-regions were commonly observed in the HNSCC tumours but not in the RCA xenografts. Visually, HNSCC tumours exhibited pOxyR subregions that were macroscopically associated with pimonidazole-positive regions, though pimonidazole adduct formation was more extensive than pOxyR voxels in these regions. In contrast, the RCA xenografts exhibited few pOxyR voxels (Figure 5.9A). Compared to the RCA model, a significantly greater pOxyR fraction was determined across pooled HNSCC xenografts ($p < 0.01$) (not shown), but not for any individual HNSCC model (Figure 5.9B). pOxyR fraction and pimonidazole-derived hypoxic fraction positively correlated across all the tumours ($r^2 = 0.36$, $p < 0.001$), but not in the HNSCC xenografts alone ($r^2 = 0.11$, $p = 0.11$) (Figure 5.9D).

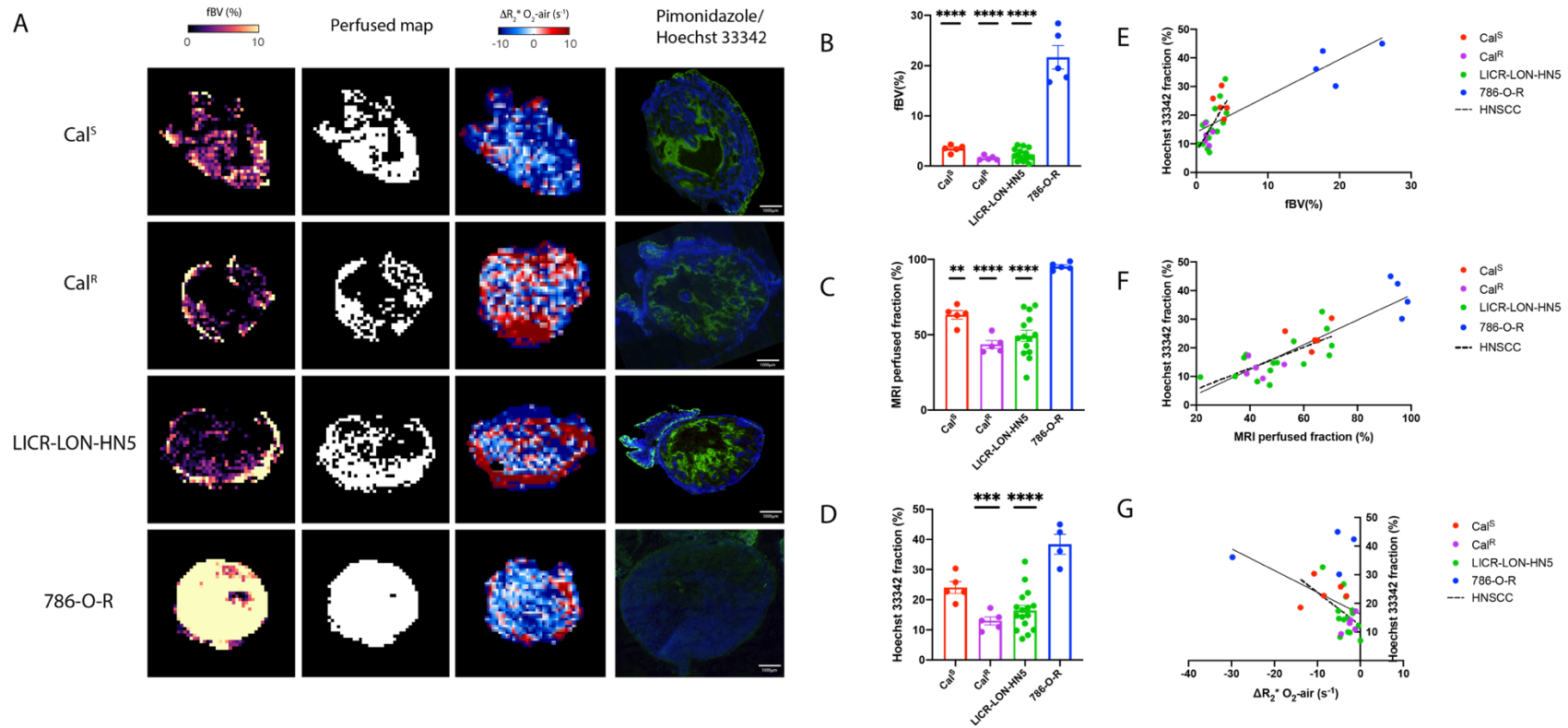


Figure 5.8 Characterisation of tumour perfusion

A) Parametric maps of (from left to right): fBV, MRI perfusion as defined using an empirical fBV threshold of 2%, $\Delta R_2^* O_{2-air}$ and composite fluorescence images (scale bar=1mm) of pimonidazole adducts (green, hypoxia) and Hoechst 33342 uptake (blue, perfusion), from representative Cal^S, Cal^R, LICR-LON-HN5 and 786-O-R tumours. Summary of tumour median B) fBV C) MRI perfused fractions and D) Hoechst 33342 uptake fraction values for each model. Bars are mean \pm 1 s.e.m. Significance lines are relative to 786-O-R. ** $p < 0.01$; *** $p < 0.001$; **** $p < 0.0001$. Relationships between Hoechst 33342-derived perfused fraction and E) tumour median fBV (solid line: all tumours, $r^2 = 0.66$, $p < 0.0001$; dashed line: HNSCC xenografts only, $r^2 = 0.48$, $p = 0.0001$), F) MRI perfused fraction (solid line: all tumours, $r^2 = 0.73$, $p < 0.0001$; dashed line: HNSCC xenografts only, $r^2 = 0.50$, $p < 0.0001$), G) $\Delta R_2^* O_{2-air}$ (solid line: all tumours, $r^2 = 0.18$, $p = 0.02$; dashed line: HNSCC xenografts only, $r^2 = 0.30$, $p < 0.01$).

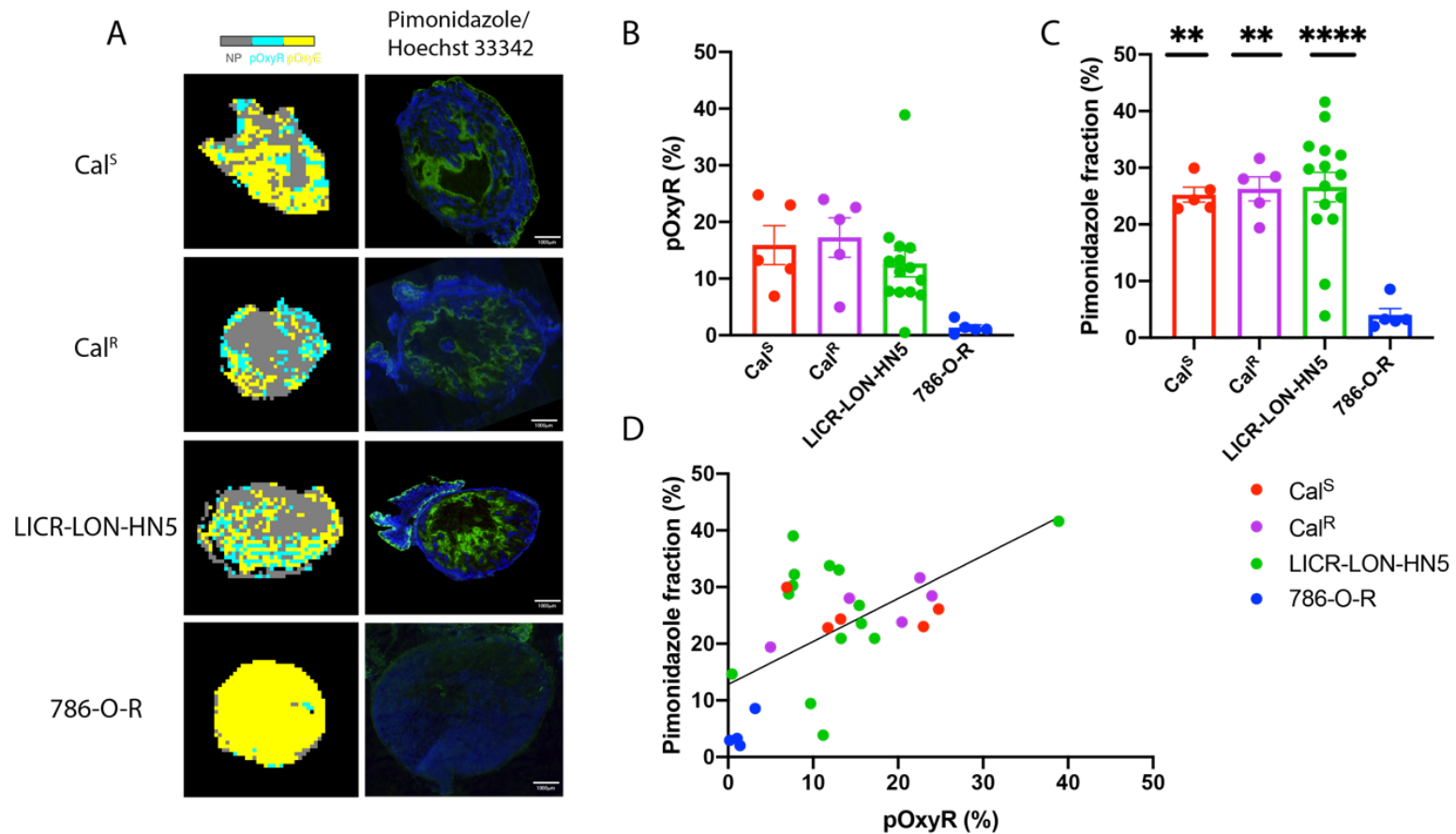


Figure 5.9 Characterisation of hypoxia using tumour pOxyR.

A) Parametric maps of pOxyR voxels (cyan), pOxyE voxels (yellow) and non-perfused voxels (grey) (left panel), and composite fluorescence images of pimonidazole adducts (green, hypoxia) and Hoechst 33342 uptake (blue, perfusion), from representative Cal^S, Cal^R, LICR-LON- HN5 and 786-O-R tumours. Summary of B) tumour pOxyR fractions and C) pimonidazole adduct fraction values for each model. Bars are mean \pm 1 s.e.m. Significance lines are relative to 786-O-R. ** $p < 0.01$; **** $p < 0.0001$. D) Relationship between tumour pOxyR fraction and pimonidazole-derived hypoxic fraction (solid line: all tumours, $r^2 = 0.36$, $p < 0.001$).

5.2.3.6 Comparison between OE-MRI and susceptibility

MRI derived biomarkers

In order to identify any pattern in hypoxia extent that could be detected by both OE- and susceptibility MRI, the relationship between R_1 and R_2^* parameters is shown in Figure 5.10. Baseline R_1 and baseline R_2^* were not spatially associated (Figure 5.10A); however, a weak correlation was found between tumour median baseline R_1 and baseline R_2^* ($r^2=0.19$, $p=0.02$) (Figure 5.10B). $\Delta R_{1\ O_2\text{-air}}$ and baseline R_2^* were not co-localised and their tumour-wise median values did not correlate (Figure 5.10C). Generally, no spatial co-localisation or linear correlation between $\Delta R_{1\ O_2\text{-air}}$ voxels and $\Delta R_{2^*\ O_2\text{-air}}$ voxels was identified (Figure 5.10D).

Figure 5.11 shows the combination of the OE-MRI and susceptibility-MRI for the assessment of hypoxia. OxyR and pOxyR voxels that exhibited a $\Delta R_{2^*\ O_2\text{-air}}$ greater than $-0.5\ \text{s}^{-1}$ (as described in 4.2.3.2) were compared to the immunofluorescent images of pimonidazole adduct formation and Hoechst 33342 uptake of MRI-aligned tissue sections. In all the models but Cal^S, both masks spatially matched pimonidazole adduct subregions (Figure 5.11A). A significant correlation was found between pimonidazole-derived hypoxic fraction and OxyR voxels exhibiting a $\Delta R_{2^*\ O_2\text{-air}}$ greater than $-0.5\ \text{s}^{-1}$ in all tumours ($r^2=0.47$, $p<0.0001$) and in the pooled HNSCC only ($r^2=0.25$, $p=0.02$) (Figure 5.11B). A correlation was also found between pimonidazole fraction and fraction of pOxyR voxels presenting a $\Delta R_{2^*\ O_2\text{-air}}$ greater than $-0.5\ \text{s}^{-1}$ (all tumours: $r^2=0.38$, $p<0.001$; HNSCC only: $r^2=0.20$, $p=0.03$) (Figure 5.11C).

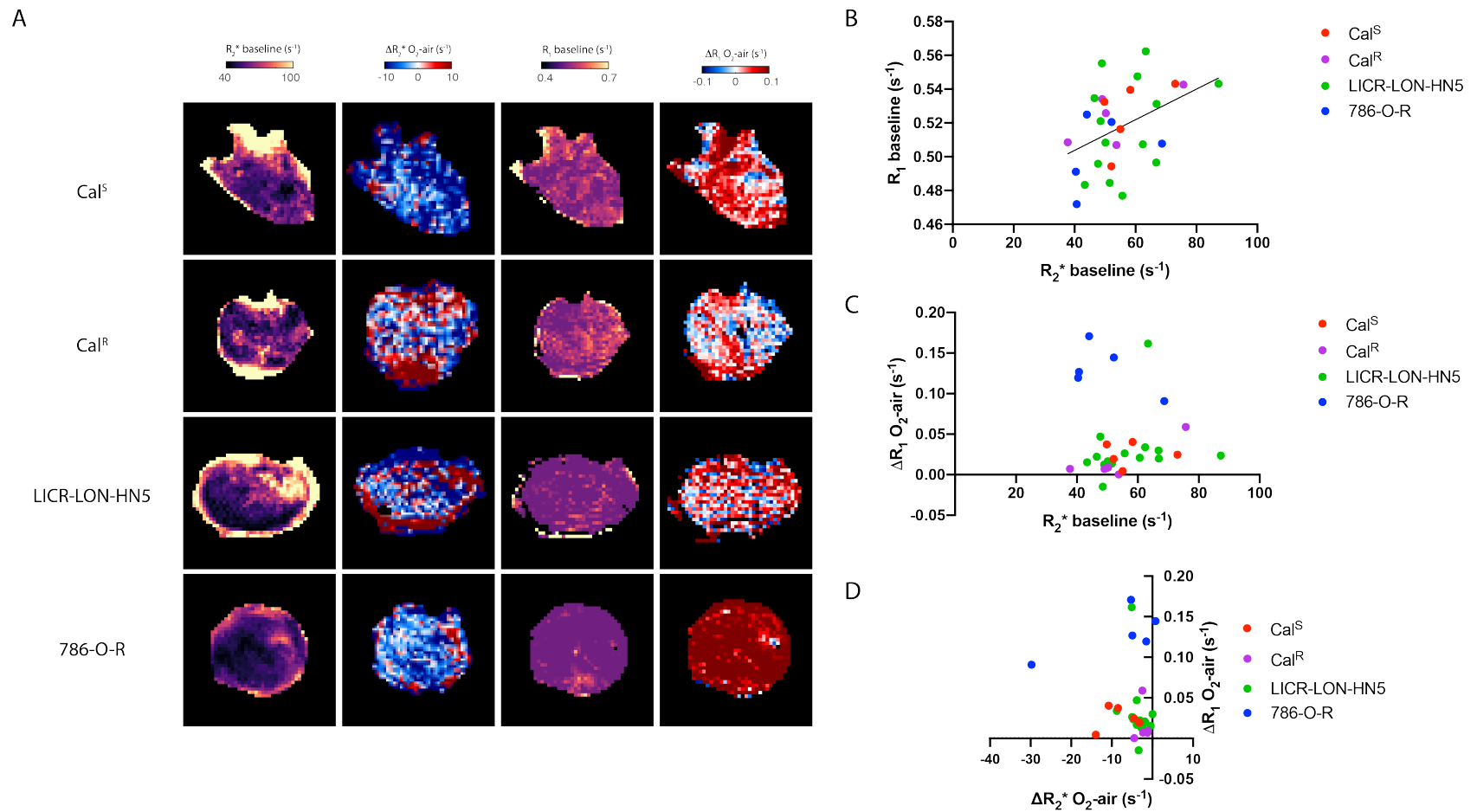


Figure 5.10 Relationship between R_1 and R_2^*

A) Parametric maps of (from left to right): baseline R_2^* , $\Delta R_2^* O_{2-air}$, baseline R_1 and $\Delta R_1 O_{2-air}$ from representative Cal^S , Cal^R , LICR-LON-HN5 and 786-O-R tumours. Relationships between tumour baseline R_2^* and B) tumour baseline R_1 (solid line: all tumours, $r^2=0.19$, $p=0.02$) and C) $\Delta R_1 O_{2-air}$. D) Relationship between $\Delta R_2^* O_{2-air}$ and $\Delta R_1 O_{2-air}$.

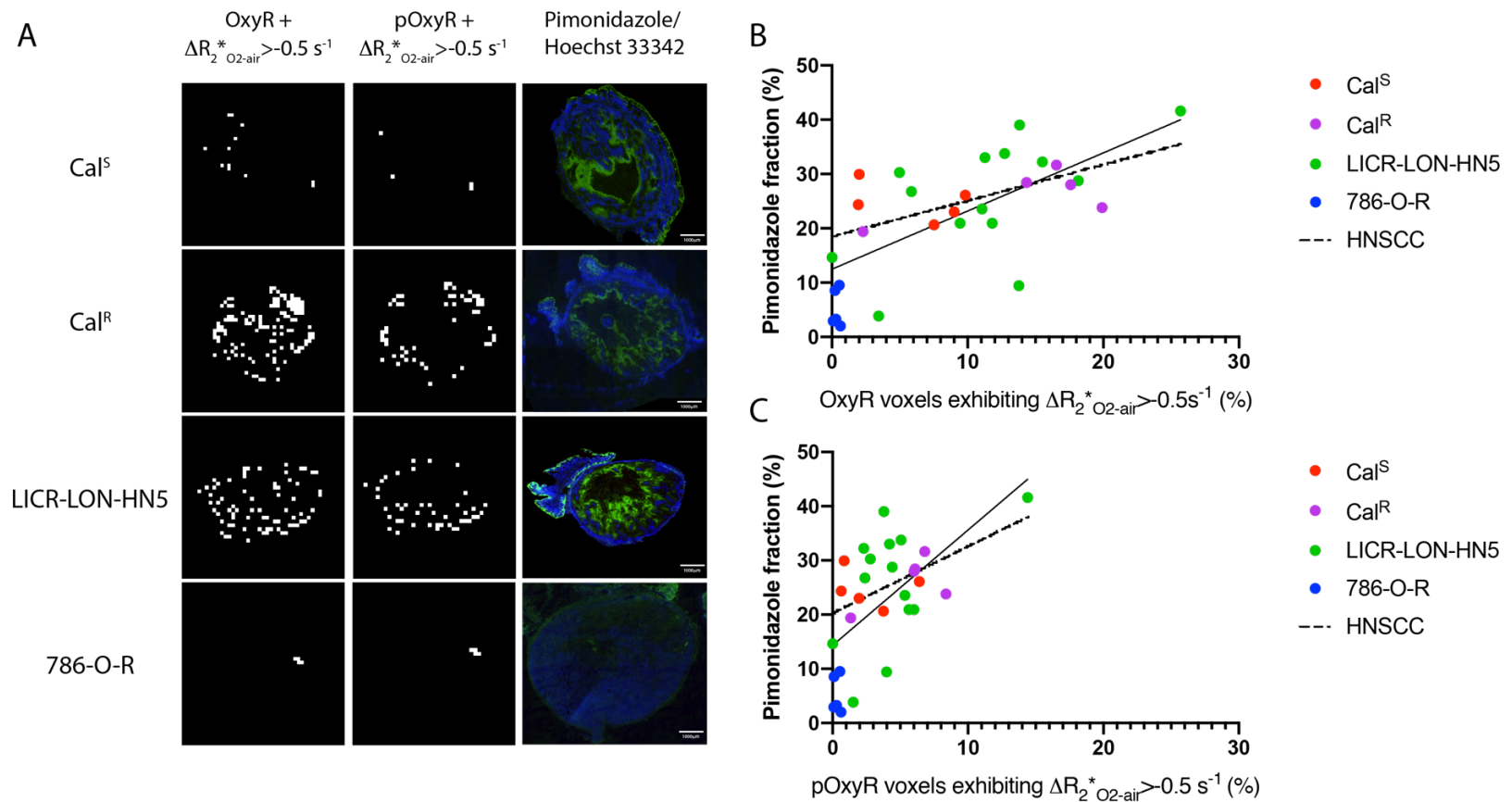


Figure 5.11 Characterisation of tumour hypoxia using combined R_1 and R_2^* -derived biomarkers.

A) Parametric maps of (from left to right): OxyR voxels exhibiting a $\Delta R_2^*_{O_2-air}$ greater than $-0.5 s^{-1}$, pOxyR voxels exhibiting a $\Delta R_2^*_{O_2-air}$ greater than $-0.5 s^{-1}$, composite fluorescence images of pimonidazole adducts (green, hypoxia) and Hoechst 33342 uptake (blue, perfusion) (scale bar = 1mm), from representative Cal^S, Cal^R, LICR-LON-HN5 and 786-O-R tumours. Relationships between pimonidazole-derived hypoxic fraction and B) OxyR voxels exhibiting a $\Delta R_2^*_{O_2-air}$ greater than $-0.5 s^{-1}$ (solid line: all tumours, $r^2=0.47$, $p<0.0001$; dashed line: HNSCC xenografts only, $r^2=0.25$, $p=0.02$), C) pOxyR voxels exhibiting a $\Delta R_2^*_{O_2-air}$ greater than $-0.5 s^{-1}$ (solid line: all tumours, $r^2=0.38$, $p<0.001$; dashed line: HNSCC xenografts only, $r^2=0.20$, $p=0.03$).

5.3 Discussion

In this study, OE-MRI was assessed for the evaluation of tumour hypoxia in preclinical models of HNSCC, predicted to exhibit a strong hypoxic phenotype. The results demonstrate that biomarkers derived from combined OE- and susceptibility MRI approaches, such as pOxyR, can map and quantify hypoxia. These biomarkers were used to introduce another combined biomarker of hypoxia that does not require perfusion information obtained from an exogenously administered contrast agent.

5.3.1 Histological characterisation of hypoxia in HNSCC xenografts

All the HNSCC models studied exhibited hypoxia, as shown by extensive pimonidazole adduct formation. Analysis of H&E staining of MRI-matched HNSCC tumour sections revealed the presence of strongly eosinophilic structures, confirmed as keratin pearls by an independent pathologist, with surrounding elongated tumour cells that recapitulated features similar to outer layers of normal epidermis. Pimonidazole adducts were identified around these keratin pearls. A similar pattern has also been observed in differentiated uterine cervical squamous cell carcinoma cells²⁹⁹. This observation infers (i) that pimonidazole staining indicates hypoxia associated with differentiation, and/or (ii) that pimonidazole adduct formation is independent of oxygenation status in differentiated areas, thereby impacting on its utility for the validation of MRI biomarkers.

Although hypoxic tumours are often poorly differentiated, there might be a link between hypoxia and differentiation³⁰⁰. An overlap between pimonidazole staining and the differentiation marker involucrin has been observed in human cervix tumours³⁰¹. Hypoxia may cause differentiation, although hypoxia has been shown to promote cancer stem cells³⁰², or conversely differentiation may result in hypoxia.

Inference (ii) is corroborated by a study showing pimonidazole adducts exclusively within keratinised regions of normoxic HNSCC, and which was not due to high reductase levels¹⁴². It is possible that the anti-pimonidazole antibody can cross-react with a cellular component other than reduced adducts, though this was excluded herein by the absence of staining in tumour sections not containing pimonidazole (data not shown). Importantly for this thesis, the possibility of some differentiation-associated pimonidazole staining that is not due to hypoxia may lead to an overestimation of the hypoxic fraction determined by histology, and hence the lack of association with pOxyR seen in 5.2.3.5.

5.3.2 Evaluation of OE-MRI for imaging hypoxia

5.3.2.1 Assessment of R_1 biomarkers for imaging hypoxia

No spatial association or quantitative correlation between baseline R_1 and pimonidazole fraction was found. Moreover, despite their different oxygenation status, HNSCC and RCA models presented comparable median baseline R_1 values, which were similar to those reported in other tumour models, such as

rat GH3 prolactinomas, PC3 prostate cancer xenografts²³⁹, U87 glioma xenografts¹⁸⁵ and rabbit VX2 carcinoma renal carcinomas³⁰³. These results were expected, as the longitudinal relaxivities of O₂ and deoxyhaemoglobin (0.01 s⁻¹.mM⁻¹ at 7T^{228,229}), and their concentrations are too small to identify hypoxic tumours solely based on their native R₁. Furthermore, other factors, such as blood inflow²³¹, size of the interstitial compartment²³², necrosis^{233,234}, tissue water content²³³, haematocrit in the blood compartment^{227,235,236}, a high concentration of deoxyhaemoglobin^{227,237} and temperature^{231,238} may have an impact on R₁, limiting its specificity and preventing a direct quantitative comparison with tumour pO₂.

A spatial association and a negative quantitative correlation between $\Delta R_{1 \text{ O}_2\text{-air}}$ and pimonidazole fraction was established. Overall, HNSCC tumours exhibited a heterogeneously and significantly smaller distribution of $\Delta R_{1 \text{ O}_2\text{-air}}$ voxels and a higher pimonidazole-derived hypoxic fraction than the 786-O-R RCA model. Values were consistent with other studies on Cal^R and Cal^S HNSCC models²²³, as well as 786-O-R RCA xenografts^{186,224}. Indeed, studies have shown that R₁ is sensitive to hyperoxia-induced changes in tumour pO₂^{186,243(p)}. The same linear relationship between pimonidazole and $\Delta R_{1 \text{ O}_2\text{-air}}$ has been observed in other tumours types, including human U87 glioma xenografts^{185,240}, the same 786-O-R RCA model herein and human SW620 colorectal carcinoma xenografts^{186,224}, and Calu-6 NSCLC xenografts²⁴⁰. Tumour median $\Delta R_{1 \text{ O}_2\text{-air}}$ was non significantly smaller in Cal^R and Cal^S, and pimonidazole fraction was non-significantly higher in Cal^R, indicative of a more hypoxic phenotype in the drug resistant tumours, and consistent with previous

studies²²³. In HNSCC, some subregions showed little or no response to hyperoxia, suggesting a locally lower level of haemoglobin oxygen saturation locally. Accordingly, these subregions colocalised with pimonidazole positive areas. The lack of response could be explained by the longitudinal oxygen gradients present from the lungs to the tumour capillary bed¹⁹⁰. Under air breathing, tumour arteriolar pO₂ is ~27 mmHg, which accounts for around 25% of blood gas pO₂^{190,304,305}. In normal tissues, these oxygen gradients can be compensated for by redundant microvessels, whereas the lack of tumour arterioles compromise sufficient oxygen delivery. Subsequently, hyperoxic challenge leads to haemoglobin-bound oxygen saturation, hence a lack of excess oxygen. These subregions were also described and associated with low tumour pO₂ in other preclinical tumour models, including Dunning R3327-AT1 rat prostate tumours²³⁸, human SW620 colorectal carcinoma xenografts¹⁸⁶ and 786-O-R RCA^{186,224}.

Some tumour subregions even exhibited a negative $\Delta R_{1\text{ O}_2\text{-air}}$, consistent with a decrease in dissolved oxygen, suggestive of transient perfusion, cycling hypoxia or vascular steal. Similar observations have been reported previously in U87 glioblastoma xenografts¹⁸⁵ and Dunning R33327-AT1 and R33327-HI prostate tumour models²⁰¹.

$\Delta R_{1\text{ O}_2\text{-air}}$ informs on oxygen delivery to the tumour tissue compartment but not on hypoxia itself so additional MRI biomarkers are required to inform on tumour hypoxia.

5.3.2.2 Assessment of OE-MRI-derived biomarkers of hypoxia

In light of the previous results, $\Delta R_{1 \text{ O}_2\text{-air}}$ voxels were thresholded to identify voxels that are refractory to oxygen challenge (OxyR voxels). OxyR voxels colocalised with pimonidazole adduct areas and a strong correlation between OxyR fraction and pimonidazole-derived hypoxic fraction was found. Unlike tumour median $\Delta R_{1 \text{ O}_2\text{-air}}$, OxyR fraction accounted for intratumoral heterogeneity of hypoxia, particularly prominent in HNSCC.

In order to exclude areas void of blood supply, which can also result in a lack of response to hyperoxia, a perfusion mask has been proposed, using DCE-MRI with a gadolinium-based contrast agent¹⁸⁶. However, the passive diffusion of gadolinium outside the vascular compartment makes it a marker of both perfusion and vessel permeability³⁰⁶. Here, fBV was used for a robust perfusion readout, using USPIO particle-based susceptibility contrast MRI. USPIO particles remain in the intravascular compartment over the MR imaging timeframe for the quantitation of fBV, a sensitive and specific biomarker of functional tumour vasculature²⁰⁰.

As described in 3.2.2.2, an fBV-derived thresholded perfusion mask, more representative of the histological perfusion data than absolute fBV, was combined with OE-MRI to identify pOxyR voxels. pOxyR voxels were spatially associated with pimonidazole adduct formation, and pOxyR fraction showed a weak correlation with pimonidazole-derived hypoxic fraction.

The limitation of this method is that the perfusion readout does not detect non-perfused but viable tumour tissue areas associated with hypoxia. Firstly, the

lack of perfusion could lead to levels of oxygenation down to anoxia, where cells are still viable but incapable of proliferation anymore. Secondly, oxygen delivery to the tumour core can happen in necrotic-appearing areas by diffusion, as shown by a higher pO_2 in a soft tissue carcinoma³⁰³. Finally, temporal resolution is not taken into account. Vascular reorganisation, typically observed in cancer, could result in non-perfused areas where cells are still viable at the time of imaging. Although cancer stem-like cells can survive under hypoxia, tumour cells eventually die from a prolonged lack of oxygen. But similarly, transient perfusion could lead to reoxygenation and thus cycling hypoxia.

Nonetheless, information on necrosis could be useful for predicting and monitoring treatment response, and could be obtained from the diffusion-weighted MRI (DW-MRI) parameter, apparent diffusion coefficient (ADC), which has been shown to be greater in necrotic tissues³⁰⁷. In HNSCC patients, DW-MRI is routinely used for tumour characterisation^{307–309}, nodal staging³¹⁰ and therapy monitoring³¹¹, but optimisation and comparison with morphological images is indispensable, due to high susceptibility artefacts in the neck region, and the presence of water-rich structures such as cysts²²⁵.

5.3.3 Comparison of OE-MRI with IS-MRI

The dependence of both R_1 and R_2^* on tissue and blood oxygenation, respectively, led to the combined study of both biomarkers to inform on tumour hypoxia. Several studies have investigated the complex and non-linear relationship between R_1 and R_2^* in tumour xenografts^{76,223,224,238,239,248,303} and in patients^{298,312}. In this study, a weak correlation between tumour baseline R_1

and R_2^* was found, but given the lack of spatial association, as well as the sensitivity of either parameter to many biological and experimental factors, such as blood inflow²³¹, size of the interstitial compartment²³², necrosis^{233,234}, tissue water content²³³, haematocrit in the blood compartment^{227,235,236}, a high concentration of deoxyhaemoglobin^{227,237} and temperature^{231,238}, this relationship may be artefactual and is difficult to interpret. Burrell *et al* found that baseline R_1 and R_2^* were sensitive to different pathophysiological phenotypes in rat prolactinomas and human prostate models that showed a different hypoxic profile²³⁹.

In this study, baseline R_2^* was not correlated with $\Delta R_{1\ O_2\text{-air}}$. As shown in 4.2.3.1, baseline R_2^* was not specific enough for the assessment of hypoxia. Either fast (i.e. a high concentration of deoxyhaemoglobin) or slow (i.e. a low blood volume) baseline R_2^* may be associated with hypoxia.

$\Delta R_{1\ O_2\text{-air}}$ and $\Delta R_{2^*\ O_2\text{-air}}$ were not spatially colocalised or quantitatively correlated. HNSCC showed small $\Delta R_{1\ O_2\text{-air}}$ and $\Delta R_{2^*\ O_2\text{-air}}$, suggesting that oxygen molecules immediately diffused from the vasculature into a hypoxic tumour tissue compartment. Conversely, well-perfused and oxygenated RCA showed a greater $\Delta R_{1\ O_2\text{-air}}$ and a similar $\Delta R_{2^*\ O_2\text{-air}}$, suggesting that excess oxygen accumulated in the vascular and interstitial compartments. This contradicts another study which describes an increase in R_1 associated with a decrease in R_2^* in soft tissue carcinoma³⁰³. Our results were consistent with the non-linear relationship observed in hypoxic rat prolactinomas, which exhibited a large negative ΔR_{2^*} and a relatively small ΔR_1 , and in well-perfused and oxygenated human prostate tumours, which presented a greater ΔR_1 and a smaller ΔR_{2^*} ²³⁹. The lack of linear correlation between ΔR_1 and ΔR_{2^*} was

coherent with similar observations in hypoxic rat prostate tumours²⁰¹. These results describe a complex relationship between R_1 and R_2^* response to hyperoxia, most likely dependent on the tumour type and pathophysiology.

These results led to the evaluation of combined of OxyR and $\Delta R_{2^*}^{*O_2-air}$ for the assessment of hypoxia.

In 4.2.5, I proposed a susceptibility MRI-based biomarker, based on voxels refractory to hyperoxia ($\Delta R_{2^*}^{*O_2-air}$ greater than $-0.5s^{-1}$), that informs on hypoxia related to a chaotic vascular structure and function, typical of HNSCC tumour models. Combined with OxyR or pOxyR mapping, they identified and quantified subregions exhibiting a poor perfusion and a poor tissue oxygenation. These subregions were related to hypoxia as identified by pimonidazole adduct formation. The fBV-based perfusion mask may thus be redundant, which is clinically favourable as it decreases the risks associated with the use of exogenous contrast agents, allows shorter scan times and an improved patient compliance.

Collectively, these results show that combining R_1 and R_2^* thresholded markers may be useful to characterise different but complementary aspects underlying the pathophysiology of hypoxia. The theoretical relationship between hyperoxia-induced $\Delta R_{1 O_2-air}$ and $\Delta R_{2^*}^{*O_2-air}$ is represented in Figure 5.12. Tumour hypoxia is characterised by a high concentration of deoxyhaemoglobin, marked by a fast R_2^* . Hyperoxia challenge induces oxygen binding to haemoglobin molecules, hence a decrease in R_2^* and an absence of change or a small decrease in R_1 due to the paramagnetic properties of the iron molecules included in haemoglobin. In the case of mild hypoxia, oxygen binds to the small or negligible amount of deoxyhaemoglobin,

resulting in a decrease in R_2^* , but most of the excess oxygen remain in the extravascular compartments, hence an increase in R_1 . Deep hypoxia may be characterised by a lack of functional vasculature, for example due to the diameter of capillaries that do not allow the passage of haemoglobin, or a lower haematocrit. In this case, depending on the blood volume, R_2^* may be slower. Hyperoxia-induced surplus of dissolved oxygen molecules may extravasate into the interstitial compartment, generating a small increase in R_1 but a lack of response in R_2^* . Normoxia is described by a high concentration of diamagnetic oxyhaemoglobin, indicated by a slower R_2^* . Accumulation of dissolved oxygen molecules caused by the inhalation of 100% oxygen cause an increase in R_1 , and lack of response to R_2^* . Increase of R_2^* may occur due to the potential vasoconstrictive effect of oxygen, increasing blood flow.

Absence of vasculature, e.g. necrosis, translates in a lack of response to hyperoxia. A fast R_2^* may be measured due to the paramagnetic properties of necrosis-induced debris or blood breakdown products, e.g. hemichromes.

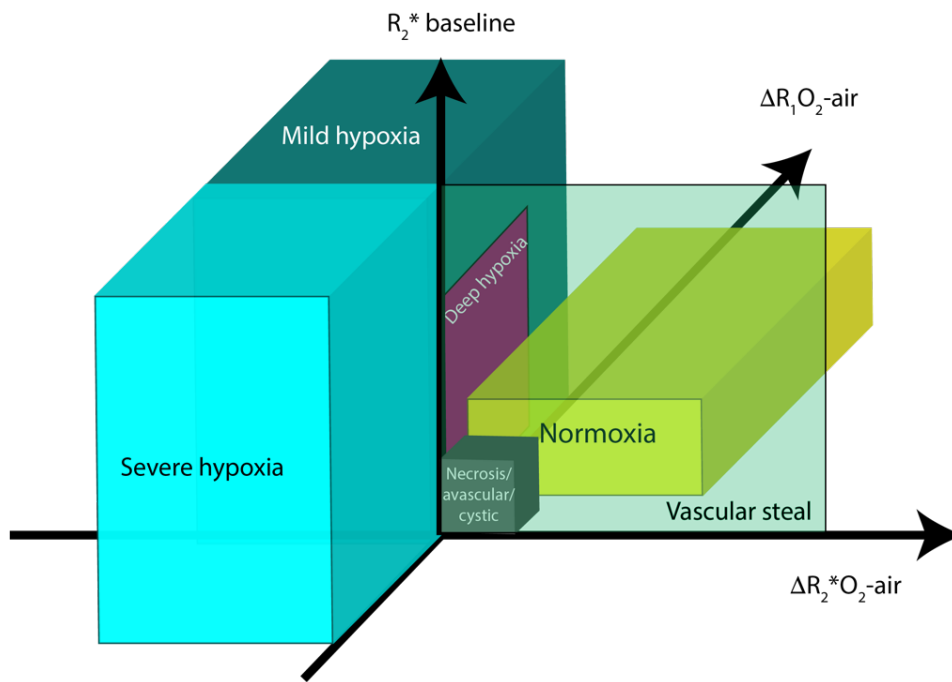


Figure 5.12 Schematic representation of the theoretical relationships between hyperoxia-induced ΔR_{1O_2-air} and $\Delta R_{2^*O_2-air}$.
 Developed and adapted from Burrell et al, 2013 and Cao-Pham et al, 2017^{239,243}.

5.4 Conclusion

In this chapter, OE-MRI was successfully performed in HNSCC xenografts. OxyR and pOxyR voxels accurately identified and assessed the extent of hypoxia. A perfusion readout may not be indispensable for very hypoxic tumours such as HNSCC. Combined OE-MRI and susceptibility-MRI is useful to inform on different but complementary underlying biology of tumour oxygenation in HNSCC xenografts.

Further validation of this biomarker, including its sensitivity to the effects of clinical candidate compounds that modify hypoxia, is necessary. This is addressed in the next chapter.

Chapter 6 Assessment of HNSCC response to atovaquone using OE-MRI

Given its clear role in conferring treatment resistance, numerous strategies designed to alleviate tumour hypoxia for therapeutic gain are being investigated (summarised in 1.1.5). One recent approach has focussed on targeting one of the hallmarks of cancer, metabolic reprogramming⁷³. Cancer cells adapt to oxygen deprivation by upregulating glycolytic pathways and downregulating oxidative phosphorylation, even in the presence of oxygen (Warburg effect). Inhibiting mitochondrial respiration and reducing the oxygen consumption rate (OCR) can improve oxygen availability in the tumour tissue. Atovaquone, an antimalarial drug, has been found to decrease the OCR, through inhibition of mitochondrial complex III, and subsequently hypoxia, in *in vitro* and *in vivo* FaDu HNSCC and HCT116 colorectal carcinoma models, as well as a H1299 lung carcinoma spheroid model, consequently increasing their radiosensitivity¹⁻³. Its effects on hypoxia are being assessed in an early phase 1 clinical trial in non-small lung adenocarcinoma patients in the UK. In this chapter, the atovaquone-induced changes in hypoxia in LICR-LON-HN5 HNSCC xenografts, shown to exhibit a strong hypoxic phenotype in the previous chapters, was investigated using OE-MRI.

6.1 Results

6.1.1 Tumour growth characteristics

The growth characteristics of the LICR-LON-HN5 xenografts used in this study are shown in Figure 6.1, and were similar to those reported in 4.2.1. Tumours were palpable ~5 days after subcutaneous injection of cells. Once tumours reached a volume of 150mm³, they were stratified to be treated with either 50 mg/kg/day p.o. atovaquone or vehicle for either 3 or 7 days. Atovaquone did not induce any tumour growth inhibition (Figure 6.1A). Tumour doubling time was not significantly different between control and treated tumours (unpaired t-test, p=0.57) (Figure 6.1C). Tumour volumes at the time of MRI were similar between the two groups (unpaired t-test, p=0.42)(Figure 6.1D). Mouse body weight remained stable over the timecourse of the experiment (Figure 6.1B), and did not vary between groups (unpaired t-test, p=0.17) (Figure 6.1E).

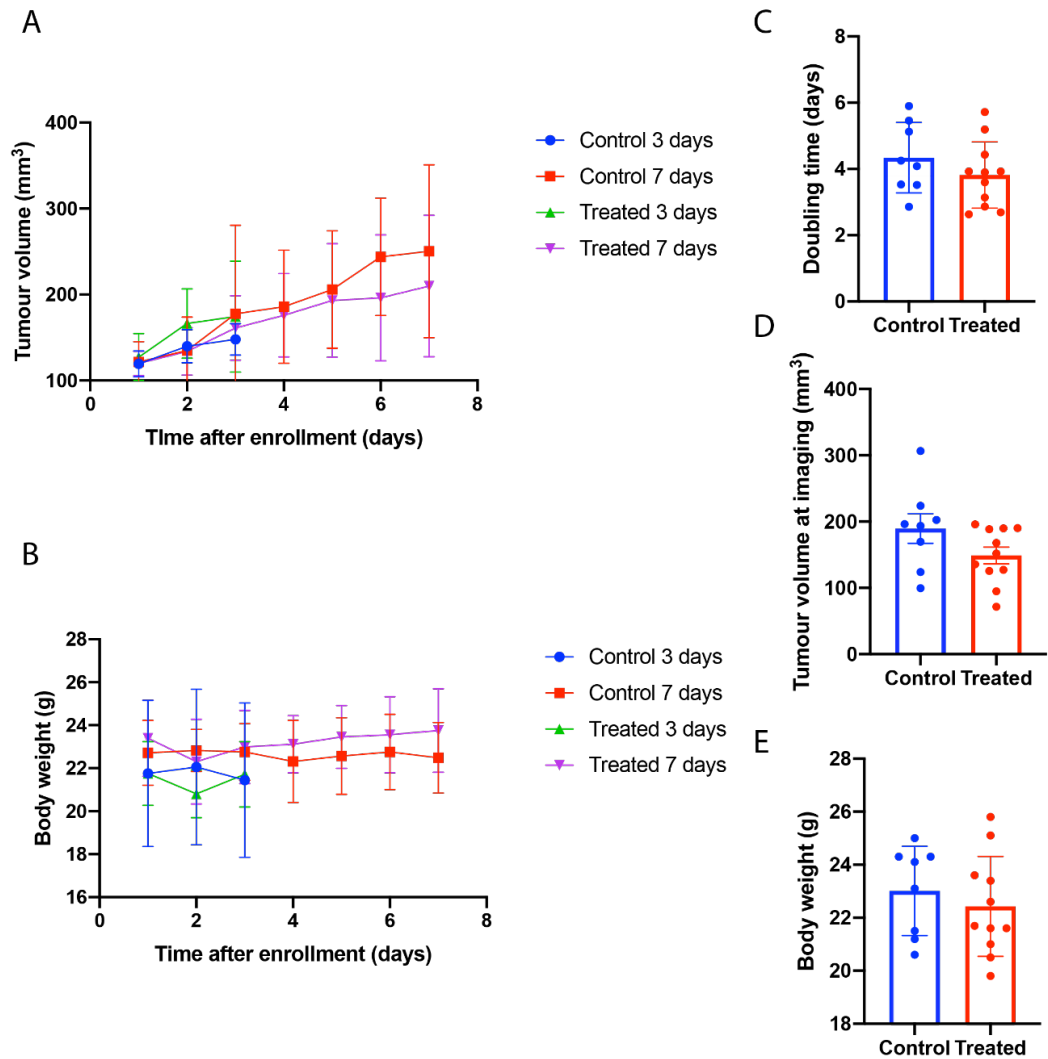


Figure 6.1 Characterisation of LICR-LON-HN5 xenograft growth with atovaquone treatment.

A) Tumour volume after enrolment, in control group for 3 days (n=3), control group for 7 days (n=5), treated for 3 days (n=5), treated for 7 days (n=6). B) Tumour volume doubling times for control and treated groups. C) Tumour volume at the time of MRI of LICR-LON-HN5 xenografts. Tumour volumes were determined using segmentation from ROIs drawn on contiguous T₂-weighted images for each tumour-containing slice using the DICOM image viewer Horus. D) Mouse body weight after enrolment in control group 3 days, control group for 7 days, treated for 3 days, treated for 7 days. E) Mouse bodyweight at time of MRI in control and treated groups. Individual data points, and the group mean \pm 1 s.e.m. are shown.

6.1.2 Histopathological assessment of atovaquone-induced changes in hypoxia

Immunofluorescent staining was performed on sections aligned with the MR imaging plane to assess LICR-LON-HN5 response to atovaquone, using pimonidazole as a fluorescent marker of hypoxia and Hoechst 33342 as a fluorescent marker of perfusion^{6,7} (Figure 6.2).

In accordance with previous results (cf. 4.2.2 and 5.2.2), pimonidazole adduct formation was observed towards the tumour core, whereas Hoechst 33342 uptake was spatially distributed towards the tumour rim (Figure 6.2A). No significant difference in pimonidazole-derived hypoxic fraction (one-way ANOVA, $p=0.17$) (Figure 6.2C) or Hoechst 33342-derived perfused fraction (one-way ANOVA, $p=0.47$) (Figure 6.2D) was found between the different treatment groups, although large intertumoural variability was apparent across both groups.

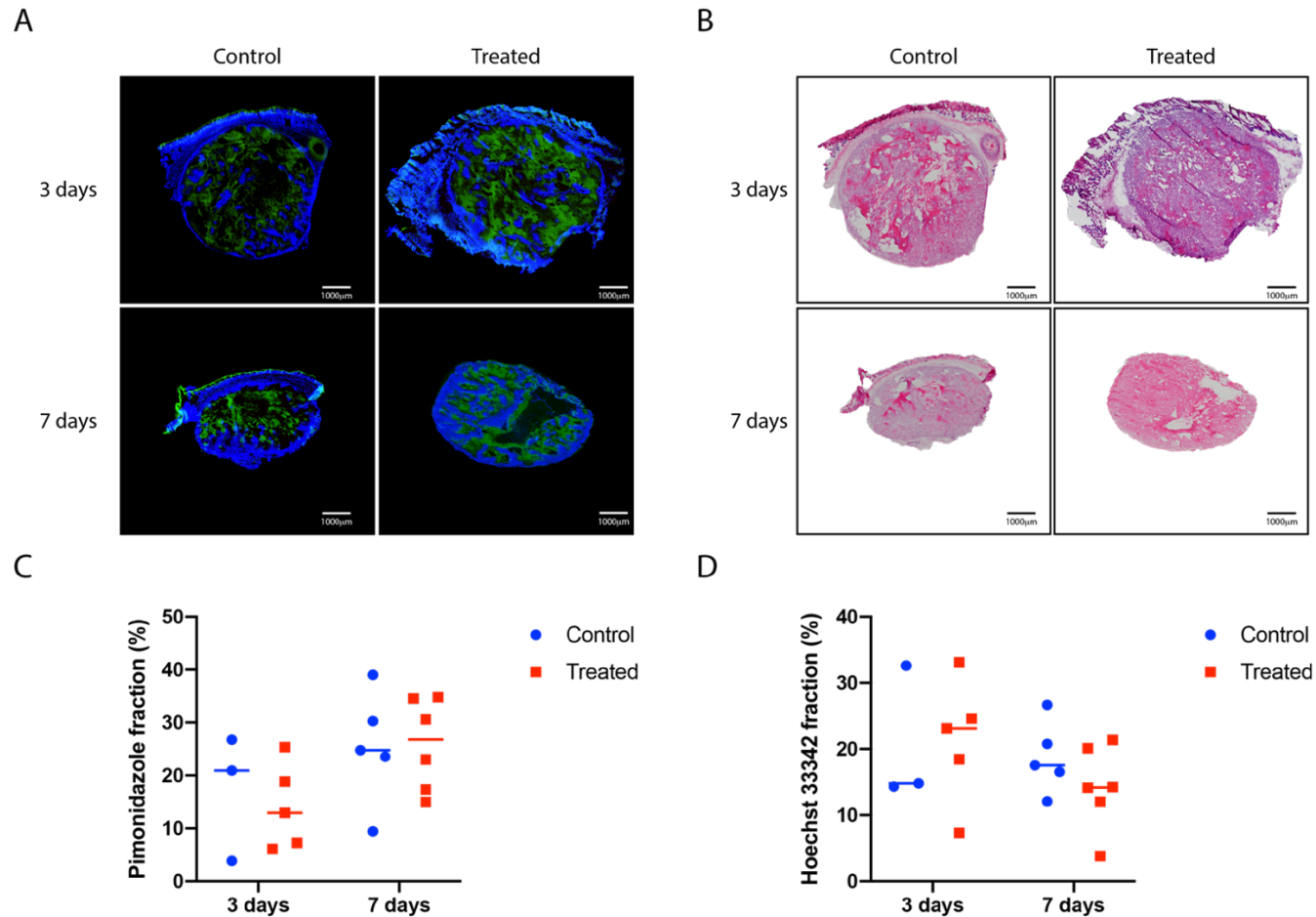


Figure 6.2. Histological characterisation of tumour hypoxia and perfusion.

A) Composite fluorescence images of pimonidazole adducts (green, hypoxia) and Hoechst 33342 uptake (blue, perfusion), and B) bright field images of haematoxylin & eosin staining from representative LICR-LON-HN5 xenografts, treated daily with 50 mg/kg p.o. of atovaquone over 3 days (top right) or 7 days (bottom right), or with water for 3 days (top left) or 7 days (bottom left). Tumour median C) pimonidazole adduct fraction and D) Hoechst 33342 uptake fraction. Individual data points are shown, with bars indicating the group means.

6.1.3 Assessment of atovaquone-induced changes in tumour hypoxia using OE-MRI

Figure 6.3 displays the MRI parametric maps of baseline R_2^* , $\Delta R_2^*_{O_2-air}$, fBV, baseline R_1 , $\Delta R_1_{O_2-air}$, OxyR and pOxyR acquired from a representative LICR-LON-HN5 tumour of the different treatment groups. Also shown are the biomarkers described in 5.2.3.6: OxyR or pOxyR voxels exhibiting a $\Delta R_2^*_{O_2-air}$ greater than -0.5 s^{-1} . LICR-LON-HN5 xenografts presented extensive intratumoral spatial heterogeneity in the different MRI biomarkers, similar to that reported in 4.2.3 and 5.2.3. Neither the administration of atovaquone nor the treatment duration of either 3 or 7 days impacted on the spatial extent or dynamic range of the different MRI parameters studied.

The quantitative analysis of the MRI parameters is summarised in Figure 6.4. Atovaquone did not significantly impact on tumour-wise median values of baseline R_2^* (one-way ANOVA, $p=0.79$) (Figure 6.4A), $\Delta R_2^*_{O_2-air}$ (one-way ANOVA, $p=0.59$) (Figure 6.4B), baseline R_1 (one-way ANOVA, $p=0.93$) (Figure 6.4C), $\Delta R_1_{O_2-air}$ (one-way ANOVA, $p=0.40$) (Figure 6.4D), under hyperoxia. Neither the treatment nor the treatment duration significantly affected the OE-MRI-derived parameters OxyR fraction (one-way ANOVA, $p=0.33$) (Figure 6.4E), pOxyR fraction (one-way ANOVA, $p=0.78$) (Figure 6.4F), OxyE fraction (one-way ANOVA, $p=0.46$) (Figure 6.4G) or pOxyE fraction (one-way ANOVA, $p=0.41$) (Figure 6.4H). Tumour-wise fBV (one-way ANOVA, $p=0.21$) and non-perfused fraction (one-way ANOVA, $p=0.32$) were not significantly different (data not shown).

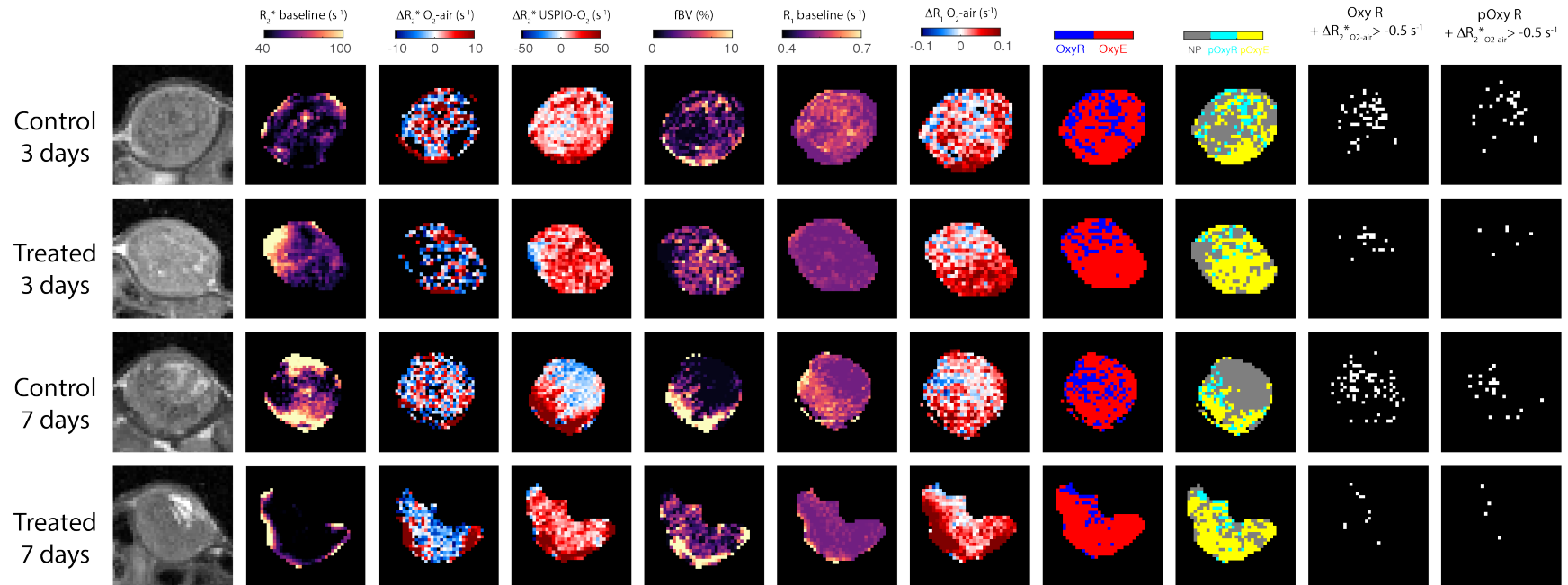


Figure 6.3 Anatomical images and corresponding functional MRI maps of HNSCC xenograft response to atovaquone.

T₂-weighted images of LICR-LON-HN5 xenografts treated daily with either 50mg/kg of atovaquone or water for 3 or 7 days, and the associated parametric maps of baseline R_2^ , $\Delta R_2^*_{O_2-air}$, $\Delta R_2^*_{USPIO-O_2}$, fractional blood volume (fBV), baseline R_1 , $\Delta R_1_{O_2-air}$, oxygen-refractory (OxyR, blue) and oxygen-enhanced (OxyE, red) voxels, perfused oxygen-refractory (pOxyR, cyan) and perfused oxygen-enhanced (pOxyE, yellow) voxels, OxyR voxels presenting a $\Delta R_2^*_{O_2-air}$ greater than $-0.5s^{-1}$, pOxyR voxels exhibiting a $\Delta R_2^*_{O_2-air}$ greater than $-0.5s^{-1}$.*

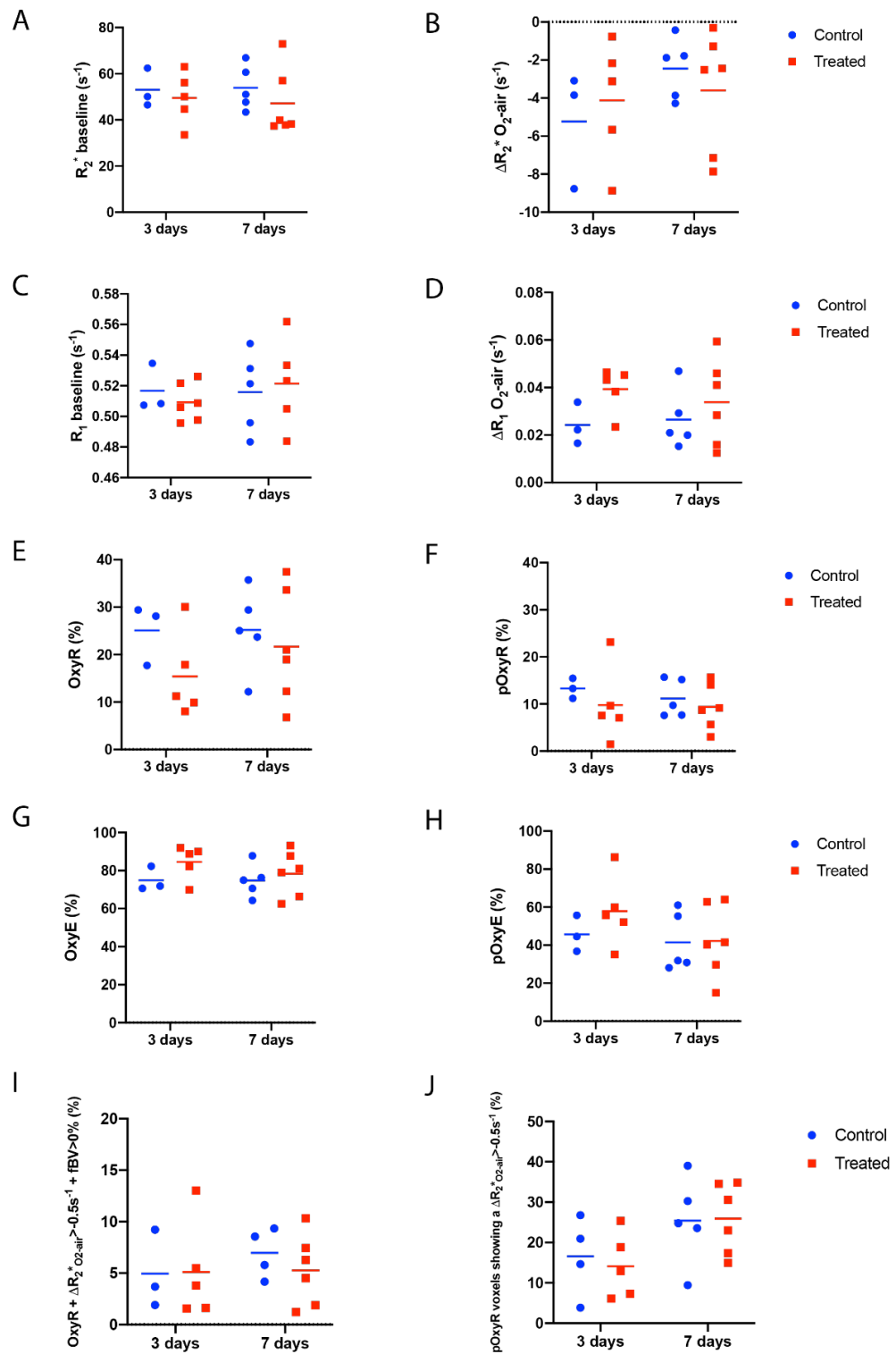


Figure 6.4 Quantitative analysis of LICR-LON-HN5 xenograft response to atovaquone.

LICR-LON-HN5 tumour-wise median values of A) R_2^* baseline, B) $\Delta R_2^*_{O_2-air}$, C) R_1 baseline, D) $\Delta R_1_{O_2-air}$, E) OxyR fraction, F) pOxyR fraction, G) OxyE fraction, H) pOxyE, I) OxyR voxels presenting a $\Delta R_2^*_{O_2-air}$ greater than $-0.5 s^{-1}$, and J) OxyR voxels presenting a $\Delta R_2^*_{O_2-air}$ greater than $-0.5 s^{-1}$ and a positive fBV. Individual data points are shown, with bars indicating the group means.

6.2 Discussion

Atovaquone has been reported to alleviate hypoxia and increase radiosensitivity of FaDu HNSCC, HCT116 colorectal carcinoma spheroids and xenografts, and H1299 lung carcinoma spheroids¹¹³. This chapter presents an evaluation of OE-MRI for the assessment of any atovaquone-induced modification in hypoxia in LICR-LON-HN5 HNSCC xenografts. Application of the different MRI parametric maps and the OE-MRI derived biomarkers described in 5.2.3, as well as histopathology, suggested a lack of any apparent atovaquone-induced modification of hypoxia.

6.2.1 Atovaquone did not inhibit LICR-LON-HN5 tumour growth

Once tumour volume reached 150 mm³, LICR-LON-HN5 xenografts were assigned to the different treatment groups. The study was not randomised in order to ensure even tumour volumes in each group at enrolment. Atovaquone did not significantly inhibit tumour growth, corroborating previous findings on mice bearing FaDu HNSCC and HCT116 colorectal carcinoma xenografts¹¹³.

6.2.2 LICR-LON-HN5 HNSCC xenografts did not respond to atovaquone

In this study, histological analysis showed no change in hypoxia, assessed using pimonidazole adducts. These results differ from those of Ashton *et al* that showed a significant alleviation of hypoxia in FaDu HNSCC and HCT116 colorectal carcinoma xenografts¹¹³. The results herein could be explained by

the metabolic phenotype of the LICR-LON-HN5 model. It is hypothesised that atovaquone, by inhibiting electron chain complex III, increases oxygen accumulation and availability and subsequently inhibits mitochondrial respiration³¹³. The absence of response might be explained by the different level of mitochondrial biogenesis of LICR-LON-HN5 compared to FaDu, another HNSCC line. Glycolysis may be the predominant metabolic pathway in LICR-LON-HN5, and the oxygen-induced shift towards oxidative phosphorylation may not occur in these tumours, regardless of the concentration of excess oxygen. Another explanation could be related to the histological phenotype of the LICR-LON-HN5 tumours, which present differentiated areas in which pimonidazole adducts accumulate, around keratin-pearl-like regions (5.2.2). In this setting, pimonidazole staining may be unrelated to hypoxia, and therefore unsuitable to assess atovaquone-induced hypoxia alleviation. Regardless of keratin pearl formation, well-differentiated HNSCC tumour sub-regions may also lack micro-vessels, similar to the avascular normal squamous epithelium⁸⁵. Therefore, well-differentiated cells may not have been exposed to atovaquone concentrations that are sufficient enough to induce hypoxia relief, unlike the poorly-differentiated and well-vascularised FaDu model which was shown to respond to atovaquone¹¹³. To address this, an investigation on a positive control, such as FaDu 3D spheroids, is required.

6.2.3 OE-MRI did not detect any atovaquone-induced change in hypoxia in LICR-LON-HN5 xenografts

In this study, LICR-LON-HN5 xenografts presented a heterogeneous spatial distribution and quantitative analysis of baseline R_1 , $\Delta R_{1\ O_2\text{-air}}$, baseline R_2^* , $\Delta R_{2^*\ O_2\text{-air}}$, OxyR and pOxyR voxels comparable to the MRI data presented in 4.2.3 and 5.2.3. The absence of any significant differences between treatment groups suggest that, for the treatment durations tested here, LICR-LON-HN5 tumours may be insensitive to atovaquone, or that OE-MRI is not sufficiently sensitive to detect the degree of hypoxia alleviation. The similarity between OxyR and pOxyR results imply that a perfusion readout may be unnecessary in highly hypoxic HNSCC tumours such as the LICR-LON-HN5, as suggested in 5.2.3. The OE-MRI derived biomarker combining OxyR voxels and $\Delta R_{2^*\ O_2\text{-air}}$, proposed in 5.2.3.4, did not identify any significant change between treatment groups. Although maximum efficacy of atovaquone has been demonstrated after 7 days of treatment before²⁷⁴, duration of treatment did not impact on results presented here. A significant decrease in pOxyR volume fraction and a trend towards an increase in pOxyE volume fraction has been observed in Calu6 lung adenocarcinoma xenografts after 7 days of atovaquone treatment²⁷⁴. However, the Calu6 model exhibited a markedly smaller initial fraction of pimonidazole adducts than LICR-LON-HN5²⁴⁰, corroborating the hypothesis that the prevalence of oxidative phosphorylation over glycolysis may enhance the effects of atovaquone treatment.

The main limitation of this study is the lack of positive control to ensure the efficacy of atovaquone to alleviate hypoxia. An *in vitro* experiment using LICR-

LON-HN5 and FaDu HNSCC spheroids cultivated in a hypoxic chamber is needed. The intertumoural variability observed in the different groups could be eliminated by an individual pre-treatment MRI acquisition.

These findings warrant further investigation of the influence of metabolic and structural phenotype on tumour response to atovaquone. A more comprehensive longitudinal study, with pre- and post-treatment MRI and bigger treatment groups, would be more informative.

6.3 Conclusion

In conclusion, a lack of LICR-LON-HN5 HNSCC tumour response to atovaquone was shown. The lack of response may be related to the metabolic and histological phenotype of the hypoxic LICR-LON-HN5 HNSCC model and needs further investigation.

Chapter 7 General discussion

7.1 Summary of main findings

The work reported in this thesis aimed to evaluate MRI biomarkers of hypoxia in HNSCC preclinical models, and to meet the following objectives:

1. To optimise an OE-MRI protocol on a new 7T MRI system;
2. To assess susceptibility MRI-derived putative biomarkers of hypoxia;
3. To evaluate the potential of OE-MRI for imaging and quantifying hypoxia
4. To assess the sensitivity of OE-MRI-derived biomarkers to pharmacologically-induced changes in hypoxia.

In Chapter 3, a novel OE-MRI protocol was developed on a new state-of-the-art Bruker 7T Biospec system. The protocol was designed to incorporate susceptibility MRI within the same imaging session in order to provide accurate and stable measurements of R_1 and R_2^* under air and 100% oxygen breathing, and after intravenous administration of USPIO particles. Once issues around R_1 stability had been resolved, a mask was defined in order to provide more accurate perfusion information.

Chapter 4 focussed on the use of IS and SC-MRI to assess hypoxia in HNSCC xenografts. $\Delta R_2^*_{O_2\text{-air}}$, but not baseline R_2^* , correlated with pimonidazole-derived hypoxic fraction across the HNSCC xenografts investigated. Baseline R_2^* informed on tumour perfusion and vascular architecture, themselves

linked to hypoxia. The identification of tumour voxels non-responsive to hyperoxia may provide useful information on cycling hypoxia.

In Chapter 5, OE-MRI was successfully performed in HNSCC xenografts. OxyR voxels accurately identified and informed on the extent of tumour hypoxia. Thresholding the OxyR data with a perfusion mask may not be necessary to identify poorly oxygenated regions in tumours exhibiting a strong hypoxic phenotype, such as HNSCC. Pimonidazole staining was positive in keratinised areas of the tumours, which may be due to either non-specific staining, or to the potential relationship of hypoxia with differentiation. This needs to be investigated further.

Chapter 6 described an evaluation of the effects of atovaquone on alleviating tumour hypoxia using OE-MRI. A lack of change in pOxyR fraction was observed after 3 or 7 days of atovaquone treatment.

7.2 OE-MRI for detecting and imaging hypoxia

7.2.1 Novelty of the OE-MRI protocol

This research identified histologically validated hypoxia biomarkers using OE-MRI in HNSCC xenografts. To my knowledge, this work is the first pre-clinical evaluation of OE-MRI for the assessment of hypoxia in HNSCC. The technique is robust, stable, and its relatively short acquisition time allows the incorporation of susceptibility MRI measurements in the same imaging session. SC-MRI using USPIO particles as a contrast agent provided important sensitive and specific information about perfusion, compared to

gadolinium-based contrast agents.

The LICR-LON-HN6 HNSCC model, studied *in vivo* for the first time, was found to be less hypoxic by histology and IS-MRI than the other three HNSCC models studied, and similar to the 766-O-R RCA model. The LICR-LON-HN6 model may thus provide a useful comparator for future investigations of hypoxia assessment and evaluation of response to therapy, including radiation and/or hypoxia-alleviation novel strategies.

7.2.2 Advantages and limitations of OE-MRI

7.2.2.1 R_1 measurements

An IR-TrueFISP sequence was used in this work for its high accuracy in quantifying R_1 from a single central slice, and provides good signal to noise. Its inherent flow compensated property could negate any R_1 changes associated with putative vasoconstrictive effects of breathing 100% oxygen³¹⁴. However, as described in Chapter 3, the IR-TrueFISP sequence relies on good field homogeneity and frequency, and a robust flip angle²⁶³. Others have used a variable flip angle (VFA) spoiled gradient echo (SGRE) sequence for determination of R_1 , enabling multi-slice acquisitions for larger/whole tumour coverage^{224,240,244}. The SGRE sequence relies on the acquisition of a minimum of two datasets with different flip angles, with R_1 quantified from the contrast difference³¹⁵. The acquisition time is faster than IR-TrueFISP, thus allowing the imaging of whole organs in less than a minute. Moreover, this sequence is widely used in the clinic for DCE MRI-derived R_1 calculations. However, the range of accurate R_1 measurements is limited if only two flip angles are used, and image quality can suffer from patient motion³¹⁶.

7.2.2.2 SC-MRI using USPIO particles

A novelty of the OE-MRI method used herein is the adoption of intravenously administered USPIO particles to assess tumour perfusion using SC-MRI. DCE-MRI using low molecular weight gadolinium-based contrast agents, e.g. gadolinium-diethylenetriamine penta-acetic acid (Gd-DTPA), is the most widely used approach for imaging tumour perfusion, and has been used in conjunction with OE-MRI to identify non-perfused hypoxic regions. However, low molecular weight gadolinium chelates diffuse passively out of the vascular compartment, thereby informing on both perfusion and vessel permeability³⁰⁶. Radiation-induced increased vascular permeability³¹⁷ may potentially impact on the interpretation of Gd-DTPA uptake, and hence the use of OE-MRI thresholded with a Gd-based perfusion mask to assess response to radiotherapy is questionable.

Another MRI technique to assess tumour perfusion is dynamic susceptibility contrast-MRI (DSC-MRI). Based on the rapid acquisition T_2^* measurements made during the first circulatory pass of an intravenously administered gadolinium-based contrast agent, DSC-MRI informs on perfusion parameters such as relative blood volume, mean transit time and wash-out. Although mainly used in brain, DSC-MRI has been used to distinguish malignant from benign tumours, recurrent tumours from post-radiation changes, as well as different pathological subtypes in HNC patients^{318–320}. DSC image acquisition is rapid (seconds), allowing time to image several slices for greater anatomical coverage. However, DSC-MRI is challenging to perform in mice, as the gradient duty cycle typically available on dedicated preclinical scanners precludes sufficient temporal resolution to detect a first pass transient in the

face of such rapid blood circulation. In the clinic, DSC-MRI also has limitations^{321,322}. The extravasation of a gadolinium-based contrast agent requires leakage corrections, which are not standardised. Compared to the MGE sequence used for SC-MRI, the echo planar imaging (EPI) sequence used to acquire DSC-MRI images is more sensitive to susceptibility artefacts, prevalent in the head and neck region (breathing, swallowing or involuntary movements, air-tissue interface). Other factors, such as blood flow rate and size of the extracellular compartment, can affect the reliability of DSC-MRI measurements. HNSCC, less perfused than other histological subtypes of HNC, showed a lower DSC signal drop. The low contrast, associated with a low spatial resolution, induce partial volume effect that could affect the estimation of blood volume³¹⁹.

DCE-MRI and DSC-MRI could help distinguishing between perfused and non-perfused voxels, but accurate quantification of blood volume is limited^{321–323}. Moreover, the safety of gadolinium-based contrast agents remains a concern. For example, gadolinium uptake causes nephrogenic systemic fibrosis in patients with renal insufficiency^{324,325} and its deposition in brain structures has been recently reported³²⁶.

Alternatively, USPIO particles, due to their large molecular size (typically 20–30 nm in diameter), remain in the vascular compartment at a steady concentration, with a circulating half-life of 14 hours in humans, against 2 hours for gadolinium^{327,328}. The long intravascular half-life of USPIO particles enables the acquisition of steady-state, high-resolution measurements of R_2^* . The USPIO-induced change in R_2^* can be used to quantify fBV, a more sensitive and specific biomarker of functional tumour vasculature²⁷⁹.

The clinical development of the USPIO particle preparation P904 used herein has been halted. However, the aim is to transition to using ferumoxytol, indicated for the treatment of iron deficiency anaemia in adult patients with chronic kidney disease, but which is being used off-label as a safe USPIO particle contrast for MRI. Ferumoxytol is being increasingly used for clinical MRI investigations in both adults and children, and in drug trials^{212,329,330}.

As a prelude, a preliminary SC-MRI feasibility study using ferumoxytol was performed in mice bearing subcutaneous SW1222 colorectal xenografts by Dr Jessica Boulton (Figure 7.1). The mouse kidney fBV of ~26% was similar to that reported in the literature³³¹, and SC-MRI repeated 24 hours later showed no elevated baseline R_2^* values, suggesting renal clearance of ferumoxytol (data not shown). An fBV of ~9% was determined in the SW122 tumour, which is in excellent agreement with data from a previous study using the USPIO particle preparation ferumoxtran²⁰⁰.

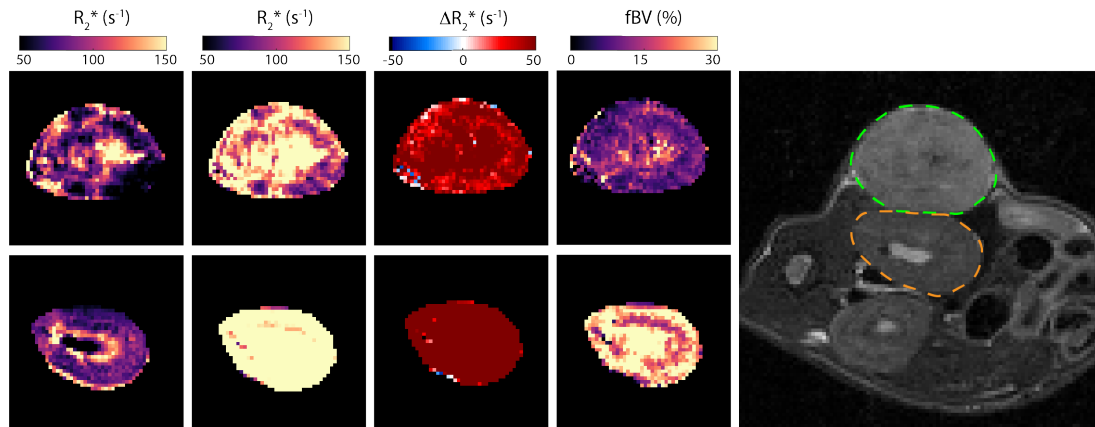


Figure 7.1 SC-MRI study using ferumoxytol of a mouse bearing a subcutaneous SW1222 colorectal xenograft using ferumoxytol. Tumour (top row) and kidney (bottom) parametric maps, with tissue/organ delineation shown on the T_2 -weighted image (right). Preliminary feasibility study by Dr Jessica Boulton.

7.2.3 Histological validation of MRI biomarkers

Imaging biomarkers require stringent validation through establishing imaging-pathology correlation before translation to the clinic.

Producing good-quality, co-registered histopathological images from frozen tissue sections cut from the HNSCC xenografts for validation of the MRI data proved challenging. Although they can be easily identified and excluded from the MRI image analysis, the presence of large acellular cysts, common in the Cal^S and Cal^R tumour models, affected the integrity of the tumour structure for histological processing. Consequently, the alignment with MRI images was difficult. Rapid freezing of tissue was used to allow staining and fluorescence detection of pimonidazole adducts and Hoechst 33342 on the same section, enabling an assessment of the extent, distribution and relationship of hypoxia and perfused tumour vasculature. The formalin fixation and paraffin embedding technique, for which chromogenic pimonidazole staining is possible, could provide more intact tissue. In order to perform good quality

pimonidazole and H&E staining on both frozen and FFPE sections, tumours were cut in half, which may have altered tissue integrity. This step may have been done after fixation but would require care to identify the imaging slice. Tissue perfusion with fixative could be performed to ensure structural integrity. Immunohistochemical detection of a pan-endothelial marker such as CD34 could be used as an alternative histological marker of tumour vasculature, although it does not inform on the perfusion status of vessels in the same way as Hoechst 33342³³². Other HNSCC tumourigenic HNSCC cell lines, such as FaDu, may prove easier to work with in this regard²⁵³.

Accurate comparison of MRI and histological images was limited by the difference in slice or section thickness. The spatially heterogeneous characteristics highlighted on a 1mm MRI slice will differ from a 10 μ m histological frozen tissue section. Recent computational approaches using machine learning could help ensure the accurate registration between the MRI parametric maps and the histological tumour sections. They rely on the resizing of digitised whole-slide histological images to match the resolution of the MRI data and to identify characteristic landmarks on the anatomical T₂-weighted images, such as tumour shape, orientation or position, ensuring an accurate alignment with the MRI images^{277(p)}.

The studies covered in this thesis also suggest that the degree of keratinisation in HNC models could affect quantification of reduced 2-nitroimidazole adducts. The link between keratinisation and hypoxia is still vague. However, hypoxia is known to inhibit cancer cell differentiation and promoting cancer stem cells³⁰⁰. The implication for the clinic is unclear, but it is interesting to note that keratinised, well- differentiated head and neck

tumours have been found to be more radioresistant than poorly differentiated lesions³³³.

7.2.4 Clinical translation of OE-MRI

Currently, there is a lack of routinely used imaging biomarkers of hypoxia in the clinic. The development of OE-MRI in the clinic would enable the assessment of hypoxia as an entry criterion for clinical trials involving hypoxia alleviation, and patient stratification for treatment.

OE-MRI can be easily translated onto conventional clinical scanners. Oxygen breathing is a standard intervention in emergency medicine, therefore its approval for routine clinical use is straightforward. Moreover, the rapid tumour response to oxygen breathing and the relatively short acquisition time make OE-MRI attractive for the clinic. OE-MRI has been successfully implemented on a clinical 3T MRI scanner at the Royal Marsden Hospital (RMH), and 10 healthy volunteers and 3 patients with histologically confirmed advanced HNC were imaged (Figure 7.2). R_1 measurements were stable and repeatable, and showed a significant lack of response to hyperoxia in lymph node metastases of HNC patients compared to the lymph nodes of healthy volunteers²⁴⁴. DCE-MRI derived initial area under the gadolinium curve at 60 seconds (IAUGC₆₀) biomarker provided information on tumour perfusion, to subsequently determine the pOxyR fraction. The feasibility of OE-MRI in the clinic has also been demonstrated in other cancer types. Five patients with histologically proven glioblastoma multiforme showed a heterogeneous R_1 response to 100% oxygen challenge, comparable to pimonidazole-confirmed preclinical data acquired from U87MG human glioma xenografts¹⁸⁵. A relationship

between pOxyR fraction and Glut-1 hypoxia score was shown in eight patients with renal cell carcinoma²²⁴. OE-MRI was successfully performed on ten men with biopsy confirmed prostate cancer³¹². Perfused OxyR voxels detected radiotherapy-induced reduction of hypoxia in non-small cell lung cancer patients²⁴⁰. Positive response to chemoradiotherapy was detected by an increase in T_1 in anal squamous cell carcinoma patients²⁴⁵.

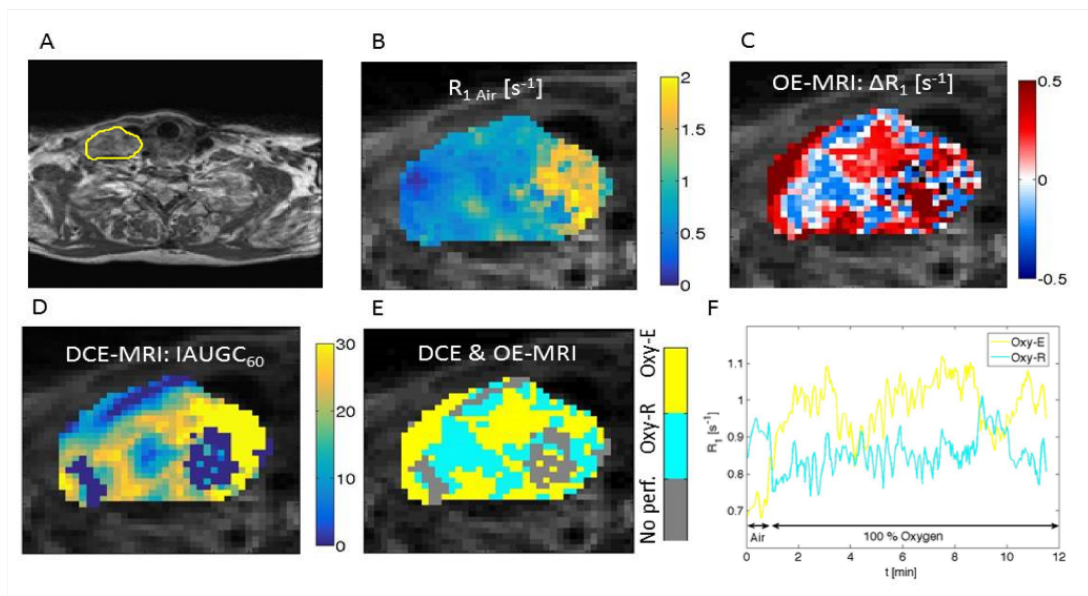


Figure 7.2 MRI parametric maps of a representative advanced HNC patient. A) T_2 -weighted axial anatomical image of the HNC lymph node metastasis (delineated in yellow). B) Baseline R_1 , C) ΔR_1 , D) DCE-MRI derived $IAUGC_{60}$ and E) pOxyR parametric maps from the tumour. F) Temporal R_1 response to hyperoxic (100% O_2) challenge. Taken from Panek et al., 2018²⁴⁴.

7.3 OE-MRI applications for therapy

7.3.1 OE-MRI as a predictive imaging tool for tumour response to therapy

As a prelude to investigating the predictive aspect of OE-MRI, a preliminary *in vitro* study was conducted using the LICR-LON-HN5 and LICR-LON-HN6 cell lines to help inform on an optimal radiation dose to cause growth control in HNSCC tumours *in vivo* (Figure 7.3). To mimic oxygen, nutrient and proliferation gradients present *in vivo*, 3D spheroids of each cell line were generated. Spheroid response to radiation, administered using a small animal radiation research platform (SARRP, xStrahl), was evaluated by monitoring spheroid volume and assessing cell viability at the end of the experiment. Spheroid segmentation and volume calculation was performed by an experienced operator, Dr Carol Box. LICR-LON-HN5 spheroid morphology was characterized by a grape-like aspect with cell clusters on the rims, whereas LICR-LON-HN6 spheroid shape was regular with well-defined rims. LICR-LON-HN5 spheroid volumes remained stable after irradiation, but a non-significant growth delay was apparent 20 days after irradiation with single doses equal to or greater than 6 Gy, consistent with a previous study²⁷³. A marked decrease in cell viability was also detected at these doses. LICR-LON-HN6 spheroids showed a volume decrease 12 days after single doses equal to or greater than 6 Gy. Radiosensitivity of LICR-LON-HN5 spheroids, based on the assessment of cell viability using CTG®, was greater, although not significant, than LICR-LON-HN6. However, response to radiotherapy depends on cell cycle status, growth and death rates³³⁴. Whilst viability decreased at

doses higher than 6 Gy, the LICR-LON-HN5 spheroid volume remained stable, possibly due to the retention of non viable cells, whereas the LICR-LON-HN6 spheroids shrank, indicating detachment of dead cells. Extrapolation of this data to *in vivo* models, however, remains complex as aspects of the tumour microenvironment, such as the vasculature which plays an important role in radioresponse, are not represented in the tumour spheroid model. The prognostic efficacy of OE-MRI was assessed for the response of R3327-AT1 rat prostate tumours to hypofractionated radiation, and validated by histology using pimonidazole and CCI-103F hypoxia markers. An increased $\Delta R_{1\ O_2\text{-air}}$ between baseline and one week later was associated with a positive response to radiation ²⁴¹.

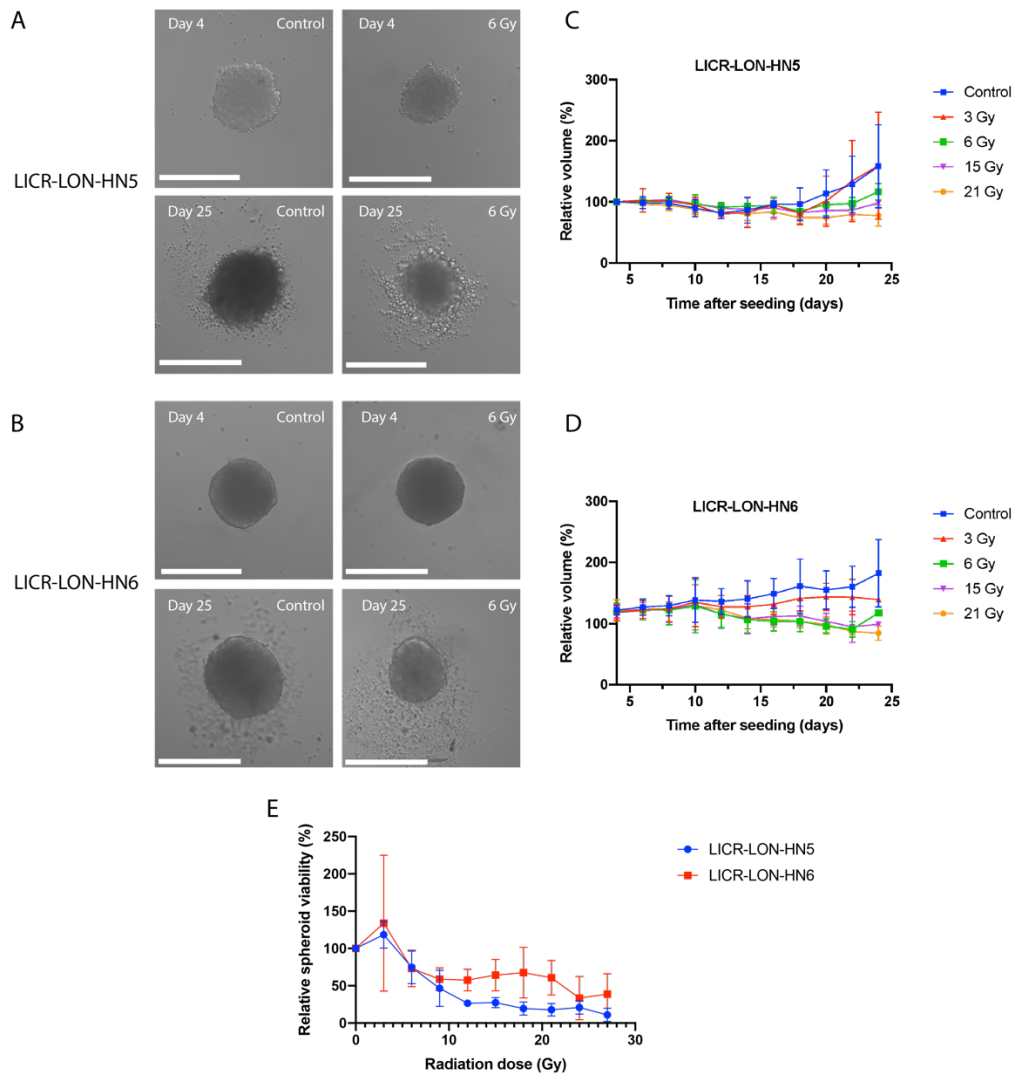


Figure 7.3 LICR-LON-HN5 and LICR-LON-HN6 spheroid response to radiotherapy.

Microscopy images of representative A) LICR-LON-HN5 and B) LICR-LON-HN6 spheroids. Scale bars are 500 μm . Growth curves show irradiated spheroid volumes normalised to the volume at the start of treatment (day 4 post-seeding) of C) LICR-LON-HN5 and D) LICR-LON-HN6 cell lines. E) Spheroid viability measured by CellTiterGlo[®] assay 24 days after irradiation. Luminescence values for irradiated spheroids were normalised to those of control, non-treated spheroids. Each data point is a mean of 3-6 spheroids and results are representative of $n=3$ repeat experiments.

7.3.2 OE-MRI for monitoring tumour response to pharmacological modification of hypoxia

In this study, the sensitivity of OE-MRI to the hypoxia-alleviating drug atovaquone was assessed in LICR-LON-HN5 xenografts. No significant difference was found between groups treated for 3 or 7 days and controls. In retrospect, the efficacy of atovaquone should have been tested prior to *in vivo* MRI. This could have been done using LICR-LON-HN5 3D spheroids which develop a hypoxic core after approximately 25 days in culture, as assessed by pimonidazole staining³³⁵. The metabolic biogenesis of this cell line should also be investigated prior to any treatment experiment as the response to atovaquone may be cell line-dependent. Conversely, FaDu HNSCC spheroids displayed an atovaquone-induced decrease in hypoxia¹¹³. Differentiation may affect response to atovaquone as, unlike LICR-LON-HN5, FaDu is a poorly differentiated HNSCC cell line^{85,255}. Moreover, an individual pre-treatment MRI acquisition would remove any intertumoural variability that might affect the results. Although a significant effect of atovaquone has been shown in renal carcinoma models as early as 24 hours²⁷⁴, atovaquone may alleviate hypoxia in HNSCC on a longer timeframe.

OE-MRI has been used pre-clinically to monitor the response of Calu6 NSCLC and U87 glioma xenograft tumours, and clinically in NSCLC patients, to a single fraction of 10Gy radiation and fractionated chemoradiotherapy respectively²⁴⁰. OE-MRI detected a decrease in pOxyR fraction in both xenografts and in the patient tumours, confirmed by pimonidazole staining. OE-MRI also mapped and quantified Calu6 xenograft response to the

hypoxia-modifying treatments banoxantrone and atovaquone²⁷⁴. The OE-MRI data was consistent with the known mechanism of action of these drugs: the hypoxia-activated cytotoxic prodrug banoxantrone specifically targeted hypoxic regions, resulting in a decrease in pOxyR voxels and an increase in non-perfused voxels. The electron transport chain complex III-inhibitor drug atovaquone improved oxygen availability, verified by a decrease in pOxyR and an increase in pOxyE voxels.

7.4 Future work

7.4.1 Validation of OE-MRI biomarkers for hypoxia

Further studies are needed to evaluate OE-MRI in other tumour types in which hypoxia is known to adversely affect patient prognosis. A body of evidence indicates that hypoxia plays an important role in treatment resistance and poor prognosis in paediatric rhabdomyosarcoma, the most common soft tissue sarcoma in childhood and adolescence³³⁶. OE-MRI studies have been initiated using RH41 RMS xenografts. A substantial proportion of pOxyR voxels and pimonidazole adducts have been identified (Figure 7.4), making the RH41 a suitable model in which to evaluate hypoxia in RMS using OE-MRI.

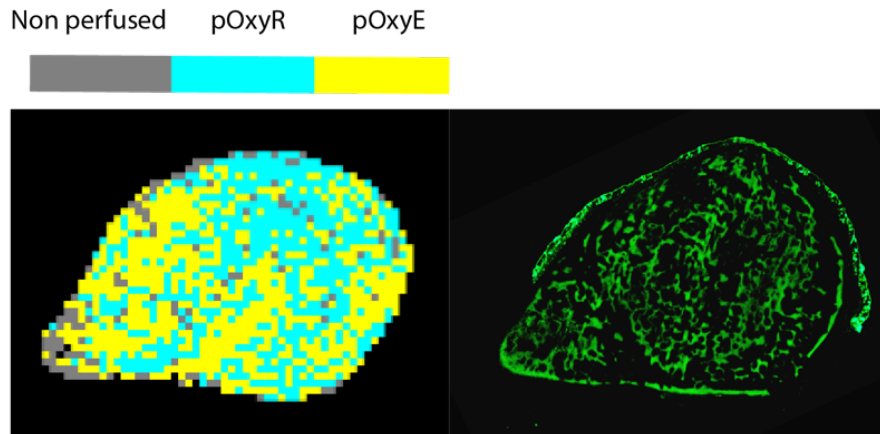


Figure 7.4 OE-MRI investigation of an RH41 rhabdomyosarcoma xenograft. *pOxyR* parametric map (left) and pimonidazole adduct image (right). Investigation conducted by Dr Jessica Boulton.

7.4.2 OE-MRI biomarkers for prediction and monitoring of tumour response

7.4.2.1 Radiotherapy

A logical extension of this work is the evaluation of OxyR and pOxyR markers to predict tumour response to radiation. After assessment of hypoxia by OE-MRI, LICR-LON-HN5 xenograft tumours will be treated on the SARRP with a single radiation dose of ~6 Gy, based on the preliminary work *in vitro* presented in section 7.3.1. The acquisition of R_1 data may need optimisation to provide whole tumour coverage and fast acquisition, through the use of VFA-SGRE pulse sequence instead of IR-TrueFISP.

Another application of OE-MRI is the targeting of hypoxic sub-regions with increased radiation doses. This experiment requires great optimisation. Dose calculation models for the SARRP have only been verified for whole tumours. Therefore adequate achievable accuracy must be sought using small

collimators³³⁷. Fast image registration and segmentation algorithms, as well as MRI data transfer and incorporation into the SARRP radiation planning software must be developed.

For both experiments, a holding bed for safe transport of an anaesthetised mouse without any position change must be designed for use with both instruments, in order to ensure an accurate registration of both MRI and SARRP³³⁸. An ideal solution to this issue would be the development of a preclinical hybrid MR-SARRP system, similar to the clinical magnetic resonance- linear accelerator (MR-LINAC) system introduced recently³³⁹.

Tumour response will subsequently be monitored by anatomical T₂-weighted MRI for tumour volume and growth delay, DW-MRI for cell viability (DW-MRI), and OE-MRI for hypoxia. *Ex vivo* immunohistochemistry will also be performed for necrosis (H&E staining), hypoxia (pimonidazole) and DNA damage (e.g. γ H2AX).

7.4.2.2 Pharmacological modification of hypoxia

Optimisation of the atovaquone protocol is needed to ensure drug delivery. The LICR-LON-HN5 model chosen for the experiment may not be adequate to evaluate the sensitivity of OE-MRI to detect response to hypoxia modification, as it may not respond to atovaquone-induced decrease in OCR, despite its hypoxic phenotype. Alternatively, other OCR modifying drugs, such as metformin or ITPP, could be tested. Insulin and NS-398 have also been found to decrease oxygen consumption in FSall fibrosarcoma xenografts^{119,340,341}. If the effects on hypoxia are demonstrated, a combination

of radiation and hypoxia- sensitisers could potentially be performed and evaluated by OE-MRI.

7.5 Conclusion

To conclude, this work describes the development and evaluation of OE-MRI derived biomarkers for imaging hypoxia in HNSCC xenograft models. OE-MRI derived OxyR fraction revealed the hypoxic phenotype of HNSCC xenografts. USPIO contrast agent provided an accurate evaluation of perfusion. Biomarkers based on combined OE- and susceptibility- MRI can inform on different but complementary underlying biology of hypoxia in HNSCC xenografts.

OE-MRI can identify and quantify hypoxia in HNSCC tumours and could provide a cost- effective, easily translatable imaging tool for patient stratification and treatment management. Further work is needed to ensure clinical translation and utility for therapy for patient benefit.

1. Integrity of the cell lines used in this thesis

	TH01	D21S11	D5S818	D13S317	D7S820	D16S539	CSF1PO	AMEL	TPOX
Cal ^S	6, 9.3	28, 29	11, 12	10, 11	10	11, 12	10, 12	X	8
Cal ^R	6, 9.3	28, 29	11, 12	10, 11	10	11, 12	10, 12	X	8
LICR- LON- HN5	9.3	28, 31.2	13	11	11	11, 13	11, 13	X	8
LICR- LON-HN6	6,9	29,31	11,12	9,14	10,11	8,12	11,13	X	8
786-O-R	6, 9.3	29, 30	9	8	11, 12	12	10	X	8
Positive control	6, 9.3	29, 31.2	12	9, 11	8, 11	9, 13	12	X, Y	8

Table 1-1 STR profile of the different cell lines studied in this thesis.

Allelic ladder: good. Negative control: good.

2. Determination of tumour volume and delineation

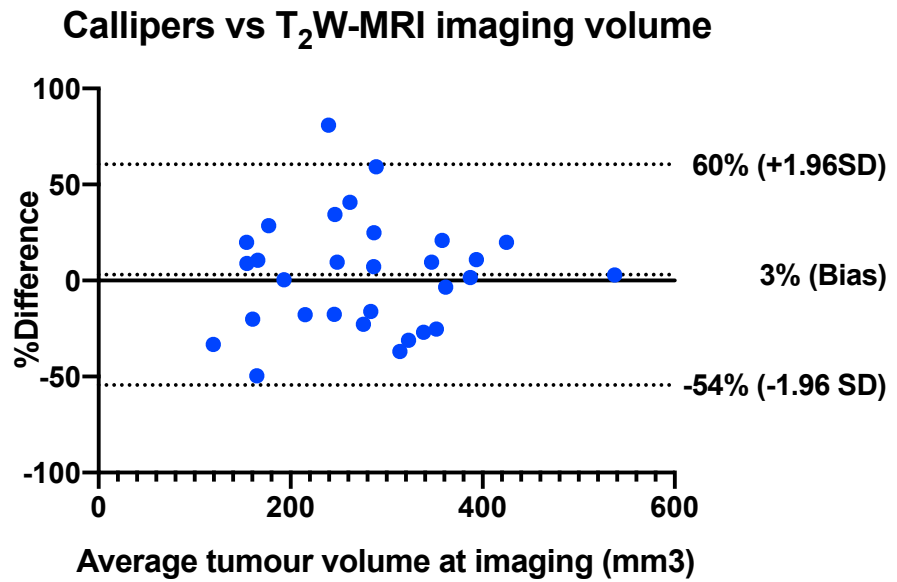


Figure 2-1 Comparison of tumour volume assessment methods. Bland-Altman showing the difference of tumour volume at imaging calculated from the tumour diameter measured using callipers and T₂-weighted MR images.

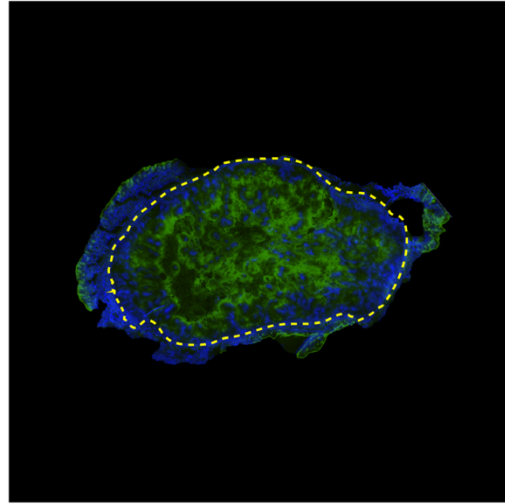


Figure 2-2 Example of tumour delineation on histological sections.
An ROI was delineated over the H&E image (yellow dashed line). Overlying skin, which was kept attached to the tumour to facilitate slide orientation, was excluded from analysis.

3. Other examples of MRI parametric maps

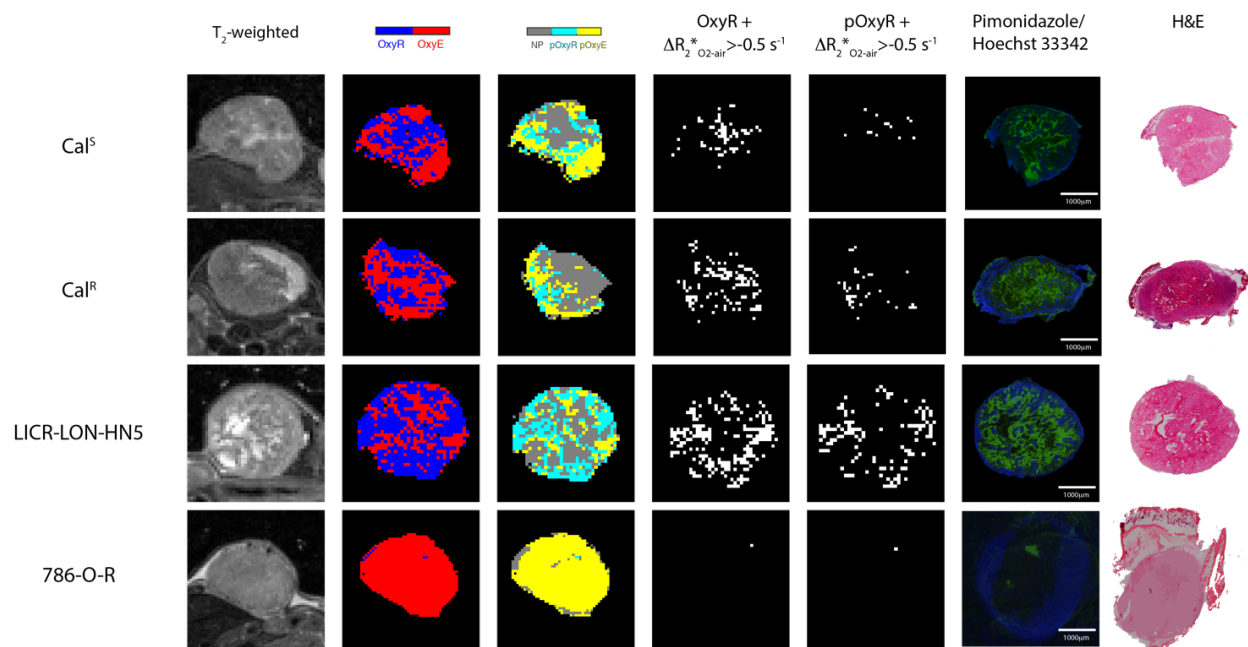


Figure 3-1 Examples of anatomical and functional imaging data obtained using OE-MRI.

T_2 -weighted anatomical images and the associated parametric maps of oxygen-refractory (OxyR, blue) and oxygen-enhanced (OxyE, red) voxels, perfused oxygen-refractory (pOxyR, cyan), oxygen-enhanced (pOxyE, yellow) voxels and non-perfused (NP, grey) voxels, OxyR voxels exhibiting a $\Delta R_{2}^{*O_2-air} > -0.5 \text{ s}^{-1}$, pOxyR voxels exhibiting a $\Delta R_{2}^{*O_2-air} > -0.5 \text{ s}^{-1}$, composite fluorescence images of pimonidazole adducts (green, hypoxia) and Hoechst 33342 uptake (blue, perfusion) (scale bar = 1mm), from representative Cal^S, Cal^R, LICR-LON-HN5 and 786-O-R (RCA) xenograft tumours.

Bibliography

1. Bray F, Ferlay J, Soerjomataram I, Siegel RL, Torre LA, Jemal A. Global cancer statistics 2018: GLOBOCAN estimates of incidence and mortality worldwide for 36 cancers in 185 countries. *CA Cancer J Clin*. 2018;68(6):394-424. doi:10.3322/caac.21492
2. Head and neck cancers mortality statistics. Cancer Research UK. Published February 8, 2017. Accessed August 5, 2020. <https://www.cancerresearchuk.org/health-professional/cancer-statistics/statistics-by-cancer-type/head-and-neck-cancers/mortality>
3. Head and neck cancers incidence statistics. Cancer Research UK. Published February 8, 2017. Accessed August 5, 2020. <https://www.cancerresearchuk.org/health-professional/cancer-statistics/statistics-by-cancer-type/head-and-neck-cancers/incidence>
4. Mello FW, Melo G, Pasetto JJ, Silva CAB, Warnakulasuriya S, Rivero ERC. The synergistic effect of tobacco and alcohol consumption on oral squamous cell carcinoma: a systematic review and meta-analysis. *Clin Oral Investig*. 2019;23(7):2849-2859. doi:10.1007/s00784-019-02958-1
5. Göttgens E-L, Ostheimer C, Span PN, Bussink J, Hammond EM. HPV, hypoxia and radiation response in head and neck cancer. *Br J Radiol*. 2018;92(1093):20180047. doi:10.1259/bjr.20180047
6. Gillison ML, Koch WM, Capone RB, et al. Evidence for a Causal Association Between Human Papillomavirus and a Subset of Head and Neck Cancers. *JNCI J Natl Cancer Inst*. 2000;92(9):709-720. doi:10.1093/jnci/92.9.709
7. Hashibe M, Brennan P, Chuang S, et al. Interaction between Tobacco and Alcohol Use and the Risk of Head and Neck Cancer: Pooled Analysis in the International Head and Neck Cancer Epidemiology Consortium. *Cancer Epidemiol Prev Biomark*. 2009;18(2):541-550. doi:10.1158/1055-9965.EPI-08-0347
8. Licitra L, Perrone F, Bossi P, et al. High-risk human papillomavirus affects prognosis in patients with surgically treated oropharyngeal squamous cell carcinoma. *J Clin Oncol*. 2006;24(36):5630-5636.
9. Lassen P, Eriksen JG, Hamilton-Dutoit S, Tramm T, Alsner J, Overgaard J. HPV-associated p16-expression and response to hypoxic modification of radiotherapy in head and neck cancer. *Radiother Oncol*. 2010;94(1):30-35. doi:10.1016/j.radonc.2009.10.008
10. Fakhry C, Westra WH, Li S, et al. Improved Survival of Patients With Human Papillomavirus–Positive Head and Neck Squamous Cell

Carcinoma in a Prospective Clinical Trial. *JNCI J Natl Cancer Inst.* 2008;100(4):261-269. doi:10.1093/jnci/djn011

11. Nijkamp MM, Span PN, Bussink J, Kaanders JHAM. Interaction of EGFR with the tumour microenvironment: Implications for radiation treatment. *Radiother Oncol.* 2013;108(1):17-23. doi:10.1016/j.radonc.2013.05.006
12. O-charoenrat P, Rhys-Evans PH, Archer DJ, Eccles SA. C-erbB receptors in squamous cell carcinomas of the head and neck: clinical significance and correlation with matrix metalloproteinases and vascular endothelial growth factors. *Oral Oncol.* 2002;38(1):73-80. doi:10.1016/S1368-8375(01)00029-X
13. Box C, Zimmermann M, Eccles S. Molecular markers of response and resistance to EGFR inhibitors in head and neck cancers. *Front Biosci.* 2013;18:520-542.
14. Sacco AG, Cohen EE. Current Treatment Options for Recurrent or Metastatic Head and Neck Squamous Cell Carcinoma. *J Clin Oncol.* 2015;33(29):3305–3313. doi:10.1200/jco.2015.62.0963
15. Marur S, Forastiere AA. Head and Neck Squamous Cell Carcinoma: Update on Epidemiology, Diagnosis, and Treatment. *Mayo Clin Proc.* 2016;91(3):386-396. doi:10.1016/j.mayocp.2015.12.017
16. Vaupel P, Mayer A. Hypoxia in cancer: significance and impact on clinical outcome. *Cancer Metastasis Rev.* 2007;26(2):225–239. doi:10.1007/s10555-007-9055-1
17. Nordsmark M, Bentzen SM, Rudat V, et al. Prognostic value of tumor oxygenation in 397 head and neck tumors after primary radiation therapy. An international multi-center study. *Radiother Oncol.* 2005;77(1):18-24. doi:http://dx.doi.org/10.1016/j.radonc.2005.06.038
18. Brizel DM, Sibley GS, Prosnitz LR, Scher RL, Dewhirst MW. Tumor hypoxia adversely affects the prognosis of carcinoma of the head and neck. *Int J Radiat Oncol.* 1997;38(2):285-289. doi:http://dx.doi.org/10.1016/S0360-3016(97)00101-6
19. Kaanders JHAM, Wijffels KIEM, Marres HAM, et al. Pimonidazole binding and tumor vascularity predict for treatment outcome in head and neck cancer. *Cancer Res.* 2002;62(23):7066–7074.
20. Höckel M, Schlenger K, Aral B, Mitze M, Schäffer U, Vaupel P. Association between Tumor Hypoxia and Malignant Progression in Advanced Cancer of the Uterine Cervix. *Cancer Res.* 1996;56(19):4509-4515.
21. Brizel DM, Scully SP, Harrelson JM, et al. Tumor oxygenation predicts for the likelihood of distant metastases in human soft tissue sarcoma. *Cancer Res.* 1996;56(5):941–943.

22. Hale LP, Braun RD, Gwinn WM, Greer PK, Dewhirst MW. Hypoxia in the thymus: role of oxygen tension in thymocyte survival. *Am J Physiol-Heart Circ Physiol.* 2002;282(4):H1467-H1477. doi:10.1152/ajpheart.00682.2001
23. Vaupel P, Kallinowski F, Okunieff P. Blood Flow, Oxygen and Nutrient Supply, and Metabolic Microenvironment of Human Tumors: A Review. *Cancer Res.* 1989;49(23):6449.
24. Höckel M, Vaupel P. Tumor Hypoxia: Definitions and Current Clinical, Biologic, and Molecular Aspects. *JNCI J Natl Cancer Inst.* 2001;93(4):266–276. doi:10.1093/jnci/93.4.266
25. Rademakers SE, Span PN, Kaanders JHAM, Sweep FCGJ, van der Kogel AJ, Bussink J. Molecular aspects of tumour hypoxia. *Mol Oncol.* 2008;2(1):41-53. doi:10.1016/j.molonc.2008.03.006
26. Nordmark M, Eriksen JG, Gebiski V, Alsner J, Horsman MR, Overgaard J. Differential risk assessments from five hypoxia specific assays: The basis for biologically adapted individualized radiotherapy in advanced head and neck cancer patients. *Radiother Oncol.* 2007;83(3):389-397. doi:10.1016/j.radonc.2007.04.021
27. Nordmark M, Overgaard M, Overgaard J. Pretreatment oxygenation predicts radiation response in advanced squamous cell carcinoma of the head and neck. *Radiother Oncol.* 1996;41(1):31-39. doi:10.1016/S0167-8140(96)91811-3
28. Nordmark M, Overgaard J. A confirmatory prognostic study on oxygenation status and loco-regional control in advanced head and neck squamous cell carcinoma treated by radiation therapy. *Radiother Oncol.* 2000;57(1):39-43. doi:10.1016/S0167-8140(00)00223-1
29. Nordmark M, Overgaard J. Tumor hypoxia is independent of hemoglobin and prognostic for loco-regional tumor control after primary radiotherapy in advanced head and neck cancer. *Acta Oncol.* 2004;43(4):396-403. doi:10.1080/02841860410026189
30. Rudat V, Vanselow B, Wollensack P, et al. Repeatability and prognostic impact of the pretreatment pO₂ histography in patients with advanced head and neck cancer. *Radiother Oncol.* 2000;57(1):31-37. doi:10.1016/S0167-8140(00)00200-0
31. Rickard AG, Palmer GM, Dewhirst MW. Clinical and Pre-clinical Methods for Quantifying Tumor Hypoxia. In: Gilkes DM, ed. *Hypoxia and Cancer Metastasis*. Vol 1136. Advances in Experimental Medicine and Biology. Springer International Publishing; 2019:19-41. doi:10.1007/978-3-030-12734-3_2

32. Thomlinson RH, Gray LH. The Histological Structure of Some Human Lung Cancers and the Possible Implications for Radiotherapy. *Br J Cancer*. 1955;9(4):539-549.
33. Koch CJ, Evans SM. Optimizing hypoxia detection and treatment strategies. *Semin Nucl Med*. 2015;45(2):163-176. doi:10.1053/j.semnuclmed.2014.10.004
34. Bayer C, Shi K, Astner ST, Maftai CA, Vaupel P. Acute versus chronic hypoxia: why a simplified classification is simply not enough. *Int J Radiat Oncol • Biol • Phys*. 2011;80(4):965-968. doi:10.1016/j.ijrobp.2011.02.049
35. Brown JM. Evidence for acutely hypoxic cells in mouse tumours, and a possible mechanism of reoxygenation. *Br J Radiol*. 1979;52(620):650-656. doi:doi:10.1259/0007-1285-52-620-650
36. Kimura H, Braun RD, Ong ET, et al. Fluctuations in Red Cell Flux in Tumor Microvessels Can Lead to Transient Hypoxia and Reoxygenation in Tumor Parenchyma. *Cancer Res*. 1996;56(23):5522.
37. Braun RD, Lanzen JL, Dewhirst MW. Fourier analysis of fluctuations of oxygen tension and blood flow in R3230Ac tumors and muscle in rats. *Am J Physiol-Heart Circ Physiol*. 1999;277(2):H551-H568. doi:10.1152/ajpheart.1999.277.2.H551
38. Skala MC, Fontanella AN, Lan L, Izatt JA, D.v.m MWD. Longitudinal optical imaging of tumor metabolism and hemodynamics. *J Biomed Opt*. 2010;15(1):011112. doi:10.1117/1.3285584
39. Baudelet C, Ansiaux R, Jordan BF, Havaux X, Macq B, Gallez B. Physiological noise in murine solid tumours using T2*-weighted gradient-echo imaging: a marker of tumour acute hypoxia? *Phys Med Biol*. 2004;49(15):3389–3411. doi:10.1088/0031-9155/49/15/006
40. Goncalves MR, Johnson SP, Ramasawmy R, Pedley RB, Lythgoe MF, Walker-Samuel S. Decomposition of spontaneous fluctuations in tumour oxygenation using BOLD MRI and independent component analysis. *Br J Cancer*. 2015;113(8):1168-1177. doi:10.1038/bjc.2015.270
41. Panek R, Welsh L, Baker LCJ, et al. Noninvasive Imaging of Cycling Hypoxia in Head and Neck Cancer Using Intrinsic Susceptibility MRI. *Clin Cancer Res*. 2017;23(15):4233–4241. doi:10.1158/1078-0432.ccr-16-1209
42. Chaplin DJ, Durand RE, Olive PL. Acute hypoxia in tumors: Implications for modifiers of radiation effects. *Int J Radiat Oncol*. 1986;12(8):1279-1282. doi:10.1016/0360-3016(86)90153-7
43. van der Heijden M, de Jong MC, Verhagen CVM, et al. Acute Hypoxia Profile is a Stronger Prognostic Factor than Chronic Hypoxia in

Advanced Stage Head and Neck Cancer Patients. *Cancers*. 2019;11(4):583. doi:10.3390/cancers11040583

44. Horsman MR, Mortensen LS, Petersen JB, Busk M, Overgaard J. Imaging hypoxia to improve radiotherapy outcome. *Nat Rev Clin Oncol*. 2012;9(12):674-687. doi:10.1038/nrclinonc.2012.171
45. Overgaard J. Hypoxic modification of radiotherapy in squamous cell carcinoma of the head and neck; A systematic review and meta-analysis. *Radiother Oncol*. 2011;100(1):22–32. doi:10.1016/j.radonc.2011.03.004
46. The Nobel Prize in Physiology or Medicine 2019. NobelPrize.org. Accessed August 5, 2020. <https://www.nobelprize.org/prizes/medicine/2019/summary/%3E>
47. Harris AL. Hypoxia — a key regulatory factor in tumour growth. *Nat Rev Cancer*. 2002;2(1):38–47. doi:10.1038/nrc704
48. Pires IM, Bencokova Z, Milani M, et al. Effects of acute versus chronic hypoxia on DNA damage responses and genomic instability. *Cancer Res*. 2010;70(3):925-935. doi:10.1158/0008-5472.CAN-09-2715
49. Baran N, Konopleva M. Molecular Pathways: Hypoxia-Activated Prodrugs in Cancer Therapy. *Clin Cancer Res*. 2017;23(10):2382-2390. doi:10.1158/1078-0432.CCR-16-0895
50. Baskar R, Lee KA, Yeo R, Yeoh K-W. Cancer and Radiation Therapy: Current Advances and Future Directions. *Int J Med Sci*. 2012;9(3):193-199. doi:10.7150/ijms.3635
51. Churchill-Davidson I, Foster CA, Wiernik G, et al. The Place of Oxygen in Radiotherapy. *Br J Radiol*. 1966;39(461):321–331. doi:10.1259/0007-1285-39-461-321
52. Wenzl T, Wilkens JJ. Modelling of the oxygen enhancement ratio for ion beam radiation therapy. *Phys Med Biol*. 2011;56(11):3251–3268. doi:10.1088/0031-9155/56/11/006
53. Gray LH, Conger AD, Ebert M, Hornsey S, Scott OCA. The Concentration of Oxygen Dissolved in Tissues at the Time of Irradiation as a Factor in Radiotherapy. *Br J Radiol*. 1953;26(312):638–648. doi:10.1259/0007-1285-26-312-638
54. Harrison L, Blackwell K, Harrison L, et al. *Hypoxia and Anemia: Factors in Decreased Sensitivity to Radiation Therapy and Chemotherapy? Oncologist* 9.; 2004.
55. Pignon J-P, Maître A le, Maillard E, Bourhis J. Meta-analysis of chemotherapy in head and neck cancer (MACH-NC): An update on 93

randomised trials and 17,346 patients. *Radiother Oncol.* 2009;92(1):4-14. doi:10.1016/j.radonc.2009.04.014

56. Winkvist E, Agbassi C, Meyers BM, Yoo J, Chan KKW, the Head and Neck Disease Site Group. Systemic therapy in the curative treatment of head and neck squamous cell cancer: a systematic review. *J Otolaryngol - Head Neck Surg.* 2017;46(1):29. doi:10.1186/s40463-017-0199-x
57. Schantz SP, Harrison LB, Forastiere A, Shantz SP. Tumors of the nasal cavity and paranasal sinuses, nasopharynx, oral cavity, and oropharynx. Published online 2001.
58. Chung CH, Ely K, McGavran L, et al. Increased epidermal growth factor receptor gene copy number is associated with poor prognosis in head and neck squamous cell carcinomas. *J Clin Oncol.* 2006;24(25):4170-4176.
59. Temam S, Kawaguchi H, El-Naggar AK, et al. Epidermal growth factor receptor copy number alterations correlate with poor clinical outcome in patients with head and neck squamous cancer. *J Clin Oncol.* 2007;25(16):2164-2170.
60. Kimura H, Sakai K, Arao T, Shimoyama T, Tamura T, Nishio K. Antibody-dependent cellular cytotoxicity of cetuximab against tumor cells with wild-type or mutant epidermal growth factor receptor. *Cancer Sci.* 2007;98(8):1275-1280.
61. Fan Z, Baselga J, Masui H, Mendelsohn J. Antitumor effect of anti-epidermal growth factor receptor monoclonal antibodies plus cis-diamminedichloroplatinum on well established A431 cell xenografts. *Cancer Res.* 1993;53(19):4637-4642.
62. Burtneß B, Goldwasser MA, Flood W, Mattar B, Forastiere AA. Phase III randomized trial of cisplatin plus placebo compared with cisplatin plus cetuximab in metastatic/recurrent head and neck cancer: an Eastern Cooperative Oncology Group study. *J Clin Oncol.* 2005;23(34):8646-8654.
63. Vermorken JB, Mesia R, Rivera F, et al. Platinum-Based Chemotherapy plus Cetuximab in Head and Neck Cancer. *N Engl J Med.* 2008;359(11):1116-1127. doi:10.1056/NEJMoa0802656
64. Hitt R, López-Pousa A, Martínez-Trufero J, et al. Phase III study comparing cisplatin plus fluorouracil to paclitaxel, cisplatin, and fluorouracil induction chemotherapy followed by chemoradiotherapy in locally advanced head and neck cancer. *J Clin Oncol.* 2005;23(34):8636-8645.
65. Blanchard P, Bourhis J, Lacas B, et al. Taxane-Cisplatin-Fluorouracil As Induction Chemotherapy in Locally Advanced Head and Neck Cancers:

An Individual Patient Data Meta-Analysis of the Meta-Analysis of Chemotherapy in Head and Neck Cancer Group. *J Clin Oncol*. 2013;31(23):2854-2860. doi:10.1200/JCO.2012.47.7802

66. Cosse J-P, Michiels C. Tumour hypoxia affects the responsiveness of cancer cells to chemotherapy and promotes cancer progression. *Anti-Cancer Agents Med Chem Former Curr Med Chem-Anti-Cancer Agents*. 2008;8(7):790-797.
67. Ferris RL. Immunology and Immunotherapy of Head and Neck Cancer. *J Clin Oncol*. 2015;33(29):3293-3304. doi:10.1200/JCO.2015.61.1509
68. Burtneß B, Harrington KJ, Greil R, et al. Pembrolizumab alone or with chemotherapy versus cetuximab with chemotherapy for recurrent or metastatic squamous cell carcinoma of the head and neck: a randomised, open-label, phase 3 study. *The Lancet*. 2019;394(10212):1915-1928. doi:10.1016/S0140-6736(19)32591-7
69. Chouaib S, Noman MZ, Kosmatopoulos K, Curran MA. Hypoxic stress: obstacles and opportunities for innovative immunotherapy of cancer. *Oncogene*. 2017;36(4):439-445. doi:10.1038/onc.2016.225
70. Dewhirst MW, Mowery YM, Mitchell JB, Cherukuri MK, Secomb TW. Rationale for hypoxia assessment and amelioration for precision therapy and immunotherapy studies. *J Clin Invest*. Published online January 2019. doi:10.1172/jci126044
71. Leone RD, Horton MR, Powell JD. Something in the Air: Hyperoxic Conditioning of the Tumor Microenvironment for Enhanced Immunotherapy. *Cancer Cell*. 2015;27(4):435-436. doi:10.1016/j.ccell.2015.03.014
72. Hanahan D, Weinberg RA. The Hallmarks of Cancer. *Cell*. 2000;100(1):57-70. doi:10.1016/S0092-8674(00)81683-9
73. Hanahan D, Weinberg RA. Hallmarks of Cancer: The Next Generation. *Cell*. 2011;144(5):646-674. doi:10.1016/j.cell.2011.02.013
74. Henk JM. Does hyperbaric oxygen have a future in radiation therapy? *Int J Radiat Oncol*. 1981;7(8):1125-1128. doi:10.1016/0360-3016(81)90173-5
75. Becker A, Kuhnt T, Liedtke H, Krivokuca A, Bloching M, Dunst J. Oxygenation measurements in head and neck cancers during hyperbaric oxygenation. *Strahlenther Onkol*. 2002;178(2):105-108.
76. Matsumoto K, Bernardo M, Subramanian S, et al. MR assessment of changes of tumor in response to hyperbaric oxygen treatment. *Magn Reson Med*. 2006;56(2):240-246. doi:10.1002/mrm.20961

77. Janssens G, Rademakers S, Terhaard C, et al. Accelerated Radiotherapy With Carbogen and Nicotinamide for Laryngeal Cancer: Results of a Phase III Randomized Trial. *J Clin Oncol Off J Am Soc Clin Oncol.* 2012;30:1777-1783. doi:10.1200/JCO.2011.35.9315
78. Henk JM, Kunkler PB, Smith CW. Radiotherapy and hyperbaric oxygen in head and neck cancer: Final Report of First Controlled Clinical Trial. *The Lancet.* 1977;310(8029):101-103. doi:10.1016/S0140-6736(77)90116-7
79. Nijkamp MM, Span PN, Terhaard CHJ, et al. Epidermal growth factor receptor expression in laryngeal cancer predicts the effect of hypoxia modification as an additive to accelerated radiotherapy in a randomised controlled trial. *Eur J Cancer.* 2013;49(15):3202-3209. doi:10.1016/j.ejca.2013.06.024
80. Gallez B, Jordan BF, Baudelet C, Misson P-D. Pharmacological modifications of the partial pressure of oxygen in murine tumors: Evaluation using in vivo EPR oximetry. *Magn Reson Med.* 1999;42(4):627-630. doi:10.1002/(SICI)1522-2594(199910)42:4<627::AID-MRM2>3.0.CO;2-M
81. Chaplin DJ, Horsman MR, Trotter MJ. Effect of Nicotinamide on the Microregional Heterogeneity of Oxygen Delivery Within a Murine Tumor. *JNCI J Natl Cancer Inst.* 1990;82(8):672-676. doi:10.1093/jnci/82.8.672
82. Kyzas PA, Stefanou D, Batistatou A, Agnantis NJ. Prognostic significance of VEGF immunohistochemical expression and tumor angiogenesis in head and neck squamous cell carcinoma. *J Cancer Res Clin Oncol.* 2005;131(9):624-630.
83. Montag M, Dyckhoff G, Lohr J, et al. Angiogenic growth factors in tissue homogenates of HNSCC: expression pattern, prognostic relevance, and interrelationships. *Cancer Sci.* 2009;100(7):1210-1218.
84. Gary MT, Chan AW, Yu K-H, et al. Strong immunohistochemical expression of vascular endothelial growth factor predicts overall survival in head and neck squamous cell carcinoma. *Ann Surg Oncol.* 2007;14(12):3558-3565.
85. Bhattacharya A. Lack of Microvessels in Well-Differentiated Regions of Human Head and Neck Squamous Cell Carcinoma A253 Associated with Functional Magnetic Resonance Imaging Detectable Hypoxia, Limited Drug Delivery, and Resistance to Irinotecan Therapy. *Clin Cancer Res.* 2004;10(23):8005–8017. doi:10.1158/1078-0432.ccr-04-1306
86. Bates DO, Harper SJ. Regulation of vascular permeability by vascular endothelial growth factors. *Vascul Pharmacol.* 2002;39(4-5):225–237. doi:10.1016/s1537-1891(03)00011-9

87. Bozec A, Etienne-Grimaldi M-C, Fischel J-L, et al. The mTOR-targeting drug temsirolimus enhances the growth-inhibiting effects of the cetuximab–bevacizumab–irradiation combination on head and neck cancer xenografts. *Oral Oncol.* 2011;47(5):340-344. doi:10.1016/j.oraloncology.2011.02.020
88. Willett CG, Boucher Y, Di Tomaso E, et al. Direct evidence that the VEGF-specific antibody bevacizumab has antivascular effects in human rectal cancer. *Nat Med.* 2004;10(2):145-147.
89. Zhang H, Yun S, Batuwangala TD, et al. A dual-targeting antibody against EGFR-VEGF for lung and head and neck cancer treatment. *Int J Cancer.* 2012;131(4):956-969. doi:10.1002/ijc.26427
90. Argiris A, Karamouzis MV, Gooding WE, et al. Phase II Trial of Pemetrexed and Bevacizumab in Patients With Recurrent or Metastatic Head and Neck Cancer. *J Clin Oncol.* 2011;29(9):1140-1145. doi:10.1200/JCO.2010.33.3591
91. Yoo DS, Kirkpatrick JP, Craciunescu O, et al. Prospective Trial of Synchronous Bevacizumab, Erlotinib, and Concurrent Chemoradiation in Locally Advanced Head and Neck Cancer. *Clin Cancer Res.* 2012;18(5):1404-1414. doi:10.1158/1078-0432.CCR-11-1982
92. Seiwert TY, Haraf DJ, Cohen EEW, et al. Phase I Study of Bevacizumab Added to Fluorouracil- and Hydroxyurea-Based Concomitant Chemoradiotherapy for Poor-Prognosis Head and Neck Cancer. *J Clin Oncol.* 2008;26(10):1732-1741. doi:10.1200/JCO.2007.13.1706
93. Fein DA, Lee WR, Hanlon AL, et al. Pretreatment hemoglobin level influences local control and survival of T1-T2 squamous cell carcinomas of the glottic larynx. *J Clin Oncol.* 1995;13(8):2077-2083.
94. Dubray B, Mosseri V, Brunin F, et al. Anemia is associated with lower local-regional control and survival after radiation therapy for head and neck cancer: a prospective study. *Radiology.* 1996;201(2):553-558.
95. Lee WR, Berkey B, Marcial V, et al. Anemia is associated with decreased survival and increased locoregional failure in patients with locally advanced head and neck carcinoma: a secondary analysis of RTOG 85-27. *Int J Radiat Oncol Biol Phys.* 1998;42(5):1069-1075.
96. Becker A, Stadler P, Lavey RS, et al. Severe anemia is associated with poor tumor oxygenation in head and neck squamous cell carcinomas. *Int J Radiat Oncol Biol Phys.* 2000;46(2):459-466.
97. Welsh L, Panek R, Riddell A, et al. Blood transfusion during radical chemo-radiotherapy does not reduce tumour hypoxia in squamous cell cancer of the head and neck. *Br J Cancer.* 2017;116(1):28-35. doi:10.1038/bjc.2016.386

98. Henke M, Laszig R, Rübe C, et al. Erythropoietin to treat head and neck cancer patients with anaemia undergoing radiotherapy: randomised, double-blind, placebo-controlled trial. *The Lancet*. 2003;362(9392):1255-1260. doi:10.1016/S0140-6736(03)14567-9
99. Machtay M, Pajak TF, Suntharalingam M, et al. Radiotherapy With or Without Erythropoietin for Anemic Patients With Head and Neck Cancer: A Randomized Trial of the Radiation Therapy Oncology Group (RTOG 99-03). *Int J Radiat Oncol*. 2007;69(4):1008-1017. doi:10.1016/j.ijrobp.2007.04.063
100. Overgaard J, Hoff CM, Hansen HS, et al. DAHANCA 10 – Effect of darbepoetin alfa and radiotherapy in the treatment of squamous cell carcinoma of the head and neck. A multicenter, open-label, randomized, phase 3 trial by the Danish head and neck cancer group. *Radiother Oncol*. 2018;127(1):12-19. doi:10.1016/j.radonc.2018.02.018
101. Raleigh JA, Koch CJ. Importance of thiols in the reductive binding of 2-nitroimidazoles to macromolecules. *Biochem Pharmacol*. 1990;40(11):2457-2464. doi:http://dx.doi.org/10.1016/0006-2952(90)90086-Z
102. Varia MA, Calkins-Adams DP, Rinker LH, et al. Pimonidazole: A Novel Hypoxia Marker for Complementary Study of Tumor Hypoxia and Cell Proliferation in Cervical Carcinoma. *Gynecol Oncol*. 1998;71(2):270-277. doi:http://dx.doi.org/10.1006/gyno.1998.5163
103. Kedderis GL, Miwa GT. The metabolic activation of nitroheterocyclic therapeutic agents. *Drug Metab Rev*. 1988;19(1):33-62. doi:10.3109/03602538809049618
104. Kizaka-Kondoh S, Konse-Nagasawa H. Significance of nitroimidazole compounds and hypoxia-inducible factor-1 for imaging tumor hypoxia. *Cancer Sci*. 2009;100(8):1366–1373. doi:10.1111/j.1349-7006.2009.01195.x
105. Overgaard J, Sand Hansen H, Overgaard M, et al. A randomized double-blind phase III study of nimorazole as a hypoxic radiosensitizer of primary radiotherapy in supraglottic larynx and pharynx carcinoma. Results of the Danish Head and Neck Cancer Study (DAHANCA) Protocol 5-85. *Radiother Oncol*. 1998;46(2):135-146. doi:10.1016/S0167-8140(97)00220-X
106. Grégoire V, Overgaard J. *AF CRT +/- Nimorazole in HNSCC NCT01880359*. Accessed June 12, 2020. <https://clinicaltrials.gov/ct2/show/NCT01880359>
107. Jamieson SMF, Tsai P, Kondratyev MK, et al. Evofosfamide for the treatment of human papillomavirus-negative head and neck squamous cell carcinoma. *JCI Insight*. 2018;3(16). doi:10.1172/jci.insight.122204

108. Harms JK, Lee T-W, Wang T, et al. Impact of Tumour Hypoxia on Evofosfamide Sensitivity in Head and Neck Squamous Cell Carcinoma Patient-Derived Xenograft Models. *Cells*. 2019;8(7):717. doi:10.3390/cells8070717
109. DiSilvestro PA, Ali S, Craighead PS, et al. Phase III Randomized Trial of Weekly Cisplatin and Irradiation Versus Cisplatin and Tirapazamine and Irradiation in Stages IB2, IIA, IIB, IIIB, and IVA Cervical Carcinoma Limited to the Pelvis: A Gynecologic Oncology Group Study. *J Clin Oncol*. 2014;32(5):458-464. doi:10.1200/JCO.2013.51.4265
110. Rischin D, Peters L, Fisher R, et al. Tirapazamine, Cisplatin, and Radiation Versus Fluorouracil, Cisplatin, and Radiation in Patients With Locally Advanced Head and Neck Cancer: A Randomized Phase II Trial of the Trans-Tasman Radiation Oncology Group (TROG 98.02). *J Clin Oncol*. 2005;23(1):79-87. doi:10.1200/JCO.2005.01.072
111. Mehibel M, Singh S, Cowen RL, Williams KJ, Stratford IJ. Radiation enhances the therapeutic effect of Banoxantrone in hypoxic tumour cells with elevated levels of nitric oxide synthase. *Oncol Rep*. 2016;35(4):1925-1932. doi:10.3892/or.2016.4555
112. Albertella MR, Loadman PM, Jones PH, et al. Hypoxia-Selective Targeting by the Bioreductive Prodrug AQ4N in Patients with Solid Tumors: Results of a Phase I Study. *Clin Cancer Res*. 2008;14(4):1096-1104. doi:10.1158/1078-0432.CCR-07-4020
113. Ashton TM, Fokas E, Kunz-Schughart LA, et al. The anti-malarial atovaquone increases radiosensitivity by alleviating tumour hypoxia. *Nat Commun*. 2016;7:12308. doi:10.1038/ncomms12308
114. Fiorillo M, Lamb R, Tanowitz HB, et al. Repurposing atovaquone: Targeting mitochondrial complex III and OXPHOS to eradicate cancer stem cells. *Oncotarget*. 2016;7(23). doi:10.18632/oncotarget.9122
115. Zannella VE, Dal Pra A, Muaddi H, et al. Reprogramming Metabolism with Metformin Improves Tumor Oxygenation and Radiotherapy Response. *Clin Cancer Res*. 2013;19(24):6741-6750. doi:10.1158/1078-0432.CCR-13-1787
116. Wheaton WW, Weinberg SE, Hamanaka RB, et al. Metformin inhibits mitochondrial complex I of cancer cells to reduce tumorigenesis. Dang CV, ed. *eLife*. 2014;3:e02242. doi:10.7554/eLife.02242
117. Cao-Pham T-T, Tran-Ly-Binh A, Heyerick A, et al. Combined endogenous MR biomarkers to assess changes in tumor oxygenation induced by an allosteric effector of hemoglobin. *NMR Biomed*. 2020;33(2):e4181. doi:10.1002/nbm.4181
118. Ansiaux R, Dewever J, Grégoire V, Feron O, Jordan BF, Gallez B. Decrease in Tumor Cell Oxygen Consumption after Treatment with

Vandetanib (ZACTIMA™; ZD6474) and its Effect on Response to Radiotherapy. *Radiat Res.* 2009;172(5):584-591. doi:10.1667/RR1744.1

119. Jordan BF, Crockart N, Baudelet C, Cron GO, Ansiaux R, Gallez B. Complex relationship between changes in oxygenation status and changes in R: The case of insulin and NS-398, two inhibitors of oxygen consumption. *Magn Reson Med.* 2006;56(3):637-643. doi:10.1002/mrm.20963
120. University Health Network, Toronto. *The Potential for Metformin to Improve Tumor Oxygenation in Locally Advanced Cervix Cancer: A Phase II Randomized Trial.* clinicaltrials.gov; 2020. Accessed June 11, 2020. <https://clinicaltrials.gov/ct2/show/NCT02394652>
121. *Atovaquone as Tumour HypOxia Modifier (ATOM) NCT02628080.*; 2015. <https://clinicaltrials.gov/ct2/show/NCT02628080>
122. Ashton TM, McKenna WG, Kunz-Schughart LA, Higgins GS. Oxidative Phosphorylation as an Emerging Target in Cancer Therapy. *Clin Cancer Res.* 2018;24(11):2482-2490. doi:10.1158/1078-0432.CCR-17-3070
123. Hendrickson K, Phillips M, Smith W, Peterson L, Krohn K, Rajendran J. Hypoxia imaging with [F-18] FMISO-PET in head and neck cancer: potential for guiding intensity modulated radiation therapy in overcoming hypoxia-induced treatment resistance. *Radiother Oncol.* 2011;101(3):369-375. doi:10.1016/j.radonc.2011.07.029
124. Rischin D, Hicks RJ, Fisher R, et al. Prognostic Significance of [18F]-Misonidazole Positron Emission Tomography–Detected Tumor Hypoxia in Patients With Advanced Head and Neck Cancer Randomly Assigned to Chemoradiation With or Without Tirapazamine: A Substudy of Trans-Tasman Radiation Oncology Group Study 98.02. *J Clin Oncol.* 2006;24(13):2098-2104. doi:10.1200/JCO.2005.05.2878
125. Hassan Metwally MA, Ali R, Kuddu M, et al. IAEA-HypoX. A randomized multicenter study of the hypoxic radiosensitizer nimorazole concomitant with accelerated radiotherapy in head and neck squamous cell carcinoma. *Radiother Oncol.* 2015;116(1):15-20. doi:10.1016/j.radonc.2015.04.005
126. Prestwich RJD, Sykes J, Carey B, Sen M, Dyker KE, Scarsbrook AF. Improving Target Definition for Head and Neck Radiotherapy: A Place for Magnetic Resonance Imaging and 18-Fluoride Fluorodeoxyglucose Positron Emission Tomography? *Clin Oncol.* 2012;24(8):577-589. doi:<http://dx.doi.org/10.1016/j.clon.2012.04.002>
127. Bhatnagar P, Subesinghe M, Patel C, Prestwich R, Scarsbrook AF. Functional Imaging for Radiation Treatment Planning, Response Assessment, and Adaptive Therapy in Head and Neck Cancer. *RadioGraphics.* 2013;33(7):1909-1929. doi:10.1148/rg.337125163

128. Horsman MR, Mortensen LS, Petersen JB, Busk M, Overgaard J. Imaging hypoxia to improve radiotherapy outcome. *Nat Rev Clin Oncol*. 2012;9(12):674-687. doi:10.1038/nrclinonc.2012.171
129. Griffiths JR, Robinson SP. The OxyLite: a fibre-optic oxygen sensor. *Br J Radiol*. 1999;72(859):627-630. doi:10.1259/bjr.72.859.10624317
130. Rademakers SE, Lok J, Kogel AJ van der, Bussink J, Kaanders JH. Metabolic markers in relation to hypoxia: staining patterns and colocalization of pimonidazole, HIF-1 α , CAIX, LDH-5, GLUT-1, MCT1 and MCT4. *BMC Cancer*. 2011;11(1). doi:10.1186/1471-2407-11-167
131. Hammond EM, Asselin M-C, Forster D, Connor JPB, Senra JM, Williams KJ. The Meaning, Measurement and Modification of Hypoxia in the Laboratory and the Clinic. *Clin Oncol*. 2014;26(5):277-288. doi:10.1016/j.clon.2014.02.002
132. Swartz JE, Pothen AJ, Stegeman I, Willems SM, Grolman W. Clinical implications of hypoxia biomarker expression in head and neck squamous cell carcinoma: a systematic review. *Cancer Med*. 2015;4(7):1101-1116. doi:10.1002/cam4.460
133. Jankovic B, Aquino-Parsons C, Raleigh JA, et al. Comparison between pimonidazole binding, oxygen electrode measurements, and expression of endogenous hypoxia markers in cancer of the uterine cervix. *Cytometry B Clin Cytom*. 2006;70B(2):45-55. doi:10.1002/cyto.b.20086
134. Airley RE, Loncaster J, Raleigh JA, et al. GLUT-1 and CAIX as intrinsic markers of hypoxia in carcinoma of the cervix: Relationship to pimonidazole binding. *Int J Cancer*. 2003;104(1):85-91. doi:https://doi.org/10.1002/ijc.10904
135. Zhong H, Chiles K, Feldser D, et al. Modulation of Hypoxia-inducible Factor 1 α Expression by the Epidermal Growth Factor/Phosphatidylinositol 3-Kinase/PTEN/AKT/FRAP Pathway in Human Prostate Cancer Cells: Implications for Tumor Angiogenesis and Therapeutics. *Cancer Res*. 2000;60(6):1541-1545.
136. Ragnum HB, Røe K, Holm R, et al. Hypoxia-Independent Downregulation of Hypoxia-Inducible Factor 1 Targets by Androgen Deprivation Therapy in Prostate Cancer. *Int J Radiat Oncol*. 2013;87(4):753-760. doi:10.1016/j.ijrobp.2013.07.023
137. Tanaka H, Yamamoto M, Hashimoto N, et al. Hypoxia-Independent Overexpression of Hypoxia-Inducible Factor 1 α as an Early Change in Mouse Hepatocarcinogenesis. *Cancer Res*. 2006;66(23):11263-11270. doi:10.1158/0008-5472.CAN-06-1699
138. Janssen HLK, Haustermans KMG, Sprong D, et al. HIF-1 α , pimonidazole, and iododeoxyuridine to estimate hypoxia and perfusion

- in human head-and-neck tumors. *Int J Radiat Oncol.* 2002;54(5):1537-1549. doi:10.1016/S0360-3016(02)03935-4
139. Kaluz S, Kaluzová M, Liao S-Y, Lerman M, Stanbridge EJ. Transcriptional control of the tumor- and hypoxia-marker carbonic anhydrase 9: A one transcription factor (HIF-1) show? *Biochim Biophys Acta BBA - Rev Cancer.* 2009;1795(2):162-172. doi:10.1016/j.bbcan.2009.01.001
 140. Kunkel M, Moergel M, Stockinger M, et al. Overexpression of GLUT-1 is associated with resistance to radiotherapy and adverse prognosis in squamous cell carcinoma of the oral cavity. *Oral Oncol.* 2007;43(8):796-803. doi:10.1016/j.oraloncology.2006.10.009
 141. Agrawal A, Guttapalli A, Narayan S, Albert TJ, Shapiro IM, Risbud MV. Normoxic stabilization of HIF-1 α drives glycolytic metabolism and regulates aggrecan gene expression in nucleus pulposus cells of the rat intervertebral disk. *Am J Physiol-Cell Physiol.* 2007;293(2):C621-C631. doi:10.1152/ajpcell.00538.2006
 142. Janssen HLK, Hoebbers FJ, Sprong D, et al. Differentiation-associated staining with anti-pimonidazole antibodies in head and neck tumors. *Radiother Oncol.* 2004;70(1):91–97. doi:10.1016/j.radonc.2003.09.012
 143. Höckel M, Schlenger K, Knoop C, Vaupel P. Oxygenation of Carcinomas of the Uterine Cervix: Evaluation by Computerized O₂ Tension Measurements. *Cancer Res.* 1991;51(22):6098-6102.
 144. Bussink J, Kaanders JH a. M, Strik AM, Vojnovic B, Kogel AJ van der. Optical Sensor-Based Oxygen Tension Measurements Correspond with Hypoxia Marker Binding in Three Human Tumor Xenograft Lines. *Radiat Res.* 2000;154(5):547-555. doi:10.1667/0033-7587(2000)154[0547:OSBOTM]2.0.CO;2
 145. Hoogsteen IJ, Marres HAM, Bussink J, van der Kogel AJ, Kaanders JHAM. Tumor microenvironment in head and neck squamous cell carcinomas: Predictive value and clinical relevance of hypoxic markers. A review. *Head Neck.* 2007;29(6):591-604. doi:10.1002/hed.20543
 146. Tatum JL, Kelloff GJ, Gillies RJ, et al. Hypoxia: importance in tumor biology, noninvasive measurement by imaging, and value of its measurement in the management of cancer therapy. *Int J Radiat Biol.* 2006;82(10):699-757. doi:10.1080/09553000601002324
 147. Dewhirst MW, Bिरer SR. Oxygen-Enhanced MRI Is a major advance in tumor hypoxia imaging. *Cancer Res.* 2016;76(4):769-772. doi:10.1158/0008-5472.CAN-15-2818
 148. Biomarkers and surrogate endpoints: Preferred definitions and conceptual framework. *Clin Pharmacol Ther.* 2001;69(3):89-95. doi:10.1067/mcp.2001.113989

149. O'connor JP, Aboagye EO, Adams JE, et al. Imaging biomarker roadmap for cancer studies. *Nat Rev Clin Oncol*. 2017;14(3):169.
150. Lee NY, Mechalakos JG, Nehmeh S, et al. Fluorine-18-Labeled Fluoromisonidazole Positron Emission and Computed Tomography-Guided Intensity-Modulated Radiotherapy for Head and Neck Cancer: A Feasibility Study. *Int J Radiat Oncol*. 2008;70(1):2-13. doi:10.1016/j.ijrobp.2007.06.039
151. Zschaeck S, Löck S, Hofheinz F, et al. Individual patient data meta-analysis of FMISO and FAZA hypoxia PET scans from head and neck cancer patients undergoing definitive radio-chemotherapy. *Radiother Oncol*. 2020;149:189-196. doi:10.1016/j.radonc.2020.05.022
152. Dolbier WR, Li A-R, Koch CJ, Shiue C-Y, Kachur AV. [18F]-EF5, a marker for PET detection of hypoxia: synthesis of precursor and a new fluorination procedure. *Appl Radiat Isot*. 2001;54(1):73-80. doi:10.1016/S0969-8043(00)00102-0
153. Komar G, Seppänen M, Eskola O, et al. 18F-EF5: A New PET Tracer for Imaging Hypoxia in Head and Neck Cancer. *J Nucl Med*. 2008;49(12):1944-1951. doi:10.2967/jnumed.108.053785
154. Gallez B, Baudelet C, Jordan BF. Assessment of tumor oxygenation by electron paramagnetic resonance: principles and applications. *NMR Biomed*. 2004;17(5):240-262. doi:10.1002/nbm.900
155. Bobko AA, Dhimitruka I, Eubank TD, Marsh CB, Zweier JL, Khramtsov VV. Trityl-based EPR probe with enhanced sensitivity to oxygen. *Free Radic Biol Med*. 2009;47(5):654-658. doi:10.1016/j.freeradbiomed.2009.06.007
156. Tran LB, Bol A, Labar D, et al. Hypoxia imaging with the nitroimidazole 18F-FAZA PET tracer: a comparison with OxyLite, EPR oximetry and 19F-MRI relaxometry. *Radiother Oncol*. 2012;105(1):29-35. doi:10.1016/j.radonc.2012.04.011
157. Yasui H, Matsumoto S, Devasahayam N, et al. Low-field magnetic resonance imaging to visualize chronic and cycling hypoxia in tumor-bearing mice. *Cancer Res*. 2010;70(16):6427-6436. doi:10.1158/0008-5472.CAN-10-1350
158. Swartz HM, Williams BB, Zaki BI, et al. Clinical EPR: Unique Opportunities and Some Challenges. *Acad Radiol*. 2014;21(2):197-206. doi:10.1016/j.acra.2013.10.011
159. Aboagye EO, Maxwell RJ, Kelson AB, et al. Preclinical Evaluation of the Fluorinated 2-Nitroimidazole N-(2-hydroxy-3,3,3-trifluoropropyl)-2-(2-nitro-1-imidazolyl) Acetamide (SR-4554) as a Probe for the Measurement of Tumor Hypoxia. *Cancer Res*. 1997;57(15):3314-3318.

160. Seddon BM, Maxwell RJ, Honess DJ, et al. Validation of the Fluorinated 2-Nitroimidazole SR-4554 as a Noninvasive Hypoxia Marker Detected by Magnetic Resonance Spectroscopy. *Clin Cancer Res.* 2002;8(7):2323-2335.
161. Salmon HW, Siemann DW. Utility of ¹⁹F MRS detection of the hypoxic cell marker EF5 to assess cellular hypoxia in solid tumors. *Radiother Oncol.* 2004;73(3):359-366. doi:10.1016/j.radonc.2004.07.018
162. Robinson SP, Griffiths JR. Current issues in the utility of ¹⁹F nuclear magnetic resonance methodologies for the assessment of tumour hypoxia. *Philos Trans R Soc Lond B Biol Sci.* 2004;359(1446):987-996. doi:10.1098/rstb.2003.1376
163. Hunjan S, Mason RP, Constantinescu A, Peschke P, Hahn EW, Antich PP. Regional Tumor Oximetry: ¹⁹F NMR Spectroscopy of Hexafluorobenzene 11Presented in part at the International Society for Magnetic Resonance in Medicine Workshop on Cancer Physiology and Metabolism, Baltimore, MD, 7–9 August 1996. *Int J Radiat Oncol.* 1998;41(1):161-171. doi:10.1016/S0360-3016(98)00020-0
164. Hunjan S, Zhao D, Constantinescu A, Hahn EW, Antich PP, Mason RP. Tumor oximetry: demonstration of an enhanced dynamic mapping procedure using fluorine-19 echo planar magnetic resonance imaging in the Dunning prostate R3327-AT1 rat tumor. *Int J Radiat Oncol.* 2001;49(4):1097-1108. doi:10.1016/S0360-3016(00)01460-7
165. Zhao D, Jiang L, Hahn EW, Mason RP. Comparison of ¹H blood oxygen level-dependent (BOLD) and ¹⁹F MRI to investigate tumor oxygenation. *Magn Reson Med.* 2009;62(2):357-364. doi:10.1002/mrm.22020
166. Wu L, Liu F, Liu S, Xu X, Liu Z, Sun X. Perfluorocarbons-Based ¹⁹F Magnetic Resonance Imaging in Biomedicine. *Int J Nanomedicine.* 2020;15:7377-7395. doi:10.2147/IJN.S255084
167. Shi Y, Oeh J, Eastham-Anderson J, et al. Mapping In Vivo Tumor Oxygenation within Viable Tumor by (¹⁹F)-MRI and Multispectral Analysis. *Neoplasia N Y N.* 2013;15(11):1241-1250.
168. Star-Lack JM, Adalsteinsson E, Adam MF, et al. In Vivo ¹H MR Spectroscopy of Human Head and Neck Lymph Node Metastasis and Comparison with Oxygen Tension Measurements. *Am J Neuroradiol.* 2000;21(1):183-193.
169. Matsumoto S, Saito K, Yasui H, et al. EPR oxygen imaging and hyperpolarized ¹³C MRI of pyruvate metabolism as noninvasive biomarkers of tumor treatment response to a glycolysis inhibitor 3-bromopyruvate. *Magn Reson Med.* 2013;69(5):1443-1450. doi:10.1002/mrm.24355

170. Iversen AB, Ringgaard S, Laustsen C, et al. Hyperpolarized magnetic resonance spectroscopy for assessing tumor hypoxia. *Acta Oncol.* 2015;54(9):1393-1398. doi:10.3109/0284186X.2015.1070964
171. Vaupel P, Okunieff P, Kallinowski F, Neuringer LJ. Correlations between ³¹P-NMR Spectroscopy and Tissue O₂ Tension Measurements in a Murine Fibrosarcoma. *Radiat Res.* 1989;120(3):477. doi:10.2307/3577798
172. Tozer GM, Griffiths JR. The contribution made by cell death and oxygenation to ³¹P MRS observations of tumour energy metabolism: effects of cell death and oxygenation on tumour ³¹P spectra. *NMR Biomed.* 1992;5(5):279-289. doi:10.1002/nbm.1940050515
173. Warburg O. On the Origin of Cancer Cells. *Science.* 1956;123(3191):309–314. doi:10.1126/science.123.3191.309
174. Semenza GL. HIF-1 mediates the Warburg effect in clear cell renal carcinoma. *J Bioenerg Biomembr.* 2007;39(3):231–234. doi:10.1007/s10863-007-9081-2
175. Dadgar S, Troncoso JR, Rajaram N. Optical spectroscopic sensing of tumor hypoxia. *J Biomed Opt.* 2018;23(6):067001. doi:10.1117/1.JBO.23.6.067001
176. Knox HJ, Kim TW, Zhu Z, Chan J. Photophysical Tuning of N-Oxide-Based Probes Enables Ratiometric Photoacoustic Imaging of Tumor Hypoxia. *ACS Chem Biol.* 2018;13(7):1838-1843. doi:10.1021/acscchembio.8b00099
177. Choi W, Oh D, Kim C. Practical photoacoustic tomography: Realistic limitations and technical solutions. *J Appl Phys.* 2020;127(23):230903. doi:10.1063/5.0008401
178. McRobbie DW, Moore EA, Graves MJ, Prince MR. *MRI: From Picture to Proton.* 2nd ed. Cambridge University Press; 2006.
179. Tofts PS, Brix G, Buckley DL, et al. Estimating kinetic parameters from dynamic contrast-enhanced T1-weighted MRI of a diffusable tracer: Standardized quantities and symbols. *J Magn Reson Imaging.* 1999;10(3):223-232. doi:10.1002/(SICI)1522-2586(199909)10:3<223::AID-JMRI2>3.0.CO;2-S
180. Donaldson SB, Betts G, Bonington SC, et al. Perfusion Estimated With Rapid Dynamic Contrast-Enhanced Magnetic Resonance Imaging Correlates Inversely With Vascular Endothelial Growth Factor Expression and Pimonidazole Staining in Head-and-Neck Cancer: A Pilot Study. *Int J Radiat Oncol.* 2011;81(4):1176-1183. doi:10.1016/j.ijrobp.2010.09.039

181. Baker LC, Box C, Sikka A, Box G, Eccles SA, Robinson SP. Evaluating imaging biomarkers of acquired resistance to targeted EGFR therapy in xenograft models of human squamous cell carcinoma of the head and neck (SCCHN). *Cancer Res.* 2014;73 (8 Supplement):4459–4459. doi:10.1158/1538-7445.AM2013-4459
182. Mohamed KM, Le A, Duong H, Wu Y, Zhang Q, Messadi DV. Correlation between VEGF and HIF-1 α expression in human oral squamous cell carcinoma. *Exp Mol Pathol.* 2004;76(2):143-152. doi:10.1016/j.yexmp.2003.10.005
183. Hauge A, Wegner CS, Gaustad J-V, Simonsen TG, Andersen LMK, Rofstad EK. DCE-MRI of patient-derived xenograft models of uterine cervix carcinoma: associations with parameters of the tumor microenvironment. *J Transl Med.* 2017;15(1). doi:10.1186/s12967-017-1331-4
184. Newbold K, Castellano I, Charles-Edwards E, et al. An exploratory study into the role of dynamic contrast-enhanced magnetic resonance imaging or perfusion computed tomography for detection of intratumoral hypoxia in head-and-neck cancer. *Int J Radiat Oncol • Biol • Phys.* 2009;74(1):29-37. doi:10.1016/j.ijrobp.2008.07.039
185. Linnik IV, Scott ML, Holliday KF, et al. Noninvasive tumor hypoxia measurement using magnetic resonance imaging in murine U87 glioma xenografts and in patients with glioblastoma. *Magn Reson Med.* 2014;71(5):1854-1862. doi:10.1002/mrm.24826
186. O'Connor JP, Boulton JK, Jamin Y, et al. Oxygen-Enhanced MRI Accurately Identifies, Quantifies, and Maps Tumor Hypoxia in Preclinical Cancer Models. *Cancer Res.* 2016;76(4):787-795. doi:10.1158/0008-5472.CAN-15-2062
187. Baudalet C, Gallez B. How does blood oxygen level-dependent (BOLD) contrast correlate with oxygen partial pressure (pO₂) inside tumors? *Magn Reson Med.* 2002;48(6):980–986. doi:dunn
188. Howe FA, Robinson SP, McIntyre DJO, Stubbs M, Griffiths JR. Issues in flow and oxygenation dependent contrast (FLOOD) imaging of tumours. *NMR Biomed.* 2001;14(7-8):497–506. doi:10.1002/nbm.716
189. Padhani AR, Krohn KA, Lewis JS, Alber M. Imaging oxygenation of human tumours. *Eur Radiol.* 2007;17(4):861-872. doi:10.1007/s00330-006-0431-y
190. Dewhirst MW, Ong ET, Rosner GL, et al. Arteriolar oxygenation in tumour and subcutaneous arterioles: effects of inspired air oxygen content. *Br J Cancer Suppl.* 1996;27:S241-S246.
191. Robinson SP, Rijken PFJW, Howe FA, et al. Tumor vascular architecture and function evaluated by non-invasive susceptibility MRI

- methods and immunohistochemistry. *J Magn Reson Imaging*. 2003;17(4):445–454. doi:10.1002/jmri.10274
192. Burrell JS, Walker-Samuel S, Boulton JKR, et al. Investigating the Vascular Phenotype of Subcutaneously and Orthotopically Propagated PC3 Prostate Cancer Xenografts Using Combined Carbogen Ultrasmall Superparamagnetic Iron Oxide MRI: *Top Magn Reson Imaging*. 2016;25(5):237-243. doi:10.1097/RMR.000000000000102
 193. Gray LH, Steadman JM. Determination of the oxyhaemoglobin dissociation curves for mouse and rat blood. *J Physiol*. 1964;175(2):161-171. doi:10.1113/jphysiol.1964.sp007509
 194. Jensen FB. Red blood cell pH, the Bohr effect, and other oxygenation-linked phenomena in blood O₂ and CO₂ transport. *Acta Physiol Scand*. 2004;182(3):215-227. doi:10.1111/j.1365-201X.2004.01361.x
 195. Snyder SA, Lanzen JL, Braun RD, et al. Simultaneous administration of glucose and hyperoxic gas achieves greater improvement in tumor oxygenation than hyperoxic gas alone. *Int J Radiat Oncol*. 2001;51(2):494-506. doi:10.1016/S0360-3016(01)01654-6
 196. Betts JG, Young KA, Wise JA, et al. Transport of Gases. In: *Anatomy and Physiology*. OpenStax; 2013. Accessed June 2, 2020. <https://openstax.org/books/anatomy-and-physiology/pages/22-5-transport-of-gases>
 197. Rijpkema M, Kaanders JHAM, Joosten FBM, van der Kogel AJ, Heerschap A. Effects of breathing a hyperoxic hypercapnic gas mixture on blood oxygenation and vascularity of head-and-neck tumors as measured by magnetic resonance imaging. *Int J Radiat Oncol*. 2002;53(5):1185-1191. doi:10.1016/S0360-3016(02)02825-0
 198. Karczmar GS, River JN, Li J, Vijayakumar S, Goldman Z, Lewis MZ. Effects of hyperoxia on T₂* and resonance frequency weighted magnetic resonance images of rodent tumours. *NMR Biomed*. 1994;7(1-2):3-11. doi:10.1002/nbm.1940070103
 199. Rodrigues LM, Howe FA, Griffiths JR, Robinson SP. Tumor R₂* is a prognostic indicator of acute radiotherapeutic response in rodent tumors. *J Magn Reson Imaging*. 2004;19(4):482-488. doi:10.1002/jmri.20024
 200. Burrell JS, Walker-Samuel S, Baker LCJ, et al. Investigating temporal fluctuations in tumor vasculature with combined carbogen and ultrasmall superparamagnetic iron oxide particle (CUSPIO) imaging. *Magn Reson Med*. 2011;66(1):227-234. doi:10.1002/mrm.22779
 201. Zhao D, Pacheco-Torres J, Hallac RR, et al. Dynamic oxygen challenge evaluated by NMR T₁ and T₂* – insights into tumor oxygenation. *NMR Biomed*. 2015;28(8):937-947. doi:10.1002/nbm.3325

202. Baker LCJ, Boulton JKR, Jamin Y, et al. Evaluation and Immunohistochemical Qualification of Carbogen-Induced ΔR_2^* as a Noninvasive Imaging Biomarker of Improved Tumor Oxygenation. *Int J Radiat Oncol*. 2013;87(1):160-167. doi:10.1016/j.ijrobp.2013.04.051
203. Taylor NJ, Baddeley H, Goodchild KA, et al. BOLD MRI of human tumor oxygenation during carbogen breathing. *J Magn Reson Imaging*. 2001;14(2):156-163. doi:10.1002/jmri.1166
204. Alonzi R, Padhani AR, Maxwell RJ, et al. Carbogen breathing increases prostate cancer oxygenation: a translational MRI study in murine xenografts and humans. *Br J Cancer*. 2009;100(4):644-648. doi:10.1038/sj.bjc.6604903
205. Boulton JKR, Borri M, Jury A, et al. Investigating intracranial tumour growth patterns with multiparametric MRI incorporating Gd-DTPA and USPIO-enhanced imaging: Dual contrast enhanced MRI of intracranial tumours. *NMR Biomed*. 2016;29(11):1608-1617. doi:10.1002/nbm.3594
206. Gambarota G, Leenders W, Maass C, et al. Characterisation of tumour vasculature in mouse brain by USPIO contrast-enhanced MRI. *Br J Cancer*. 2008;98(11):1784-1789. doi:10.1038/sj.bjc.6604389
207. Kumar V, Boucher Y, Liu H, et al. Noninvasive Assessment of Losartan-Induced Increase in Functional Microvasculature and Drug Delivery in Pancreatic Ductal Adenocarcinoma. *Transl Oncol*. 2016;9(5):431-437. doi:10.1016/j.tranon.2016.07.004
208. Walker-Samuel S, Boulton JKR, McPhail LD, Box G, Eccles SA, Robinson SP. Non-invasive in vivo imaging of vessel calibre in orthotopic prostate tumour xenografts. *Int J Cancer*. 2012;130(6):1284-1293. doi:10.1002/ijc.26112
209. Sigal R, Vogl T, Casselman J, et al. Lymph node metastases from head and neck squamous cell carcinoma: MR imaging with ultrasmall superparamagnetic iron oxide particles (Sinerem MR) – results of a phase-III multicenter clinical trial. *Eur Radiol*. 2002;12(5):1104-1113. doi:10.1007/s003300101130
210. Baghi M, Mack MG, Hambek M, et al. The Efficacy of MRI with Ultrasmall Superparamagnetic Iron Oxide Particles (USPIO) in Head and Neck Cancers. *Anticancer Res*. 2005;25(5):3665-3670.
211. Schwenk MH. Ferumoxytol: a new intravenous iron preparation for the treatment of iron deficiency anemia in patients with chronic kidney disease. *Pharmacotherapy*. 2010;30(1):70-79. doi:10.1592/phco.30.1.70
212. Bashir MR, Bhatti L, Marin D, Nelson RC. Emerging applications for ferumoxytol as a contrast agent in MRI. *J Magn Reson Imaging*. 2014;41(4):884-898. doi:10.1002/jmri.24691

213. Vasanawala SS, Nguyen K-L, Hope MD, et al. Safety and technique of ferumoxytol administration for MRI. *Magn Reson Med*. 2016;75(5):2107–2111. doi:10.1002/mrm.26151
214. Gahramanov S, Raslan AM, Muldoon LL, et al. Potential for Differentiation of Pseudoprogression From True Tumor Progression With Dynamic Susceptibility-Weighted Contrast-Enhanced Magnetic Resonance Imaging Using Ferumoxytol vs. Gadoteridol: A Pilot Study. *Int J Radiat Oncol Biol Phys*. 2011;79(2):514–523. doi:10.1016/j.ijrobp.2009.10.072
215. Varallyay CG, Nesbit E, Fu R, et al. High-Resolution Steady-State Cerebral Blood Volume Maps in Patients with Central Nervous System Neoplasms Using Ferumoxytol, a Superparamagnetic Iron Oxide Nanoparticle. *J Cereb Blood Flow Metab*. 2013;33(5):780–786. doi:10.1038/jcbfm.2013.36
216. Hoskin PJ, Carnell DM, Taylor NJ, et al. Hypoxia in Prostate Cancer: Correlation of BOLD-MRI With Pimonidazole Immunohistochemistry—Initial Observations. *Int J Radiat Oncol*. 2007;68(4):1065-1071. doi:10.1016/j.ijrobp.2007.01.018
217. Wiedenmann N, Bunea H, Rischke HC, et al. Effect of radiochemotherapy on T2* MRI in HNSCC and its relation to FMISO PET derived hypoxia and FDG PET. *Radiat Oncol*. 2018;13(1):159. doi:10.1186/s13014-018-1103-1
218. Chopra S, Foltz WD, Milosevic MF, et al. Comparing oxygen-sensitive MRI (BOLD R2*) with oxygen electrode measurements: A pilot study in men with prostate cancer. *Int J Radiat Biol*. 2009;85(9):805-813. doi:10.1080/09553000903043059
219. Alonzi R. Evaluation of the oxygenation and vascularity of prostate cancer using magnetic resonance imaging. Published online 2007.
220. McPhail LD, Robinson SP. Intrinsic susceptibility MR imaging of chemically induced rat mammary tumors: relationship to histologic assessment of hypoxia and fibrosis. *Radiology*. 2010;254(1):110-118. doi:10.1148/radiol.2541090395
221. Al-Hallaq HA, River JN, Zamora M, Oikawa H, Karczmar GS. Correlation of magnetic resonance and oxygen microelectrode measurements of carbogen-induced changes in tumor oxygenation. *Int J Radiat Oncol • Biol • Phys*. 1998;41(1):151-159.
222. Dunn JF, O'Hara JA, Zaim-Wadghiri Y, et al. Changes in oxygenation of intracranial tumors with carbogen: a BOLD MRI and EPR oximetry study. *J Magn Reson Imaging*. 2002;16(5):511-521. doi:10.1002/jmri.10192
223. Baker LCJ, Sikka A, Price JM, et al. Evaluating Imaging Biomarkers of Acquired Resistance to Targeted EGFR Therapy in Xenograft Models

of Human Head and Neck Squamous Cell Carcinoma. *Front Oncol.* 2018;8. doi:10.3389/fonc.2018.00271

224. Little RA, Jamin Y, Boulton JKR, et al. Mapping Hypoxia in Renal Carcinoma with Oxygen-enhanced MRI: Comparison with Intrinsic Susceptibility MRI and Pathology. *Radiology.* Published online June 2018;171531. doi:10.1148/radiol.2018171531
225. Panek R, Welsh L, Dunlop A, et al. Repeatability and sensitivity of T2* measurements in patients with head and neck squamous cell carcinoma at 3T: Sensitivity of T2* in HNSCC at 3T. *J Magn Reson Imaging.* 2016;44(1):72-80. doi:10.1002/jmri.25134
226. O'Connor JP, Naish JH, Jackson A, et al. Comparison of normal tissue R1 and R2 modulation by oxygen and carbogen. *Magn Reson Med.* 2009;61(1):75-83. doi:10.1002/mrm.21815
227. Silvennoinen MJ, Kettunen MI, Kauppinen RA. Effects of hematocrit and oxygen saturation level on blood spin-lattice relaxation. *Magn Reson Med.* 2003;49(3):568-571. doi:10.1002/mrm.10370
228. Grgac K, Zijl PCM van, Qin Q. Hematocrit and oxygenation dependence of blood 1H2O T1 at 7 tesla. *Magn Reson Med.* 2013;70(4):1153-1159. doi:10.1002/mrm.24547
229. Blockley NP, Jiang L, Gardener AG, Ludman CN, Francis ST, Gowland PA. Field strength dependence of R1 and R2* relaxivities of human whole blood to prohaemoglobin, vasovist, and deoxyhemoglobin. *Magn Reson Med.* 2008;60(6):1313-1320. doi:10.1002/mrm.21792
230. Zhang X, Petersen ET, Ghariq E, et al. In vivo blood T1 measurements at 1.5 T, 3 T, and 7 T. *Magn Reson Med.* 2013;70(4):1082-1086. doi:10.1002/mrm.24550
231. Zaharchuk G, Busse RF, Rosenthal G, Manley GT, Glenn OA, Dillon WP. Noninvasive Oxygen Partial Pressure Measurement of Human Body Fluids In Vivo Using Magnetic Resonance Imaging. *Acad Radiol.* 2006;13(8):1016-1024. doi:10.1016/j.acra.2006.04.016
232. Weissleder R, Cheng HC, Marecos E, Kwong K, Bogdanov A. Non-invasive in vivo mapping of tumour vascular and interstitial volume fractions. *Eur J Cancer.* 1998;34(9):1448-1454. doi:10.1016/S0959-8049(98)00195-6
233. Rofstad EK, Steinsland E, Kaalhus O, Chang YB, Høvik B, Lyng H. Magnetic Resonance Imaging of Human Melanoma Xenografts *in Vivo*: Proton Spin—lattice and Spin—spin Relaxation Times Versus Fractional Tumour Water Content and Fraction of Necrotic Tumour Tissue. *Int J Radiat Biol.* 1994;65(3):387-401. doi:10.1080/09553009414550451

234. Macrì MA, Casieri C, de Luca F, et al. Spin-lattice relaxation in murine tumors after in vivo treatment with interferon α/β or tumor necrosis factor α . *Magn Reson Med*. 1992;23(1):12-20. doi:10.1002/mrm.1910230103
235. Lu H, Clingman C, Golay X, van Zijl PCM. Determining the longitudinal relaxation time (T1) of blood at 3.0 Tesla. *Magn Reson Med*. 2004;52(3):679-682. doi:10.1002/mrm.20178
236. Wu W-C, Jain V, Li C, et al. In vivo venous blood T1 measurement using inversion recovery true-FISP in children and adults. *Magn Reson Med*. 2010;64(4):1140-1147. doi:10.1002/mrm.22484
237. Thulborn KR, Waterton JC, Matthews PM, Radda GK. Oxygenation dependence of the transverse relaxation time of water protons in whole blood at high field. *Biochim Biophys Acta BBA - Gen Subj*. 1982;714(2):265-270. doi:10.1016/0304-4165(82)90333-6
238. Hallac RR, Zhou H, Pidikiti R, et al. Correlations of noninvasive BOLD and TOLD MRI with pO₂ and relevance to tumor radiation response. *Magn Reson Med*. 2014;71(5):1863-1873. doi:10.1002/mrm.24846
239. Burrell JS, Walker-Samuel S, Baker LCJ, et al. Exploring $\Delta R(2)^*$ and $\Delta R(1)$ as imaging biomarkers of tumor oxygenation. *J Magn Reson Imaging*. 2013;38(2):429-434. doi:10.1002/jmri.23987
240. Salem A, Little RA, Latif A, et al. Oxygen-enhanced MRI Is Feasible, Repeatable, and Detects Radiotherapy-induced Change in Hypoxia in Xenograft Models and in Patients with Non-small Cell Lung Cancer. *Clin Cancer Res*. 2019;25(13):3818-3829. doi:10.1158/1078-0432.CCR-18-3932
241. White DA, Zhang Z, Li L, et al. Developing oxygen-enhanced magnetic resonance imaging as a prognostic biomarker of radiation response. *Cancer Lett*. 2016;380(1):69-77. doi:10.1016/j.canlet.2016.06.003
242. Cao-Pham T-T, Tran L-B-A, Colliez F, et al. Monitoring Tumor Response to Carbogen Breathing by Oxygen-Sensitive Magnetic Resonance Parameters to Predict the Outcome of Radiation Therapy: A Preclinical Study. *Int J Radiat Oncol*. 2016;96(1):149-160. doi:10.1016/j.ijrobp.2016.04.029
243. Cao-Pham T-T, Joudiou N, Hul MV, et al. Combined endogenous MR biomarkers to predict basal tumor oxygenation and response to hyperoxic challenge. *NMR Biomed*. 2017;30(12):e3836. doi:10.1002/nbm.3836
244. Panek R. Oxygen-Enhanced MRI for the detection of hypoxia in patients with head and neck cancer. Electronic poster presentation presented at the: ISMRM; July 2018; Paris, France.

245. Bluemke E, Bulte D, Bertrand A, et al. Oxygen-enhanced MRI MOLLI T1 mapping during chemoradiotherapy in anal squamous cell carcinoma. *Clin Transl Radiat Oncol.* 2020;22:44-49. doi:10.1016/j.ctro.2020.03.001
246. Moosvi F, Baker JHE, Yung A, Kozlowski P, Minchinton AI, Reinsberg SA. Fast and sensitive dynamic oxygen-enhanced MRI with a cycling gas challenge and independent component analysis. *Magn Reson Med.* Published online October 2018. doi:10.1002/mrm.27584
247. Yang DM, Arai TJ, Campbell JW, Gerberich JL, Zhou H, Mason RP. Oxygen-sensitive MRI assessment of tumor response to hypoxic gas breathing challenge. *NMR Biomed.* Published online May 7, 2019:e4101. doi:10.1002/nbm.4101
248. Jordan BF, Magat J, Colliez F, et al. Mapping of oxygen by imaging lipids relaxation enhancement: A potential sensitive endogenous MRI contrast to map variations in tissue oxygenation: MRI Contrast to Map Variations in Tissue Oxygenation. *Magn Reson Med.* 2013;70(3):732-744. doi:10.1002/mrm.24511
249. Bennett HF, Swartz HM, Brown RDI, Koenig SH. Modification of Relaxation of Lipid Protons by Molecular Oxygen and Nitroxides. *Invest Radiol.* 1987;22(6):502–507.
250. Safronova MM, Colliez F, Magat J, et al. Mapping of global R1 and R2* values versus lipids R1 values as potential markers of hypoxia in human glial tumors: A feasibility study. *Magn Reson Imaging.* 2016;34(2):105-113. doi:10.1016/j.mri.2015.10.021
251. Brizel DM, Dodge RK, Clough RW, Dewhirst MW. Oxygenation of head and neck cancer: changes during radiotherapy and impact on treatment outcome. *Radiother Oncol.* 1999;53(2):113–117.
252. Sims TL, McGee M, Williams RF, et al. IFN- Restricts Tumor Growth and Sensitizes Alveolar Rhabdomyosarcoma to Ionizing Radiation. *Mol Cancer Ther.* 2010;9(3):761–771. doi:10.1158/1535-7163.mct-09-0800
253. Box C, Mendiola M, Gowan S, et al. A novel serum protein signature associated with resistance to epidermal growth factor receptor tyrosine kinase inhibitors in head and neck squamous cell carcinoma. *Eur J Cancer.* 2013;49(11):2512-2521. doi:10.1016/j.ejca.2013.03.011
254. Gioanni J, Fischel J-L, Lambert J-C, et al. Two new human tumor cell lines derived from squamous cell carcinomas of the tongue: Establishment, characterization and response to cytotoxic treatment. *Eur J Cancer Clin Oncol.* 1988;24(9):1445-1455. doi:10.1016/0277-5379(88)90335-5

255. Easty DM, Easty GC, Carter RL, Monaghan P, Butler LJ. Ten human carcinoma cell lines derived from squamous carcinomas of the head and neck. *Br J Cancer*. 1981;43(6):772-785. doi:10.1038/bjc.1981.115
256. Williams RD, Elliott AY, Stein N, Fraley EE. In vitro cultivation of human renal cell cancer: I. Establishment of cells in culture. *In Vitro*. 1976;12(9):623-627. doi:10.1007/BF02797460
257. Bridgeman VL, Wan E, Foo S, et al. Preclinical Evidence That Trametinib Enhances the Response to Antiangiogenic Tyrosine Kinase Inhibitors in Renal Cell Carcinoma. *Mol Cancer Ther*. 2015;15(1):172–183. doi:10.1158/1535-7163.mct-15-0170
258. Houghton PJ, Morton CL, Tucker C, et al. The pediatric preclinical testing program: Description of models and early testing results. *Pediatr Blood Cancer*. 2007;49(7):928-940. doi:10.1002/pbc.21078
259. Workman P, Aboagye EO, Balkwill F, et al. Guidelines for the welfare and use of animals in cancer research. *Br J Cancer*. 2010;102(11):1555-1577. doi:10.1038/sj.bjc.6605642
260. Kilkenny C, Browne WJ, Cuthill IC, Emerson M, Altman DG. Improving Bioscience Research Reporting: The ARRIVE Guidelines for Reporting Animal Research. *PLoS Biol*. 2010;8(6):e1000412. doi:10.1371/journal.pbio.1000412
261. Boulton JK, Walker-Samuel S, Jamin Y, Leiper JM, Whitley GSJ, Robinson SP. Active site mutant dimethylarginine dimethylaminohydrolase 1 expression confers an intermediate tumour phenotype in C6 gliomas. *J Pathol*. 2011;225(3):344-352. doi:10.1002/path.2904
262. Sigovan M, Boussel L, Sulaiman A, et al. Rapid-Clearance Iron Nanoparticles for Inflammation Imaging of Atherosclerotic Plaque: Initial Experience in Animal Model. *Radiology*. 2009;252(2):401-409. doi:10.1148/radiol.2522081484
263. Schmitt P, Griswold MA, Jakob PM, et al. Inversion recovery TrueFISP: Quantification of T1, T2, and spin density. *Magn Reson Med*. 2004;51(4):661–667. doi:10.1002/mrm.20058
264. Madsen EL, Fullerton GD. Prospective tissue-mimicking materials for use in NMR imaging phantoms. *Magn Reson Imaging*. 1982;1(3):135-141. doi:10.1016/0730-725X(82)90204-1
265. Blechinger JC, Madsen EL, Frank GR. Tissue-mimicking gelatin-agar gels for use in magnetic resonance imaging phantoms: Technical Reports: Gelatin-agar gels for use in MRI phantoms. *Med Phys*. 1988;15(4):629-636. doi:10.1118/1.596219
266. Baird DK, Kincaid SA, Hathcock JT, Rumph PF, Kammerman J, Visco DM. Effect of Hydration on Signal Intensity of Gelatin Phantoms Using

Low-Field Magnetic Resonance Imaging: Possible Application in Osteoarthritis. *Vet Radiol Ultrasound*. 1999;40(1):27-35. doi:10.1111/j.1740-8261.1999.tb01835.x

267. Deoni SCL, Rutt BK, Jones DK. Investigating exchange and multicomponent relaxation in fully-balanced steady-state free precession imaging. *J Magn Reson Imaging*. 2008;27(6):1421-1429. doi:10.1002/jmri.21079
268. Tropres I, Grimault S, Vaeth A, et al. Vessel size imaging. *Magn Reson Med*. 2001;45(3):397-408. doi:10.1002/1522-2594(200103)45:3<397::AID-MRM1052>3.0.CO;2-3
269. Hydroxyprobe. Hypoxyprobe™ Plus Kit product insert. Hydroxyprobe. Published 2017. Accessed July 20, 2020. <http://site.hypoxyprobe.com/knowledge-center-articles/HP-Plus-Kit-Insert.pdf>
270. Raza A, Colley HE, Baggaley E, et al. Oxygen Mapping of Melanoma Spheroids using Small Molecule Platinum Probe and Phosphorescence Lifetime Imaging Microscopy. *Sci Rep*. 2017;7(1):10743. doi:10.1038/s41598-017-11153-9
271. Tello VM, Tailor RC, Hanson WF. How water equivalent are water-equivalent solid materials for output calibration of photon and electron beams? *Med Phys*. 1995;22(7):1177-1189. doi:10.1118/1.597613
272. Costa MM, Shah A, Rivens I, et al. Photoacoustic imaging for the prediction and assessment of response to radiotherapy in vivo. *bioRxiv*. Published online May 23, 2018:329516. doi:10.1101/329516
273. Brueningk SC, Costa M, Box C, et al. EP-2335: 3D tumour spheroids as an alternative to clonogenic assays for predicting radiation response in vivo. *Radiother Oncol*. 2018;127:S1288. doi:10.1016/S0167-8140(18)32644-6
274. Little R, Tessayman V, Babur M, et al. In vivo OE-MRI quantification and mapping of response to hypoxia modifying drugs banoxantrone and atovaquone in Calu6 xenografts. In: ISMRM; 2017. <http://indexsmart.mirasmart.com/ISMRM2017/PDFfiles/2919.html>
275. Daldrup HE, Shames DM, Hussein W, Wendland MF, Okuhata Y, Brasch RC. Quantification of the extraction fraction for gadopentetate across breast cancer capillaries. *Magn Reson Med*. 1998;40(4):537-543. doi:10.1002/mrm.1910400406
276. Jamin Y, Glass L, Hallsworth A, et al. Intrinsic Susceptibility MRI Identifies Tumors with ALKF1174L Mutation in Genetically-Engineered Murine Models of High-Risk Neuroblastoma. Castro MG, ed. *PLoS ONE*. 2014;9(3):e92886. doi:10.1371/journal.pone.0092886

277. Zormpas-Petridis K, Jerome NP, Blackledge MD, et al. MRI Imaging of the Hemodynamic Vasculature of Neuroblastoma Predicts Response to Antiangiogenic Treatment. *Cancer Res.* 2019;79(11):2978-2991. doi:10.1158/0008-5472.CAN-18-3412
278. Troprès I, Lamalle L, Péoc'h M, et al. In vivo assessment of tumoral angiogenesis. *Magn Reson Med.* 2004;51(3):533-541. doi:10.1002/mrm.20017
279. Robinson SP, Boulton JKR, Vasudev NS, Reynolds AR. Monitoring the Vascular Response and Resistance to Sunitinib in Renal Cell Carcinoma *In Vivo* with Susceptibility Contrast MRI. *Cancer Res.* 2017;77(15):4127-4134. doi:10.1158/0008-5472.CAN-17-0248
280. Look DC, Locker DR. Time Saving in Measurement of NMR and EPR Relaxation Times. *Rev Sci Instrum.* 1970;41(2):250-251. doi:10.1063/1.1684482
281. Haase A. Snapshot FLASH MRI. Applications to T1, T2, and chemical-shift imaging. *Magn Reson Med.* 1990;13(1):77-89. doi:10.1002/mrm.1910130109
282. Oppelt A, Graumann R, Barfuss H, Fischer H, Hartl W, Schajor W. FISP—a new fast MRI sequence. *Electromedica.* 1986;54(1):15-18.
283. Deimling M, Heid O. Magnetization prepared true FISP imaging. In: ; 1994:495.
284. Scheffler K, Hennig J. T1 quantification with inversion recovery TrueFISP. *Magn Reson Med.* 2001;45(4):720–723. doi:10.1002/mrm.1097
285. Ogawa S, Lee T-M, Nayak AS, Glynn P. Oxygenation-sensitive contrast in magnetic resonance image of rodent brain at high magnetic fields. *Magn Reson Med.* 1990;14(1):68-78. doi:10.1002/mrm.1910140108
286. Baudelet C, Gallez B. Current Issues in the Utility of Blood Oxygen Level Dependent MRI for the Assessment of Modulations in Tumor Oxygenation. *Curr Med Imaging Rev.* 2005;1(3):229-243. doi:10.2174/157340505774574754
287. Al-Hallaq HA, River JN, Zamora M, Oikawa H, Karczmar GS. Correlation of magnetic resonance and oxygen microelectrode measurements of carbogen-induced changes in tumor oxygenation. *Int J Radiat Oncol • Biol • Phys.* 1998;41(1):151-159.
288. Robinson SP, Howe FA, Rodrigues LM, Stubbs M, Griffiths JR. Magnetic resonance imaging techniques for monitoring changes in tumor oxygenation and blood flow. *Semin Radiat Oncol.* 1998;8(3):197-207.

289. Baker LC, Boulton JK, Jamin Y, et al. Evaluation and immunohistochemical qualification of carbogen-induced DeltaR(2) as a noninvasive imaging biomarker of improved tumor oxygenation. *Int J Radiat Oncol • Biol • Phys.* 2013;87(1):160-167. doi:10.1016/j.ijrobp.2013.04.051
290. O'Connor JPB, Robinson SP, Waterton JC. Imaging tumour hypoxia with oxygen-enhanced MRI and BOLD MRI. *Br J Radiol.* Published online January 2019:20180642. doi:10.1259/bjr.20180642
291. Robinson SP, Collingridge DR, Howe FA, Rodrigues LM, Chaplin DJ, Griffiths JR. Tumour response to hypercapnia and hyperoxia monitored by FLOOD magnetic resonance imaging. *NMR Biomed.* 1999;12(2):98-106. doi:10.1002/(SICI)1099-1492(199904)12:2<98::AID-NBM556>3.0.CO;2-I
292. Neeman M, Dafni H, Bukhari O, Braun RD, Dewhirst MW. In vivo BOLD contrast MRI mapping of subcutaneous vascular function and maturation: Validation by intravital microscopy. *Magn Reson Med.* 2001;45(5):887-898. doi:10.1002/mrm.1118
293. Stubbs M, Robinson S, Rodrigues L, Parkins C, Collingridge D, Griffiths J. The effects of host carbogen (95% oxygen/5% carbon dioxide) breathing on metabolic characteristics of Morris hepatoma 9618a. *Br J Cancer.* 1998;78(11):1449-1456. doi:10.1038/bjc.1998.706
294. Liu Z, Jia X, Duan Y, et al. Excess glucose induces hypoxia-inducible factor-1 α in pancreatic cancer cells and stimulates glucose metabolism and cell migration. *Cancer Biol Ther.* 2013;14(5):428-435. doi:10.4161/cbt.23786
295. Kostourou V, Robinson SP, Whitley GStJ, Griffiths JR. Effects of Overexpression of Dimethylarginine Dimethylaminohydrolase on Tumor Angiogenesis Assessed by Susceptibility Magnetic Resonance Imaging. *Cancer Res.* 2003;63(16):4960.
296. Robinson SP, Howe FA, Griffiths JR, Ryan AJ, Waterton JC. Susceptibility Contrast Magnetic Resonance Imaging Determination of Fractional Tumor Blood Volume: A Noninvasive Imaging Biomarker of Response to the Vascular Disrupting Agent ZD6126. *Int J Radiat Oncol.* 2007;69(3):872-879. doi:10.1016/j.ijrobp.2007.06.061
297. Hannen EJM, van der Laak JAWM, Manni JJ, et al. Computer assisted analysis of the microvasculature in metastasized and nonmetastasized squamous cell carcinomas of the tongue. *Head Neck.* 2002;24(7):643-650. doi:10.1002/hed.10100
298. Remmele S, Sprinkart AM, Müller A, et al. Dynamic and simultaneous MR measurement of R1 and R2* changes during respiratory challenges for the assessment of blood and tissue oxygenation. *Magn Reson Med.* 2013;70(1):136-146. doi:10.1002/mrm.24458

299. Azuma Y, Chou S-C, Lininger RA, Murphy BJ, Varia MA, Raleigh JA. Hypoxia and Differentiation in Squamous Cell Carcinomas of the Uterine Cervix. *Clin Cancer Res.* 2003;9(13):4944.
300. Kim Y, Lin Q, Glazer P, Yun Z. Hypoxic Tumor Microenvironment and Cancer Cell Differentiation. *Curr Mol Med.* 2009;9(4):425-434. doi:10.2174/156652409788167113
301. Raleigh JA, Chou S-C, Calkins-Adams DP, Ballenger CA, Novotny DB, Varia MA. A Clinical Study of Hypoxia and Metallothionein Protein Expression in Squamous Cell Carcinomas. *Clin Cancer Res.* 2000;6(3):855-862.
302. Wu C-P, Du H-D, Gong H-L, et al. Hypoxia promotes stem-like properties of laryngeal cancer cell lines by increasing the CD133+ stem cell fraction. *Int J Oncol.* 2014;44(5):1652-1660. doi:10.3892/ijo.2014.2307
303. Winter JD, Akens MK, Cheng H-LM. Quantitative MRI assessment of VX2 tumour oxygenation changes in response to hyperoxia and hypercapnia. *Phys Med Biol.* 2011;56(5):1225-1242. doi:10.1088/0031-9155/56/5/001
304. Brizel DM, Hage WD, Dodge RK, Munley MT, Piantadosi CA, Dewhirst MW. Hyperbaric Oxygen Improves Tumor Radiation Response Significantly More Than Carbogen/Nicotinamide. *Radiat Res.* 1997;147(6):715. doi:10.2307/3579485
305. Brizel D, Lin S, Johnson J, Brooks J, Dewhirst M, Piantadosi C. The mechanisms by which hyperbaric oxygen and carbogen improve tumour oxygenation. *Br J Cancer.* 1995;72(5):1120-1124. doi:10.1038/bjc.1995.474
306. Tofts PS, Berkowitz BA. Rapid Measurement of Capillary Permeability Using the Early Part of the Dynamic Gd-DTPA MRI Enhancement Curve. *J Magn Reson B.* 1993;102(2):129-136. doi:10.1006/jmrb.1993.1075
307. Abdel Razek AA, Kandeel AY, Soliman N, et al. Role of diffusion-weighted echo-planar MR imaging in differentiation of residual or recurrent head and neck tumors and posttreatment changes. *AJNR Am J Neuroradiol.* 2007;28(6):1146-1152. doi:10.3174/ajnr.A0491
308. Wang J, Takashima S, Takayama F, et al. Head and Neck Lesions: Characterization with Diffusion-weighted Echo-planar MR Imaging. *Radiology.* 2001;220(3):621-630. doi:10.1148/radiol.2202010063
309. Sumi M, Sakihama N, Sumi T, et al. Discrimination of Metastatic Cervical Lymph Nodes with Diffusion-Weighted MR Imaging in Patients with Head and Neck Cancer. *Am J Neuroradiol.* 2003;24(8):1627.

310. Vandecaveye V, De Keyzer F, Vander Poorten V, et al. Head and Neck Squamous Cell Carcinoma: Value of Diffusion-weighted MR Imaging for Nodal Staging. *Radiology*. 2009;251(1):134-146. doi:10.1148/radiol.2511080128
311. Vandecaveye V, De Keyzer F, Nuyts S, et al. Detection of head and neck squamous cell carcinoma with diffusion weighted MRI after (chemo)radiotherapy: Correlation between radiologic and histopathologic findings. *Int J Radiat Oncol*. 2007;67(4):960-971. doi:http://dx.doi.org/10.1016/j.ijrobp.2006.09.020
312. Zhou H, Hallac R, Yuan Q, et al. Incorporating Oxygen-Enhanced MRI into Multi-Parametric Assessment of Human Prostate Cancer. *Diagnostics*. 2017;7(3):48. doi:10.3390/diagnostics7030048
313. Siregar JE, Kurisu G, Kobayashi T, et al. Direct evidence for the atovaquone action on the Plasmodium cytochrome bc 1 complex. *Parasitol Int*. 2015;64(3):295-300. doi:10.1016/j.parint.2014.09.011
314. Zormpas-Petridis K, Poon E, Clarke M, et al. Noninvasive MRI native T1 mapping detects response to MYCN-targeted therapies in the Th-MYCN model of neuroblastoma. *Cancer Res*. Published online June 28, 2020:canres.0133.2020. doi:10.1158/0008-5472.CAN-20-0133
315. Wang HZ, Riederer SJ, Lee JN. Optimizing the precision in T1 relaxation estimation using limited flip angles. *Magn Reson Med*. 1987;5(5):399-416. doi:10.1002/mrm.1910050502
316. Cheng H-LM, Wright GA. Rapid high-resolution T1 mapping by variable flip angles: Accurate and precise measurements in the presence of radiofrequency field inhomogeneity. *Magn Reson Med*. 2006;55(3):566-574. doi:10.1002/mrm.20791
317. Kobayashi H. Application of a Macromolecular Contrast Agent for Detection of Alterations of Tumor Vessel Permeability Induced by Radiation. *Clin Cancer Res*. 2004;10(22):7712-7720. doi:10.1158/1078-0432.CCR-04-1175
318. Abdel Razek AAK, Gaballa G, Ashamalla G, Alashry MS, Nada N. Dynamic Susceptibility Contrast Perfusion-Weighted Magnetic Resonance Imaging and Diffusion-Weighted Magnetic Resonance Imaging in Differentiating Recurrent Head and Neck Cancer From Postradiation Changes. *J Comput Assist Tomogr*. 2015;39(6):849-854. doi:10.1097/rct.0000000000000311
319. Razek AAKA, Elsorogy LG, Soliman NY, Nada N. Dynamic susceptibility contrast perfusion MR imaging in distinguishing malignant from benign head and neck tumors: A pilot study. *Eur J Radiol*. 2011;77(1):73-79. doi:10.1016/j.ejrad.2009.07.022

320. Abdel Razek AAK, Samir S, Ashmalla GA. Characterization of Parotid Tumors With Dynamic Susceptibility Contrast Perfusion-Weighted Magnetic Resonance Imaging and Diffusion-Weighted MR Imaging: *J Comput Assist Tomogr.* 2017;41(1):131-136. doi:10.1097/RCT.0000000000000486
321. Willats L, Calamante F. The 39 steps: evading error and deciphering the secrets for accurate dynamic susceptibility contrast MRI. *NMR Biomed.* 2013;26(8):913-931. doi:https://doi.org/10.1002/nbm.2833
322. Jahng G-H, Li K-L, Ostergaard L, Calamante F. Perfusion Magnetic Resonance Imaging: A Comprehensive Update on Principles and Techniques. *Korean J Radiol.* 2014;15(5):554-577. doi:10.3348/kjr.2014.15.5.554
323. Jin S, Kang M, Cho H. Cerebral blood perfusion deficits using dynamic susceptibility contrast MRI with gadolinium chelates in rats with post-ischemic reperfusion without significant dynamic contrast-enhanced MRI-derived vessel permeabilities: A cautionary note. *PLOS ONE.* 2018;13(7):e0201076. doi:10.1371/journal.pone.0201076
324. Marckmann P, Skov L, Rossen K, et al. Nephrogenic Systemic Fibrosis: Suspected Causative Role of Gadodiamide Used for Contrast-Enhanced Magnetic Resonance Imaging. *J Am Soc Nephrol.* 2006;17(9):2359-2362. doi:10.1681/ASN.2006060601
325. Grobner T. Gadolinium – a specific trigger for the development of nephrogenic fibrosing dermopathy and nephrogenic systemic fibrosis? *Nephrol Dial Transplant.* 2006;21(4):1104-1108. doi:10.1093/ndt/gfk062
326. Kanda T, Ishii K, Kawaguchi H, Kitajima K, Takenaka D. High Signal Intensity in the Dentate Nucleus and Globus Pallidus on Unenhanced T1-weighted MR Images: Relationship with Increasing Cumulative Dose of a Gadolinium-based Contrast Material. *Radiology.* 2013;270(3):834-841. doi:10.1148/radiol.13131669
327. Bashir MR, Mody R, Neville A, et al. Retrospective assessment of the utility of an iron-based agent for contrast-enhanced magnetic resonance venography in patients with endstage renal diseases. *J Magn Reson Imaging.* 2014;40(1):113-118.
328. McCullough BJ, Kolokythas O, Maki JH, Green DE. Ferumoxytol in clinical practice: Implications for MRI. *J Magn Reson Imaging.* 2013;37(6):1476-1479. doi:10.1002/jmri.23879
329. Ning P, Zucker EJ, Wong P, Vasanawala SS. Hemodynamic safety and efficacy of ferumoxytol as an intravenous contrast agents in pediatric patients and young adults. *Magn Reson Imaging.* 2016;34(2):152-158. doi:10.1016/j.mri.2015.10.019

330. Fredrickson J, Serkova NJ, Wyatt SK, et al. Clinical translation of ferumoxytol-based vessel size imaging (VSI): Feasibility in a phase I oncology clinical trial population. *Magn Reson Med*. 2017;77(2):814-825. doi:10.1002/mrm.26167
331. Wang F, Jiang RT, Tantawy MN, et al. Repeatability and Sensitivity of High Resolution Blood Volume Mapping in Mouse Kidney Disease. *J Magn Reson Imaging JMRI*. 2014;39(4):866-871. doi:10.1002/jmri.24242
332. Vieira SC, Silva BB, Pinto GA, et al. CD34 as a marker for evaluating angiogenesis in cervical cancer. *Pathol - Res Pract*. 2005;201(4):313-318. doi:10.1016/j.prp.2005.01.010
333. Ito Y, Kamijo T, Yokose T, et al. Microvessel density predicts the radiosensitivity of metastatic head and neck squamous cell carcinoma in cervical lymph nodes. *Int J Oncol*. Published online December 1, 2001. doi:10.3892/ijo.19.6.1127
334. Quiet CA, Weichselbaum RR, Grdina DJ. Variation in radiation sensitivity during the cell cycle of two human squamous cell carcinomas. *Int J Radiat Oncol*. 1991;20(4):733-738. doi:10.1016/0360-3016(91)90016-W
335. Brüningk SC. Analysis and simulation of combination treatments of radiation and focused ultrasound mediated heating. Published online September 2018.
336. Bernauer C, Man YK, Chisholm J, Lopicard EY, Robinson SP, Shipley JM. Hypoxia and its therapeutic possibilities in paediatric cancers. *Br J Cancer*.
337. Reinhart AM, Fast MF, Ziegenhein P, Nill S, Oelfke U. A kernel-based dose calculation algorithm for kV photon beams with explicit handling of energy and material dependencies. *Br J Radiol*. 2016;90(1069):20160426. doi:10.1259/bjr.20160426
338. Corroyer-Dulmont A, Falzone N, Kersemans V, et al. MRI-guided radiotherapy of the SK-N-SH neuroblastoma xenograft model using a small animal radiation research platform. *Br J Radiol*. 2016;90(1069):20160427. doi:10.1259/bjr.20160427
339. Lagendijk JJW, Raaymakers BW, van Vulpen M. The Magnetic Resonance Imaging–Linac System. *Semin Radiat Oncol*. 2014;24(3):207-209. doi:10.1016/j.semradonc.2014.02.009
340. Secomb TW, Hsu R, Ong ET, Gross JF, Dewhirst MW. Analysis of the Effects of Oxygen Supply and Demand on Hypoxic Fraction in Tumors. *Acta Oncol*. 1995;34(3):313-316. doi:10.3109/02841869509093981

341. Crockart N, Radermacher K, Jordan BF, et al. Tumor Radiosensitization by Antiinflammatory Drugs: Evidence for a New Mechanism Involving the Oxygen Effect. *Cancer Res.* 2005;65(17):7911-7916. doi:10.1158/0008-5472.CAN-05-1288